A thermofluid network-based methodology for integrated simulation of heat transfer and combustion in a pulverized coal-fired furnace

Prepared by:

Willem Arie van der Meer

VMRWIL011

Department of Mechanical Engineering

University of Cape Town

Supervisor:

Prof. Pieter Gerhardus Rousseau

Co-supervisor:

Prof. Louis Jestin

Thesis presented for the Degree of DOCTOR OF PHILOSOPHY in the Department of Mechanical Engineering.

UNIVERSITY OF CAPE TOWN

February 2020

Key Words: ZONAL METHOD; COAL COMBUSTION; PROCESS CONDITION MONITORING; FURNACE EXIT TEMPERATURE; FURNACE HEAT TRANSFER; SYSTEM LEVEL MODELLING TOOL.

Abstract

Coal-fired power plant boilers consist of several complex subsystems that all need to work together to ensure plant availability, efficiency and safety, while limiting emissions. Analysing this multi-objective problem requires a thermofluid process model that can simulate the water/steam cycle and the coal/air/flue gas cycle for steady-state and dynamic operational scenarios, in an integrated manner. The furnace flue gas side can be modelled using a suitable zero-dimensional model in a quasi-steady manner, but this will only provide an overall heat transfer rate and a single gas temperature. When more detail is required, CFD is the tool of choice. However, the solution times can be prohibitive.

A need therefore exists for a computationally efficient model that captures the three-dimensional radiation effects, flue gas exit temperature profile, carbon burnout and O_2 and CO_2 concentrations, while integrated with the steam side process model for dynamic simulations. A thermofluid network-based methodology is proposed that combines the zonal method to model the radiation heat transfer in three dimensions with a one-dimensional burnout model for the heat generation, together with characteristic flow maps for the mass transfer.

Direct exchange areas are calculated using a discrete numerical integration approximation together with a suitable smoothing technique. Models of Leckner and Yin are applied to determine the gas and particle radiation properties, respectively. For the heat sources the burnout model developed by the British Coal Utilisation Research Association is employed and the advection terms of the mass flow are accounted for by superimposing a mass flow map that is generated via an isothermal CFD solution.

The model was first validated by comparing it with empirical data and other numerical models applied to the IFRF single-burner furnace. The full scale furnace model was then calibrated and validated via detailed CFD results for a wall-fired furnace operating at full load. The model was shown to scale well to other load conditions and real plant measurements. Consistent results were obtained for sensitivity studies involving coal quality, particle size distribution, furnace fouling and burner operating modes. The ability to do co-simulation with a steam-side process model in Flownex® was successfully demonstrated for steady-state and dynamic simulations.

Declarations

I, Willem Arie van der Meer, hereby declare the work contained in this thesis to be my own. All information which has been gained from various journal articles, text books or other sources has been referenced accordingly. I have not allowed, and will not allow, anyone to copy my work with the intention of passing it off as their own work or part thereof.

Signature: Signed by candidate

Name: Willem Arie van der Meer

Date: 2020/08/07

I hereby confirm that I have been granted permission by the University of Cape Town's Doctoral Degrees Board to include parts of the following publication(s) in my PhD thesis, and where co-authorships are involved, my co-authors have agreed that I may include the publication(s):

- Van der Meer, W.A., Rousseau, P.G. & Jestin, L. 2016. A system level model of the heat transfer of a single down-fired burner in a rectangular furnace based on a zonal approach. *Second Eskom Power Plant Engineering Institute Student Workshop*, Eskom Academy of Learning, 11 & 12 July.
- Van der Meer, W.A., Rousseau, P.G. & Jestin, L. 2016. A system level modeling approach for combustion and radiative heat transfer in a single-burner furnace based on a zonal method. *4th International Conference on Contemporary Problems of Thermal Engineering, CPOTE 2016*. 14-16 September 2016. Katowice, Poland: Institute of Thermal Technology.
- Van der Meer, W.A., Rousseau, P.G. & Jestin, L. 2016. A methodology for the integrated system simulation of the heat transfer and combustion in a coal-fired boiler furnace. *10th South African Conference on Computational and Applied Mechanics*. 3-5 October 2016. Potchefstroom.
- Van der Meer, W.A., Rousseau, P.G. & Naidoo, R. 2019. A thermofluid network based methodology for integrated system simulation of heat transfer and combustion in a coal-fired furnace. *Thermal Science and Engineering Progress*. 10:253-267.

Signature: Signed by candidate

Name: Willem Arie van der Meer

Date: 2020/08/07

Acknowledgements

The author wants to thank the following:

- The One who gave me the gifts of knowledge in the field as well as the time and perseverance to complete the research contained as a contribution in this document.
- The THRIP program, M-Tech Industrial and the Eskom Power Plant Engineering Institute (EPPEI) for the funding and support provided.
- My supervisor, Prof. Pieter Rousseau, for this guidance, personally and technically throughout the research.
- My co-supervisor, Prof. Louis Jestin, for this technical guidance throughout the research.
- Dr. Ryno Laubscher and Reshendren Naidoo for their technical collaboration and contribution to some of the work used in the research.
- The Taylors for accommodating me every time in Rondebosch when I went for a period's stay near the University of Cape Town for meetings and to present my work.
- Ms. Whitney Monnaemang for her valuable input doing a Master's focussing on technical work that I could easily integrate into my work as well as helping out with proofreading my work.
- My family and friends for enquiring and supporting me throughout the years.

Table of contents

List of figures

List of tables

List of nomenclature

Variables

a	Fraction [-] / Variable absorptivity calculations
ASH	Ash fraction in coal as received [-]
b	Variable absorptivity calculations
A	Surface area [m^2]
α	Excess air coefficient [-]
β	Extinction coefficient [m]
c	Variable absorptivity calculations
C	Carbon fraction in coal as received [-] or pre-exponent factor [$g/m^2 \cdot s \cdot atm$]
C'	Unburned coal fraction [-]
d	Diameter [m]
DAR	Dry air required [kg air / kg coal]
dt	Travel time for a parcel of fixed carbon [s]
du	Burnout for a parcel of fixed carbon [-]
E	Blackbody emissive power [kW/m^2] or Activation energy [kJ/mol]
ε	Surface emissivity [-]
$\Delta\varepsilon$	Emissivity correction factor [-]
G	Mass without ash content [kg]
$\overline{GG}$	Total exchange area from volume i to volume j [m^2]
$\overline{GS}$	Total exchange area from volume i to surface j [m^2]
H	Hydrogen fraction in coal as received [-]
HAR	Humid air required [kg air / kg coal]
k	Factor in fly ash, luminous flame or coal flame absorptivity calculations [-]
κ	Planck-mean gas/extinction factor contribution due absorption [m^{-1}]
h	Enthalpy [kJ/kg]
K	Reaction rate [$g/m^2 \cdot s \cdot atm$]
L	Optical mean beam length [m or cm]
$\dot{m}$	Total mass flow rate [kg/s]

Q	Efficiency factor [m^{-3}]
$\dot{Q}$	The heat transfer [kW]
R	Heat transfer resistance [$m^{-2}K/W$]
n	Number [-]
N	Number of particles [-] or nitrogen fraction in coal as received [-]
O	Oxygen fraction in coal as received [-]
p	Total pressure [bar]
p_a	Partial pressure [bar]
P_E	Variable absorptivity calculations
r	Distance [m]
R	Universal gas constant [kJ/mol·K]
r	Maximum residual
r_{NO_2}	Nitrogen oxidization ratio [-]
ρ	Density [kg/m^3]
S	Surface area after devolatilisation [m^2] or sulphur fraction in coal as received [-]
σ	Absorptivity
$\overline{SG}$	Total exchange area from surface to volume [m^2]
SP	Set-point
$\overline{ss}$	Surface to surface direct exchange area [m^2]
$\overline{SS}$	Total exchange area from surface to surface [m^2]
t	Ratio of gas and reference temperature in absorptivity calculations [-]
T	Temperature [K]
TAR	Theoretical air required [kg air/kg coal]
T''	Temperature at furnace exit [K]
θ	Angle between surfaces or volumes [°]
UC	Fraction of unburned fixed carbon [-]
V	Volume of each zone [m^3]
VC	Fraction volatile carbon [-]
$VM(x)$	Fraction of total volatile matter evolved (burned) [-]
$VM(x_0)$	Total volatile matter in the coal [-]

u	Concentration [1/kg]
w	Mass of unburned fixed carbon relative the mass of all the consituents in the coal [-]
ω	Humidity ratio [kg/kg]
x	Distance of particles travelled from burner [m]
x_1	Factor in coal flame absorptivity calculations [-]
x_2	Factor in coal flame absorptivity calculations [-]
x_f	Distance to complete evolution [m]
ζ	Ratio of water vapour to water vapour and carbon dioxide partial pressure [-]

Subscripts and superscripts

0	At zero partial pressure, reference point or immediately after devolatilisation
abs	Absorption
ash	Ash content
c	Luminous flame or coal
co	Coal flame
diff	Diffusion
e	Gas and particles exiting a zone.
f	Fluid or Fouling
F	Fuel
fa	Fly ash
g	Volume (gas)
heat	Heat transfer
i	Surface, volume or zone *i* or inlet plane for gas and particles entering a zone
j	Surface or volume or zone *j*
load	Operating load
m	Mean
p	Particles
PA	Primary air
rad	Radiation heat transfer

s	Surface
SA	Secondary air
source	Heat source
t	Total
temp	Temperature
ti	Tube inside
UC	Unburned carbon
v	Volumes
w	Wall
z	Bin number or particle size fraction

Acronyms and abbreviations

ANN	Artificial Neural Networks
API	Application Program Interface
BCURA	British Coal Utilization Research Association
BFB	Bubbling Fluidised Bed
BOST	Boiler Simulation Tool
CCP	Carbon Capture Plant
CFB	Circulating Fluidised Bed
CFD	Computational Fluid Dynamics
CPD	Chemical Percolation Devolatilization
CPFD	Computational Particle Fluid Dynamics
CP	Crossover Pass
CTF	Combustion Test Facility
DAEM	Distributed Actived Energy Model
DEA	Direct Exchange Area
DO	Discrete Ordinate
DTF	Drop Tube Furnace
FEGT	Furnace Exit Gas Temperature

FGD	Flue Gas Desulphurization
FG-DVC	Functional Group Depolymerization Vaporization Cross-linking
GA	Genetic Algorithms
IFRF	International Flame Research Foundation
NO	Nitric oxide
RH	Reheater
RNM	Reactor Network Model
ROM	Reduced Order Model
RSM	Reynolds Stress Model
RTE	Radiative Heat Transfer Equation
SCR	Selective Catalytic Reduction
SH	Superheater
SP	Second Pass
TEA	Total Exchange Area

1. Introduction

1.1 Background

The power utility industry is under continuous pressure to lower electricity production costs while at the same time complying with ever stricter regulations. South African power generation is dominated by large coal-fired power plants that were designed for baseload operation. These are now required to be much more flexible to accommodate intermittent renewable generation from solar and wind added to the grid. In addition, a fine balance is still required between ensuring safety, maintaining capacity, improving efficiency, reducing emissions, minimising production cost and preserving reliability and availability (EPRI, 2001) while lowering electricity production costs. A multi-objective study is therefore required to find the right balance between these competing and opposing objectives. Such a study necessitates the development of tools that allow analysis at an integrated system level.

In such an analysis, the main parameters within the boiler that influence plant performance are the boiler exit steam temperature, excess air, coal quality, feedwater temperature, furnace exit gas temperature (FEGT), slagging and fouling, as well as the superheater and reheater temperatures (EPRI, 2001:2-7; Bhatt, 2007:2150; Ranade and Gupta (2015:143); Sankar, Santhosh Kumar & Balasubramanian, 2019:643). To further complicate matters, many of these operating variables are interdependent. One of the most significant parameters in this list is the coal quality because total fuel cost can often be as much as 70-80% of the total production cost (EPRI, 2000). It is therefore necessary to study the impact of "coal switching" or varying coal quality to determine its effect on the operating variables and what can be adjusted to maintain the primary system objectives within satisfactory limits. An improper understanding of coal quality may cause a loss in boiler efficiency, increased boiler slagging and fouling, reduced steam capacity, excessive superheater tube metal temperatures, increased NOx, SOx and particulate emissions, as well as increased corrosion and erosion (EPRI, 2000; Nalbandian, 2011).

Together with the coal quality, the ability to control the furnace exit gas temperature (FEGT) is critical to preserve proper boiler operation and performance related to emission, reliability and safety (EPRI, 2000:2-33). The FEGT is measured between the radiation zone (where the combustion occurs) and the convective pass (start of the superheater tubes). Slagging and fouling problems increase when the FEGT is higher than the ash fusion temperature. This results in an

increased level of soot blowing and a negative overall impact on reliability. Therefore, if the FEGT can be reduced, the slagging/fouling of superheaters can be minimized and less soot blowing will be required (EPRI, 2000:5-18). This strengthens the case for effective measurement and modelling of the FEGT, which can lead to better performance by converting from a two-point control (burner and boiler exit temperature) to a three-point control (burner, FEGT and boiler exit temperature). The FEGT profile will impact the heat exchanger temperature variation in the flow path after the boiler furnace and the extreme temperature variation in the superheater and reheater temperature influences the operation cost and safety (Ranade & Gupta, 2015:137-138) due to boiler tube failures.

Due to the interdependency of the parameters and variables influencing the primary system objectives, it would be ideal to have access to an integrated model at an appropriate level of detail that captures all the significant phenomena and processes. The overall objective of this study is therefore to develop such a system level process model of a coal-fired boiler furnace. At a system level, the important parameters to consider are the flame behaviour, the furnace temperature distribution (especially focussing on the FEGT), excess air variations and changes in coal quality.

Sankar, Santhosh Kumar and Balasubramanian (2019:644) explained that continuous measurement of the FEGT is extremely difficult. Over time the ash in the flue gas can damage the instrumentation. The FEGT is dependent on the heat absorbed in the water walls of the boiler furnace. The amount of heat absorbed is proportional to the size of the boiler furnace, cleanliness of the water walls and coal quality. Therefore, the FEGT can be calculated by measuring the heat absorption at various locations in the furnace. According to Sankar, Santhosh Kumar and Balasubramanian (2019:644) there are methods to measure the heat flux to the water walls, but the permutations of furnace geometry and operating conditions are too many to make the experimental option feasible in countries such as India with power generation in short supply. They concluded that numerical methods complement the results from experimental measurements to provide more comprehensive insight into the processes inside a boiler furnace while leading to more accurate predictions of the FEGT. CFD (computational fluid dynamics) is commonly used in efforts to provide such solutions. However, the time required per solution is typically very long and does not allow for investigations of dynamic plant operations (Sankar, Santhosh Kumar & Balasubramanian, 2019:662).

A zero-dimensional approach does not allow for the prediction of all the important parameters because of the dependency on mill selection, burner operation and three-dimensional furnace heat

absorption rate. The Gurvich method (also known as the Blokh method) is a semi-empirical method employed by boiler designers for a well-stirred model (Sankar, Santhosh Kumar & Balasubramanian, 2019:643), which can provide solutions for some of these parameters. Other models that can accomplish these tasks within a reasonable time are encapsulated in codes such as FURNACE (Karasina et al., 1982; Abryutin et al., 1998; Karasina et al., 2000; Karasina et al., 2010) and HotGEN (Hesselmann, 1998).

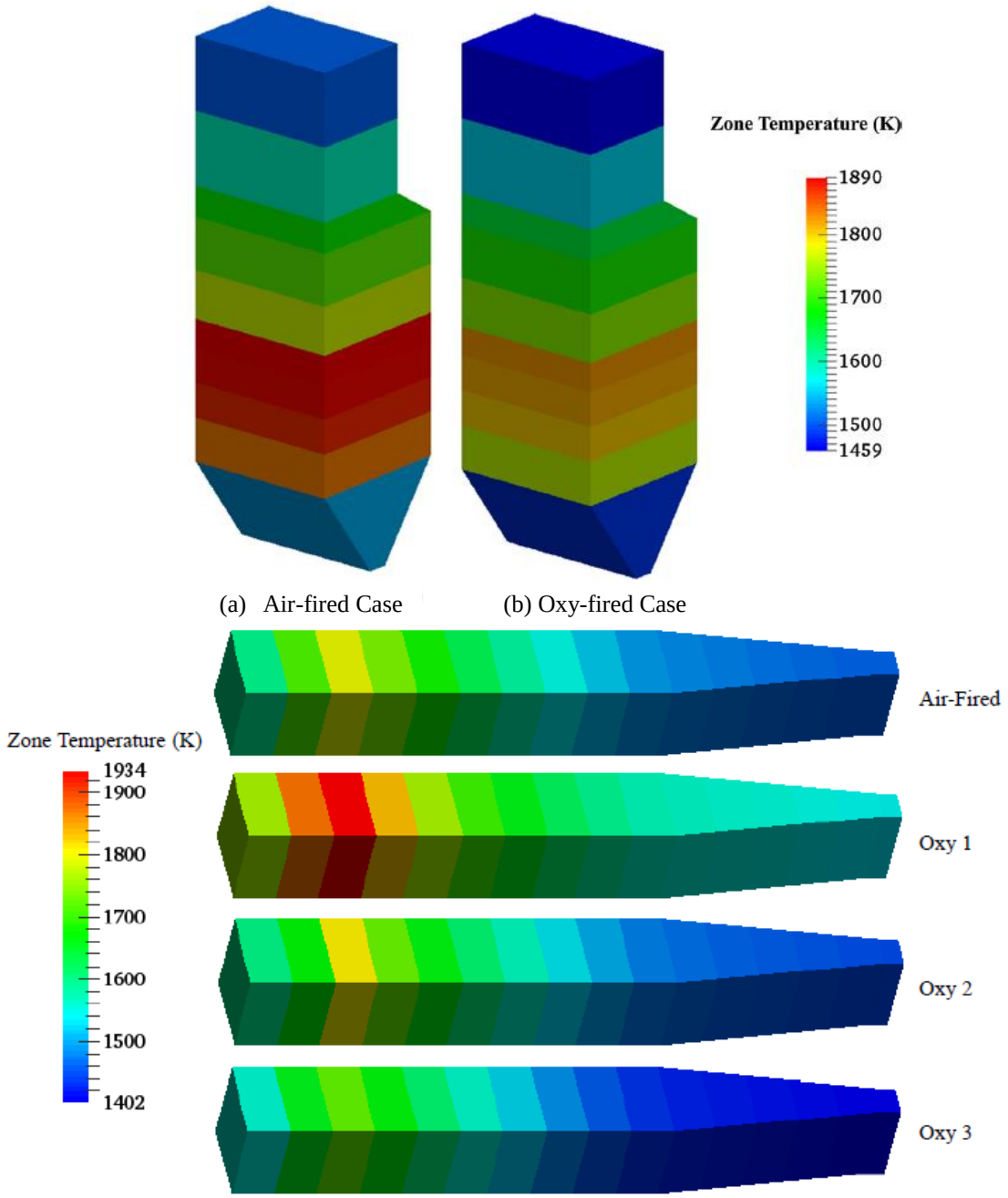

Figure 1 - The predicted zone temperatures from Ma et al. (2016:150&153) for Hunter Unit 3 (top) and Combustion test facility (CTF).

The most recent development of a comparable approach was presented by Ma et al. (2016). Their first-principle hybrid model converges in approximately one minute on a personal computer. The proposed model provides good predictions for the case studies presented showing that it is the latest benchmark approach for quick solving, three-dimensional heat flux furnace modelling tools. To increase the solution speed of the algorithms, however, simplifying assumptions were made which can limit the applicability of this tool. One of the assumptions was to reduce the mass transfer to a one-dimensional flow field along the height of the boiler with mass added in the zones containing the burners or over-fire ports. This limits the model to studying scenarios where the conditions on a given level within the boiler are homogenized with no multi-dimensional flow effects or differences in the behaviour of burners situated on the same level. Similarly, the temperature profile is captured along the height of the furnace, but the model is limited in providing a representative profile at the plane of the furnace exit as seen in the simulation results in Figure 1. The first-principle hybrid model of Ma et al. (2016) was demonstrated on two different furnaces in air-fired and oxy-fired mode, i.e. a 1325 MWth utility boiler (Hunter Unit 3) and a 0.5 MWth oxy-combustion test furnace.

Hu et al. (2017) and Hu et al. (2018a) also proposed a comparable approach by assuming plug flow for circulating fluidised bed boilers which has the same constraints. Hence, this excludes investigations entailing how the two-dimensional temperature profile of the gas below the superheater near the furnace exit impacts the attemperation flow imbalance. Also, how the maldistribution in mass flow between individual burners and uneven pulverized fuel propagates from the burners through the furnace and the impact on the FEGT profile.

In a recent review of modelling approaches for pulverized coal fired boilers, which did not make any mention of the model presented by Ma et al. (2016), Sankar, Santhosh and Balasubramanian (2019) concluded that a combination of CFD and RNM (reactor network model) models will be the optimal choice to obtain quick solution times while providing sufficient detail. The aim of this study is therefore to develop a methodology for a systems level process model that strikes a suitable balance between the level of detail obtained with a detail CFD model and the utility and speed of a RNM.

1.2 Hypothesis

It is proposed that a suitable systems level process model of a coal-fired boiler furnace can be developed with sufficient detail to capture the required multi-dimensional effects mentioned above, while retaining the speed and utility of a thermofluid network-based approach.

The furnace control volume of interest includes the evaporator walls (or water walls) and the combustion chamber up to the plane just below the superheaters with radiation heat transfer as the dominant mode of heat transfer. The plane below the superheaters is the location of the FEGT. An example of such a volume is shown in Figure 2.

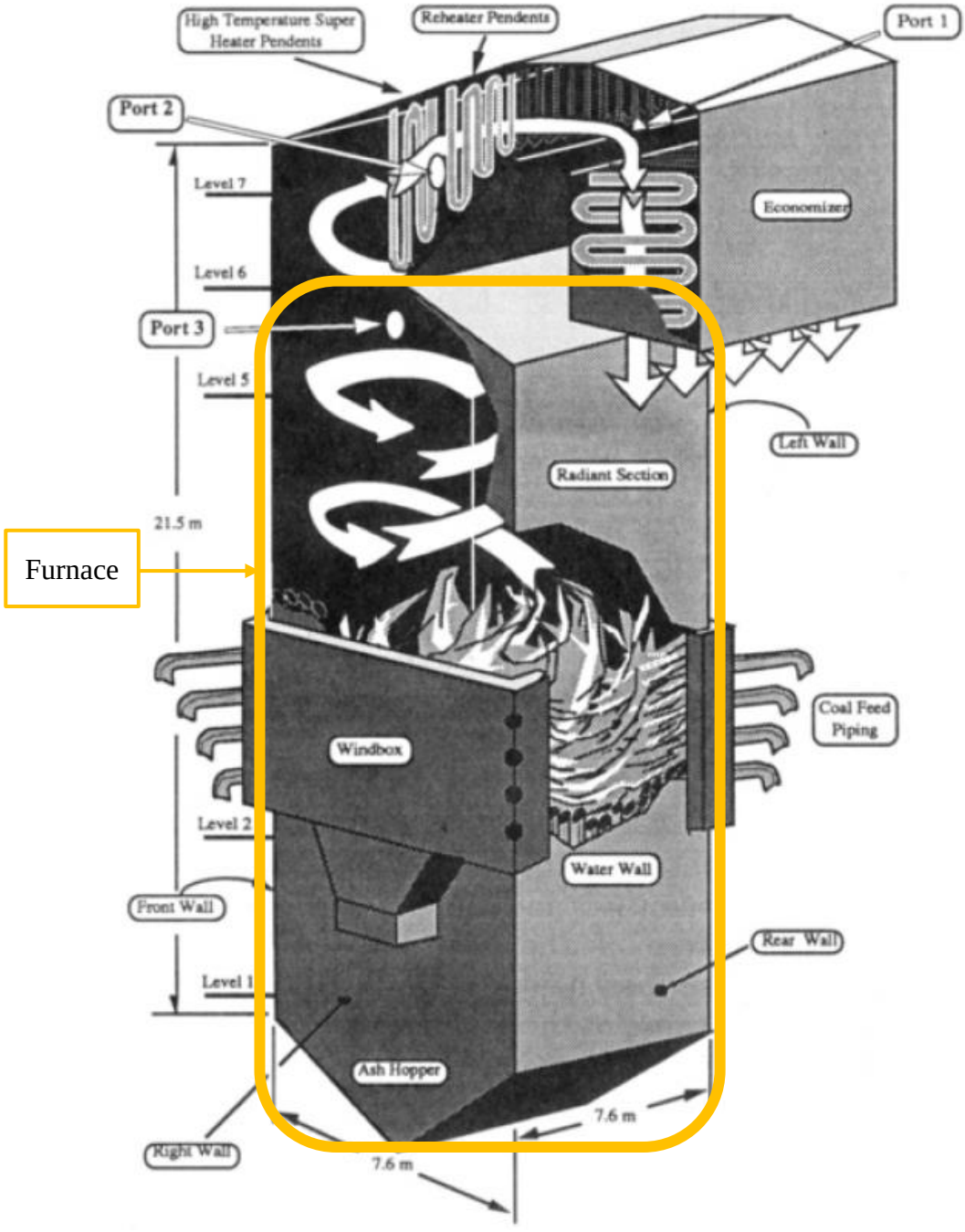

Figure 2 - Rendition of a coal-fired boiler with the furnace region indicated (Hill & Smoot, 1993:879).

The methodology will have to provide sufficient resolution to capture multi-dimensional effects, while retaining the simplicity of a network approach, as opposed to a full CFD approach. The

proposed methodology does not need to capture the complex swirling flows or detail combustion kinetics in the flame region, but should provide sufficiently accurate three-dimensional results for the furnace as a whole. This approach will fit within the CFD-RNM category defined by Sankar, Santhosh Kumar and Balasubramanian (2019). In contrast to the approach of Ma et al. (2016), Hu et al. (2017) and Hu et al. (2018a) the methodology strives to account for the three-dimensional flow field and temperature variations in order to predict the furnace exit temperature distribution with reasonable accuracy within a short time. These results will be useful as inputs for studies requiring the temperature and velocity distribution at a boundary that represents the furnace exit (refer to Figure 3). One example is the study of Drosatos et al. (2014) of a macro heat exchanger model that focussed on the prediction of the superheater, reheater and economiser performance.

Lastly, the methodology extends beyond the latest reactor network approaches demonstrated on reheating furnaces by Hu et al. (2017), Hu et al. (2018b) and Hu et al. (2019) by incorporating a source model to account for the combustion when applying the methodology to pulverized coal combustion boilers.

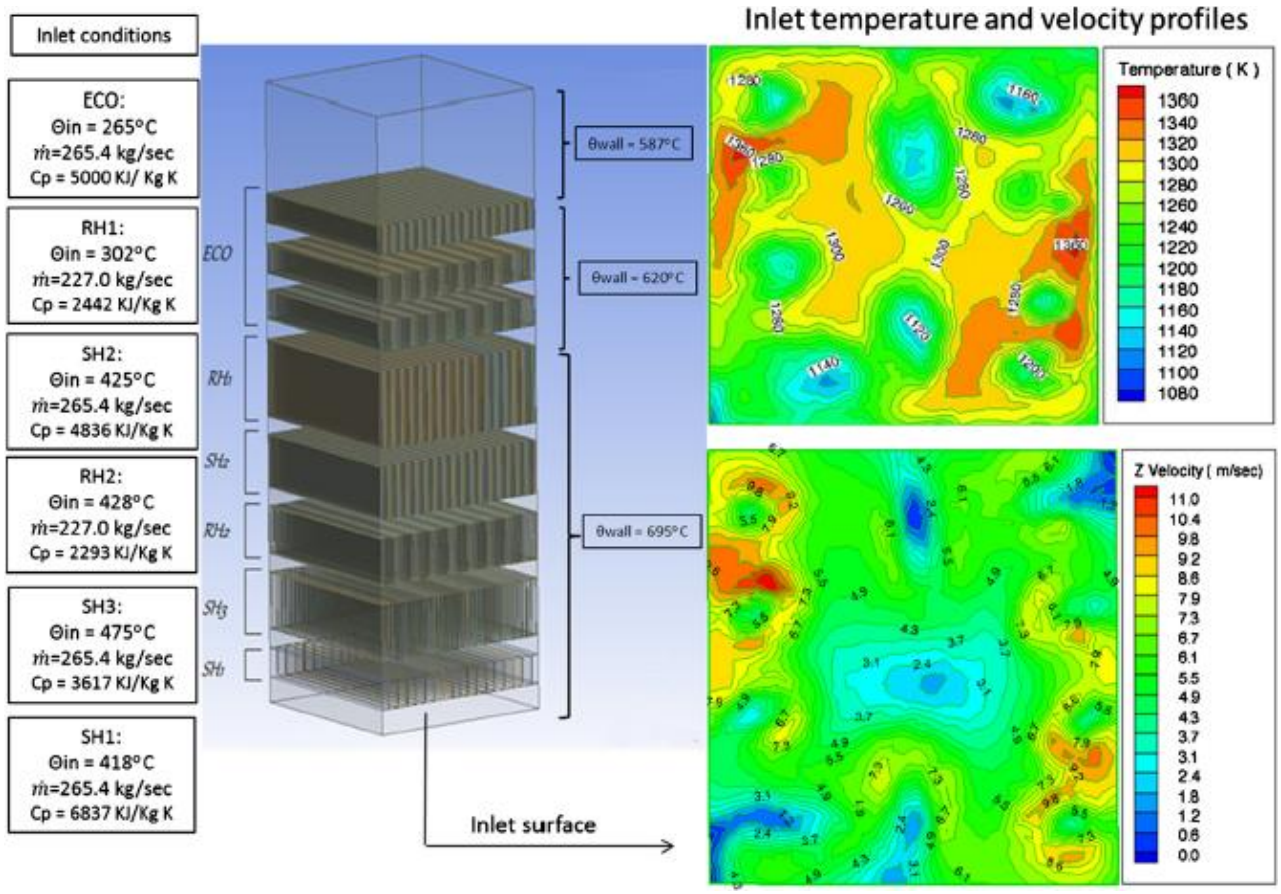

Figure 3 - The boundary condition inputs for the furnace exit of the macro heat exchanger model of a boiler's superheaters, reheaters and economiser (Drosatos et al., 2014:643).

The main requirements that were set for the proposed network-based furnace model when applied to a utility scale boiler are that is must be able to:

1. Determine a two-dimensional temperature field at the furnace exit.
2. Determine the combustion efficiency (unburned carbon leaving the furnace).
3. Determine the heat flux to the evaporator (water walls) along the height of the furnace as well as at the furnace exit plane.
4. Allow quick solution times.

Conceptual aspects of the methodology were introduced in Van der Meer, Rousseau and Jestin (2016a, 2016b, 2016c) and the first iteration of the complete methodology published in Van der Meer, Rousseau and Naidoo (2019) when applied to a single-burner furnace. Since then the methodology was modified and updated based on new findings and expanded to be applicable to a furnace with multiple burners. The furnace network model developed as part of the methodology was also integrated with a system level code (Flownex® SE) to perform a co-simulation. The system level code is used to model the flow within the evaporator tubes that recirculate to and from the steam drum, as well as the heat transfer between the furnace walls and the fluid inside the tubes.

1.3 Outline of document

In this document the literature review relevant to developing the network-based furnace model will be presented in chapter 2. This will be followed by the methodology (chapter 3) aimed at addressing the hypothesis presented in section 1.2. The verification and validation of the models will be presented in chapters 4.1 and 4.2. In chapter 5, different case studies will be presented using the multiple-burner configuration (validated in chapter 4.2) showing the possible applications of the network-based furnace model. Chapter 6 summarises the limitations and applicability of the new methodology. Finally, the document will be concluded in chapter 7, which includes recommendations for further work.

2. Literature review

2.1 Multi-objective system analysis

Due to the complex interdependency of the parameters and variables[1] influencing the primary system objectives[2] in a coal-fired power plant, the most plausible approach is to aim for an integrated model that captures all the significant phenomena and processes. Such an analysis can be performed by including the boiler furnace behaviour into an integrated process model. An example of a process flow diagram for an integrated process model is shown in Figure 4 taken from Edge et al. (2013:248). By integrating the processes, the detail modelling of the furnace can focus on minimising unburned carbon, reducing the production of NOx and SOx as well as providing optimum temperature distributions.

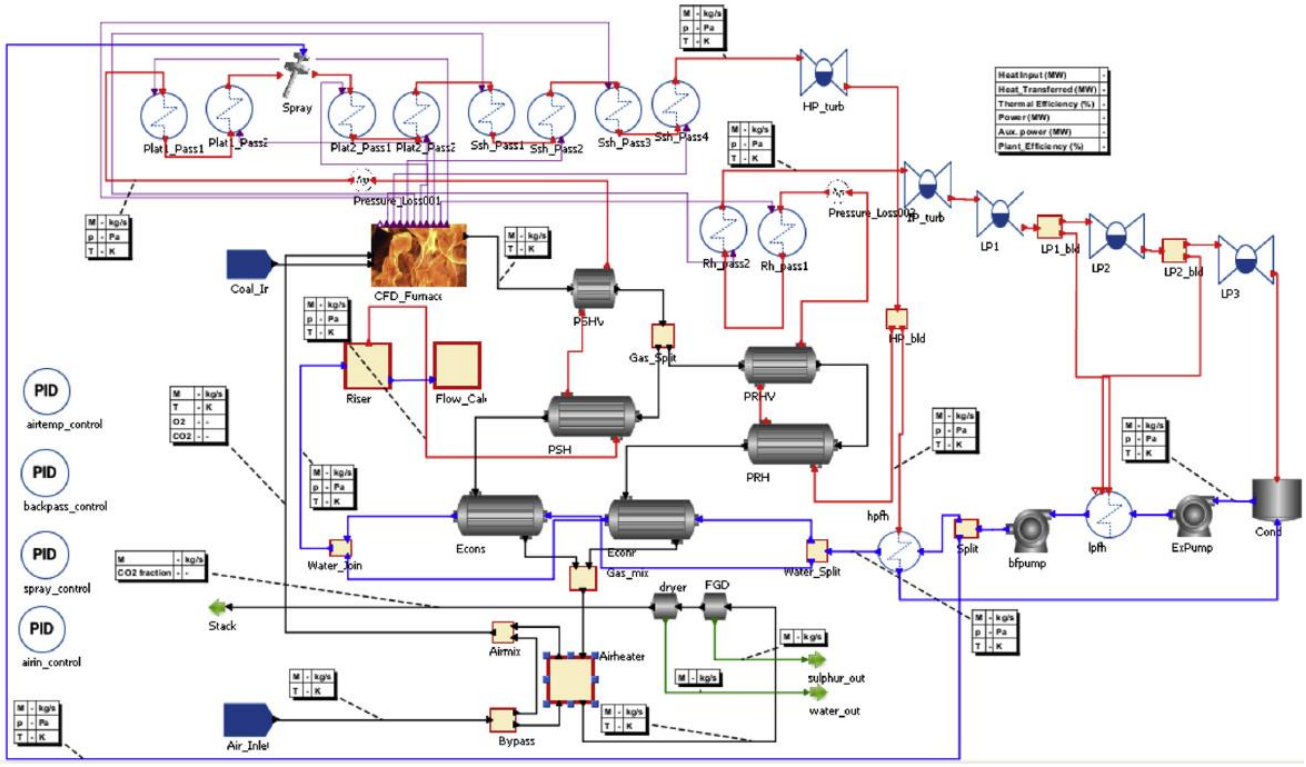

Figure 4 - Process flow diagram of the integrated furnace model in Ansys® Fluent and process model in gPROMS (Edge et al., 2013:248).

[1] The parameters and variables are boiler exit steam temperature, excess air, coal quality, feedwater temperature, furnace exit gas temperature (FEGT), slagging, fouling, and superheater and reheater temperatures.

[2] The primary system objectives are safety, capacity, efficiency, emissions, production cost, reliability and availability.

Publications based on a system network approach emerged from the early 2000s after the successful implementation of commercial software using linear or nonlinear programming or artificial neural networks (EPRI, 2000:6-1). The focus of these software applications was mainly on NOx reduction and heat rate optimisation. The heat rate is defined as "the amount of heat input into a system divided by the amount of power generated by a system" (EPRI, 1998:6-1). Heat rate improvement has the combined benefit of fuel-saving and the reduction of harmful emissions.

As seen in the work published by Kalogirou (2003), Hao et al. (2003) and Liu and Bansal (2011), the start-up years of the system network approach focussed on using multi-object codes based on artificial neural networks (ANN) and genetic algorithms (GA). One of the benefits of these methods is that it is relatively fast in computing time and can provide online solutions. These approaches entail modelling a system with a set of nonlinear equations of which the coefficients have to be determined. These coefficients are then determined as an experienced guess value (based on available data) and adapted from actual historical performance data for each plant. These data must be based on a wide range of plant usage in order for it to be meaningful. ANN models are therefore limited to the range of the historical plant performance data during the benchmark period.

The interest of industry in these approaches declined over the years due to the following reasons (EPRI, 2005:4-2):

- The initial motivation for the optimisation project no longer existed.
- Changes to the hardware required for recalibration of the optimisation system were challenging.
- Operators and performance engineers perceived that the benefits from the optimisation system did not outweigh the costs (with changing coal quality which is a variable outside the control of the optimisation software).
- The optimisation system was shut down as soon as the plant champion was transferred out of the power plant.
- The software was installed on some older units without digital control systems and adequate instrumentation, and proved to be ineffective when a limited number of control variables were available.

It is significant that the parameter of changing coal quality features in the list above. This might be one of the possible reasons why the development path changed toward more fundamental approaches. Park et al. (2010), Edge et al. (2011), Laubscher and Rousseau (2019c), Schuhbauer et al. (2014) and Rousseau and Laubscher (2019) presented a solution by coupling a process model in

a system network code with a detailed numerical analysis (solved in a CFD code) for the gas side of a pulverized coal-fired furnace. Hovi et al. (2017) and Hu et al. (2018a) demonstrated the applicability of coupling with a process for a bubbling fluidised bed (BFB) boiler. The same was applied for an oxyfuel furnace by Edge et al. (2012, 2013) and Fei et al. (2015). Edge et al. (2011, 2012, 2013) and Fei et al. (2015) only used CFD to create a reduced order model (ROM) and transferred these characteristics to the process model. Simpler approaches were also taken such as the work done by Tzolakis et al. (2012) and Brunnemann et al. (2012) wherein they used a system network code and implemented a simple mass and energy balance for the furnace. The reduced order approaches indicated that certain studies for the process models required quick solving results to emulate the furnace behaviour. Most of this research mainly focussed on presenting a method usable for "what-if" studies.

The studies were also not limited to coal quality, with the emergence of emissions control becoming an important objective. Hovi et al. (2017) investigated the increase of emissions occurring during fast changes in combustion conditions. For this, an integrated transient BFB and process model of the steam cycle were required. They also raised the concern that unfavourable conditions within the furnace and rapid temperature changes can cause damage to the boiler piping.

Instead of reducing the emissions in the furnace, new systems can also be added downstream to remove the emissions. Research focussing on the removal of emissions at the respective subsystems are listed below:

- Selective catalytic reduction (SCR) which removes NOx (Si et al., 2008; Peta et al., 2015).
- Carbon capture plants (CCP) which remove CO_2 (Sanpasertparnich et al., 2010; Harkin, Hoadley & Hooper, 2011; Brunnemann et al., 2012; Edge et al., 2013).
- Flue gas desulphurisation (FGD) which removes SO_2 (Sanpasertparnich & Aroonwilas, 2009).

From the available resources, it was observed that the process models focussing on integrated studies of the steam/water and coal/air to gas cycle generally fall within the following two categories:

- A fundamentally consistent system network code and integrating (or coupling) the furnace section with a CFD code or a simple reactor model for the furnace.
- A multi-object system which uses ANN or a simple approach to do a mass and energy balance for each system.

The approach using a system network code and integrating it with a CFD model of the furnace currently provides the best available tool to do a multi-objective optimisation. The critical limitation of this approach is that the CFD analysis is expensive on computational time, with 15-hour solving time reported for some studies (Sankar, Santhosh Kumar & Balasubramanian, 2019:661), eliminating the applicability for predictive modelling during online operations. Based on the requirement to do online monitoring and control of all the important boiler objectives, a faster solving network-based furnace methodology is required to integrate with a system network code.

The following section will focus on research regarding boiler furnaces and narrowing down the models that can be integrated to provide a faster solving furnace model with the level of detail required as stated in the hypothesis.

2.2 Boiler furnace models

Sankar, Santhosh Kumar and Balasubramanian (2019) provided the most recent review of the computational modelling tools for coal-fired boilers. The review is extensive and concisely reports on the developments in the field extending over the previous fifty years. It is therefore a valuable resource that will be referred to often in the literature review below, while potential gaps relevant for this study will also be included and elaborated on.

2.2.1 Zero-dimensional models

Zero-dimensional models assume an ideal well-stirred reactor, i.e. a homogeneous distribution of temperature and radiation properties. One approach implemented in software used for simulating process models incorporates a mass and energy balance while calculating equilibrium by minimizing Gibbs free energy of the outlet stream (Ma et al, 2016:138). The carbon burnout and heat absorption to the water wall and superheaters still need to be specified and cannot be predicted by the models.

Another approach as described by Brunnemann et al. (2012:614) for a coal-fired power plant is a simplified combustion chamber model consisting of a mass and energy balance for each substance in the flue gas mixture. The flue gas outlet temperature, slag fraction, slag temperature and concentration of the CO, NOx and SOx in the flue gas should be provided. The model provides the combustion chamber heat transfer and stoichiometric ratio as results.

2.2.2 Semi-empirical models

Ma et al (2016:138) concluded that zero-dimensional models are not fit for purpose in designing the furnace geometry, burners and operating parameters. Semi-empirical methods such as the Gurvich method, published by Blokh (1987), are more suitable and used by boiler designers (Sankar, Santhosh Kumar & Balasubramanian, 2019:643). The method incorporates test data from pilot plants and actual operating boilers to compute the FEGT.

Since an empirical relation is dependent on the parameter ranges such as the furnace geometry on which the test data are based, the applicable range of accurate prediction is limited. According to Sankar, Santhosh Kumar and Balasubramanian (2019:643) the FEGT influences the following:

1. The fouling and slagging on the water walls, superheater and reheater.
2. The efficiency of the boiler due to the temperature of the flue gas transported to the airheater exit.
3. The heat rate performance of the plant due to the attemperation mass flow required in the superheater and reheater.
4. The thermal performance of the superheater and reheater.

Hence, continuous monitoring of the FEGT is essential to ensure the efficient operation of the boiler. However, zero-dimensional or semi-empirical models only provide a single temperature at the furnace exit. For an accurate prediction of the attemperation and thermal performance of the superheater nearest to the furnace, the temperature profile is necessary. A three-dimensional profile can be simulated by means of numerical methods like CFD or zoned-based models, as discussed in the following two sections.

2.2.3 Computational fluid dynamics

According to Ranade and Gupta (2015:5), “computational fluid dynamics (CFD) tools have evolved over the years as a powerful design and predictive tool to simulate complex equipment”. CFD encapsulates knowledge and techniques to solve mathematical models using computers. The governing equations based on conservation of mass, momentum and energy are solved in conjunction with turbulence, species transport and equation of state models.

Initially, CFD development applied to pulverized fuel furnaces started with two-dimensional models (Richter, 1974) and later extended to three-dimensional models, as referenced by Benesch and Kremer (1985), Hill and Smoot (1993) and Dal-Secco (2000). This continued with extensive research into the development of submodels to analyse, design, retrofit and optimise the

performance of fossil-fuel combustion (Eaton et al., 1999). Academic institutions such as Imperial College, Stuttgart University and Freiburg University (to name a few) started research groups to develop these codes.

Each contributed with a different approach and models for the Eulerian-Eulerian and Eulerian-Lagrangian frameworks to model the gas phase and particles (Stein et al., 2013). Ranade and Gupta (2015:82-83) recommended using a Eulerian-Lagrangian approach for modelling pulverized fuel furnaces - the motion of the gases is modelled in the Eulerian framework and the transport of particles modelled in the Lagrangian framework.

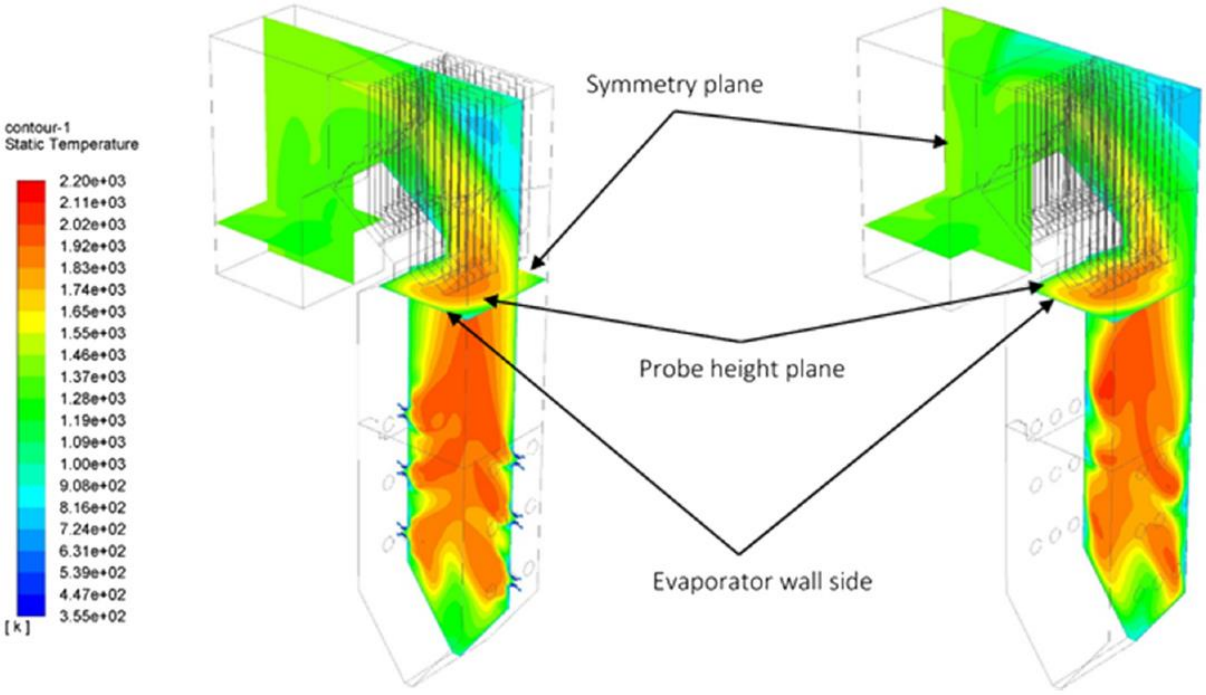

Figure 5 - Temperature contours for the CFD simulation of a pulverized coal-fired power station (Laubscher and Rousseau, 2019a:10).

The commercial sector also entered the scene with the introduction of software codes when the proven ability to perform detailed analysis with CFD became a reality. Examples are specialised furnace codes like RECOM-AIOLOS (Schnell et al., 1995) and general commercial codes like FLUENT, STAR-CCM+ and CFX. A review of applications where CFX was used can be found in Stopford (2002). Also available are open-source CFD codes such as Code Saturne developed by EDF and used by Authier et al. (2014), Madejski (2018) and Madejski and Modlinski (2019). Madjeski and Modlinski (2019) compared the results between Code Saturne and Ansys® Fluent. Ansys® Fluent was also used in the work done by Backreedy et al. (2007), Filkoski, Petrovski and Karas (2006), Filkoski (2010), Edge et al. (2012, 2013), Holkar and Hebbal (2013), Fei et al. (2015), Ranade and Gupta (2015), Rousseau and Laubscher (2019) and Laubscher and Rousseau

(2019a, 2019b, 2019c). An example of the temperature contours for the CFD simulation of a pulverized coal-fired power station is shown in Figure 5 taken from Laubscher and Rousseau (2019a:10).

The applicability of CFD models for complex reacting systems for pulverized coal-fired boilers was extended with the continuous advances in the development of high-performance computers, fluid physics models, numerical techniques and algorithms. It remains necessary to adapt the CFD techniques to develop an appropriate approach consistent for the study of each complex pulverized fuel boiler system.

In their work, Madejski and Modlinski (2019:9) focussed on the correct modelling of the boiler furnace at nominal load. Studies using CFD are also possible to analyse the coal combustion, different fuels, coal mill operation and coal particle size distribution at different loads. Ranade and Gupta (2015:143-155) performed a study including excess air, coal feed rate, burner tilt and coal blends on a 210 MWe pulverized coal-fired boiler.

Laubscher and Rousseau (2019a) investigated the burner swirl direction in a pulverized coal boiler and continued to study performance at varying loads (Laubscher & Rousseau, 2019b). These numerical investigations were also extended to study the impact of coal quality (Rousseau & Laubscher, 2019) and particle radiation properties (Laubscher & Rousseau, 2019c) using co-simulation with Flownex® SE to integrate the water-to-steam side behaviour by means of a process model. For these studies, a single temperature represented the temperature boundary at each of the superheaters and reheaters to capture the heat transfer modelling between the flue gas and water/steam side. For the co-simulation, a temperature and heat flux distribution at the water walls were accounted for by the integration with the system network code. The ability to account for a temperature distribution at the superheaters and reheaters was therefore not attained yet. However, this is possible with modification to the models.

Even though this thesis focusses on pulverized coal combustion, it is worth noting the experience in the modelling of fluidised bed reactors and reheating furnaces. Hu et al. (2016:557) and Hu et al. (2017:1896) required methods to predict the heat transfer to the water wall and superheaters. This could not be done with a zero-dimensional model, albeit while delivering the results faster than CFD can currently deliver. The work was moving towards process co-simulation with a system network code, thus necessitating faster solving techniques. For similar reasons, Fei et al. (2015:45-47) required a ROM to emulate the furnace behaviour in a process model to evaluate potential retrofitting of a coal power plant to oxy-fuel firing. The ROM was developed in Ansys® Fluent

CFD. Hu et al. (2016) regarded CFD unsuitable for studying the transient behaviour for real or near real-time modelling of an existing reheating furnace.

What is necessary is a reduced order model that requires less computing resources and time, to be suitable for on-line optimisation while correctly capturing the impact of various operating parameters. Possible models complying with these specifications will be discussed in the next section.

2.2.4 Reactor network models

Sankar, Santhosh Kumar and Balasubramanian (2019) group the reactor network models (RNM) as all the approaches that divide the furnace into multiple reactors and then solving mass and energy balances across each reactor. The radiation solution for these models is based on some form of the zonal method (see Section 2.3.1). These models are computationally less time consuming when compared to CFD-based models since the solution to the momentum equation is dispensed with, making the models suitable for simulator applications (Sankar, Santhosh Kumar & Balasubramanian, 2019:660; Ranade & Gupta, 2015:165). Detailed chemical kinetics can be included in the simulation, but methods are required to provide information regarding the flow and temperature distribution.

One of the first examples where the zonal method was applied on a large-scale boiler furnace was described by Lowe, Wall and Stewart (1975). Soon afterwards the first study from the All-Russian Research Institute applying the zonal method to a coal-fired power plant was published in Karasina et al. (1982). The original algorithm presented in Karasina et al. (1982) was then further developed in the work done by Abryutin et al. (1998) and Karasina et al. (2000). The code was named FURNACE and development also continued under a collaboration of researchers at the Israel Electrical Company and the All-Russian Research Institute. The code achieved a solving time of 12 minutes when applied to the large-scale boiler configuration illustrated in Figure 6 taken from Karasina et al. (2010:898). According to Karasina et al. (2010), the code calculates the distribution of the gas temperature over the volume of a furnace chamber, the heat flux on the walls of the furnace, distribution of the fuel and air supplied by the burners, emissions properties of the gases in the furnace and other operational factors.

The code FURNACE was implemented in the control and monitoring systems of all the coal-fired power plants in Israel (Karasina et al., 2010). Chudnovsky and Talanker (2004) and Chudnovsky et al. (2005, 2007, 2009) used the code FURNACE as part of a supervision and

diagnostic study when different coal types instead of the design coal were used. The visual monitoring system in Chudnovsky et al. (2009) was added to the system because although FURNACE provides online information about the fireball location and FEGT, it cannot provide enough detail regarding the flame temperature. This expert system provided useful information to improve the power plant operations and resulted in increased reliability, lowered emissions and increased efficiency. Alekhnovich, Artem'eva and Bogomolov (2006) and Alekhnovich, Artem'eva and Chernetskii (2012) did work where the effect of slagging and fouling was incorporated into the modelling of the thermal resistance of the water walls. This submodel is suitable for use in a zone-wise code such as FURNACE and will be able to predict the loss of heat transfer due to slagging and fouling.

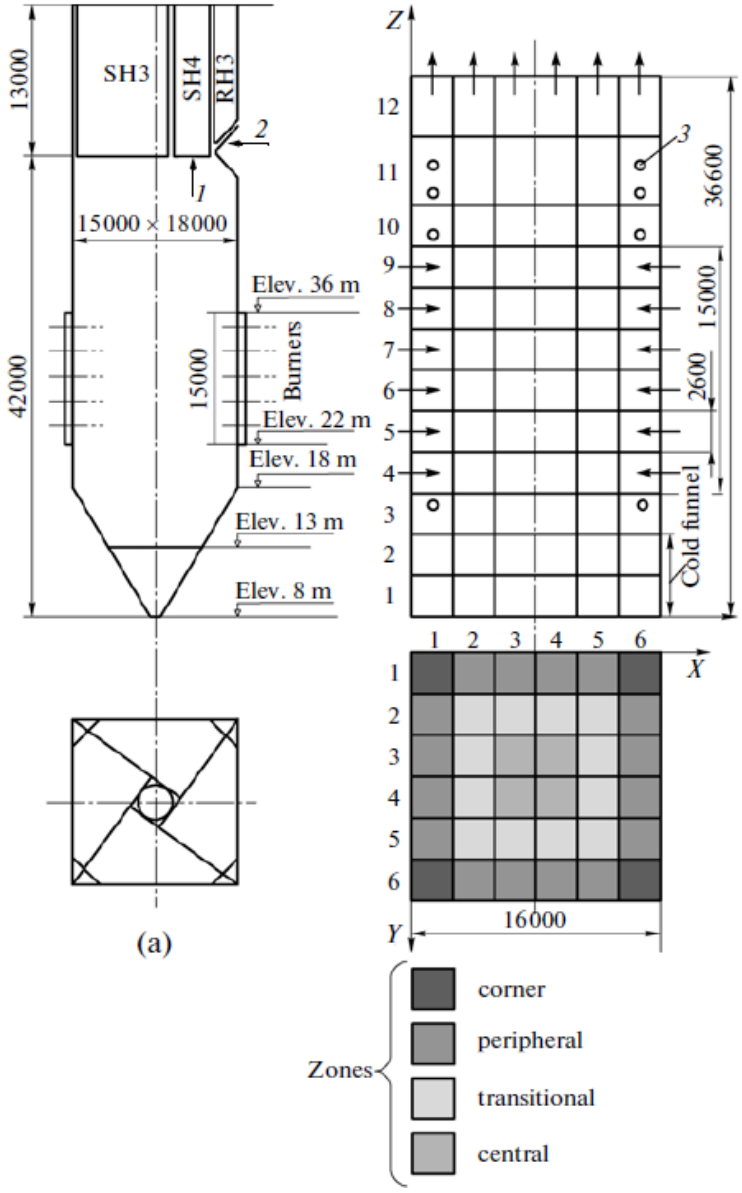

Figure 6 - A coal-fired power plant and its zonal representation (Karasina et al., 2010:898).

The methodology proposed by Hesselmann (1998) showed how offline CFD analysis can be applied to address the transfer of the gas and particles between the volumes as well as quantifying the source term. A pre-characterisation of the flow field and heat source terms using CFD was integrated into the zonal-based code HotGen (originally known as BWHOT). A heat source model was also developed using CFD in a pre-characterisation step. The results were fitted to a non-dimensional correlation previously applied to emulate the heat sources in a residual oil flame. The combination of the zonal model, the mass flow map and heat source model delivered engineering results within very short timescales. This approach was limited to emulating the heat source distribution for the characterised flame and omitted input details for different combustible matter and the subsequent conversion thereof. Therefore, this entails re-characterisation of the fitting parameters for each unique flame configuration.

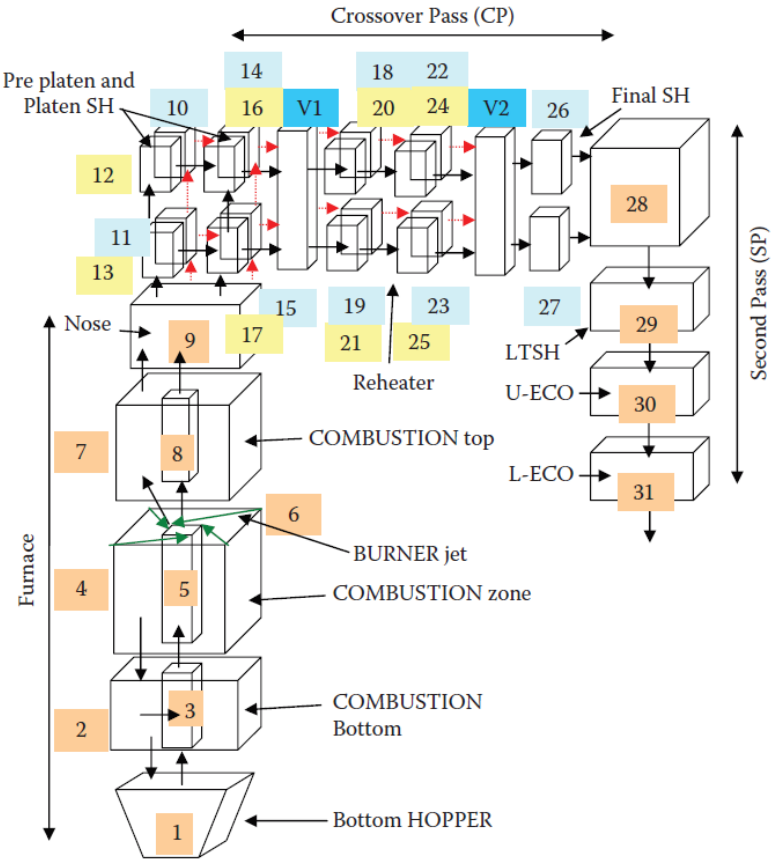

Zone number in yellow color boxes indicates right side wall and
similarly blue color indicates left side wall of the boiler,
Green arrow indicates the burner jets.

1: HOPPER;
2: COMBUSTION BOTTOM (CB) GAP; 3: COMBUSTION BOTTOM (CB) CORE;
4: FIREBALL GAP; 5: FIREBALL; 6: BURERJET;
7: COMBUSTION TOP (CT) GAP; 8: COMBUSTION TOP (CT) CORE;
9: NOSE; 10 TO 13: PRE PLATEN; 14 TO 17: PLATEN;
V1: VIRTUAL VOLUME; 18 TO 21: FRONT RH; 22 TO 25: REAR RH;
V2: VIRTUAL VOLUME; 26 TO 27: FINAL SH;
28: PASS2TOP; 29; LTSH; 30: U-ECO; 31:L-ECO

Figure 7 - A reactor network model of a 210 MW tangentially fired boiler (Ranade & Gupta, 2015:175).

Gupta (2011) suggested an approach for a RNM for the case of a complete boiler with a 210 MW tangentially fired furnace. The software package called Boiler Simulation Tool (BOST) was created based on the approach. In the approach, the boiler was divided into three parts, namely the furnace, crossover and second pass as shown in Figure 7. A low-level approach for the furnace was followed having only nine zones. Only a single temperature, therefore no temperature profile, for the FEGT was predicted.

The knowledge gained from a CFD model of the same boiler was used intensively with the characterisation such as selecting zone size dimensions and generating mass flow maps. During the model development, the emissivity of the water walls was calibrated to obtain a representative FEGT (Ranade & Gupta, 2015:200). Ranade and Gupta (2015:204) consider calibration with CFD results and measured values necessary to improve the temperature prediction of the RNM, especially the emissivity for the radiation heat transfer.

The applicability of BOST was demonstrated by changing the burner tilt to simulate the influence thereof and the results provided good agreement for engineering applications (Ranade & Gupta, 2015:198,202). The temperature variation as an important process parameter for thermal efficiency was captured with reasonable accuracy (Ranade & Gupta, 2015:204).

The most recent applications of a RNM in processes other than a pulverized coal-fired furnace were demonstrated in a reheating furnace (see Tan et al., 2013; Hu et al., 2016; Hu et al., 2018b, Hu et al., 2019), oxy-fuel coal-fired furnaces (see Ma et al., 2016; Hu et al., 2019) and fluidised bed boilers (see Hu et al., 2017; Hu et al., 2018a).

Tan et al. (2013) and Hu et al. (2016) implemented the zonal method in a three-dimensional (also tested in a simplified two-dimensional) case to simulate the thermal performance of the reheating furnace shown in Figure 8. A reheating furnace prepares the stock (or blooms) in steel plants to the desired temperature before the product continues to the next process. A model was required to provide more detailed predictions (especially for the temperature at the stock) than the existing semi-empirical solutions used in practice, but still solving within a shorter computing time than what existing CFD simulation can deliver, especially for transient runs. The zone method of radiation heat transfer analysis was combined with isothermal CFD calculations for the mass flow from either Ansys® Fluent or OpenFOAM®. The impact on flow due to density variation was allowed for in the actual non-isothermal furnace by distorting the burner geometry with the Thring-Newby scaling criterion. The effect of conduction was also necessary to account for in the reheating furnace. The view factors and exchange areas were obtained using the work from Hottel and

Sarofim (1967) and Lawson and Ziesler (1996). Complete combustion was assumed for the gas entering the furnace (Hu et al., 2016:559).

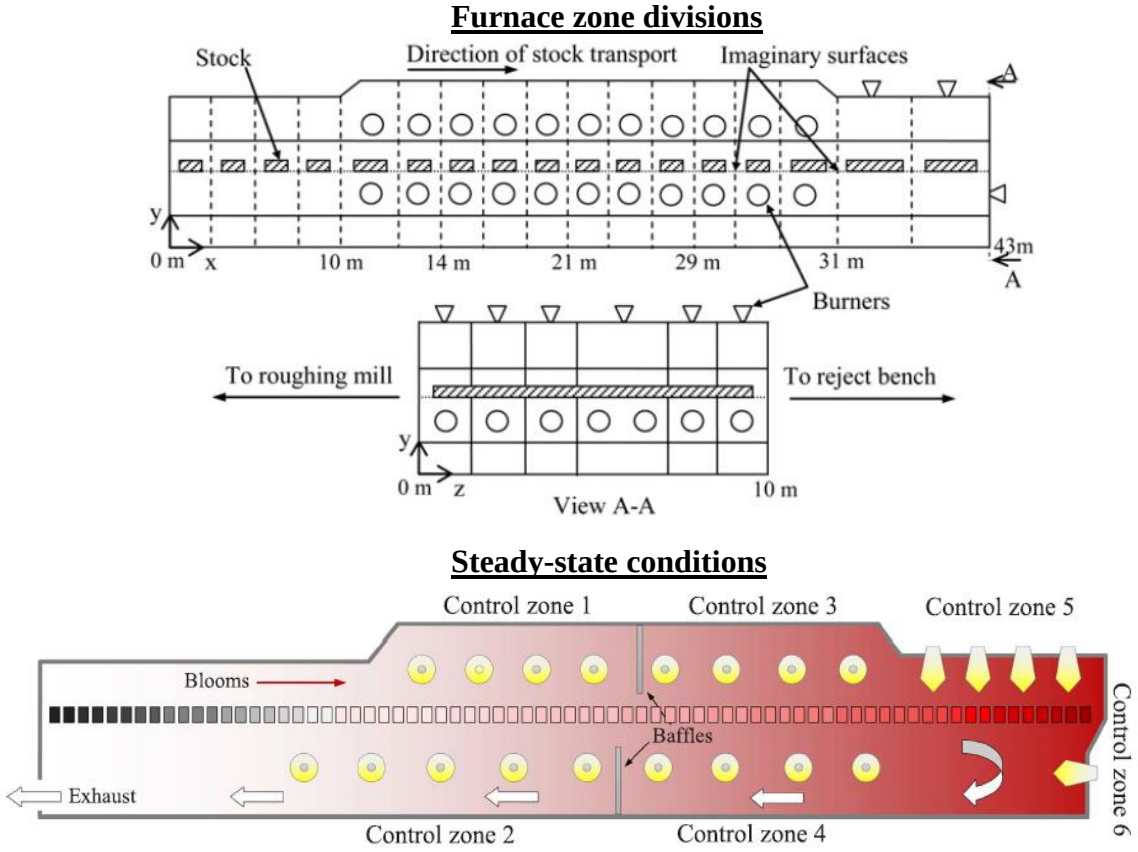

Figure 8 - Outline of a reheating furnace zone division (Tan et al., 2013:1112) and steady-steady conditions (Hu et al., 2018b:43).

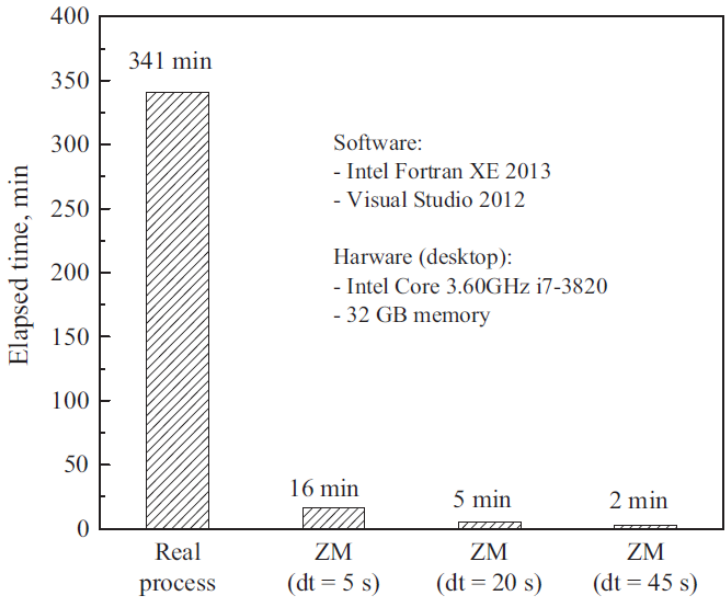

Figure 9 - Comparison of the computing time of the zone model of a reheating furnace for transient simulations at different time step sizes (Hu et al., 2016:565).

The results of the RNM of the reheating furnace compared reasonably well with the transient trail data (Hu et al. 2016:564; Hu et al. 2018b:42). The solving time was well below the real-time process time as reported by the comparison in Figure 9. Hu et al. (2018b:50) later used the model to successfully incorporate a self-adaptive control strategy to improve the operation of a reheating furnace. Hu et al. (2019) further extended the work to oxy-fuel fired reheating furnaces to predict a reduction in overall heating time (by ± 6%) and specific fuel consumption (by ± 16%).

A similar team consisting of Hu et al. (2017) and Hu et al. (2018a) applied the zonal method to the furnaces of a 0.3 MW circulating fluidised bed (CFB) boiler. Even though CFB modelling is available in commercial software such as Aspen Plus® and Computational Particle Fluid Dynamics (CPFD®), Hu et al. (2017:1896) considered the existing zero-dimensional ideal reactor models available in Aspen Plus® limiting for transient simulations. The limitations were observed in the thermal reciprocity between each reactor model as well as in requiring that the heat absorption should be specified as an input for the water wall and superheaters. The prediction of these results is necessary for the design of the geometry and evaluation of operating conditions. Also, the modelling of the radiation heat transfer is deemed important, being the dominant component which influences the heat recovery and combustion efficiency. For Hu et al. (2017:1896), the CPFD solving time of several days to weeks was too long for the prediction of the local heat and mass transfer for an integrated transient process model.

An illustration of the discretisation of the zonal method applied to a CFB is shown in Figure 10, with a finite number of isothermal volume and surface zones along the height. Plug flow was assumed since the flow is dominated in the longitudinal direction (Hu et al., 2017:1897). The devolatilisation and char combustion calculations in Aspen Plus® were used (Hu et al., 2017:1898; Hu et al., 2018a:171). The total exchange areas were calculated with a Monte-Carlo based Ray-Tracing algorithm (Hu et al., 2017:1899; Hu et al., 2018a:173). Hu et al. (2017:1900) stated that "the relatively modest computing demand and acceptable accuracy" made it feasible to integrate the zone method-based model with a process model of the entire plant for transient simulations. Hu et al. (2017:1898, 1900) mentioned that the proposed modelling approach can extend to multi-dimensional cases, but the enthalpy transport term then needs to be accounted for in all directions. A suggestion was made to use flow data from other physical models such as an isothermal CFD solution.

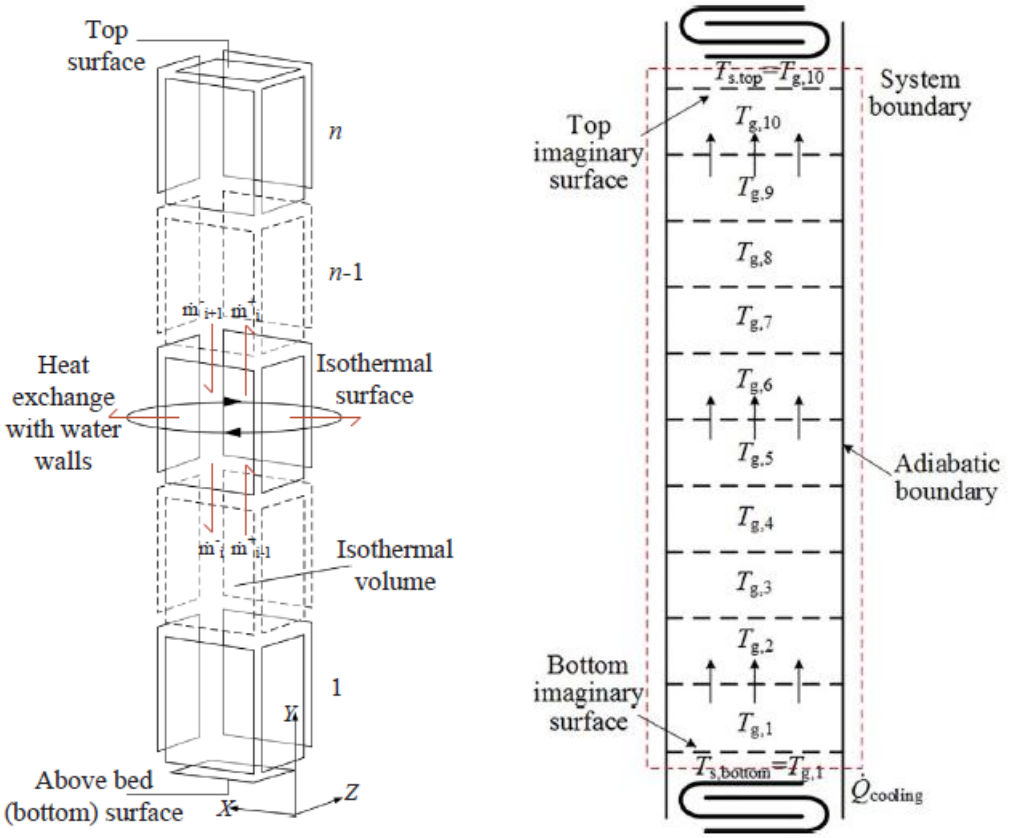

Figure 10 - Illustration of the discretisation and thermal boundary conditions (Hu et al., 2018a:173,175).

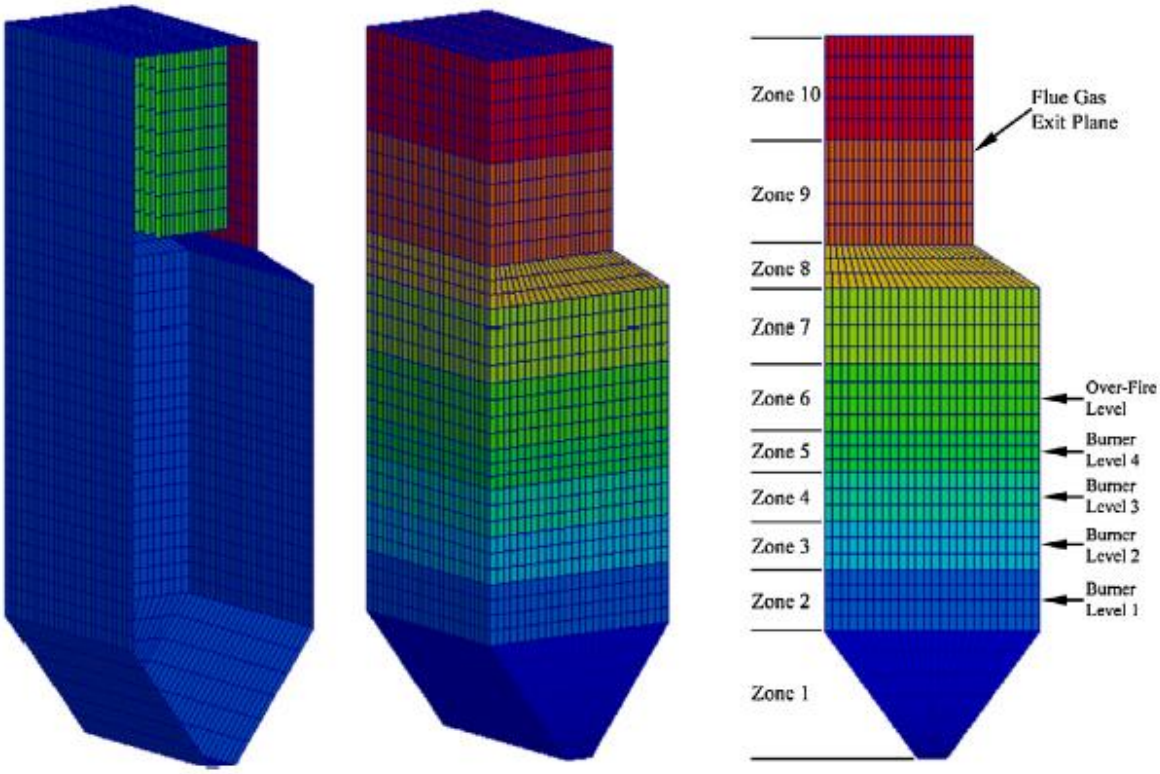

Figure 11 - Illustration of the three-dimensional radiative heat transfer mesh and one-dimensional mesh for kinetics and mass/energy flow (Ma et al., 2016:140).

Ma et al. (2016) applied a zone-wise approach to an oxy-fuel coal-fired boiler. However, the discrete ordinate (DO) method was implemented to solve for the radiation heat transfer instead of the zonal method used by all the other researchers referenced in this section. The discretisation of the first principle hybrid boiler model, as it was referred to, is illustrated in Figure 11. The discretisation is one-dimensional for the mass flow and combustion kinetics along the height of the burner and three-dimensional for the radiation heat transfer calculations. A Lagrangian framework was used to solve the heterogeneous reactions zone by zone between the char particles and gas (Ma et al., 2016:136). Ma et al. (2016:136) selected suitable submodels for the radiation properties of the gas and particles as well as the combustion kinetics for air-fired and oxy-fired furnaces. Ma et al. (2016:155) reported that a typical model converged in approximately one minute on a personal computer. The results were compared to CFD and provided comparable predictions for the furnace exit gas temperature, heat transfer to walls and unburned carbon at the furnace exit (Ma et al., 2016:156).

2.2.5 Summary of the modelling approaches for boiler furnaces

The level of detail modelled in a boiler furnace can be ordered in the following continuum from the simplest to the most complex:

- Mass and energy balance.
- Semi-empirical methods.
- Reactor network models (RNM).
- Computational fluid dynamics (CFD).

Each approach has advantages and disadvantages that will define its applicability. The simplest, such as a mass and energy balance, requires a lot of input information from the user and provides an overall heat flux as a result. More results are available when using semi-empirical methods such as the Gurvich method.

CFD is more accurate in the prediction of temperature and the flow patterns in the furnace of a boiler (Sankar, Santhosh Kumar & Balasubramanian, 2019:660). CFD software divides a given geometry into smaller finite volumes. It can make use of differencing schemes and numerical methods to solve the continuity, momentum and energy equations necessary to provide the flow, pressure and temperature fields with minimal inputs.

RNMs is a viable approach for the goals set out in this thesis. For the cases of a coal-fired furnace, albeit pulverized, fluidised bed or oxy-fuel, a typical one-dimensional mass flow (plug

flow) was assumed, but for most of the cases, the radiation heat transfer was calculated for a three-dimensional discretisation. The plug flow assumption limits the capabilities to capture multi-dimensional flow effects. All the models provided the FEGT, but no study considered the multi-dimensional temperature profile at the furnace exit and the impact on the heat transfer to the nearest heaters. The cases with the reheating furnace did account for multi-dimensional flow effects but these models did not require combustion. Hence, a possible need exists to create a pulverized fuel furnace model integrated with a process model of the water/steam side to study the multi-dimensional flow effects, i.e. the unequal distribution of flow or pulverized fuel fineness, to account for the influence on the FEGT profile and superheater performance.

To summarise, for a methodology complying with the hypothesis set out in section 1.2, a model containing characteristics of both a CFD based model or a RNM model will be required. CFD models are the most suitable in modelling flow phenomena, but a detailed representation of the chemical kinetics is not necessary. CFD models are computationally expensive, therefore shifting the selection to RNM based models that are faster to solve with the integration of a coal combustion model. These models necessitate prior knowledge of the flow patterns. Hence, a combination of CFD and RNM models will be the optimal choice to integrate into a network-based furnace model.

The following sections will elaborate on the mathematical models considered for the methodology proposed in chapter 3.

2.3 Radiation heat transfer

As reported in the work by Laubscher and Rousseau (2019a:10), Peters and Weber (1997:171) and Ranade and Gupta (2015:137), radiation heat transfer accounts for more than 89% of the heat transfer in the furnaces of coal-fired boilers. Selecting an appropriate radiation heat transfer model is therefore essential for the success of a network-based furnace model.

Calculating the radiation heat transfer requires the solution of the radiative heat transfer equation (RTE) and estimation of the radiative properties of the participating gases (mainly H_2O and CO_2) and particles. According to Ranade and Gupta (2015:100) the main approaches to solving the RTE are:

- Monte Carlo (or statistical method): This method tracks a set of photons initiating from a surface or volume until the intensity thereof falls below a defined level within the control volume. The method is the most accurate but computationally very expensive due to the number of individual photons to track.

- Zonal method: The computation domain is divided into volumes having uniform temperature and radiation properties. The radiation heat transfer between volumes and surfaces as well as volumes to surfaces is calculated with direct exchange areas. This approach is described in more detail in section 2.3.1.
- Flux methods: These methods simplify the RTE to ordinary differential equations by assuming that the intensity of radiation is uniform over defined intervals of the solid angle. One example is the DO method which can be solved in an efficient manner with existing CFD.

A comparison of the performance of the Monte Carlo model, discrete transfer model, discrete ordinates method, finite volume method, flux model, P1 approximation method and moment method as applied in CFD are available in the work done by Knaus et al. (1997), Ströhle et al. (2000), Filkoski (2010) and Holkar and Hebbal (2013). From these studies, it was shown that the most accurate method, i.e. the Monte Carlo method, required the greatest computing time and memory usage (see Table 1). The authors considered the Monte Carlo method the benchmark for heat flux accuracy and the Moment method the benchmark for computational time. The results of the other method were then normalised to the benchmark. Notable is that the DO method was widely used in recent work published by Ranade and Gupta (2015), Ma et al. (2016), Madejski (2018), Laubscher and Rousseau (2019) and Rousseau and Laubscher (2019a; 2019b; 2019c).

Table 1 - Comparison of the heat transfer and computation time for various radiation heat transfer calculation methods (Sankar, Santhosh Kumar & Balasubramanian, 2019:656).

Method	**Heat flux**	**Computational time**
Monte Carlo	100% (base)	6.82
Flux method	99.4%	1.02
Discrete transfer method	99.6%	1.34
Finite volume method	99.8%	1.09
Discrete ordinate method	100.2%	1.03
Moment method	102.7%	1 (base)

2.3.1 Zonal method

A popular method used in RNM (refer to section 2.2.4), called the zonal method and introduced by Hottel and Cohen (1958), has been widely used in combustion heat transfer models. The zonal method was developed to capture the radiation heat transfer in gas-filled enclosures with a non-isothermal temperature distribution. This method was regularly applied in studies involving combustion processes in a furnace and has been used since the 1960s because of its reduced

computational time compared to methods used in CFD codes. Examples of studies where the zonal method was applied in combustion processes or studies that were aimed at applying or improving the method are presented in the work by Sarofim (1961), Karasina et al. (1982), Tucker (1986), Sasse, Koenigsdorff and Frank (1995), Abryutin et al. (1998), Carvalho and Farias (1998), Karasina et al. (2000), Ivanović (2005), Bordbar and Hyppänen (2007), Méchi et al. (2009), Chudnovsky et al. (2009), Crnomarkovic et al. (2012), Cui, Chen and Gao (2010), Karasina et al. (2010), Alekhnovich, Artem'eva and Chernetskii (2012), Tan et al. (2013), Crnomarković et al. (2013), Ebrahimi et al. (2013), Hu et al. (2016, 2017, 2018a, 2018b, 2019).

In the zonal method, the furnace enclosure is subdivided into a number of uniform property control volumes with distinct surface areas, each containing an isothermal participating medium. Three possible direct exchange areas are identified as illustrated in Figure 12, namely between different surfaces, between surfaces and volumes, and between different volumes. These are derived based on the relative angles, distances and extinction coefficients.

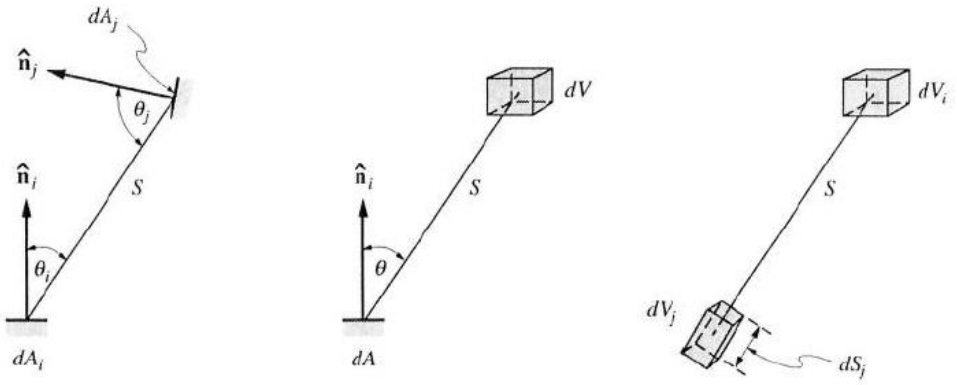

Figure 12 - Radiative exchange between surfaces, surface to volume and volume to volume (Modest, 2003:545).

The total exchange areas in the zonal method are calculated from the direct exchange areas (DEA). Empirical correlations to calculate the direct exchange areas have been provided in the work done by Hottel and Cohen (1958) and improved by Tucker (1986) to calculate the direct exchange areas without having to solve the six-fold integral.

A Monte Carlo ray-tracing method and post-processing "smoothing" were used by Hu et al. (2019:732) to calculate the exchange areas (view factors). This method is preferred for complex furnace geometries. The method traces a large number of randomly distributed rays between surfaces and volumes until each ray is intercepted by all other possible surface and volume zones within the furnace enclosure. However, the exchange areas need to be updated if the radiation heat transfer properties change significantly. Fortunately, for the reheating furnace applications, the radiation properties remain fairly constant, which is not necessarily the case for pulverized fuel

combustion. For pulverized fuel furnaces the particle concentration will be the highest near the burners while the concentration decreases further away from the burners due to the combustion of the combustible matter. The mode of particle emissivity also changes throughout the furnace volume when a particle is converted due to the burnout process from coal to ash. The CO_2 concentrations will be low near the burners but will increase further along the flow paths due to the burnout converting O_2 to CO_2.

Recently, Monnaemang (2015) developed a code in Scilab® to perform DEA calculations. The code combines discrete numerical integration for approximating direct exchange areas similar to the approach proposed by Ebrahimi et al. (2013) with two smoothing techniques, proposed by Lawson (1995) and Larsen and Howell (1986) to approximate the direct exchange areas (DEA). The work included converting the DEA to total exchange areas (TEA) for emitting and absorbing gases that include scattering. This code is currently limited to simple rectangular geometries.

2.3.2 Radiation heat transfer properties

The radiative properties of CO_2 and H_2O are the most important of the gases to consider for participation in the radiation heat transfer of coal-fired boiler furnaces. According to Ranade and Gupta (2015:103) the following approaches provide approximated radiation heat transfer properties for gases:

- Line-by-line approach: An absorption coefficient is calculated for each spectral line. The information is obtained from databases such as HITRAN96 or from the higher temperatures (extrapolated) version, HITEMP. The combustion processes are typically at the higher temperatures and therefore uncertainty regarding the accuracy exists. This approach also requires large computational resources.
- Narrow-band approach: This approach averages the absorption coefficient over a narrow spectral range rather than at each spectral line.
- Wide-band approach: This approach applies the narrow-band results by integrating the values across a band.
- Global approach: This approach combines the three approaches above by creating a reference table for the properties. The desired property is estimated based on the gas composition, pressure, temperature and weighing factors of the individual gases.

Lallemant, Sayre and Weber (1996) provided a review of the correlations available to calculate gas emissivity. From the list considered, the CO_2-H_2O vapour mixture correlation of Leckner

(1972) claimed a 10% accuracy across a wide range of temperatures and partial pressure path lengths.

Coal, char and fly ash particles form part of the participating medium in coal-fired boiler furnaces. The radiative properties are usually considered gray in the radiation heat transfer calculations due to the emitting and absorbing nature of the participating medium. Models to estimate the emissivity of particles were proposed by Smoot and Pratt (1979), Kim and Lior (1995), Yin (2015) and Zhang, Li and Zhou (2016).

2.4 Combustion models

As a simplification, a coal particle comprises of raw coal, fixed carbon, ash and inherent moisture. The raw coal is considered the sum of the fixed carbon and volatile material fractions obtained from the proximate analysis. The composition of such a particle is shown in Figure 13.

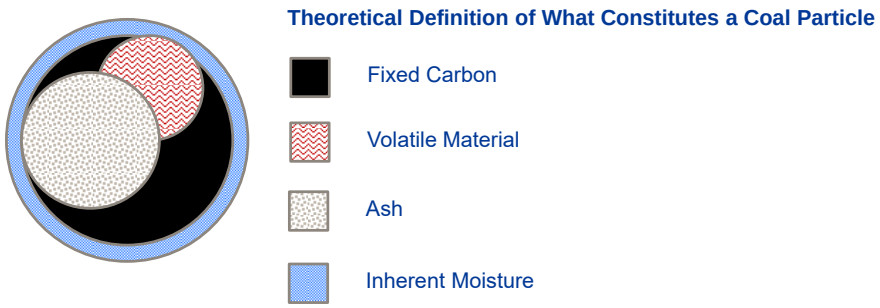

Figure 13 - A basic coal particle (Van der Meer, Rousseau & Naidoo, 2019:261).

During the combustion process, the particle can be assumed to undergo three processes: dry-out, devolatilisation and fixed carbon (char) combustion (see Figure 14). A common assumption is that the three processes occur sequentially for a given particle i.e. that dry-out must be complete before devolatilisation occurs (both in the order of milliseconds), and the second process must complete before char combustion (typically seconds) occurs. Williams, Pourkashanian and Jones (2000: 2147) stated that the contribution of the volatiles is a major factor in the flame temperature in a coal blend and in pulverized-fuel combustors the devolatilisation occurs separately from the char combustion.

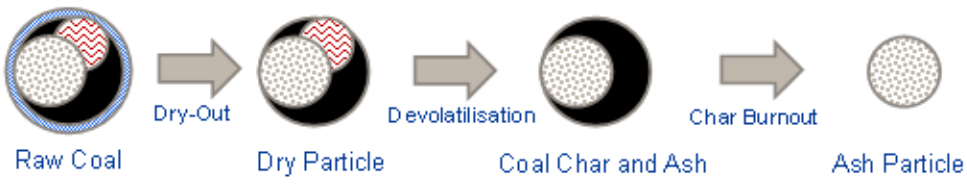

Figure 14 - Coal particle combustion processes (Van der Meer, Rousseau & Naidoo, 2019:261).

A relatively unsophisticated model and one of the early models published in the literature to calculate the combustion was developed by the British Coal Utilisation Research Association (BCURA). The mathematical model of combustion estimates the char (fix carbon) burnout, oxygen partial pressure, radiation to the walls and temperature along the axial length of a cylindrical combustion chamber (Field et al., 1967). During the initial development of the BCURA one-dimensional burnout model, the rate of devolatilisation was assumed to be instantaneous when enough oxygen was available, which yielded an unrealistically high temperature spike near the inlet. Gill (1969) improved on this by extending the model with the introduction of the progressive evolution of volatiles model, postulating a constant rate of evolution with respect to the distance from the burner.

A variety of combustion models were since published. Sankar, Santhosh Kumar and Balasubramanian (2019:647-651) summarised the char combustion models as follows:

- Global char combustion models, e.g. Field et al. (1967) and Baum and Street (1971).
- Intrinsic char combustion models, e.g. Smith (1982).
- Advanced char combustion models, e.g Sun and Hurt (2000).

Since the spatial devolatilisation model proposed by Gill (1969), a one-step reaction, two-step reaction and Distributed Actived Energy Model (DAEM) based on the Arrhenius kinetic rate were published (Sankar, Santhosh Kumar & Balasubramanian, 2019:645-646). The temperature-dependent two-step reaction model proposed by Kobayashi, Howard and Sarofim (1977) is a frequently selected model (Hovi et al. 2017). Other devolatilisation models grouped by Sankar, Santhosh Kumar and Balasubramanian (2019:645-647) as phenomenological models are Functional Group Depolymerisation Vaporisation Cross-linking (FG-DVC), Chemical Percolation Devolatilisation (CPD), FLASCHAIN and the predictive multi-step model.

2.5 Summary

The level of detail modelled in a boiler furnace can be either simple or complex depending on the need and approach used. Each approach has its applicability. A mass and energy balance is the simplest and requires a lot of input information from the user to provide an overall heat flux as a result. Semi-empirical methods such as the Gurvich method provides more results such as the FEGT. CFD provides the most detailed solutions in predicting the temperature and flow patterns in the furnace of a boiler. The RNM approaches delivered a balance between the complexity of the solution and computer solving time to reach the solution. A model containing characteristics of both

a CFD based model or a RNM model will be required. RNM based models solve faster but a coal combustion model will be needed. CFD models are computationally expensive but are required to provide knowledge of the flow patterns.

The coal-fired furnace cases assumed a typical one-dimensional mass flow (plug flow) while solving a three-dimensional radiation heat transfer field. The plug flow assumption limits the capabilities to capture multi-dimensional flow effects. The models provided a furnace exit gas temperature, but did not consider the multi-dimensional temperature profile at the furnace exit and the impact on the heat transfer to the nearest heat exchangers. The reheating furnace cases accounted for multi-dimensional flow effects but did not require combustion. Hence, a knowledge gap exists in a pulverized fuel furnace model to integrate with a process model of the water/steam side to study the multi-dimensional flow effects. This will allow studies such as how the unequal distribution of flow or pulverized fuel fineness influences the FEGT profile and superheater performance.

A popular RNM approach is the zonal method introduced by Hottel and Cohen (1958). The zonal method was widely used in combustion heat transfer models, e.g. work presented by Sarofim (1961), Karasina et al. (1982), Tucker (1986), Sasse, Koenigsdorff and Frank (1995), Abryutin et al. (1998), Carvalho and Farias (1998), Karasina et al. (2000), Ivanović (2005), Bordbar and Hyppänen (2007), Méchi et al. (2009), Chudnovsky et al. (2009), Crnomarkovic et al. (2012), Cui, Chen and Gao (2010), Karasina et al. (2010), Alekhnovich, Artem'eva and Chernetskii (2012), Tan et al. (2013), Crnomarković et al. (2013), Ebrahimi et al. (2013), Hu et al. (2016, 2017, 2018a, 2018b, 2019).

A variety of correlations to calculate the gas emissivity was reviewed by Lallemant, Sayre and Weber (1996). One of the correlations for a CO_2-H_2O vapour mixture proposed by Leckner (1972) claimed a 10% accuracy across a wide range of temperatures and partial pressure path lengths. The radiative properties of the coal, char and fly ash particles can be estimated by models proposed by Smoot and Pratt (1979), Kim and Lior (1995), Yin (2015) and Zhang, Li and Zhou (2016).

A variety of combustion models are available. An unsophisticated was developed by the British Coal Utilisation Research Association (BCURA) for the char (fix carbon) burnout estimation (Field et al., 1967) and devolatilisation (Gill, 1969). Other models, with varying complexity, are also available and reviewed in Sankar, Santhosh Kumar and Balasubramanian (2019:645-651).

Having explored the available literature relevant to developing a network-based furnace model, the methodology will be discussed next in chapter 3.

3. Network-based furnace model methodology

Different concepts of the methodology were introduced in Van der Meer, Rousseau and Jestin (2016a, 2016b, 2016c). The first iteration of the complete methodology was published in Van der Meer, Rousseau and Naidoo (2019) and applied to a single-burner furnace. The updated methodology will be presented in this chapter based on new findings and also expanded to be applicable to a furnace with multiple burners. The revisions will be discussed where applicable.

3.1 Network nodalisation

The proposed methodology combines different existing approaches into a single network-based tool, which includes the zonal approach to model the thermal radiation in three dimensions. The furnace volume is discretised into an interconnected network of nodes and one-dimensional fluid flow and heat transfer elements like that of existing system level thermofluid codes. Rousseau et al. (2015:74) provide an enlightening and concise explanation of such a system level thermofluid code named Flownex® SE which can also be referred to as a one-dimensional CFD code. The nodes coincide with the volumes in the zonal model, with flow and heat transfer occurring between the nodes determined by the interconnecting component, as illustrated in Figure 15.

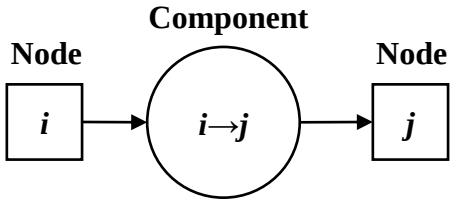

Figure 15 - System level network representation.

3.2 Spatial discretisation

The spatial discretisation scheme entails dividing the volume occupied by the furnace into a grid of smaller volumes, each representing a zone within the furnace. The size of the zone has an important impact on the results delivered by the models. If it is required to determine the detail flows and temperatures from the burner inlet through the flames up to every corner within the furnace, a very fine grid will be necessary. For the applications envisaged, such as process condition monitoring, this level of detail is not required and therefore a coarser grid can be employed. It is

only necessary for the grid to be fine enough to capture the temperature distribution at the furnace exit as well as the heat flux to the furnace walls and exit plane to a sufficient degree of detail.

The aim of the model is not to study the microscopic phenomena during particle heat-up and devolatilisation that occur near the burner mouth, which would require a very fine grid within this region. A macroscopic approach will entail a coarser grid which only includes the combustion products and heat transfer within the first few zones next to the burner. The fixed carbon (char) burnout has a longer residence time with these particles travelling over the length of the furnace through multiple zones. Therefore, the cell lengths should be small enough to allow sufficient accuracy of the burnout calculations.

The envisaged furnace geometry essentially has a rectangular shape and it is assumed that the curvature or angled surface at the bottom hoppers and flow outlets, as well as smaller indentations in the walls, do not have a significant effect on the flow and heat transfer within the furnace. An illustration of the envisaged discretisation where the furnace is divided into smaller hexagonal, finite and homogeneous cubes is shown in Figure 16. This discretisation was chosen to be consistent with the zonal radiation heat transfer model discussed in section 3.4. The red coloured surface represents the inlet zone for a burner while the blue surfaces represent the walls with the outlet zone(s) on the opposite side of the inlet. This discretisation is typical for a furnace with a single-burner configuration as modelled in section 4.2.1.

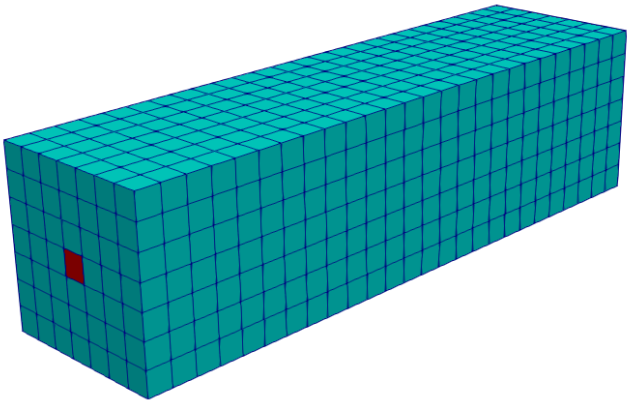

Figure 16 - Zone-wise representation of the spatial discretisation.

The flow of interest has a high Peclet number and to ensure numerical stability, an upwind differencing scheme is employed. Downwind and central differencing schemes can also be employed but only show minor variances for the cases validated later on. It is assumed that the gas entering through the faces will continue to mix perfectly within the zone.

3.3 Energy balance

The temperature at the face of each outflowing stream is calculated by applying overall energy conservation to each zone, including the burnout and heat transfer occurring while neglecting potential and kinetic energy effects. The gas and particles are combined and considered as a homogeneous mixture with energy flowing in and out of the zone while accounting for radiation heat transfer and convection heat transfer within the zone. A Lagrangian particle tracking approach is implemented for bins different particle sizes and it is assumed that the particles travel with the same velocity as the gas stream through each zone. Therefore, the following energy balance is applied to each zone:

$$\dot{m}_e h_e - \dot{m}_i h_i + \dot{Q}_{source} - \dot{Q}_{rad} = 0 \tag{1}$$

where $\dot{m}_i$ is the total mass flow rate into the zone, $\dot{m}_e$ the total mass flow rate exiting the zone, h_i the enthalpy of the mixture entering the zone, h_e the enthalpy of the mixture exiting the zone, $\dot{Q}_{source}$ the source term where heat is added and $\dot{Q}_{rad}$ the radiation heat transfer. In Van der Meer, Rousseau and Naidoo (2019:256), the energy balance was separate for the particles and gases as per the formulation in Gill (1969). During the development of the methodology for multiple burners, the contribution of convection heat transfer between the particles and gases caused instabilities during the numerical solving process. Therefore, the approach reverted to a combined energy balance as in Field et al. (1967) where the particles and gases were considered a single mixture. The gases and particles can be separated with further development of the methodology.

3.4 Radiation heat transfer model

With radiation being the dominant mode of heat transfer in a furnace, a model is required to calculate the radiation heat transfer within a three-dimensional participating medium. This is primarily to provide the furnace exit temperature profile as well as the heat flux to the surfaces of the furnace wall. The zonal method introduced by Hottel and Cohen (1958) to model radiation heat transfer in gas-filled enclosures with a non-isothermal temperature distribution will be employed because it has been applied widely since the 1960s in studies involving combustion processes in furnaces. Successful application of the mathematical model was discussed in section 2.2.4 and 2.3.1. This approach is computationally less expensive than models such as the Monte Carlo methods and therefore beneficial when developing a quick-solving tool.

The direct exchange factors for the surface to surface exchange ($\overline{s_i s_j}$) when a gray absorbing/emitting medium is present in the space between the surfaces can be calculated with (the surface to volume and volume to volume is available in Modest, 2003:546):

$$\overline{s_i s_j} = \int_{A_i}\int_{A_j} e^{-\beta_{ij} r_{ij}} \frac{\cos\theta_i \cos\theta_j}{\pi r_{ij}^2} dA_j dA_i \tag{2}$$

$e^{-\beta r}$ is known as the transmission factor and is the factor that differentiates between a non-participating and participating medium and β_{ij} is the extinction factor and includes the effects of scattering and absorption (κ_{ij}). The direct exchange factors can then be used to calculate the total exchange factor to include the surface emissivities – this procedure is also well documented in Modest (2003:539-561). Given this and solving the energy conservation laws in a radiation exchange network, the unknown temperatures and heat fluxes can be obtained with the following equations (Modest, 2003:539-561):

For the energy balance per surface *i:*

$$\dot{Q}_{s,i} = \sum_{j=1}^{N} \overline{S_i S_j} E_{s,j} + \sum_{j=1}^{K} \overline{S_i G_j} E_{g,j} - A_i \varepsilon_i E_{s,j} \tag{3}$$

For the energy balance per volume *i:*

$$\dot{Q}_{g,i} = \sum_{j=1}^{N} \overline{G_i S_j} E_{s,j} + \sum_{j=1}^{K} \overline{G_i G_j} E_{g,j} - 4 V_i \beta_i E_{g,j} \tag{4}$$

where $\dot{Q}_{s,i}$ and $\dot{Q}_{g,i}$ are the net radiation heat transfer for each surface and volume, $\overline{S_i S_j}$ the total surface to surface exchange area, $\overline{S_i G_j}$ the total surface to volume exchange area, $\overline{G_i S_j}$ the total volume to surface exchange area, $\overline{G_i G_j}$ the total volume to volume exchange area, A the surface area, ε the emissivity, V the volume, E the blackbody emissive power and β the extinction factor. The model developed by Monnaemang (2015) will be employed in calculating the direct exchange areas which will be converted to total exchange areas as required in the zonal method.

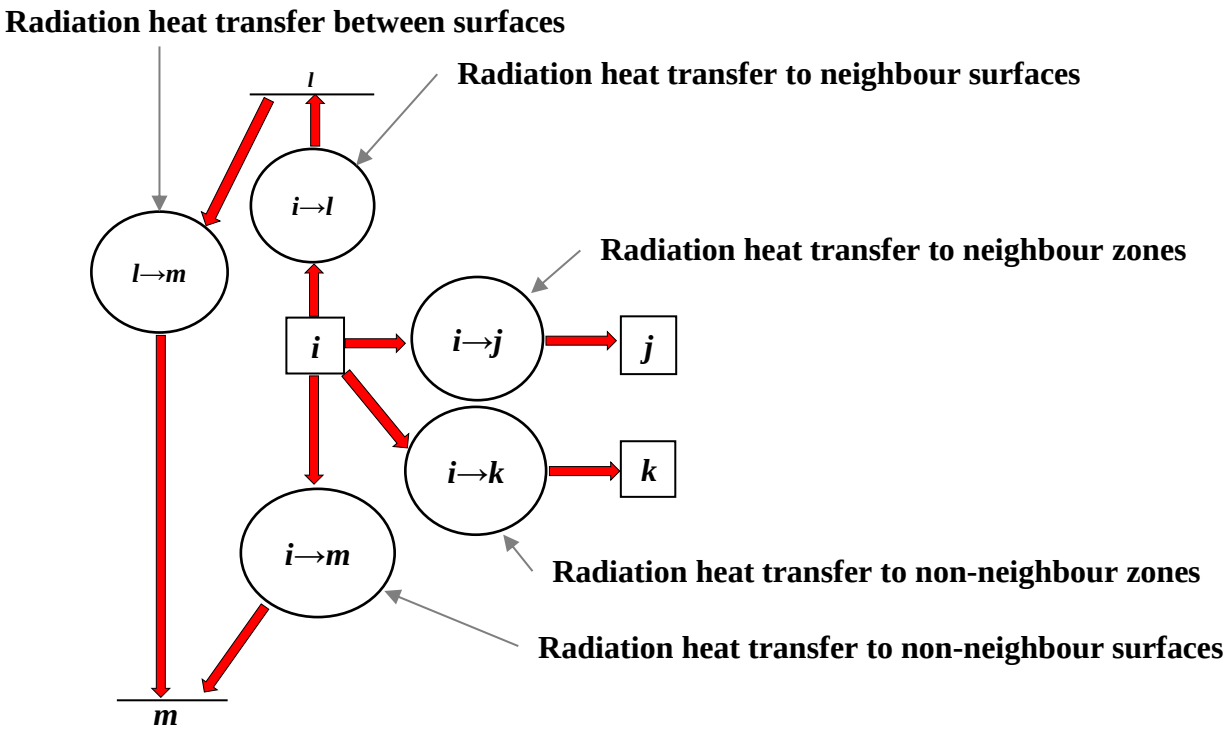

Figure 17 - Network flow representation of the radiation heat transfer (each zone represents a discretised volume).

The multi-dimensional network of the radiation heat transfer between the neighbouring and non-neighbouring zones is illustrated in Figure 17. The network consists of nodes, representing either a volume or a surface, and components quantifying the heat exchange between each of the nodes. The zonal method calculates the quantity of radiation heat transfer.

The wall emissivity and extinction coefficient are necessary for the calculation of DEA. The wall emissivity is a material property, while the extinction coefficients are calculated by summation of the absorption and scattering coefficients of the gas and particles. The scattering coefficient will be neglected throughout this study because the particle size parameter and particle volume fraction fall outside the range that it needs to be accounted for in pulverized coal combustion (Modest, 2003:362-363), but can easily be added in the future. The extinction coefficient contribution due to gas absorption is related to the local gas absorptivity and optical mean beam length by:

$$\kappa_{g,i} = \frac{-\ln(1-\sigma_{g,i})}{L_m} \tag{5}$$

where κ_g is the Planck-mean gas absorption coefficient for zone *i*, σ_g the absorptivity for the gas in zone *i* and L_m the optical mean beam length. The optical mean beam length is related to the total volume (V_i) and total area (A_i) of each zone by:

$$L_m = 3.6\frac{V_i}{A_i} \tag{6}$$

Leckner's (1972) model for calculating the absorption coefficients for the participating gases (H_2O and CO_2) will be used. The explicit formulation simplifies implementation. The model as presented in the textbook by Modest (2003) calculates the absorptivity and emissivity of water vapour and carbon dioxide as a function of mixture pressure (p), component partial pressure (p_{a,CO_2} or p_{a,H_2O}), gas temperature and mean beam length (L_m). The first step is to calculate the zero partial pressure emissivity for water vapour (ε_{0,H_2O}) and carbon dioxide (ε_{0,CO_2}) from:

$$\varepsilon_0 = exp\left[\sum_{i=0}^{M}\sum_{j=0}^{N} c_{ji}\left(\frac{T_g}{T_0}\right)^j \left(log_{10}\, p_a L_m\right)^i\right] \tag{7}$$

where T_g is the gas temperature and T_0 the reference temperature. The constants are available in Table 2.

Table 2 - Correlation constants for the determination of the total emissivity for water vapour and carbon dioxide.

Water vapour				**Carbon dioxide**				
p_0	1 bar			p_0	1 bar			
T_0	1000 K			T_0	1000 K			
t	$\frac{T_g}{T_0}$			t	$\frac{T_g}{T_0}$			
P_E	$\left(p + 2.56 p_a / \sqrt{t}\right)\big/ p_0$			P_E	$\left(p + 0.28 p_a\right)\big/ p_0$			
$\left(p_a L_b\right)_m$	$13.2t^2$			$\left(p_a L_b\right)_m$	$0.054 / t^2$ for $t < 0.7$ $0.225t^2$ for $t > 0.7$			
a	2.144 for $t < 0.75$ $1.888 + 2.053 log_{10}\, t$ for $t > 0.75$			a	$1 + 0.1 / t^{1.45}$			
b	$1.10 / t^{1.4}$			b	0.23			
c	0.5			c	1.47			
M,N	2,2			M,N	2,2			
c_{ji}	j=0	j=1	j=2	c_{ji}	j=0	j=1	j=2	j=3
i=0	-2.2118	-1.1987	0.035596	i=0	-3.9893	2.7669	-2.1081	0.39163
i=1	0.85667	0.93048	-0.14391	i=1	1.2710	-1.1090	1.0195	-0.21897
i=2	-0.10838	-0.17156	0.045915	i=2	-0.23678	0.19731	-0.19544	0.044644

The emissivity for water vapour (ε_{H_2O}) and carbon dioxide (ε_{CO_2}) are calculated from the zero partial pressure emissivity with:

$$\varepsilon\left(p_a L_m, p, T_g\right) = \varepsilon_0 \left\{1 - \frac{(a-1)(1-P_E)}{a+b-1+P_E} exp\left(-c\left[log_{10}\frac{\left(p_a L_b\right)_m}{p_a L_m}\right]^2\right)\right\} \tag{8}$$

When both water vapour and carbon dioxide are simultaneously present in a mixture, a correction factor is necessary. The emissivity correction factor ($\Delta\varepsilon$) is calculated from the water vapour and carbon dioxide partial pressure, as well as the mean beam length as follows:

$$\Delta\varepsilon = \left[\frac{\zeta}{10.7+101\zeta} - \left(\frac{1}{10.7+101\zeta}\right)\zeta^{10.4}\right]\left[log_{10}(p_{a,CO_2} + p_{a,H_2O})L_b\right]^{2.76} \tag{9}$$

where

$$\zeta = \frac{p_{a,H_2O}}{p_{a,H_2O} + p_{a,CO_2}} \tag{10}$$

The emissivity of the gas mixture is then given by:

$$\varepsilon_f = \varepsilon_{CO_2} + \varepsilon_{H_2O} - \Delta\varepsilon \tag{11}$$

The water vapour and carbon dioxide absorptivity are calculated from:

$$\sigma = \left(\frac{T_g}{T_w}\right)^{0.5} \varepsilon\left(p_a L_m \frac{T_w}{T_g}, p, T_w\right) \tag{12}$$

The absorptivity of the gas mixture is then given by:

$$\sigma_g = \sigma_{CO_2} + \sigma_{H_2O} - \Delta\varepsilon\left(p_{a,H_2O} L_m \frac{T_w}{T_g}, p_{a,CO_2} L_m \frac{T_w}{T_g}\right) \tag{13}$$

The applicable range for Leckner's correlation is (Lallemant, Sayre & Weber, 1996):

$$400K < T_g < 2500K$$

$$0.0005 < p_{a,CO_2} L_m < 1atm \cdot m$$

$$0.002 < p_{a,H_2O} L_m < 10atm \cdot m$$

$$0.0005 < pL_m < 10atm \cdot m$$

The particle absorption coefficients are calculated based on the particle emissivity model reported in Yin (2015). Because scattering is neglected, the particle extinction coefficient is equal to the absorption coefficient. Yin's (2015) particle emissivity model depends on the conversion of the coal. A similar model to calculate the scattering is available when the effect needs to be accounted

for. The absorption coefficient is then calculated via Equation 5. The particle emissivity changes with the fraction of unburned fixed carbon between the emissivity for fly ash and unburned coal as follows:

$$\varepsilon_p = 0.4UC + 0.6 \tag{14}$$

The methodology in Van der Meer, Rousseau and Naidoo (2019:256) implement the model proposed by Kim and Lior (1995). The model proposed by Yin (2015) provided better results for the validation of the single-burner furnace and was therefore used as the preferred model. The formulation of alternative models is available in the appendix. The extinction coefficient contribution due to particle absorption is related to the emissivity and optical mean beam length by:

$$\kappa_{p,i} = \frac{-\ln(1-\varepsilon_{p,i})}{L_m} \tag{15}$$

The absorption coefficient for each zone is then the result of the gas and particle absorption coefficient added together.

3.5 Heat source and combustion model

The zonal method requires either the temperature or heat source distribution for each volume as input to calculate the radiation heat transfer. Because the temperature distribution is required as a result, a suitable combustion model providing the heat sources is needed for each volume. Another valuable result from the combustion models is the predicted burnout of the combustible matter giving an indication of the combustion efficiency. Various models are available to simulate the combustion because of the industry focus to maximise burnout while minimising emissions. Due to the relatively rough discretisation scheme employed by the network-based furnace model and the current focus not being on the emissions, the most suitable models are those with a quick solution time solving for the burnout of fixed carbon (char) and volatiles.

As previously mentioned in the literature review, Hesselmann (1998) developed a heat source model for HotGen utilising CFD in a pre-characterisation step. The methodology integrates a pre-characterised mass flow map and heat source model with the zonal method. This approach delivered engineering results within very short timescales. Unfortunately, this approach is limited to emulating the heat source distribution for the specific characterised flame and omits input details for different combustible matter and the subsequent conversion thereof. Therefore, this entails re-characterisation of the fitting parameters for each unique flame configuration. In the current

network-based approach, a more fundamental model is applied to quantify the burnout and heat sources to minimise the reliance on burnout pre-characterisation.

The network-based furnace model divides the multi-dimensional flow field of the furnace into a series of one-dimensional flow paths to which the combustion model may be applied. All of the BCURA combustion development was applied to one-dimensional flow. The combination of the fixed carbon burnout model of Field et al. (1967) and the devolatilisation model by Gill (1969) is therefore implemented in the network-based furnace model to calculate the heat sources for each volume (see Figure 18). These models are also quite unsophisticated making it easier to use in the first-order development of the network-based furnace model.

Figure 18 - Heat source added to each zone due to combustion (each zone represents a discretised volume).

The combination of the two models is therefore a two-step process starting with devolatilisation with the combustion of the volatiles and thereafter fixed carbon (char) combustion. The governing physics allow for moisture evaporation and devolatilisation to occur concurrently. This is typical at lower combustion temperatures (400-450 K), but for the coals studied, the temperatures were significantly above this temperature range. One of the cases was South African coal with devolatilisation temperatures of 550-640 K. Faster ignition will occur for the conditions where the moisture evaporation and devolatilisation occur concurrently. The earlier ignition will shift the flame position towards the furnace walls and increase the flame temperature. It is expected that this effect is negligible when the amount of volatile matter and moisture is significantly lower than the fixed carbon (char).

It is also possible for the fixed carbon (char) burnout to occur concurrently with the devolatilisation. However, moisture evaporation and devolatilisation are fast processes when compared to the very slow process of fixed carbon (char) burnout. The main contributing factors to the radiation heat transfer in a pulverized-fuel boiler are participation of the particle and CO_2(gas) radiation. The change in particle radiation and CO_2(gas) radiation is significantly dependent on the fixed carbon (char) burnout. On a global scale within the furnace, faster ignition and burnout of the constituent in the coal would slightly change the flame position and length in the furnace. The change in flame position and length impacts whether more or less radiation heat transfer will occur near the burners or further along the flow paths in the furnace.

For the current study, the complexities involved during the combustion of char were simplified to a surface reaction of the char with oxygen that may be incidental on the surface. The burnout of a parcel of fixed carbon (dUC_z) for the time travelled (dt) is given by the modelled developed by Field et al. (1969):

$$\frac{dUC_z}{dt} = \frac{(UC_z / w_z)^{2/3} S_{z0} p_{a,O_2}}{\frac{(UC_z / w_z)^{1/3}}{K_{diff,z0}} + \frac{1}{K_s}} \tag{16}$$

where UC_z is the fraction of unburned fixed carbon, w_z the mass of unburned fixed carbon relative to the mass of all the constituents in the coal, S_{z0} the surface area of the particle immediately after devolatilisation, p_{a,O_2} the partial pressure of oxygen in the free stream, $K_{diff,z0}$ the diffusional reaction rate constant for the particle and K_s the surface reaction rate. The burnout is calculated for each size fraction (*z*).

The surface reaction rate is in the form of the Arrhenius equation:

$$K_s = Ce^{\left(\frac{-E}{RT_s}\right)} \tag{17}$$

where C is a pre-exponent factor, E the activation energy, R the universal gas constant and T_s the surface temperature. Values for the pre-exponent factor and activation energy for different coals are available in Field et al. (1967:393).

The devolatilisation model of Gill (1969) that postulates a constant rate of evolution with respect to the distance from the burner is as follows:

$$VM(x) = VM(x_0)\frac{x}{x_f} \tag{18}$$

where $VM(x)$ is the fraction of total volatile matter evolved (burned) at distance x, x_f is the distance to complete evolution and $VM(x_0)$ is the total volatile matter in the coal. The equation above is applied to the carbon, hydrogen and sulphur that forms part of the volatile matter.

The combustion heat generation attributed to each zone is given by:

$$\dot{Q}_{source,i} = \dot{m}_c[32765(UC_{in} - UC_{out}) + 32765(VC_{in} - VC_{out}) + 98139(H_{in} - H_{out}) + 9256(S_{in} - S_{out})] \tag{19}$$

where $\dot{m}_c$ is the total coal mass flow rate, UC_{in} the fraction fixed carbon entering the zone, UC_{out} the fraction fixed carbon exiting the zone, VC_{in} the fraction volatile carbon entering the zone, VC_{out} the fraction volatile carbon exiting the zone, H_{in} the fraction hydrogen entering the zone, H_{out} the fraction hydrogen exiting the zone, S_{in} the fraction sulphur entering the zone and S_{out} the fraction sulphur exiting the zone.

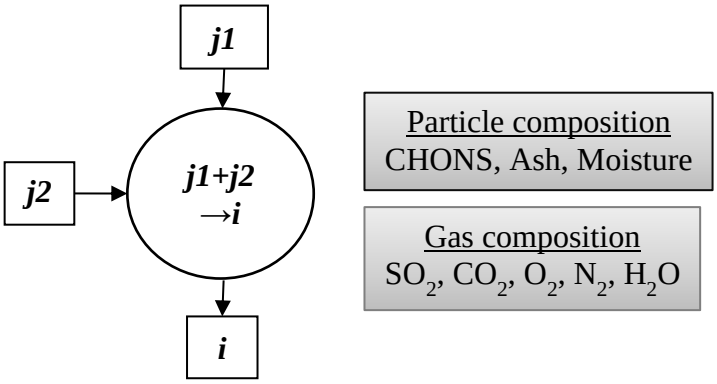

Figure 19 - In- and outflow of particle and gas compositions in a zone (each zone presents a discretised volume).

With combustion occurring within each volume, the composition of the particles and gases will change within each zone. The calculation of the composition balance for the in-flowing streams and conversion to products attributed to the out-flowing stream is executed by the system-based component shown schematically in Figure 19.

The mixture of coal and air that enters the furnace will contribute to the combustion. The change in coal particle composition is a result of the burnout calculation and conversion to gaseous products. The change in the combustible matter is provided in the combustion. The guidelines in the Eskom (2010) *Boiler Mass and Energy Balance Guideline and User Manual* can be used to calculate the theoretical air required (TAR), dry air required (DAR) and humid air required (HAR) when the as-received values for the Carbon (C), Hydrogen (H), Oxygen (O), Nitrogen (N), Sulphur (S) as well as the humidity ratio (ω), excess air ratio (α_F), unburned carbon (C') and the nitrogen oxidization ratio (r_{NO_2})are available. The formulae for the TAR, DAR and HAR are as follows:

$$TAR = \frac{1}{0.23}\left(\frac{32}{12}(C - C') + S + 8H + \frac{32}{14} r_{NO_2} N - O\right) \tag{20}$$

$$DAR = \left(1 + \alpha_F\right) TAR \tag{21}$$

$$HAR = \left(1+\omega\right) DAR \tag{22}$$

The combustion calculation for the fixed carbon is executed for discrete bins of particle sizes. Due to the varying residence times expected for the particles, the particle size distribution needs to be accounted for in each zone. The approach implemented will be explained in the following section.

3.6 Mass transfer model

The energy balance in section 3.3 indicates that each zone will have gas and particles passing through it. The advection of heat through the furnace impacts the accuracy of the temperature profile prediction at the furnace exit. This implies that the magnitude of the mass flow through each zone is required. When the zonal method was first introduced, a well-stirred combustion chamber was typically assumed. This was a suitable approximation at the time when furnaces were relatively small. With furnaces becoming larger, the burner region forms a smaller part of the total volume and therefore this simplification is no longer satisfactory. This is already evident with Lowe, Wall and Stewart (1975) having to assume a mass flow map when implementing the zonal method. They based their mass flow map on experience while not having the benefit of modern CFD tools.

With computational fluid dynamics (CFD) tools being more accessible, it became easier to determine the flow vectors within arbitrary geometries and Hesselmann (1998) applied this tool to create mass flow maps for a wall-fired furnace. The pre-calculated mass flow map was integrated with the heat source model to enable the zonal based furnace code, called HotGen, to predict the temperature profile for the wall-fired furnace. Hu et al. (2016) and Hu et al. (2018b) demonstrated successfully a similar approach using isothermal CFD mass flow maps in reheating furnace applications. These publications showed that decoupling the momentum balance from the energy balance still provided sufficiently accurate results whilst keeping the solution time short. A similar methodology is followed in the current model by creating a structured mesh in OpenFOAM® and solving for an isothermal mass flow distribution. The solution can be exported and converted to a static map containing the "From zone", "To zone" and "Mass flow rate" entries as required by the mass flow rate network-based component shown schematically in Figure 20.

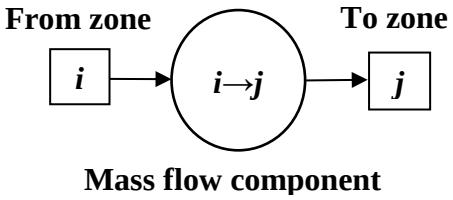

Figure 20 - In- and outflow mass between zones (each zone presents a discretised volume).

It was assumed that the particles flow at the same velocity as the gases. An average particle size is assigned to a finite number of bins (*z*) that each covers a given range of particle sizes. The representation for the in- and outflowing streams of bin 1 to *z* in a zone is shown schematically in Figure 21.

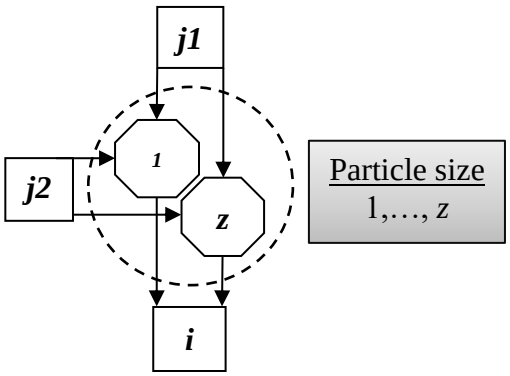

Figure 21 - In- and outflow of different particles sizes in a zone (each zone represents a discretised volume).

For an inlet boundary on a zone, the original particle size distribution will be allocated to each of the bins as appropriate. For the other inlet boundaries into a zone, the particles will be at different stages of combustion and therefore the distribution of particles between the bins will be different. The particles entering each zone will be added to the others with the same bin number as per the following mass-weighted average to calculate a new representative particle size for the bin within the zone before burnout:

$$d_z = \frac{\dot{m}_{z,i} d_{z,i} + \dot{m}_{z,j} d_{z,j}}{\dot{m}_{z,i} + \dot{m}_{z,j}} \tag{23}$$

where d_z is the weighted average particle size for bin *z* flowing into the zone, $\dot{m}_{z,i}$ the total mass flow rate of the particles in bin *z* from zone *i*, $\dot{m}_{z,j}$ the total mass flow rate of the particles in bin *z* from zone *j*, $d_{z,i}$ the particle size in bin *z* from zone *i* and $d_{z,j}$ the particle size in bin *z* from zone *j*. The particle size from zone *i* and *j* is the recalculated size from that particular zone's weighted

average particle size after taken into account the burnout of fixed carbon. The mass of unburned carbon for each of the particle sizes is calculated in a similar manner.

After the combustion calculations are executed, the newly calculated particle sizes and mass of unburned fixed carbon for each bin will be distributed between all the outflowing streams based on the mass flow rates. The inputs for the coal particle distribution will be in the form of the Rosin-Rammler law (Madejski, 2018:4).

Field et al. (1967:391) performed a sensitivity study using 4, 7 and 13 bins of particle sizes. The carbon burnout along the length used for this study is shown in Figure 22. For this study, the solution was considered to be bin number independent from seven bins and higher. Madejski (2018:4) made use of only five bins of particle sizes. Four bins will be used for this study considering that this amount already provided reasonable accuracy as well as to prevent overcomplicating the model development and troubleshooting with too many bin registers.

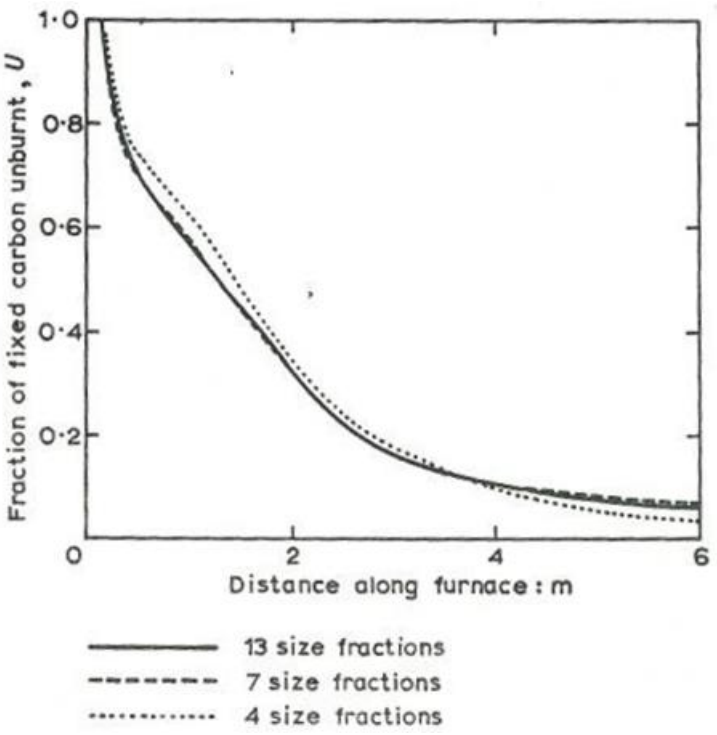

Figure 22 - The effect of the number of fractions used to represent the size distribution (Field et al., 1967:391).

3.7 Boundary conditions

The three boundaries, namely burner inlet, furnace exit and furnace wall, as shown in Figure 23 need to be considered. The furnace exit plane is considered as a plane to have a generic approach allowing for different configurations at the furnace exit. The FEGT is also one of the important

parameters as set out in the hypothesis in section 1.2. Some furnaces have a superheater at the exit and others not. If there is a superheater, then the geometry might vary based on the boiler design.

The coal quality and particle size distribution need to be defined at each burner inlet. Additionally, the mass flow and temperature of the coal, as well as the primary and secondary combustion air into the furnace, must be provided as boundary values. The methodology in Van der Meer, Rousseau and Naidoo (2019) only allowed for a single inlet boundary while the latest revision allows for multiple burner inlets with different mixtures.

The gas and particles will exit the furnace volume through the furnace exit plane. Even though the furnace exit is not a physical boundary, the radiation heat transfer model requires the temperature to be set on this plane. The temperature should be a representative temperature for the radiation heat transfer as experienced by the gas near the exit. Depending in the furnace being modelled, this can either be a nearby surface temperature of the heat exchanger tubes or the gas temperature of the neigbouring zone. The latter is also known as a Neumann or a zero-gradient boundary condition.

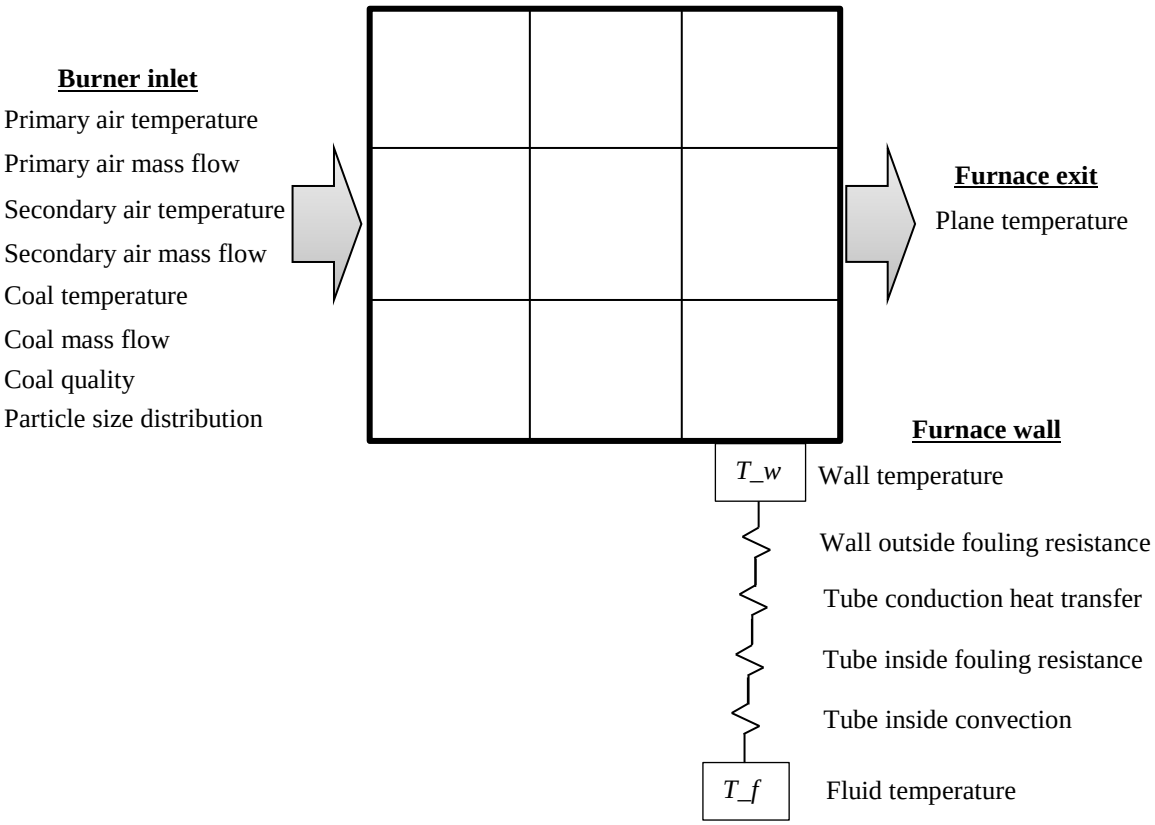

Figure 23 - Schematic of the boundary conditions.

Two options are available for the boundary on the furnace walls. The first is a fixed temperature on the walls. The heat flux on the furnace walls will be a result from the calculations. The second is

the fluid temperature inside the tubes. This allows the convection and conduction heat transfer mechanisms as well as fouling to be incorporated in the heat transfer calculations by means of:

$$\dot{Q}_{rad} = \frac{T_w - T_f}{R_t} \tag{24}$$

where is the T_f fluid temperature and R_t is the total heat transfer resistance given by:

$$R_t = R_{ti} + R_{fi} + R_w + R_{fo} \tag{25}$$

were R_{ti} is the tube inside resistance, R_{fi} the resistance due to fouling on the tube inside, R_w the resistance to conductivity through the wall and R_{fo} the resistance due to fouling on the outside. The tube inside resistance is indirectly proportional to the convection heat transfer coefficient and the surface area. The resistance to conductivity through the wall is proportional to the tube wall thickness and indirectly proportional the wall thermal conductivity. The heat flux and the temperature on the furnace walls are results from the calculations when the fluid temperature is specified as boundary.

3.8 Convergence criteria

The temperature, radiation heat transfer from zones and fixed carbon mass fraction residuals are monitored for convergence. The convergence criteria for the average change between the temperatures (r_{temp}), the average change of the radiation heat transfer from each zone (r_{heat}) and the average fixed carbon mass fraction (r_{UC}) between iteration *n-1* and *n* serve as convergence criteria as follows:

$$r_{temp} = \frac{\sum_{i=1}^{n_v} (T^n{}_{g,i} - T^{n-1}{}_{g,i})}{n_v} < 0.1K \tag{26}$$

$$r_{heat} = \frac{\sum_{i=1}^{n_v} (\dot{Q}^n_{rad,k} - \dot{Q}^{n-1}_{rad,k})}{n_v} < 1kW \tag{27}$$

$$r_{UC} = \frac{\sum_{i=1}^{n_v} (UC^n{}_i - UC^{n-1}{}_i)}{n_v} < 0.0001 \tag{28}$$

3.9 Summary of the furnace network model (FNM)

A schematic of the network-based approach for a furnace model as proposed in section 3.1 to section 3.6 is shown in Figure 24. Hereafter, this will be referred to as the furnace network model (FNM).

To set up a network-based model of a furnace, the discretisation of the wall's in- and out-flow boundaries need to be defined. An isothermal mass flow distribution using CFD is obtained and imported into a code that solves iteratively for the heat transfer, heat sources due to combustion and concentration changes. Under-relaxation is also included in the code to promote solving stability when deemed necessary. Even though the FNM solves for a temperature and gas distribution throughout the furnace, the parameters that the model aims to provide accurate predictions for are the heat transfer to the walls, furnace exit gas temperature as well as the unburned carbon and oxygen concentration at the furnace outlet.

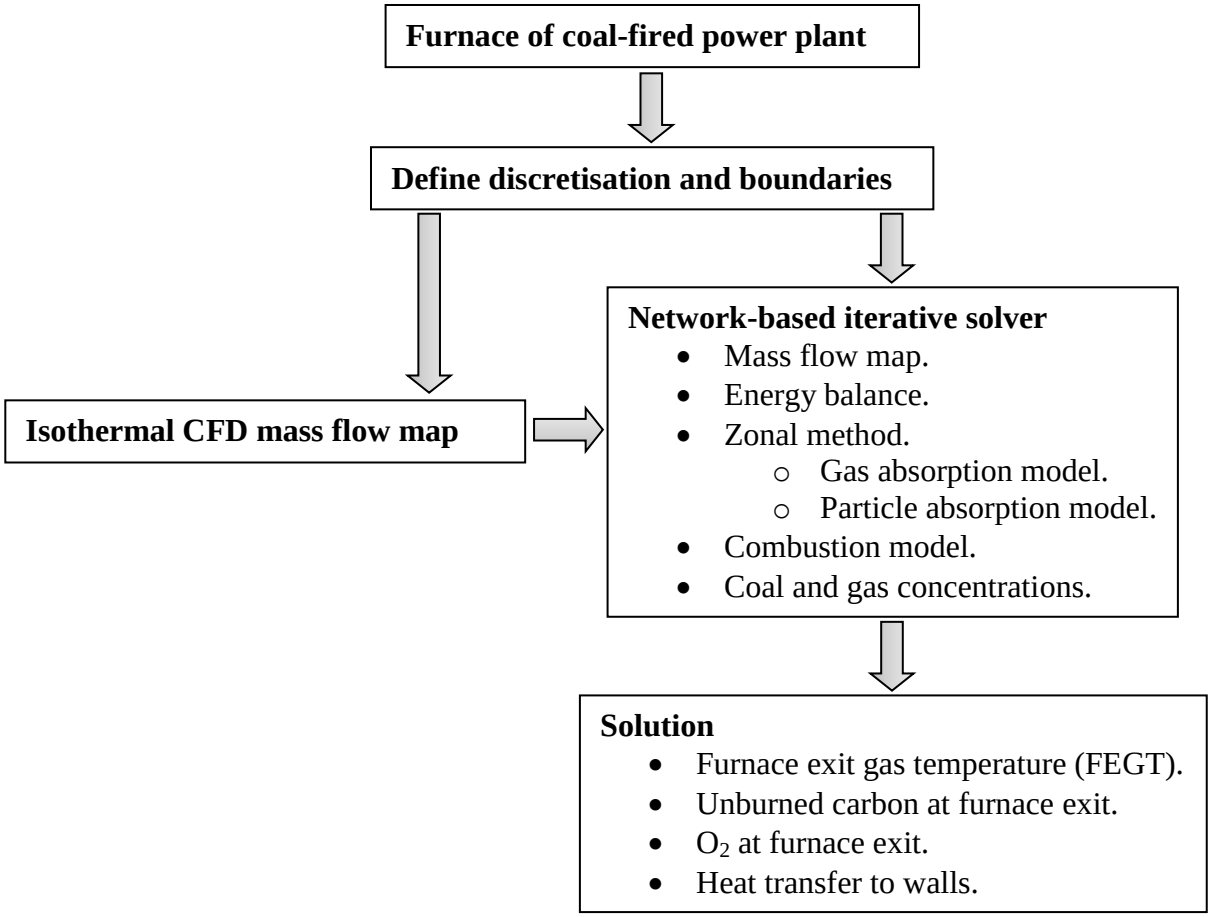

Figure 24 - Furnace network model (FNM) flow diagram.

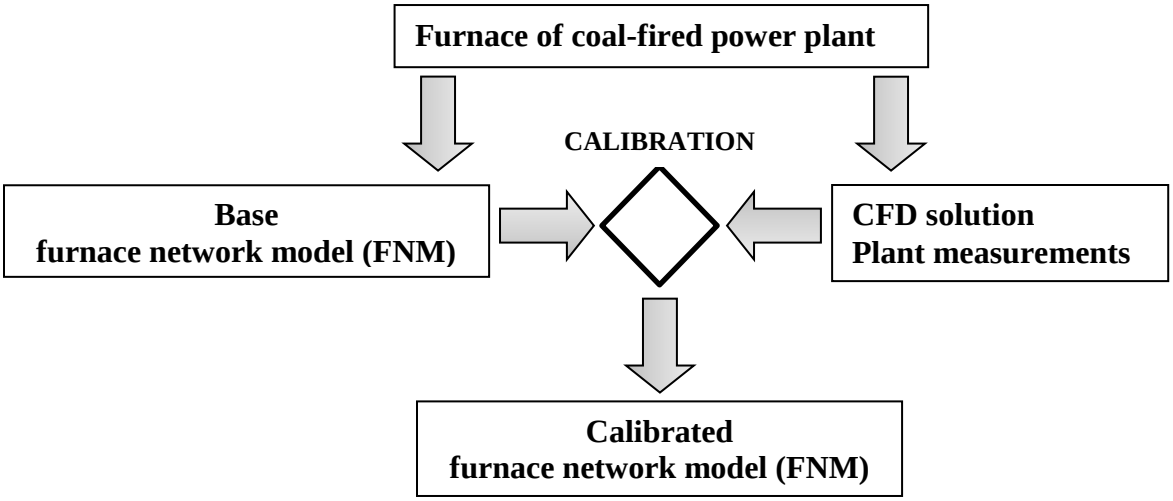

Figure 25 - Methodology for the network-based furnace model.

The systematic flow diagram of the complete methodology is shown in Figure 25. A baseline FNM is created for the furnace of a coal-fired power plant. This model will be compared to measurements and higher fidelity benchmarks such as CFD models for calibration (the calibration will be described in the following section). The result will be a multi-dimensional reduced order model capable of providing predictions as set out in the requirements for the hypothesis (section 1.2).

3.10 Calibration

The reaction coefficients in the combustion model and the absorption coefficients for the zonal method have a considerable impact on the accurate prediction of the burnout and radiation heat transfer. The BCURA model was selected as the combustion model for its simplicity and development as a one-dimensional solution. Unfortunately, this model is outdated and a lot of progress has been made since. Additionally, very few correlations for reaction coefficients for different coal types were published in the work of Field et al. (1967) and Gill (1969) for use with the model. The reaction coefficients also vary considerably for the different coal qualities, which necessitates experiments or advanced software to provide a custom fit correlation for each coal composition.

Whilst the roughly discretised zone-wise methodology proposed provides an efficient method of capturing the complex physics that occur in a coal-fired furnace on a macroscopic scale, a lot of detail is lost within the combustion kinetics that requires a finer grid and more complex models. Therefore, it will be informative to compare the technique to a higher fidelity method such as a three-dimensional computational fluid dynamics model with reacting flow. A CFD model includes

the effects of turbulent combustion by the implementation of a turbulent combustion model and the associated chemical reactions, hence providing a realistic view of the local rates of reaction. Such a model allows for the prediction of the basic combustion parameters such as gas temperature and the spatial concentration of O_2 and CO_2. By comparing the results of the network-based furnace model to the model capturing more detail, the constants in the reaction coefficient model can be calibrated until the results correlate. Effectively, the base model will be updated to a more representative model with a calibration step. Calibration is common in the pulverized fuel applications when considering literature published to characterise the kinetic parameters of the pulverized fuel. See for example the characterisation in CFD simulations using a drop tube furnace (DTF) and experimental data in Authier et al. (2014) and Ranade and Gupta (2015:53-74). The RNM model of Gupta (2011) and Ranade and Gupta (2015:200) also required calibration of the water wall emissivity to obtain better FEGT temperatures. The calibrated network-based furnace model proposed in this thesis will also be a reduced order model of a CFD, but with a more fundamental consistent foundation than the ROM created in studies such as Fei et al. (2015) based on a polynomial fit on data. Despite including some apparent weakness to the methodology with a higher-dimensional model by including the need for calibration, the development should always aim to minimise or remove the need thereof. Matching global results for a higher-dimensional model may be inadequate for certain predictions such as the localised heat transfer near the furnace burner. The end-user should always consider the applicability of the parameter results investigated. The capabilities and limitations of the current methodology will be presented in chapter 6.

A range of different models is available to calculate the absorption coefficient for the particles and participating gases (see section 2.3.2). This provides uncertainty in selecting the appropriate one for each application and only experience or tests will narrow down the options for each application. It is also significant to note that in some of the published works, a value was just selected without an elaborate discussion on how this value was obtained (an example of which is Peters and Weber (1997:141)), but what is clear is that the value selected resulted in good comparative results. Even though the models selected for the absorption coefficients of the particles and gases in the base network-based furnace model were derived mostly from the work published for pulverized coal combustion, it can be expected that these values might have to be calibrated to provide more representative results. This calibration can be done with the assistance of measurements and a CFD solution. The process of calibration and verification of the current model will be described in the following chapter.

4. Verification and Validation

The verification of the code for the methodology proposed is essential during software development to ensure the correctness of the solution. To ensure that there are no errors in the code, it was verified by means of scrutinizing mass balance and heat balance calculations as well as comparing these calculations with secondary benchmarks. In the verification section, the verification of the fluid and radiation properties functions, mass flow map, as well as the calculations of the concentrations, radiation heat transfer and combustion, will be presented.

The validation aims to provide proof that the proposed methodology can model an actual furnace by providing sufficiently accurate predictions of the furnace behaviour. This will be done by comparing the results to experimental measurements as well as predictions of other applicable semi-empirical zero-dimensional models and higher fidelity CFD simulations. This is to ensure that the proposed methodology can meet the requirements as set out in the hypothesis.

The code of the FNM was initially programmed in Scilab® version 5.5.2 as presented in Van der Meer, Rousseau and Jestin (2016a, 2016b, 2016c) and Van der Meer, Rousseau and Naidoo (2019), but later converted to Matlab® 2019R. The code in both the programming languages was verified via the tests in this chapter and compared with one another to check whether the results are the same. The verification results are described in the following section.

4.1 Verification

4.1.1 Functions

Certain calculations are repetitively employed throughout the code and therefore written as a function to be called on when required. To verify each function, a secondary benchmark with the same input values was created and compared to the result calculated by the procedure. Functions to calculate the following were verified:

1. The enthalpy of the mixture of gas and particles in each zone based on temperature and constituent mass fractions.
2. The temperature of the mixture of gas and particles in each zone based on enthalpy and constituent mass fractions.
3. The absorption and emissivity coefficient for H_2O (gas) and CO_2 (gas).

4. The emissivity of the particles.
5. The exchange areas necessary in the radiation heat transfer calculations.

The FNM employs two flue gas property functions. For these flue gas property functions, it was assumed that the expected mass fractions for hydrogen, sulphur and nitrogen dioxide will be low enough thus having an insignificant impact on the mixed fluid properties. Therefore, a zero mass fraction value to these constituents was enforced even if a trace value was provided and the mass fractions for the rest of the constituents recalculated to sum to unity.

The first function calculates the enthalpy of the mixture of gas and particles in each zone when the temperature and constituent mass fractions are provided. The inputs provided to the function and the enthalpy calculated are shown in Table 3. The enthalpy calculated corresponded well with the value from the benchmarks shown in Figure 80 in the appendix. The benchmark was created in the Flownex® SE fluid library using the same correlations derived for each gas constituent as implemented in the code for the FNM. The verification range was for three points over the expected temperature range of the simulations.

Table 3 - A summary of the inputs provided and results calculated for the enthalpy function.

Inputs	**Unit**	**Value**		
Temperature A1	K	500.0000		
Temperature A2	K	1000.0000		
Temperature A3	K	1800.0000		
Carbon	-	0.0590		
H_2	-	0.0000		
O_2	-	0.2080		
N_2	-	0.6340		
S	-	0.0000		
Ash	-	0.0630		
CO_2	-	0.0210		
H_2O	-	0.0070		
NO_2	-	0.0000		
SO_2	-	0.0080		
Result	**Unit**	**Benchmark**	**FNM**	**Difference**
Enthalpy A1	kJ/kgK	240.2859	240.2859	0.0000%
Enthalpy A2	kJ/kgK	768.9918	768.9918	0.0000%
Enthalpy A3	kJ/kgK	1693.6662	1693.6662	0.0000%

The second function calculates the temperature of the mixture of gas and particles in each zone when the enthalpy and constituent mass fractions are provided. The inputs provided to the function and the temperature calculated are shown in Table 4. The enthalpy calculated corresponds well with the value from the same benchmark used to verify the enthalpy calculations.

Table 4 - A summary of the inputs provided and results calculated for the temperature function.

Case	Inputs	Unit	Value		
A1	Enthalpy	kJ/kgK	240.2859		
A2	Enthalpy	kJ/kgK	768.9918		
A3	Enthalpy	kJ/kgK	1693.6662		
A1-A3	Carbon	-	0.0590		
	H_2	-	0.0000		
	O_2	-	0.2080		
	N_2	-	0.6340		
	S	-	0.0000		
	Ash	-	0.0630		
	CO_2	-	0.0210		
	H_2O	-	0.0070		
	NO_2	-	0.0000		
	SO_2	-	0.0080		
	Result	**Unit**	**Benchmark**	**FNM**	**Difference**
A1	Temperature	K	500.0000	500.0000	0.0000%
A2	Temperature	K	1000.0000	1000.0000	0.0000%
A3	Temperature	K	1800.0000	1800.0000	0.0000%

The FNM has the following four radiation property functions:

1. The absorption coefficient for H_2O (gas)
2. The absorption coefficient for CO_2 (gas).
3. The emissivity for the particles.
4. The exchange areas necessary in the radiation heat transfer.

The gas and particle extinction factors are required for the exchange area calculations. The inputs provided to the functions and the coefficients calculated for water vapour and carbon dioxide particles are shown in Table 5 and Table 6. The calculations were verified with three cases having inputs within the expected ranges. The calculated results from the functions corresponded well with the value from the benchmarks. The calculated results from the benchmarks for the gas absorptivity are shown in Figure 81 in the appendix. The benchmarks were implemented in a spreadsheet based on the mathematical models for absorptivity in section 3.4. Using equation 14, the particle

emissivity can be calculated as 0.7240, 0.6600 or 0.6040 when the unburned carbon content is 0.3100, 0.1500 or 0.0100.

Table 5 - A summary of the inputs provided and results calculated for the water vapour and carbon dioxide absorptivity functions.

Case	Inputs	Unit	Value		
B1	Pressure	bar	0.8500		
	H_2O partial pressure	bar	0.0765		
	CO_2 partial pressure	bar	0.1190		
	Mean beam length	m	10.1340		
	Temperature of gas	K	1100.0000		
	Temperature of surface	K	300.0000		
B2	Pressure	bar	0.8500		
	H_2O partial pressure	bar	0.0765		
	CO_2 partial pressure	bar	0.1190		
	Mean beam length	m	0.8000		
	Temperature of gas	K	1800.0000		
	Temperature of surface	K	400.0000		
B3	Pressure	bar	0.9900		
	H_2O partial pressure	bar	0.0300		
	CO_2 partial pressure	bar	0.0700		
	Mean beam length	m	10.1340		
	Temperature of gas	K	500.0000		
	Temperature of surface	K	300.0000		
	Result	**Unit**	**Benchmark**	**FNM**	**Difference**
B1	H_2O absorptivity	-	0.5072	0.5072	0.0000%
	CO_2 absorptivity	-	0.2024	0.2024	0.0000%
B2	H_2O absorptivity	-	0.1741	0.1741	0.0000%
	CO_2 absorptivity	-	0.1166	0.1166	0.0000%
B3	H_2O absorptivity	-	0.3241	0.3241	0.0000%
	CO_2 absorptivity	-	0.1456	0.1456	0.0000%

Table 6 - A summary of the inputs provided and results calculated for the particle emissivity function.

Case	Inputs	Unit	Value		
C1	Carbon content	-	0.3100		
C2		-	0.1500		
C3		-	0.0100		
	Result	**Unit**	**Benchmark**	**FNM**	**Difference**
C1	Particle emissivity	-	0.7240	0.7240	0.0000%
C2		-	0.6600	0.6600	0.0000%
C3		-	0.6040	0.6040	0.0000%

The code for the radiation heat transfer and the exchange areas are almost identical to that described by Monnaemang (2015). The main difference is that the FNM was updated to include non-homogeneous extinction coefficient distributions for the gas and particles. Therefore, the calculation of the radiation heat transfer exchange properties can be verified by using the same code developed by Monnaemang (2015) for a homogeneous case. The inputs and summary of the maximum differences are shown in Table 7. The value calculated for each cell in the matrix is shown in Figure 82 to Figure 88 in the appendix. The calculated results in the FNM correspond well with the value from the benchmarks. The matrixes in the comparison are the specific group that combines all the manipulations, contains the geometry and radiation property information, and are explicitly used in the radiation heat flux calculations.

Table 7 - A summary of the inputs provided and results calculated for the coal and fly ash particles extinction factor functions.

Inputs	**Unit**	**Value**
Length in x, y, z-direction	m	3x3x3
Discretisation in x, y, z-direction	-	2x2x2
Wall emissivity	-	0.85
Scattering coefficient	1/m	0.00
Absorption coefficient	1/m	0.15
Results	**Matrix**	**Difference**
	C	0.0000%
	D	0.0000%
	P	0.0000%
	Q	0.0000%
	R	0.0000%
	W	0.0000%
	T	0.0000%

4.1.2 Solvers

The methodology of the FNM solves in groups of code for the change in particle sizes, mass and volume fractions as well as the radiation heat transfer. To verify these solvers, a secondary calculation or test was derived to confirm reliable execution. The verifications were executed on the three-dimensional, multiple-burner furnace which combines all the geometry and flow path complexities. The following features were verified:

1. The imported mass flow map and concentration calculations.
2. Radiation heat transfer calculations.

3. Combustion calculations.

The mass flow map was imported from a compressible, isothermal, turbulent solution obtained in OpenFOAM® having the same geometry and discretisation as the FNM. A mass balance for the flow into and out of each zone can confirm whether the imported map satisfies the requirement of continuity. The results in Table 8 show that the difference is below $1x10^{-4}$, which is deemed acceptable.

Table 8 - A summary of the average and maximum in- and outflow difference over the faces of each zone.

Difference	Value
Average over zone	$2.0505x10^{-5}$
Maximum over zones	$9.0000x10^{-5}$

To test the concentration solver, two tests were derived by varying the fixed carbon mass fractions in the four bins at the burner inlets. The combustion and radiation heat transfer during solving were disabled for these runs. The mass averaged values for each bin will correspond between the inlets and the outlet when the concentration calculations converged and solved correctly.

Table 9 - A summary of the burner inlet inputs for the concentration solver tests.

Fixed carbon mass fraction for:	**Test 1: Uniform**			
	Burner 1 to 9	**Burner 10 to 18**	**Burner 19 to 27**	**Burner 28 to 36**
Bin 1	0.08498	0.08498	0.08498	0.08498
Bin 2	0.08498	0.08498	0.08498	0.08498
Bin 3	0.08498	0.08498	0.08498	0.08498
Bin 4	0.08498	0.08498	0.08498	0.08498
Fixed carbon mass fraction for:	**Test 2: Non-uniform**			
	Burner 1 to 9	**Burner 10 to 18**	**Burner 19 to 27**	**Burner 28 to 36**
Bin 1	0.3399	0.0000	0.0000	0.0000
Bin 2	0.0000	0.3399	0.0000	0.0000
Bin 3	0.0000	0.0000	0.3399	0.0000
Bin 4	0.0000	0.0000	0.0000	0.3399

The set of inputs at the burners is shown in Table 9. The fixed carbon mass fraction was uniformly distributed for each bin at each burner for the first test. For the second test, four sets of a quarter of the burners had a single bin with a mass fraction of one and the rest set at zero.

Test 1 converged quicker than Test 2, but that should be expected to have a more uniform distribution. The rest of the results are shown in Table 10. For Test 1, the values for the bins compared the best while for Test 2, the differences were minor. The concentration solver results are

sensitive to the convergence criteria and the user should be aware of this. The accuracy is also influenced by the difference of the in- and outflow in each zone and therefore a flow map with a mass balance is essential.

Table 10 - A summary of the difference calculated at the inlet and outlet for the fixed carbon mass fraction for the concentration solver tests.

Fixed carbon mass fraction for:	Test 1: Uniform		
	Inlets	Outlet	Difference
Bin 1	0.0849750	0.0849750	0.00000%
Bin 2	0.0849750	0.0849750	0.00000%
Bin 3	0.0849750	0.0849750	0.00000%
Bin 4	0.0849750	0.0849750	0.00000%
	Test 2: Non-uniform		
	Inlets	Outlet	Inlets
Bin 1	0.08497500	0.08501997	0.05292%
Bin 2	0.08497500	0.08497500	0.00000%
Bin 3	0.08497500	0.08426632	-0.83398%
Bin 4	0.08497500	0.08506568	0.10671%

With a mass and energy balance enforced on each zone, an energy balance over the entire control volume verifies the fidelity of the iterative solution of the FNM. A summary of five different energy balance tests is shown in Table 11. The enthalpy of the mass (gas and particles) entering the volume from the burners will change due to heat transfer and heat sources before leaving through the outlet. The combustion will add heat to the source term and heat will be transferred to or from the walls.

Table 11 - A summary of the gas and particle enthalpy change, combustion heat source and radiation heat transfer to wall energy balance between the inlet and outlet with the different solvers selected.

	Solver active			Energy balance [kW]			
	Concentration	Radiation heat transfer	Combustion	Heat to wall	Source term	Enthalpy change	Difference
Test 1	Yes	No	No	0.0	0.0	0.0	0.0%
Test 2	Yes	No	No	0.0	0.0	0.0	0.0%
Test 3	Yes	Yes	No	-10.9	0.0	11.0	1.0%
Test 4	Yes	No	Yes	0.0	1801.1	1818.8	1.0%
Test 5	Yes	Yes	Yes	841.6	1801.1	968.1	0.9%

Tests 1 and 2 are the energy balance of the mass and constituent verifications for the concentration calculations in the previous section. No difference in the energy balance is noticed for these two tests. When the radiation heat transfer and combustion calculations are active during the solver process (refer to Tests 3 to 5), then small deviations in the overall energy balance are noticed.

This is most likely due to the convergence criteria for the iterative solution and the small differences in the zone mass balances.

The verification tests showed that the code correctly solves for the models implemented by passing the set of benchmark tests. The code for the FNM can be used with confidence during the validation to predict the behaviour of an actual furnace as described in the following section.

4.2 Validation

The methodology and underlying models of the FNM went through revisions since the initial proposition described in Van der Meer, Rousseau and Naidoo (2019). Therefore, the same experimental results are used as validation before continuing to a more complex setup with multiple burners. The CFD results in the comparison are the same as presented in Van der Meer, Rousseau and Naidoo (2019) but a revision of the work related to the FNM will be presented for the single-burner furnace.

4.2.1 Single-burner experimental facility – IFRF furnace no. 1

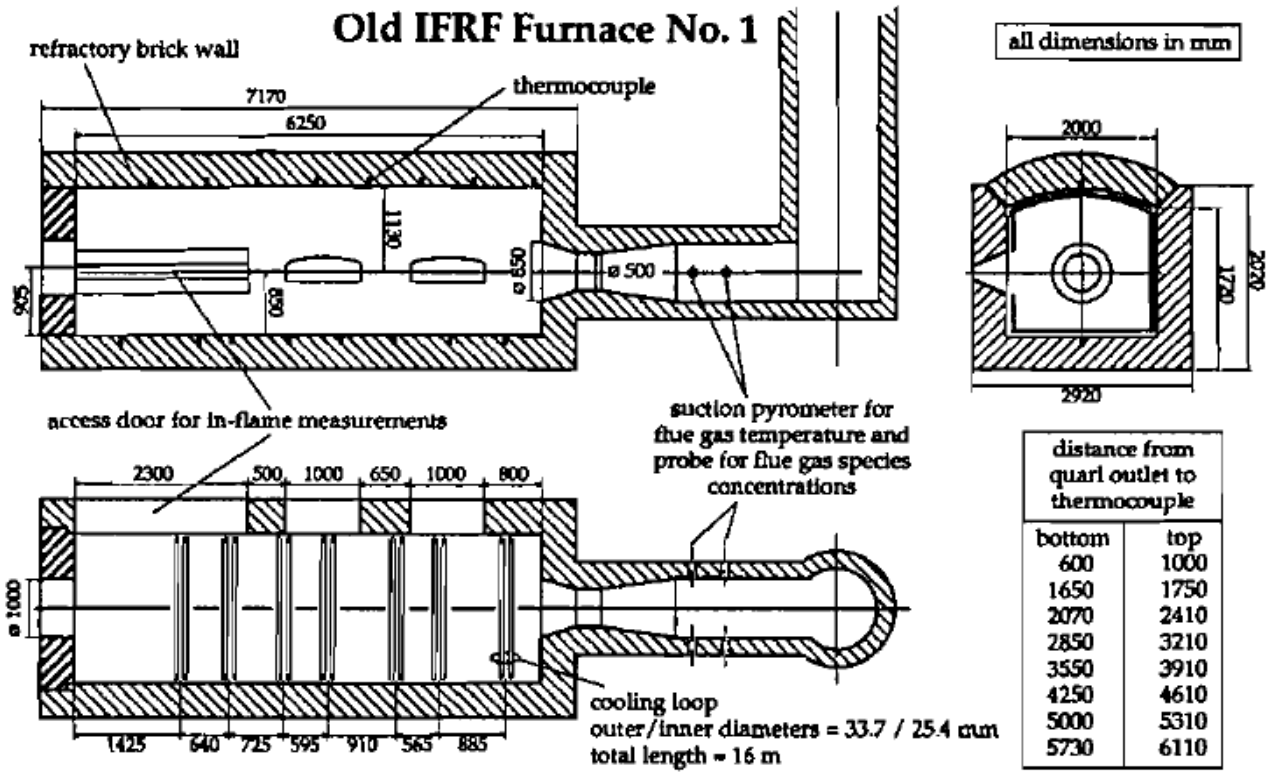

Figure 26 - The old IFRF furnace no. 1 (Peters & Weber, 1997:132).

The first validation presented for the FNM is a comparison with the measurements from the MMF5-2 investigation of an unstaged swirl-stabilised pulverized coal flame generated in the old IFRF furnace no. 1 (see Figure 26). The temperatures, heat extraction, particle and gas concentrations were measured in the flame region and flue gas chimney. Peters and Weber (1997) developed a mathematical model to predict these parameters which will be used together with the CFD results generated by Van der Meer, Rousseau and Naidoo (2019) as the benchmark comparisons. The CFD model development was already explained in Van der Meer, Rousseau and Naidoo (2019:260-261) but repeated in the following section for completeness.

4.2.2 Single-burner furnace: Modelling setup of the CFD model

The computational tool chosen was the commercial CFD package ANSYS Fluent v17.2. This model allowed for the prediction of the basic combustion parameters such as gas temperature and the spatial concentration of O_2 and CO_2. The model employed a global chemistry model that simulated the direct conversion of fuel components to CO_2 and also employed a simple single rate devolatilisation model. Both approaches were considered reasonable as the focus of the research was on the global behaviour of the flame rather than the microscopic evolution of the flame near the burner mouth.

The combustion behaviour of the coal in the experimental study of Peters and Weber (1996) was modelled by implementing a steady-state, three-dimensional turbulent combustion model. The standard k-ε turbulence model was used for this study. It provided a good balance between resolving key flow characteristics whilst still being computationally economical. It is acknowledged that other models such as the k-ω model and Reynolds Stress Model (RSM) would provide better resolution of the physical interaction with the walls and the swirling behaviour of the flame respectively. Research conducted by Breussin, Pigari and Weber (1996) shows that both the RNG k-ε model and the standard k-ε turbulence model produce flames that are shorter and more intense than the RSM model, which is contrary the findings of other researchers. Hence, the new variables that these models introduce would require an extensive sensitivity study to understand their physical significance on flame characteristics. A pragmatic approach was therefore demonstrated by Peters and Weber (1997), where the simplest form of the k-ε turbulence model provided an adequate prediction of the bulk flame structure. This pragmatic approach is sufficient for this study.

The coal combustion problem was simulated using a two-phase Euler-Lagrangian methodology. The reacting gas species were treated as a continuous phase incorporating a multi-species gas

model. The coal particles were treated as a discrete phase and their trajectories were modelled using a Lagrangian particle tracking model that allowed for mass and energy transfer with the continuous phase. The non-premixed combustion scenario was adopted as the fuel and oxidiser were not completely mixed before sufficient enthalpy is available to initiate combustion. The details of the fundamental conservation quantities of the flow field are discussed in Versteeg and Malalasekera (1997).

The current model assumes a simplification of the true composition of coal. This particle composition is illustrated in Figure 13 and comprises of raw coal, char, ash and inherent moisture. The raw coal is considered to be the sum of the fixed carbon and volatile material fractions obtained from the proximate analysis. Hence, the char component is only explicitly needed in cases when the particle has already undergone a gasification process. The three fundamental processes during the combustion process are as explained in section 2.4. The real complexities involved during the combustion of char were simplified to a surface reaction of the char with oxidant that may be incident on the surface. The default kinetics and diffusion-limited model were used for this study. Details of this model are explained in the ANSYS Fluent theory guide (Ansys, 2015). The inherent moisture initially specified with the particle is transferred to the continuous phase via a quasi-static single component evaporation model.

The finite rate eddy dissipation model in ANSYS Fluent (Ansys, 2015) was used to model the turbulent chemistry interaction. This works under the premise that the combustion chemistry is fast-acting and the rate of combustion largely dependent on turbulent mixing. The model adopts the well-tested constants of Magnussen and Hjertager (1977) whilst including an Arrhenius limiting term that ensures that combustion only occurs above the ignition point. The assumed volatile material is released for the volatile pseudo-species on contact with an oxidiser molecule, provided that the local temperature is above the volatile vaporisation temperature. The mass transfer of volatile gases and tars from a particle subjected to high heat rates (~15 000 K/s) was modelled using a constant rate formulation. The rate constant was calculated to be 33 s^{-1} based on the devolatilisation data provided by Peters and Weber (1997).

The convective heat transfer was modelled using the Ranz-Marshall formulation. This model is valid for spherical particles with low slip velocities (Ansys, 2015). the discrete ordinates radiation model was selected for the radiative heat transfer solution. The effect of the participating gases (CO_2 and H_2O) was incorporated by adjusting the absorption coefficient of the flue gas mixture by implementing the weighted sum of grey gases model. The code has an additional model that

accounts for the scattering and absorption of thermal radiation due to the presence of particles in the participating medium. The particles are treated as grey and hence the absorption coefficients are constant.

4.2.3 Single-burner furnace: Mathematical model of Peters and Weber (1997)

The mathematical model presented by Peters and Weber (1997) used a two-dimensional, body-fitted curvilinear, non-staggered, cylindrical polar-coordinate computation grid. The grid contained 192 cells in the axial direction and 104 cells in the radial direction. In total there were 19 968 cells of which 6 656 cells were in the burner quarl region. The development focussed on providing predictions that can be compared to measurements of the velocities, turbulence quantities, temperatures, coal burnout levels and species concentrations of oxygen, carbon monoxide, carbon dioxide, nitrogen oxides precursors and nitrogen oxides. The prediction of the convection and radiation heat transfer were also incorporated and compared to the measurements.

The turbulence was modeled with the standard k-epsilon model. The turbulent combustion model incorporated a two-step reaction scheme with an eddy break-up model. In the combustion modeling, it was assumed the fixed carbon (char) starts reacting after devolatilisation was complete. The fixed carbon (char) burnout rates were obtained from a pseudo char combustion model. To investigate pollutants, a model for nitric oxide (NO) formation was also included. In the nitric oxide chemistry model, the thermal-NO and fuel-NO chemical reaction rates were statistically averaged over the fluctuating temperature using a beta-probability density function. The Discrete transfer method was used to model the radiation heat transfer. A constant linear absorption coefficient was assumed and scattering neglected.

4.2.4 Single-burner furnace: Modelling setup of the network-based model

The zonal discretization of the internal volume of the furnace is shown in Figure 27, with the side length of each cubically shaped zone equal to 0.25 m. The side length is also nearly the same as the burner diameter. Along the axial length with respect to the burner inlet, the discretised volume is 6.5 m long, having 26 zones and 1.75 m in the radial direction having 7 zones.

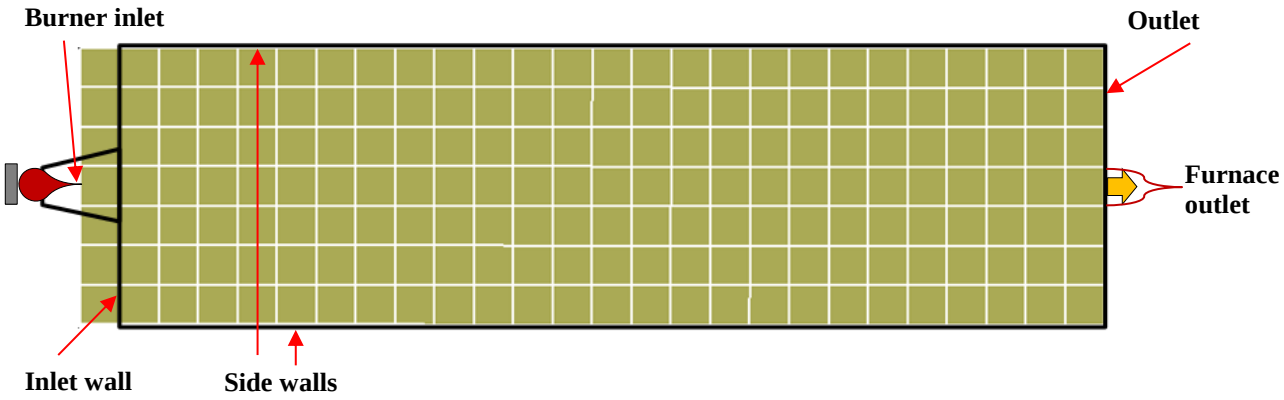

Figure 27 - Side view of zonal discretisation approximation of the single-burner furnace.

The first row of volumes was positioned near the burner inlet to capture the coal heat-up after exiting the burner mouth. In reality, this causes a few zones to fall outside the actual internal space, but it is assumed not to introduce major inaccuracies due to the flow within these volumes being significantly lower than the inlet stream.

Table 12 - A summary of the furnace and burner inputs.

Description	Value	Unit
Front wall temperature	1400	K
Side wall temperature	1000	K
Rear wall temperature	1300	K
Front wall emissivity	0.5	-
Side wall emissivity	0.4	-
Rear wall emissivity	0.5	-
Primary air mass flow rate	0.11694	kg/s
Primary air temperature	343.15	K
Secondary air mass flow rate	0.74556	kg/s
Secondary air temperature	573.15	K
Coal mass flow rate	0.07306	kg/s
Coal temperature	343.15	K

The furnace and burner inputs as used in the mathematical model of Peters and Weber (1997) are summarised in Table 12. How the inputs were quantified from the measurements were not discussed in Peters and Weber (1997). The FNM did not include the swirl. This, combined with the lower order discretisation of the isothermal mass flow map, will potentially cause less gas flow towards the walls of the furnace. A comparison of the flow streamlines between the isothermal mass flow map (see Figure 28) and the CFD model (see Figure 29) confirmed this notion from halfway along the furnace up to the outlet. The interpolated velocity profile is presented in Figure 28, but the velocity flow vectors for the isothermal CFD is also shown in Figure 89 and Figure 90 in the appendix. The streamlines for the CFD show that the flow is predominantly moved to the back of

the furnace, opposite the burner. The streamlines for the isothermal mass flow map indicate a dominant flow along the centre line of the furnace (perpendicular to the burner inlet zone) with recirculation starting from three quarters away from the burner and integrating with the dominant stream at the first quarter of the furnace volume from the burner. Similar tendencies were found in Hesselmann (1998) when comparing the mass flow between a simple scalar potential flow field calculation and a higher order detailed CFD solution. The simple scalar potential flow field calculation is comparable to the detail of modelling used to obtain the isothermal mass flow map for the network furnace code. For the particular case study investigated, the momentum force is expected to be dominant when compared to the buoyancy forces (due to temperature gradients) for the larger part of the control volume. The temperature gradient is most pronounced around the flame near the burner inlet causing some recirculation. The amount of recirculation will not be accurately captured in the isothermal mass flow map, as seen in Figure 30 where the flow is dominant through the centreline along the burner height. This could potentially result in under-prediction of the amount of air flow leaving the flame and flowing towards the furnace wall and corners in the proximity of the burner inlet.

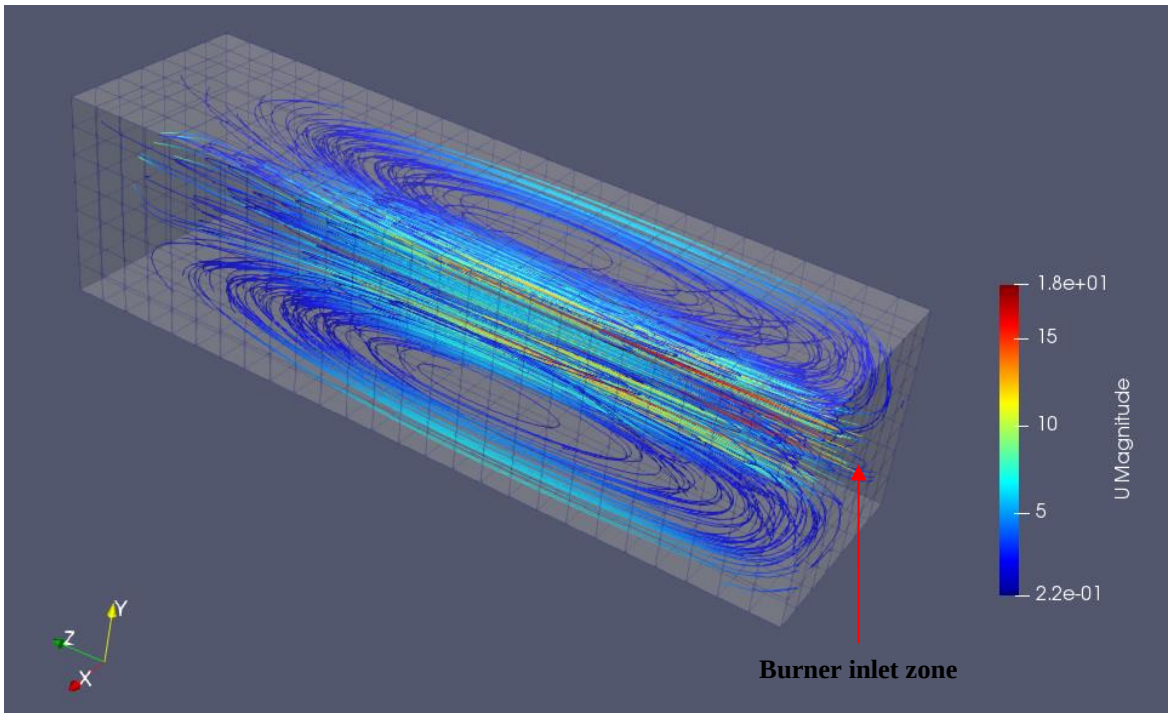

Figure 28 - Velocity profile and stream lines of the isothermal mass flow map CFD simulation for the single-burner furnace.

The isothermal mass flow map predicted more flow recirculating to the first half of the furnace when the swirl is neglected than the detailed CFD simulation. The gas temperatures in the corners near the burner are expected to be over-predicted. The higher mass flow of recirculating gases

entrained into the flame will also influence the flame temperature. The temperature profile near the outlet for the isothermal mass flow map is expected to have a larger gradient from the centre than the case where swirl is included.

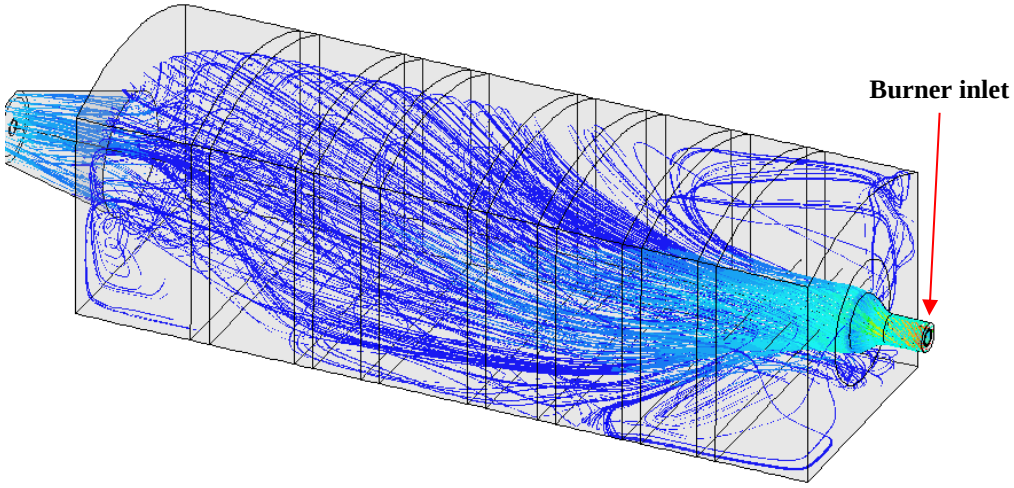

Figure 29 - Stream lines of the CFD simulations.

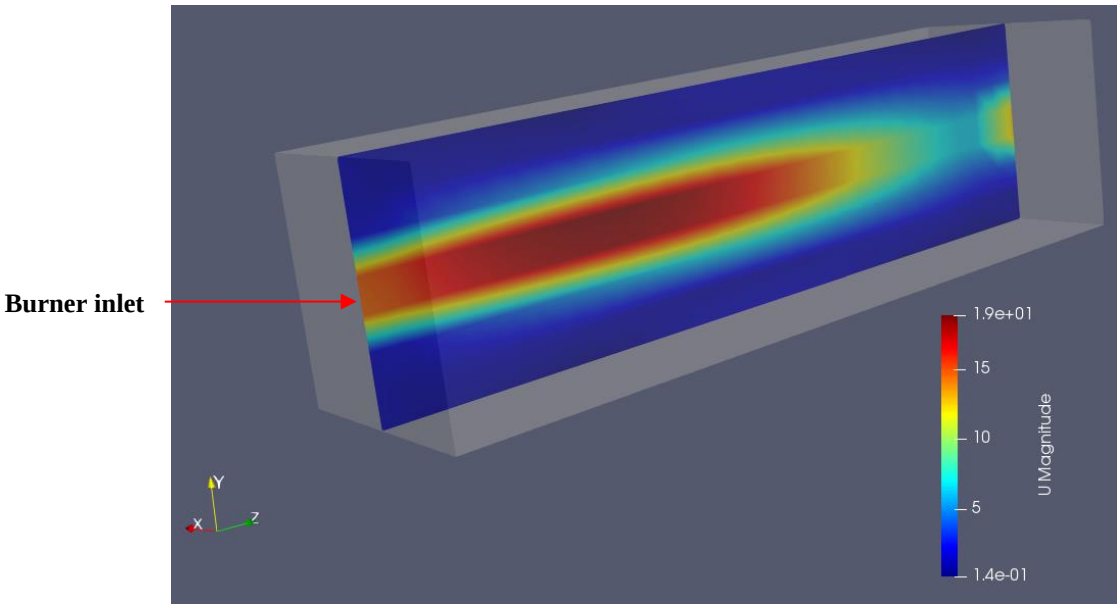

Figure 30 - Velocity profile along the centre plane of the isothermal mass flow map CFD simulation for the single-burner furnace.

A summary of the coal properties is tabulated in Table 13. The particle distribution was divided into four bins with the minimum fly ash particle diameter limited to 13 µm. The baseline correlation for the surface reaction rate was assumed to be similar to that documented in Field et al. (1967:393) for anthracite coal with a low surface reaction rate. The distance to complete volatile evolution of 0.5 m was assumed due to the experimental burnout indicating fixed carbon being combusted from this distance onwards (Peters & Weber, 1997:177).

Table 13 - A summary of the coal properties for the single-burner furnace.

Description	Value	Unit
Coal density	1000	kg/m^3
Spread factor	1.36	-
Mean particle size	45	µm
Minimum particle size	1	µm
Maximum particle size	300	µm
Ultimate analysis – Carbon	80.36	%
Ultimate analysis – Hydrogen	5.08	%
Ultimate analysis – Oxygen	12.17	%
Ultimate analysis – Nitrogen	1.45	%
Ultimate analysis – Sulphur	0.94	%
Proximate analysis – Volatiles	37.4	%
Proximate analysis – Fixed carbon	54.3	%
Proximate analysis – Ash	8.3	%

Field et al. (1967:212, 376) noticed from the experiments available that the change in particle diameters was relatively small after devolitalisation and observed a hollow structure. Therefore, for simplicity, a devolatilisation swelling factor of one was assumed. Peters and Weber (1997:143) did not account for the particle swelling during heating up and devolatilisation while not stating a reason why.

Similar to what was described by Peters and Weber (1997:141), the scattering term in the gas extinction factor has not been accounted for, but it should be noted that the absorption coefficient was set to 1.5. It is unclear how this value was selected, but from the results below it is evident that this value was most likely selected because it provided good comparative results for the radiation heat transfer calculations. Therefore, for the FNM, two predictions will be presented:

- Base: The absorption coefficient and surface reaction rate without any calibration.
- Calibrated: The absorption coefficient and surface reaction rate calculation with calibration.

For the latter case, the absorption coefficient was calibrated by assuming the same values as calculated in the base case, but normalising to an average value over the entire furnace volume of 1.5 as applied by Peters and Weber (1997:141) in their calculations. This resulted in the absorption coefficients to be higher near the burner and lower further away from the burner, instead of a homogeneous distribution. The reaction coefficients were modified using the calculated value from the correlation and multiplying it by a factor of 0.565. This matched the burnout as measured during the experiments but had a minor effect on the results due to both cases being near complete burnout.

4.2.5 Single-burner furnace: Results

The burner is a swirl type resulting in the particles not moving in a straight line. Additionally, the residence times of the particles in the near burner region are variable depending on whether the particle gets entrained from the external flame re-circulation zones. Due to a pulverized fuel flame never being in steady-state, a smooth curve such as predicted with the mathematical models is not realistic. The model results will rather reflect the expected average burnout. Therefore, the CFD results show the averaged burnout value within discrete volumes along the length of the furnace. The original experimental measurements were obtained by inserting a suction probe and sampling the particles at different locations. A carbon-in-ash analysis was used to determine the number of combustibles remaining. Figure 31 shows a comparison between the experimental results obtained from the suction pyrometry with that of the CFD and network-based models. The results from both models compare well with the measured values.

In the flame region nearest to the burner, the predicted value of the FNM is well below the measured value. However, the purpose of the model is not to provide very accurate results within this region. Beyond the 0.25 m distance, the predicted trend of the burnout profile of the network model closely follows the measured values. The burnout predicted by the FNM at the furnace exit is 100.0% (base) and 99.42% (calibrated) compared to the measured value of 99.4%. The CFD model predicted complete combustion at the furnace exit.

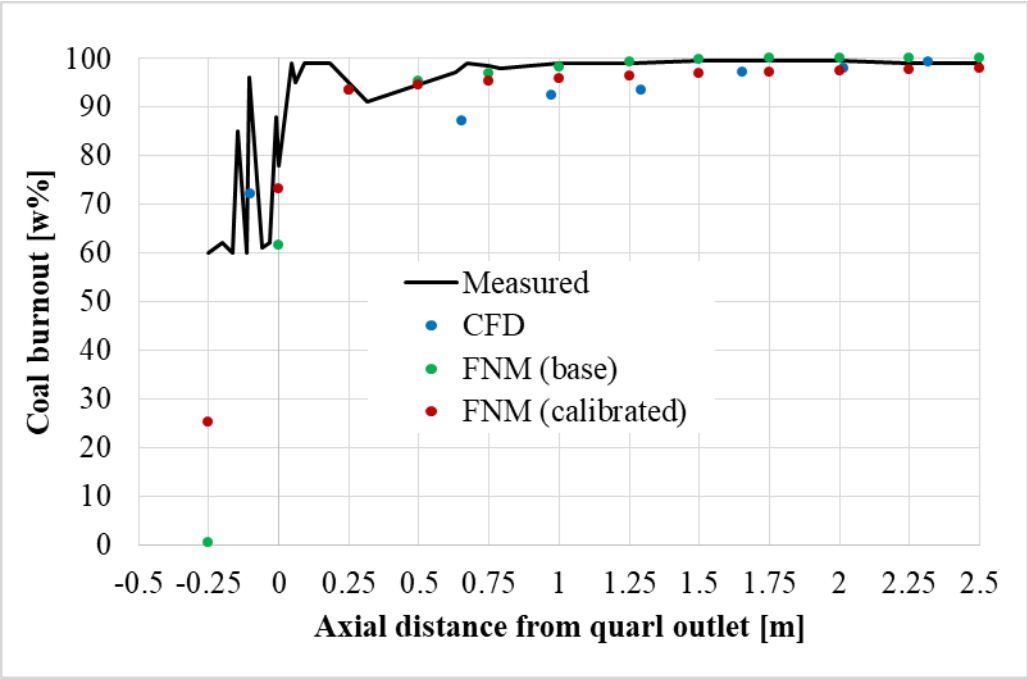

Figure 31 - Predicted and measured carbon burnout at the centre line for the single-burner furnace.

Peters and Weber (1997:133) stated that the overall thermal energy fuel input was 2.165 MW and a complete combustion case will correspond with this. The total energy input due to combustion for the FNM base case was found to be 2.107 MW, which is within 2.7% of this value. The energy input for the calibrated surface reaction rate was 2.116 MW.

Table 14 - Comparison of the heat transfer to the cooling coils for the single-burner furnace.

Description	Total heat transfer (kW)	Radiation heat transfer (kW)	Difference
IFRF flame measurement	1030		
Peters and Weber (1997:171)	1049	989	-
FNM prediction (base)		987	-0.2%
FNM prediction (calibrated)		993	0.4%

The energy removal rate of the cooling coils was determined via measurements to be 1038 kW and the comparisons to the mathematical models are summarised in Table 14. The prediction made by Peters and Weber (1997:134) compares well with the measured total heat transfer. According to their mathematical model (Peters & Weber, 1997:171), the radiation and convection heat transfer contributions were 989 kW and 60 kW, respectively. When compared to the radiation heat transfer of Peters and Weber (1997:134), the FNM code prediction differs by -0.2% (base) and 0.4% (calibrated), respectively. Therefore, the radiation heat transfer values predicted by Peters and Weber (1997:134) correspond well with that of the FNM code predictions which neglected the convection heat transfer. The convection heat transfer is therefore estimated at a 5.7% contribution of the total heat transfer and validates that it is reasonable to neglect it for the furnace heat transfer calculations.

The curves in Figure 32 show the temperature of the gas as predicted by the FNM compared to the prediction of Peters and Weber (1997:175), the CFD model and experimental measurements. The temperature profile spikes near the burner with the CFD predicted temperature profile showing a similar tendency to the FNM. The temperatures predicted by the FNM are above the measured temperatures. From 0.25 m onwards, the profile for the base FNM model is slightly higher when compared to the other mathematical models or experimental measurements, implying that less energy is being absorbed from the gas and particles. This can most likely be attributed to the lower absorption coefficients (on average 13.6% less) calculated in the radiation properties model (and therefore less radiation heat transfer occurring) when compared to a constant value of 1.5 assumed by Peters and Weber (1997:141). A second contributing factor may be the lower order isothermal flow field not accurately modelling the amount of gas flowing in close proximity to the walls,

which enhances the potential of radiation heat transfer. It is suspected that the latter is not the significant reason for this over-prediction of the temperature profile.

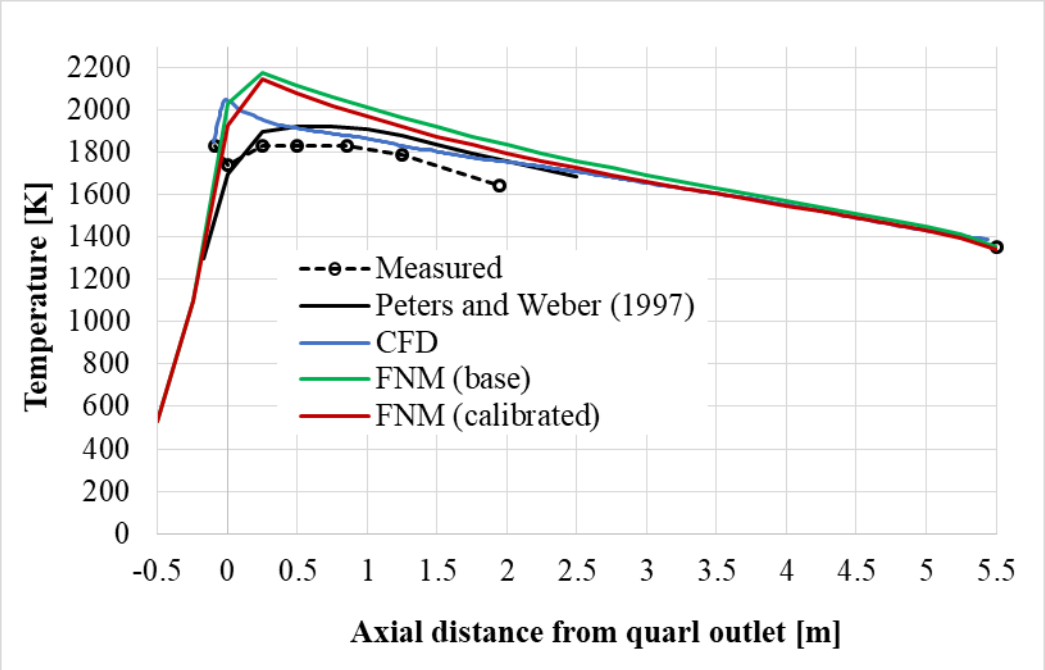

Figure 32 - Predicted and measured temperatures along the centre line for the single-burner furnace.

From 1 m onwards, the profile for both the FNM cases compares well with the other mathematical models and experimental measurements. The most significant adjustment required was for the burnout rate calculation which predicts complete burnout for the base FNM case.

The same trends are seen when comparing only the flue gas temperatures exiting the furnace as summarised in Table 15. The gas temperature predicted by the base FNM case is 4.2% below the measured value while the calibrated FNM case and Peters and Weber's (1997:170) prediction are 3.2% and 4.4% less than the measured value. Peters and Weber (1997:180) considered a temperature difference within the range of 100 K to be satisfactory and both the base and calibrated FNM predicts within this range. The good correlation between the heat fluxes and temperature profile provides confidence in the selected absorption coefficient models for the gas and particles.

Table 15 - Comparison of flue gas outlet temperature for the single-burner furnace.

Description	Temperature (K)	Difference
IFRF flame measurement	1353	-
Peters and Weber (1997:171)	1310	-3.2%
FNM prediction (base)	1296	-4.2%
FNM prediction (calibrated)	1294	-4.4%

The results in Figure 33 show the oxygen content profile as predicted by the FNM compared to the prediction of Peters and Weber (1997:175), the CFD model and the measurements. The profile of the FNM drops sharply from 21% to about 3.4% due to the burnout of more than 90% of the combustible matter. The profile for the base FNM case is below the calibrated FNM case which is consistent with the higher oxygen conversion due to the higher burnout rate. At the outlet, the predicted value is higher than the measurement. The CFD results show an overprediction when compared to the measured values, but follow the same trend and approaches the measured value at the furnace outlet. Peters and Weber (1997:170) predicts an O_2 of 3.82v% (dry) at the outlet and reasoned based on the total air mass flow and corresponding excess air level, the 3.0v% (dry) measurement to be erroneous. The predicted O_2 value of the FNM, which is higher than the measured value, is therefore closer to the expected value that corresponds with the total air mass flow provided at the burner.

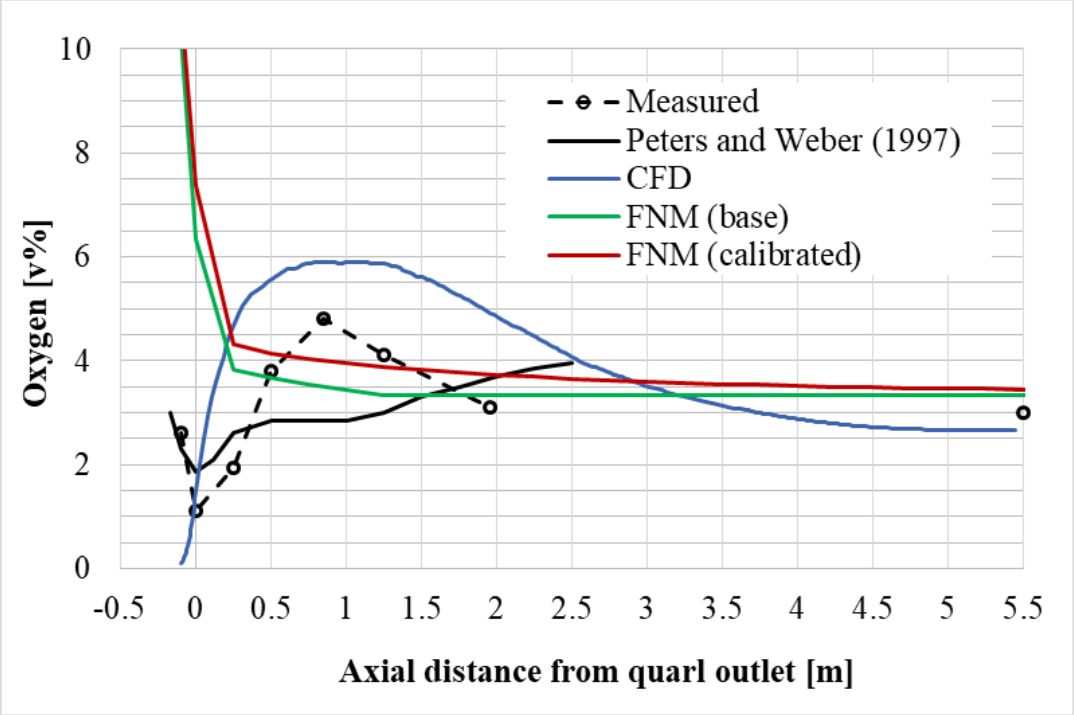

Figure 33 - Predicted and measured oxygen profile at the centre line for the single-burner furnace.

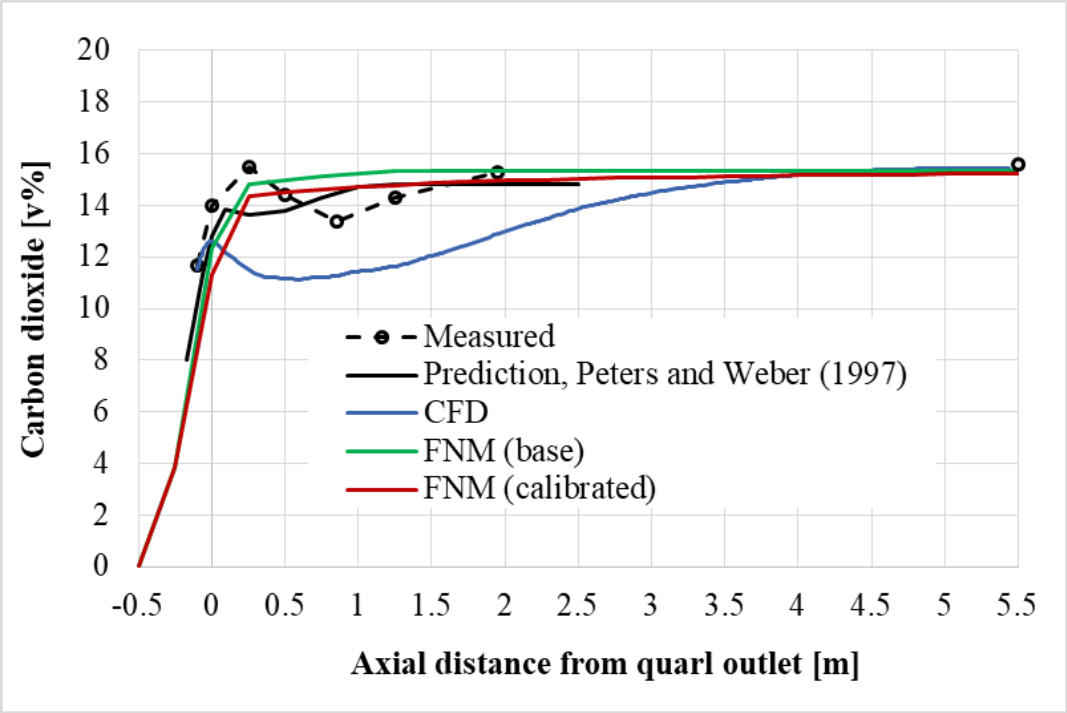

Figure 34 - Predicted and measured carbon dioxide profile at the centre line for the single-burner furnace.

The carbon dioxide profiles predicted by the FNM, Peters and Weber (1997:175), the CFD model and the experimental measurements are shown in Figure 34. The profile of the FNM closely follows the trend of Peters and Weber (1997:175) as well as the trend in the measured values. All the mathematical models predict a value close to the measured value of 15.6v% (dry) at the furnace outlet.

The decrease of the surface reaction coefficients in the calibrated FNM showed a minor impact on the results. The heat transfer comparisons in Table 14 and temperatures along the centre line shown Figure 32 of the base FNM case and calibrated FNM case closely matched each other. The delay in fixed carbon burnout due to the decrease of the surface reaction coefficients shown in Figure 31 also varies significantly for only the first few zones just after the burner inlet. The effect thereof in the delay in burnout of fixed carbon will also have a minuscule change in the local extinction coefficients of each zone when considering the difference in carbon dioxide shown in Figure 34 for the base FNM case and calibrated FNM case. Therefore, the effect of the decrease of the surface reaction coefficients is only noticeable in the few zones just after the burner inlet and insignificant in the rest of the zones.

The results in Figure 35(a) and Figure 35(b) show the two-dimensional temperature profile over the cross-section, one metre along the axial length of the furnace and near the furnace exit. Both

profiles show that the temperatures are higher in the centre and decrease towards the wall, which is consistent with the temperature profile of gas heating the walls. The profile one metre along the axial length has a sharp gradient near the centre due to the combustion heat source.

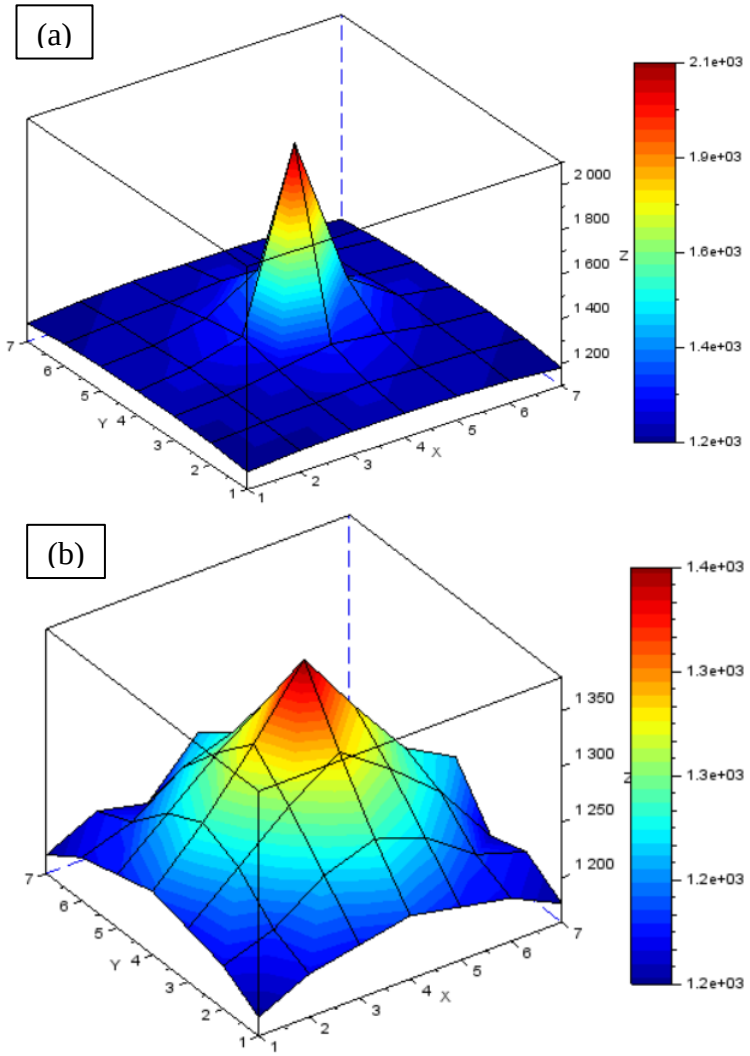

Figure 35 - Radial temperature profile (a) 1 m along the axial length and (b) near the furnace exit for the single-burner furnace.

For this single-burner base case having 2100 zones, the Scilab® code solved within 41 minutes and the Matlab® code within 4 minutes on a laptop computer (2.7 GHz CPU with 2 cores).

4.2.6 Multiple-burner furnace

The second validation presented for the FNM is a comparison with the measurements and CFD results for an opposite wall-fired pulverized coal boiler (see Figure 36 and Figure 37). The main goal for the FNM is to be applicable for such multiple burner configurations. The evaporator heat transfer, as well as the furnace exit gas temperature, oxygen concentration and carbon burnout, were

measured. Laubscher and Rousseau (2019a, 2019b) published two papers using CFD to model the geometry, the results of which will be included in the comparisons.

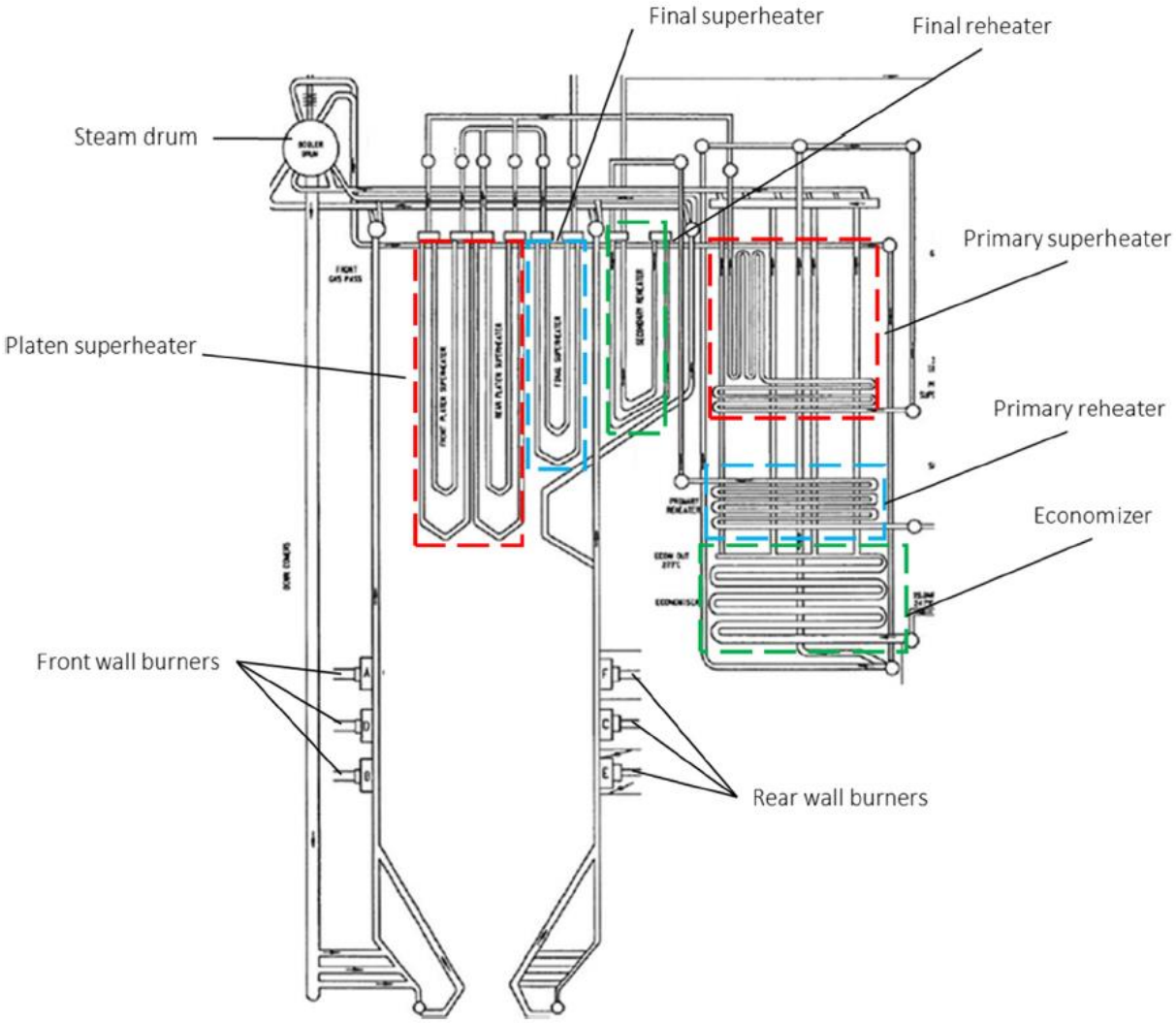

Figure 36 - Layout of 620 MWe opposing wall-fired pulverized coal-fired subcritical boiler (Laubscher & Rousseau, 2019b:3).

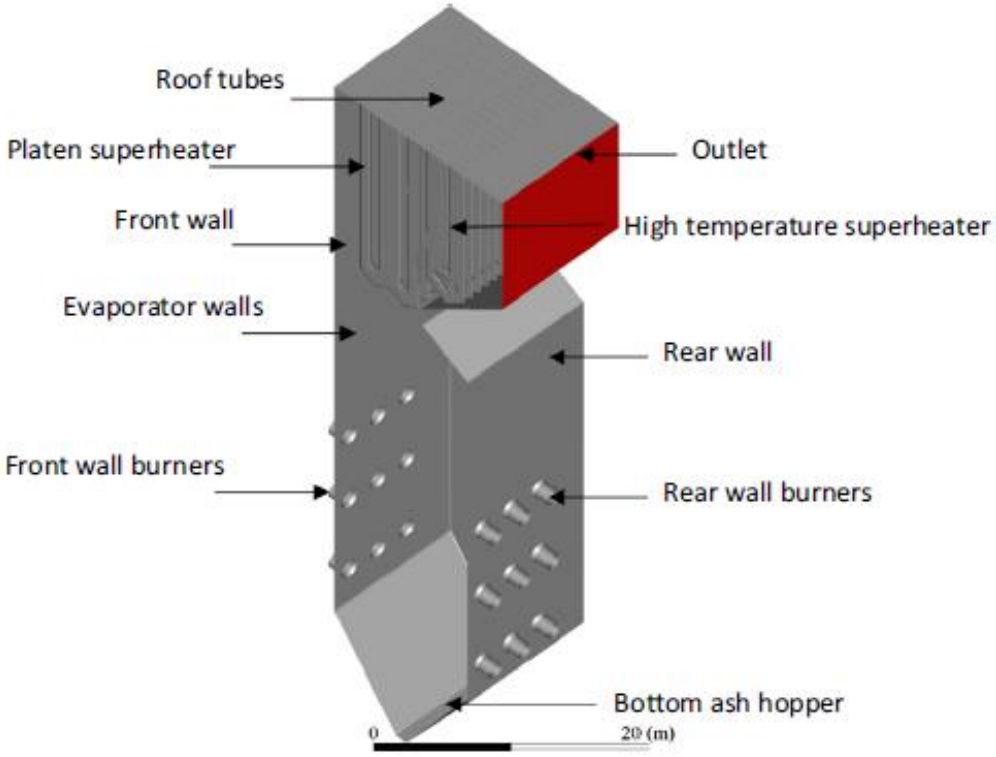

Figure 37 - Geometrical model of opposing wall-fired pulverized coal boiler (Laubscher & Rousseau, 2019a:512).

4.2.7 Multiple-burner furnace: Modelling setup of the network-based model

The zonal discretisation of the internal volume of the furnace is shown in Figure 38, with the side length of each cubically shaped zone equal to 2.815 m. This side length is also nearly the same as the burner diameter. The length of the front and rear wall with the burners has 8 zones while the depth between these walls is 5 zones. There are 16 zones along the height of the furnace. In total there are 640 cubical zones.

The actual geometry of the furnace imposed onto the zonal discretised volume is shown in Figure 38. A few of the calculation zones, partially and as a whole, fall outside of the actual geometry at the bottom hopper and the neck of the furnace. The isothermal mass flow map in Figure 39 as well as Figure 92 and Figure 93 in the appendix indicates low flow zones at the bottom of the furnace in the hopper region. Mainly re-circulation of less than 20% of each burner mass flow from the bottom burners will occur in the hopper region. It is expected that the low re-circulation noticed in the isothermal CFD will not have a significant effect on the results for this specific case of an opposite wall-fired furnace. This simplification will not always be true as Hesselmann

(1998:311,315) found large re-circulation below the bottom burner row when considering a wall-fired furnace with the burners on only one wall. At the sides, the zones also partially fall out of the geometrical volume of the actual surface. From the one side it is slightly larger and the other side slightly smaller, but overall, the surface area of the FNM will be about the same as the actual furnace.

The models selected for the methodology as presented in this thesis was used in the form to be applicable for cubically shaped zones in order to focus on testing the validity of the approach. Most furnaces are predominantly rectangular in shape and can be approximated with a combination of cubic zones. The same methodology can be updated to include the capability of non-cubically shaped zones by expanding the selected models to account for these different shapes.

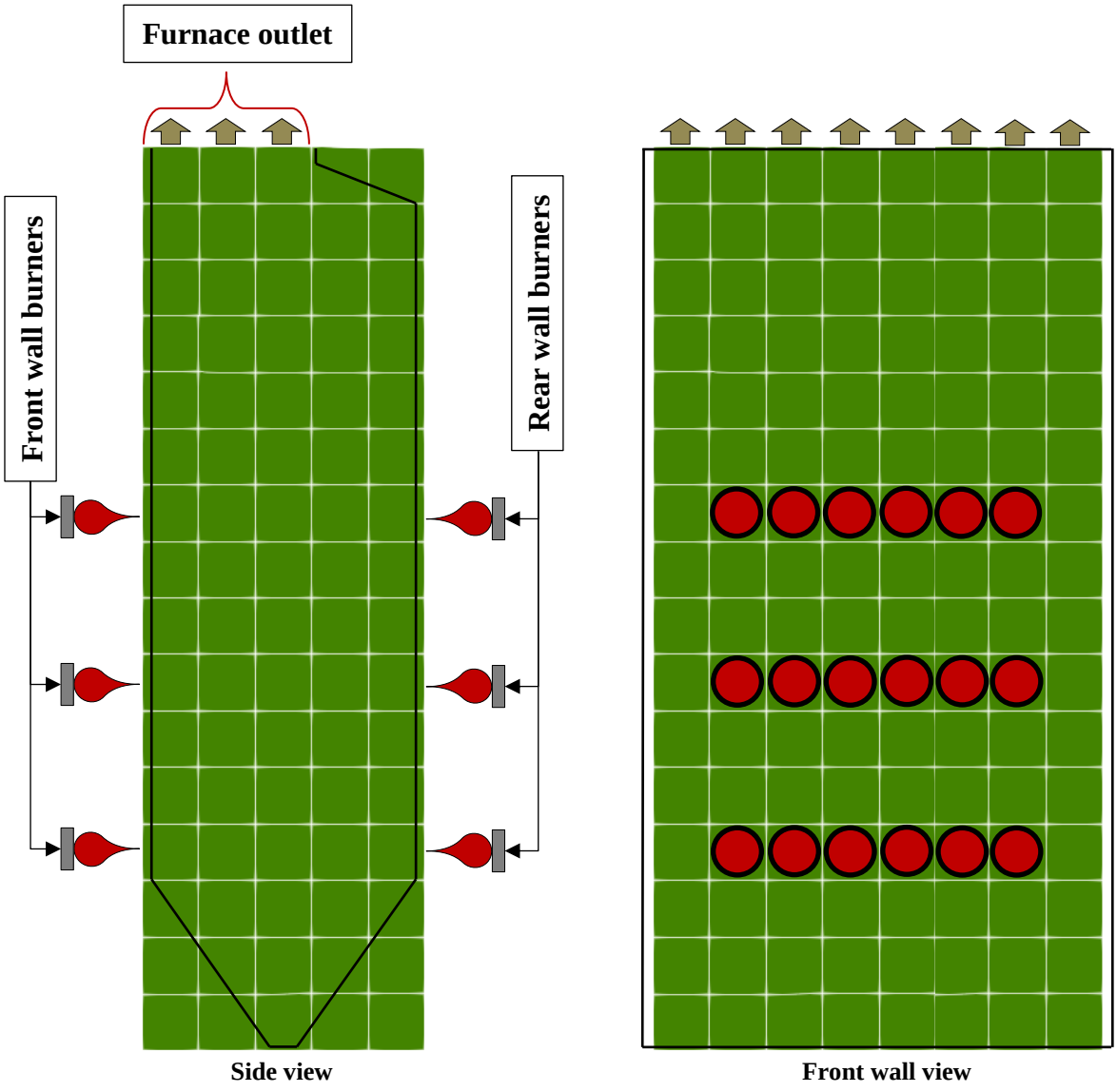

Figure 38 - Approximation of zonal discretisation for the multiple-burner furnace.

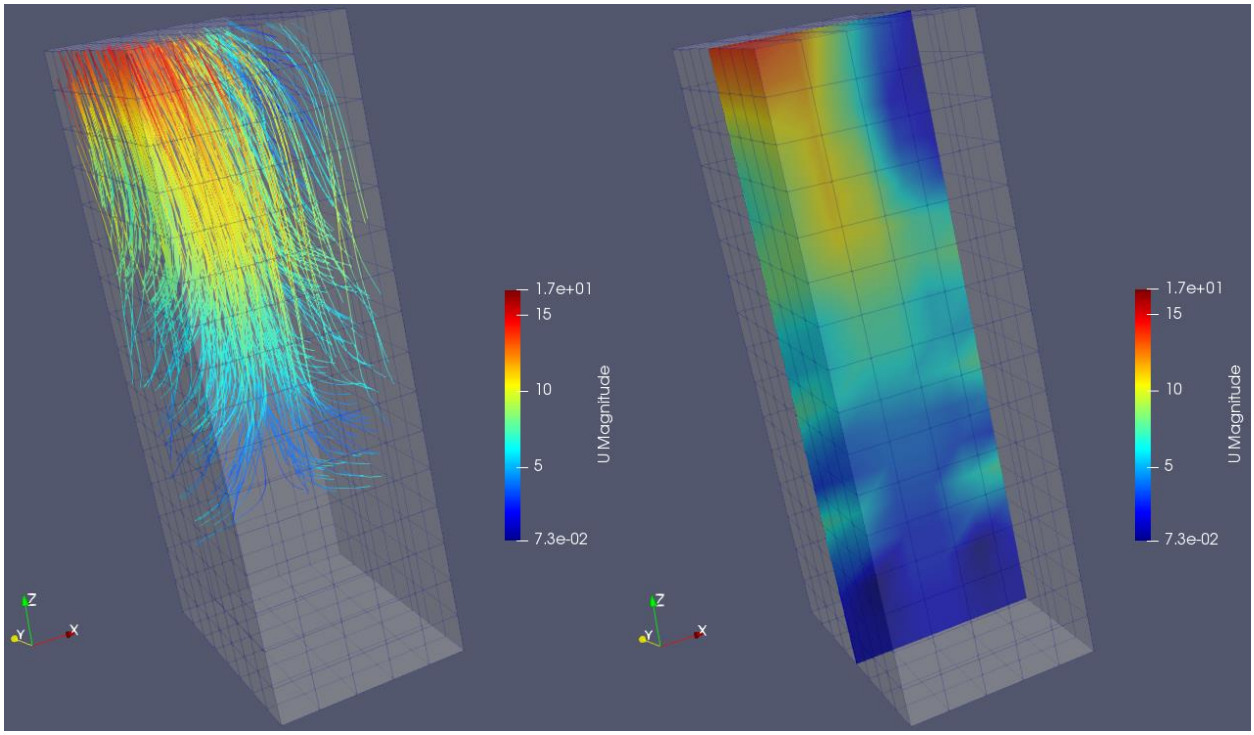

Figure 39 - Streamlines and the velocity profile of the isothermal mass flow map CFD simulation for the multiple-burner furnace.

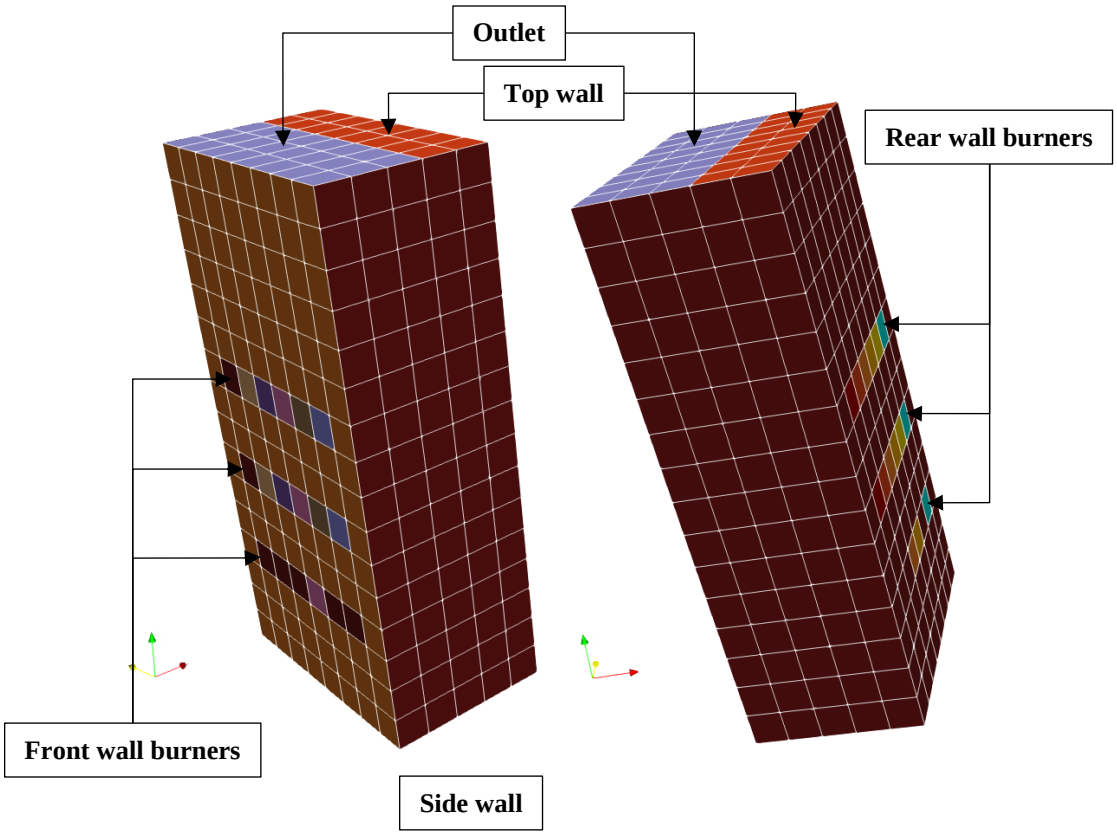

Figure 40 - Isometric views of zonal discretisation for the multiple-burner furnace.

The location of the burner inlet zones can be seen in Figure 38 and Figure 40. Each row has six burners per side and is the size of a single rectangle with the same side length as the zones. The furnace exit is at the top as indicated by the outlet in Figure 38 and Figure 40. The wall is also assumed to be a flat surface, which is not the case for the actual furnace - it will be larger due to the curvature of the water wall pipes. Because the zonal model only models the radiation heat transfer, the projected surface area is the relevant area, which is equivalent to the flat surface area as used. The larger surface area due to the curvature and fins might need to be accounted for when convection heat transfer is included.

Table 16 - A summary of the furnace and burner inputs for the multiple-burner furnace.

Description	**Value**			**Unit**
	60.5%	**81%**	**99%**	
Water wall fluid temperature	620	625	625	K
Platen superheater temperature	708	697	698	K
Furnace wall emissivity	0.85	0.85	0.85	-
Tube wall thickness	5.6	5.6	5.6	mm
Tube wall thermal conductivity	47	47	47	W/mK
Tube internal convection coefficient	20 000	20 000	20 000	W/m^2K
Primary air mass flow rate	2.81	4.01	4.74	kg/s
Primary air temperature	373	373	373	K
Secondary air mass flow rate	8.43	12.04	14.27	kg/s
Secondary air temperature	535	558	577	K
Coal mass flow rate	1.67	2.52	3.12	kg/s
Coal temperature	373	373	373	K

The furnace and burner inputs for the different load cases from Laubscher and Rousseau (2019a; 2019b) are summarised in Table 16. An isothermal mass flow map using OpenFOAM® was created for each of the three loads and imported as a mass flow map. The mass flow was an inlet boundary at each burner location with a pressure boundary at the outlet. A Reynolds-averaged turbulence model was used. A no-slip boundary was applied to the walls. Refer to Figure 92 to Figure 95 in the appendix for illustrations of the CFD results used for the mass flow map of the 60.5%, 81% and 99% load case.

A constant fluid temperature inside the water walls of the furnace (evaporator) was provided and therefore the furnace wall temperature can be calculated considering the tube wall thickness, thermal conductivity and convection coefficient provided. It should be noted that this is different from the previous case where the temperature on the wall was fixed. The tube internal convection coefficient was sourced from Laubscher and Rousseau (2019a: 514) and is high because boiling occurs along the evaporator tubes. It was assumed no fouling was present and the FNM did not

account for any swirl. Refer to section 3.7 for more on the different boundary condition configurations.

The emissivity of the platen superheater tubes was assumed to be the same as the furnace walls. The temperature at the furnace exit plane was set equal to that of the platen superheater. This temperature is in actual case not the real temperature at the exact location but effectively a pseudo-boundary condition. Even though the platen superheater is not confined within the volume of the geometry being modelled, the much lower temperature of the tubes has to be included. This is due to the much lower temperature on the tube surface when compared to the gas temperature at the furnace exit and the fourth-order relationship of radiation heat transfer through a transparent medium.

It should also be noted that it is not correct to assume the complete area to be equal to the platen superheater due to the void between the platen superheater and the front wall filled with a gas at a higher temperature. A test simulation was done by updating the furnace outlet temperature to be equal to the adjacent gas zone temperatures (Neumann boundary condition or also known as zero-gradient boundary condition) which resulted in a much higher FEGT due to the absence of radiation heat exchange of the gas near the furnace exit plane. Therefore, it was considered the most appropriate choice to set the surface at the FEGT plane equal to the platen superheater tube temperature and emissivity.

Table 17 - A summary of the coal properties for the multiple-burner furnace.

Description	Value	Unit
Coal density	1000	kg/m^3
Spread factor	1.156	-
Mean particle size	68	µm
Minimum particle size	6.8	µm
Maximum particle size	300	µm
Ultimate analysis – Carbon	41.56	%
Ultimate analysis – Hydrogen	2.22	%
Ultimate analysis – Oxygen	7.90	%
Ultimate analysis – Nitrogen	0.97	%
Ultimate analysis – Sulphur	0.94	%
Ultimate analysis – Moisture	5.50	%
Proximate analysis – Volatiles	19.60	%
Proximate analysis – Fixed carbon	34.00	%
Proximate analysis – Ash	40.90	%
Gross calorific value	15 070	kJ/kg

A summary of the coal properties is tabulated in Table 17. The minimum fly ash particle diameter was limited to 13 µm. The baseline correlation for the surface reaction rate was assumed

to be anthracite with a low surface reaction rate as documented in Field et al. (1967:393). The distance to complete volatile evolution of 2.815 m was assumed for devolatilisation within the first zone from the burner. For simplicity, a devolatilisation swelling factor of one was assumed. The heat source multiplier for the heat source term to match the fuel gross calorific value was determined to be 0.95.

Similar to the previous section, the scattering term in the gas extinction factor has not been accounted for. Two predictions will be presented for the FNM:

- Base: The absorption coefficient (as described in section 3.10) and surface reaction rate without any calibration.
- Calibrated: The absorption coefficient and surface reaction rate calculation with calibration.

The selection for the multipliers was done to closely match the CFD results for the 99% load case. The calibration was done similarly to the single-burner furnace in section 4.2.4. For the extinction coefficient, the values calculated from the models for each zone were adjusted by a factor 0.293. The reaction coefficients were multiplied by a factor of 0.229.

4.2.8 Multiple-burner furnace: Results

A comparison of the measured and predicted values is summarised in Table 18. Laubscher and Rousseau (2019a, 2019b) already validated the CFD results with the measurements and this will be considered as the benchmark to which the FNM is compared. The values for the measured FEGT were not considered in the validation because the radiation pyrometer readings represent the temperature of the gas surrounding the probe. A better comparison is the CFD results of a mass-average temperature across the furnace exit plane below the platen superheater.

The measured temperature at the furnace exit did not compare well with other well-established methods such as the Gurvich method. The Gurvich method is one of the semi-empirical methods developed during tests performed on pilot plants and utility boilers to estimate the furnace heat absorption and FEGT (Sankar, Santhosh Kumar & Balasubramanian, 2019:643-644). A coded algorithm based on the approach solves within seconds and therefore provides useful benchmark results within very short timescales. Using the Gurvich method, a model in Flownex® SE was created (refer to Figure 111 in the appendix for the model and results). The model predicted a furnace exit gas temperature of 1585 K when an unburned carbon mass fraction of 0.029% is

imposed. The commissioning schedules reported the temperature to be 1540 K (Laubscher & Rousseau, 2019a:515).

Table 18 - Comparison of the measured and predicted results at 99% load.

Parameter	Unit	Measured (min, max)	CFD	FNM (base)	Difference	FNM (calibrated)	Difference
Heat input	MW	N/A	1710	1695	-0.9%	1690	-1.2%
Evaporator heat absorption	MW	538 (556, 518)	545.56	763.3	39.9%	538.5	-1.3%
Furnace exit gas temperature	K	1404 (1349, 1460)	1678	1421	-15.3%	1661	-1.0%
Furnace exit O_2 volume fraction	v% (wet)	2.3	2.56	2.40	-6.1%	2.44	-4.7%
Unburned carbon	m%	N/A	0.0290	0.000	-100.0%	0.0286	-1.2%

The heat input values correspond well (± 1% difference) between the CFD and FNM (base and calibrated) results. The base FNM case overpredicts the carbon burnout, predicted no unburned carbon at the furnace exit. After the surface reaction rate was calibrated, the carbon burnout was within 1.2% of the CFD results. The predicted O_2 concentration for the base and calibrated FNM case compares well with the CFD and measured value. The O_2 concentration is also correctly higher in the calibrated FNM case when less carbon has been burned when compared to the base FNM case.

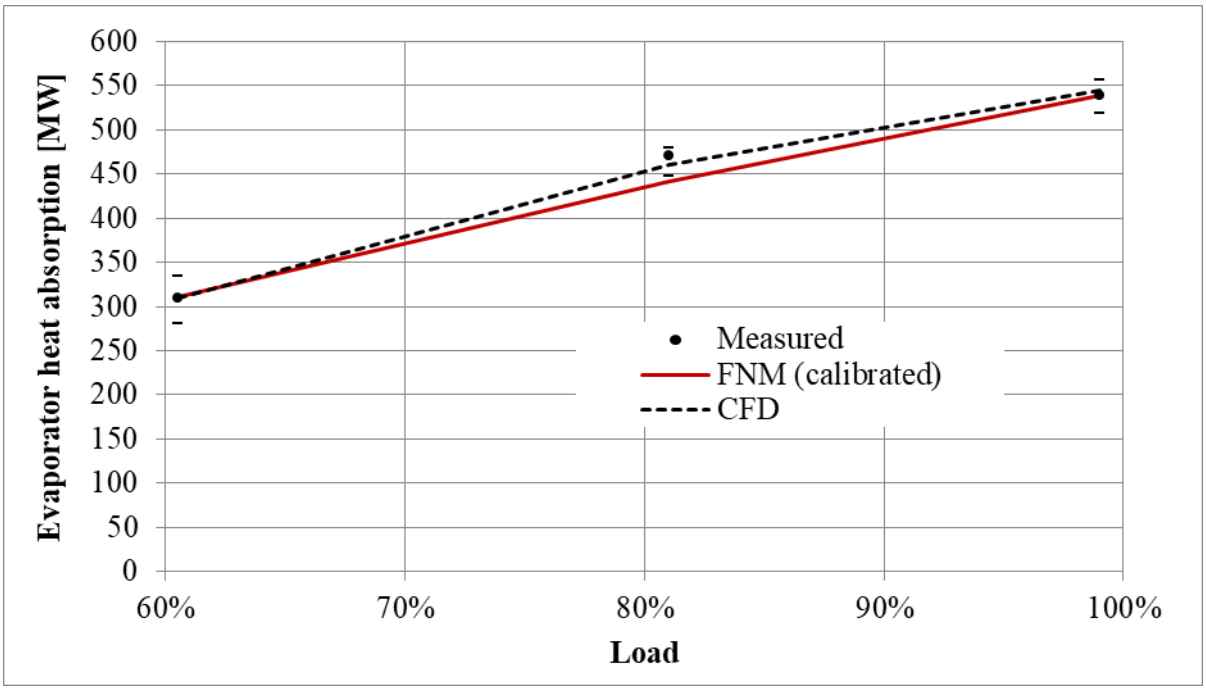

Figure 41 - Predicted and measured evaporator heat absorption.

The base FNM case overpredicted the heat transfer to the evaporator (furnace walls) and resulted in an underprediction of the furnace exit gas temperature. By modifying the extinction coefficients in the calibrated FNM case, the evaporator heat absorption matches within 1.2% and the furnace exit gas temperature by 1.0%. The calibrated FNM case is therefore a model characterised to match the 99% CFD results. This model can then be used to see how well it can predict the parameters at the other load conditions to determine the validity of the methodology of the FNM. A comparison of these predictions is shown in Figure 41 and Figure 42.

The prediction of the evaporator heat absorption by the calibrated FNM case when compared to the measured and CFD results is shown in Figure 41. The prediction of the mass-average furnace exit gas temperature by the calibrated FNM when compared to the measured and CFD results are shown in Figure 42. The heat absorption predicted by the calibrated FNM closely matches the CFD results and measurements for the 60.5% and 81% load cases within reasonable limits. The predictions are also within the minimum and maximum range as measured, except for the evaporator heat absorption slightly missing the minimum for 81% load.

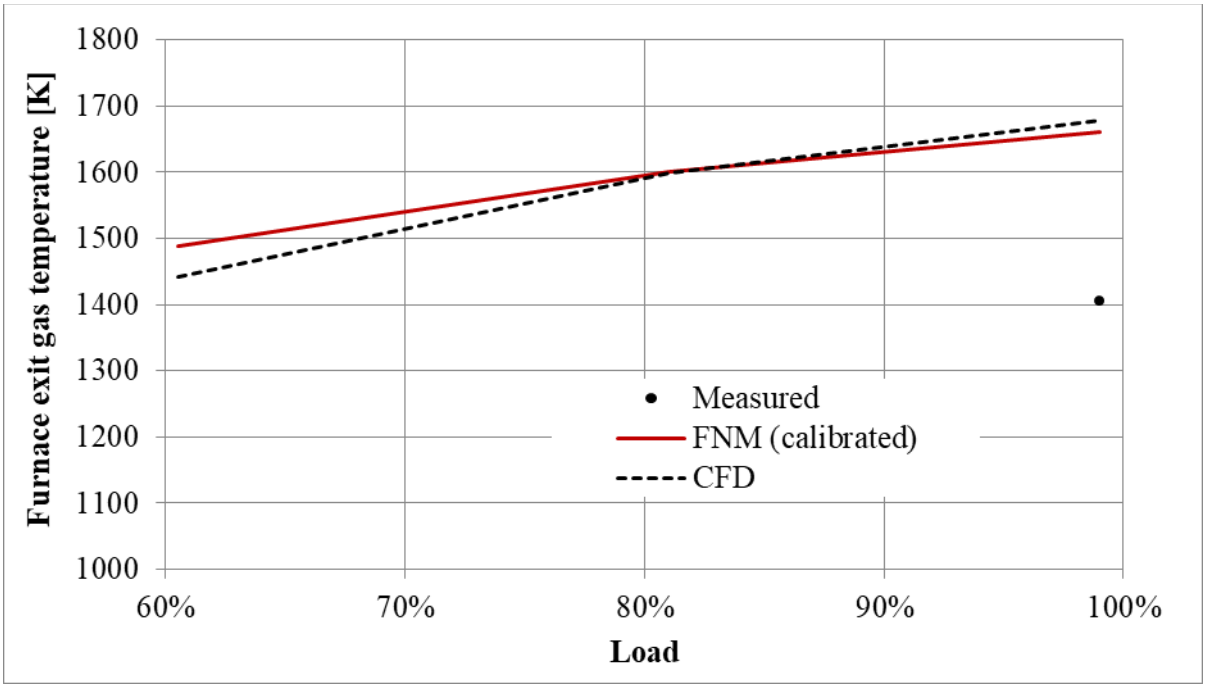

Figure 42 - Predicted and measured furnace exit gas temperatures (mass-averaged).

The predictions of the oxygen (wet) concentration and unburned carbon by the FNM when compared to CFD results are shown in Figure 43 and Figure 44. The predicted values by the calibrated FNM case closely follows the trend of the CFD, albeit the oxygen concentration of the FNM are slightly lower and the unburned carbon slightly higher. A minor divergence in the

unburned carbon is noticed for the 60.5% load case, but is no concern considering that the fraction of 0.2% is still very low.

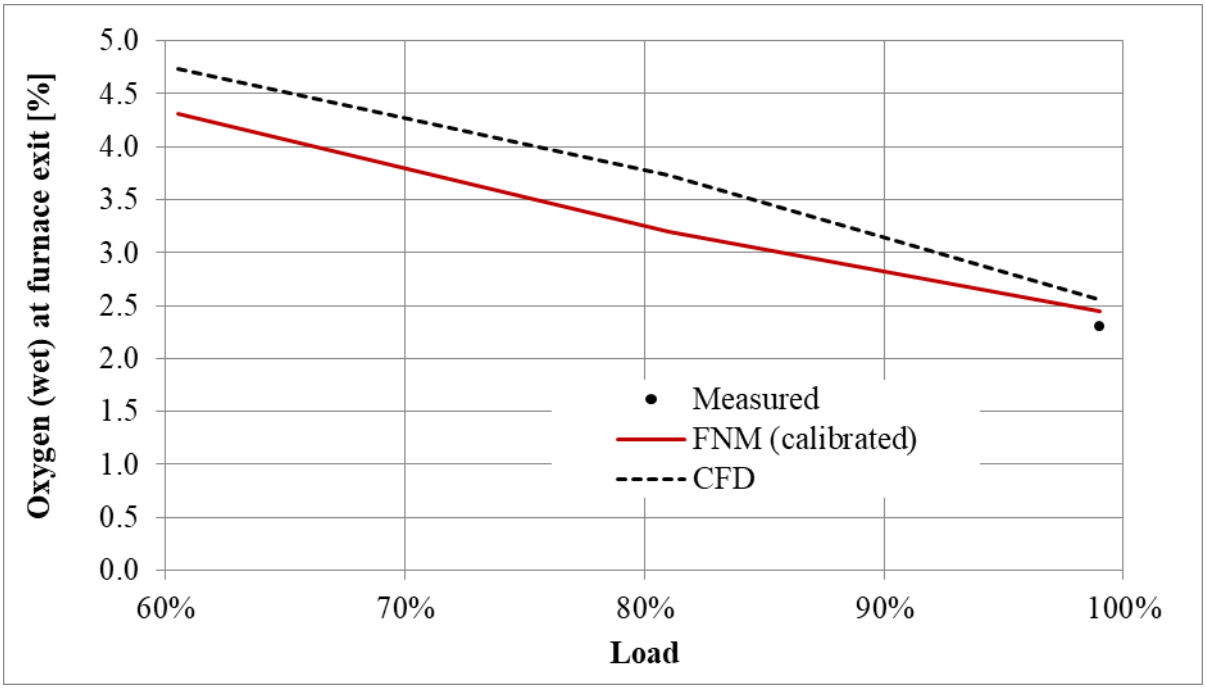

Figure 43 - Predicted and measured oxygen at furnace exit (mass-averaged).

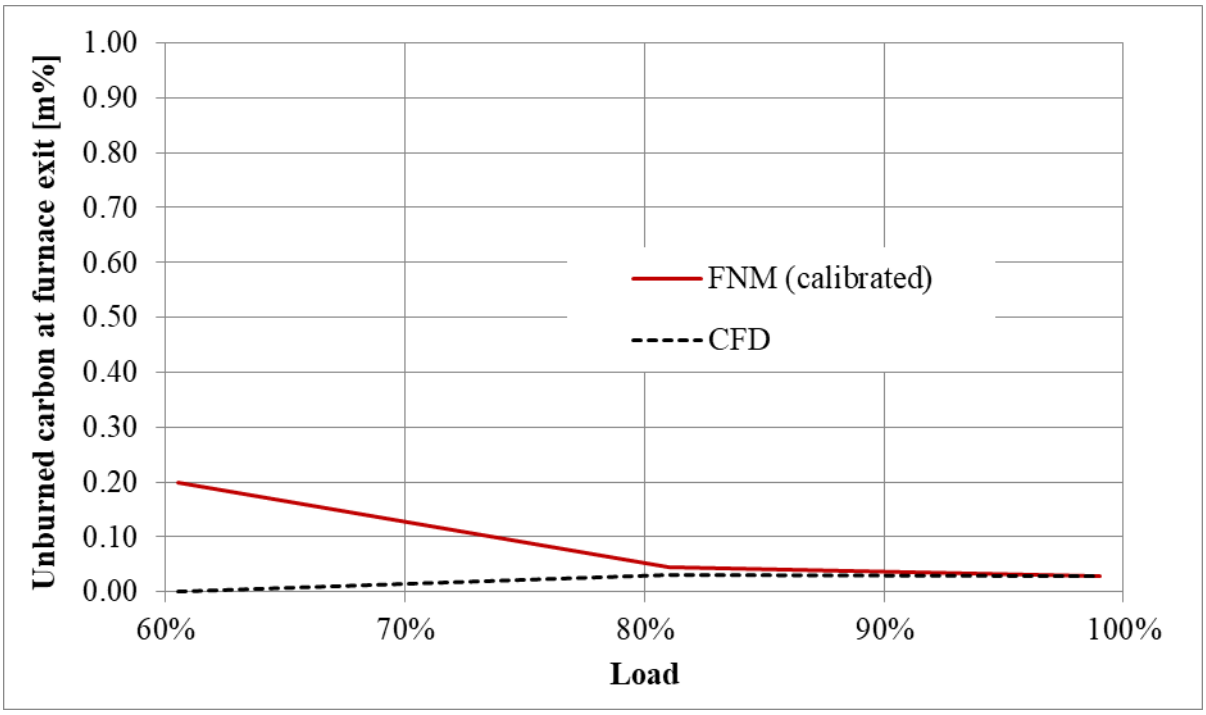

Figure 44 - Predicted and measured unburned carbon at furnace exit (mass-averaged).

Thus, after calibration of the reaction rates and extinction coefficient under certain conditions, the calibrated FNM case could accurately predict the evaporator heat absorption and furnace exit

gas temperature when the coal and air flow rate was changed to reflect the input values for other operating conditions. It is also important to note that there was no significant loss in accuracy for the ± 40% operating range for the validation data. This range, from 60.5% to 99%, is also the essential range where the parameters should be accurately predicted because during operation this will be the predominant load conditions for the furnace of the boiler.

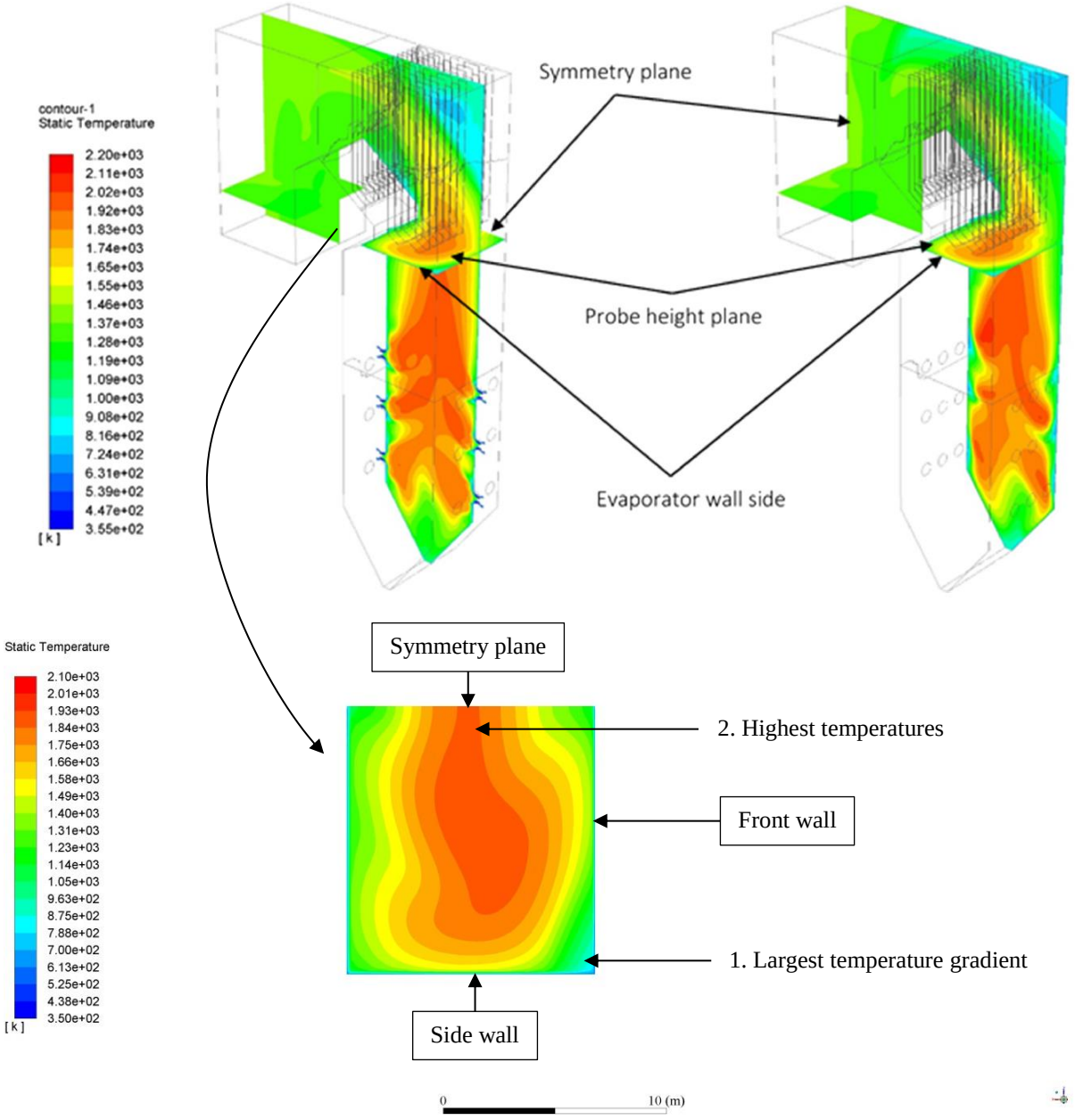

Figure 45 - Temperature distribution for the CFD results of the 99% load case as generated by Laubscher and Rousseau (2019a:515).

The CFD results presented by Laubscher and Rousseau (2019a:515) also provide temperature distributions for the 99% case along different planes as shown in Figure 45. The first temperature distribution is a plane in the vertical direction with the cut through the second burner. The second temperature distribution is the furnace exit gas temperature profile just below the platen superheater.

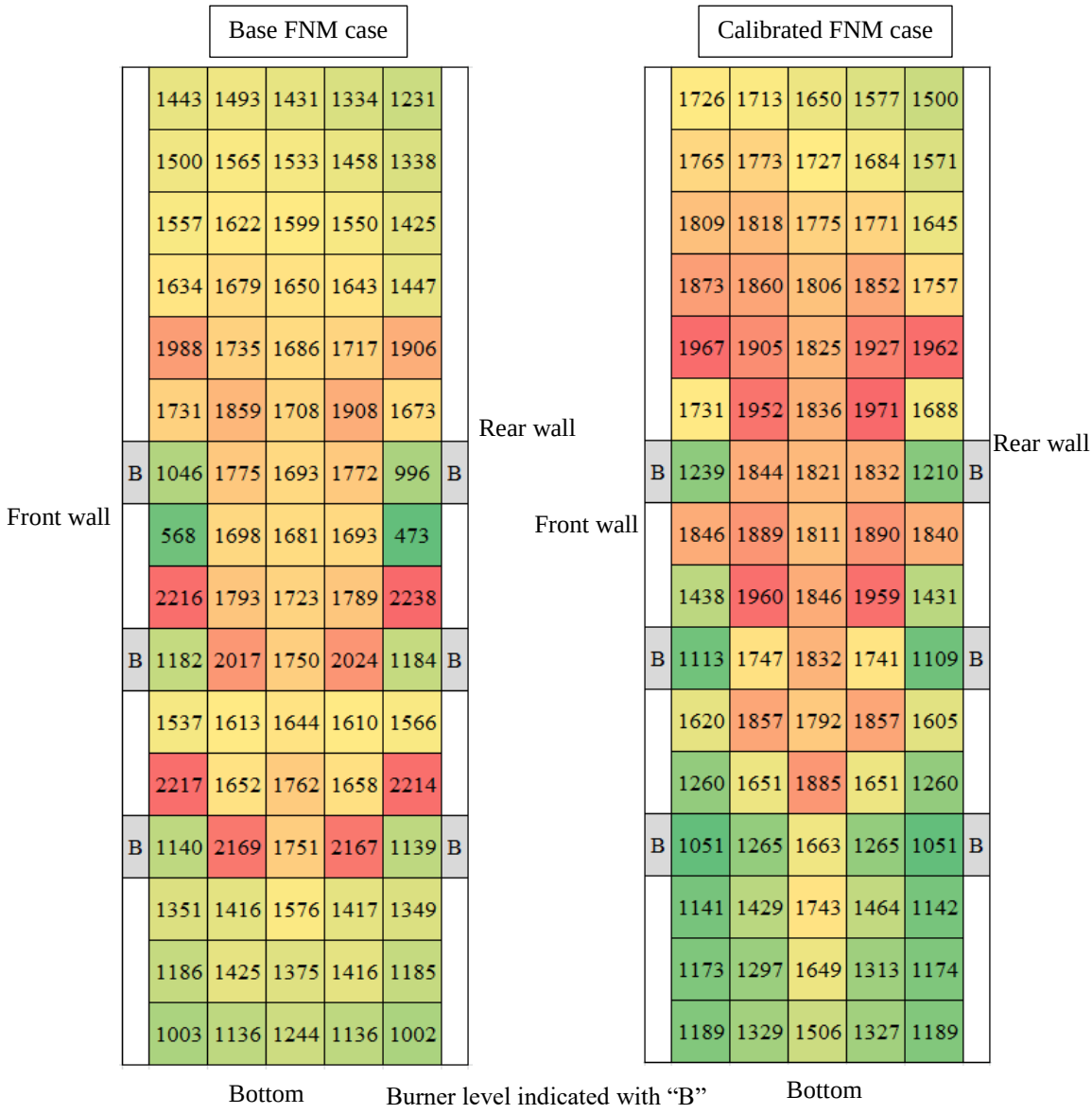

Figure 46 - The two-dimensional furnace gas temperature distribution on a plane at the centre along the height of the furnace for the base and calibrated FNM case (temperatures in kelvin).

The comparative plane to the CFD results in Figure 45 for the temperature distribution in the vertical direction for the base FNM case and the calibrated FNM case is shown in Figure 46. For all the temperature distributions, the lowest temperatures are near the bottom and the highest near the burners. The low temperatures near the bottom are due to the small amount of flue gas recirculating

in these zones and most of the combusting flow upward through the furnace. The high temperatures near the burners are due to the high addition of heat added due to combustion. The calibrated FNM case predicts a smoother temperature distribution from the centre to the walls than the base FNM case. For a few instances for the base FNM case, the temperature gradients between the neighbouring zones are extremely large. All of these instances are near the burner locations. The convection of higher temperature gases for the calibrated FNM case tends more to the front wall when approaching the furnace exit when compared to the base FNM case. The convective flow correlates with the flow bias from the burners to the furnace exit derived from the isothermal CFD simulations illustrated in Figure 39 and Figure 92. The higher temperatures towards the front wall near the furnace exit are more prominent for the calibrated FNM due to the less heat absorbed further down the furnace. Overall, the smoother temperature distribution of the calibrated FNM case provides a better comparison with the CFD results.

The comparative plane to the CFD results in Figure 45 for the temperature distribution at the furnace exit for the base FNM case and calibrated FNM case is shown in Figure 47. All the temperature profiles predict the lowest temperatures in the corners, with the corner at the front wall the lowest. For the temperature profile at the furnace exit, the distribution of the base FNM case would have been more representative of the CFD results except that the temperature values are underpredicted. Unfortunately, the calibrated FNM case predicts the highest temperatures for the temperature distribution at the furnace exit nearer to the front wall which does not accurately match the CFD results. The CFD results predict the highest temperatures in the middle of the furnace exit plane. The most likely cause propagates from the mass flow map below the furnace already noticed with the comparison from the verticle temperature profiles. The velocity magnitude and velocity vector in the x-direction as shown in Figure 92 in the appendix of the isothermal CFD simulations show that the flow pattern has a higher magnitude towards the front wall near the furnace exit. More refinement with regard to the flow map using the isothermal CFD approach will be necessary to further improve the accuracy in this regards. A solution with a finer discretisation is shown in Figure 93 in the appendix and methods will be required to integrate the flow distribution of such a solution into the flow map with a coarser discretisation.

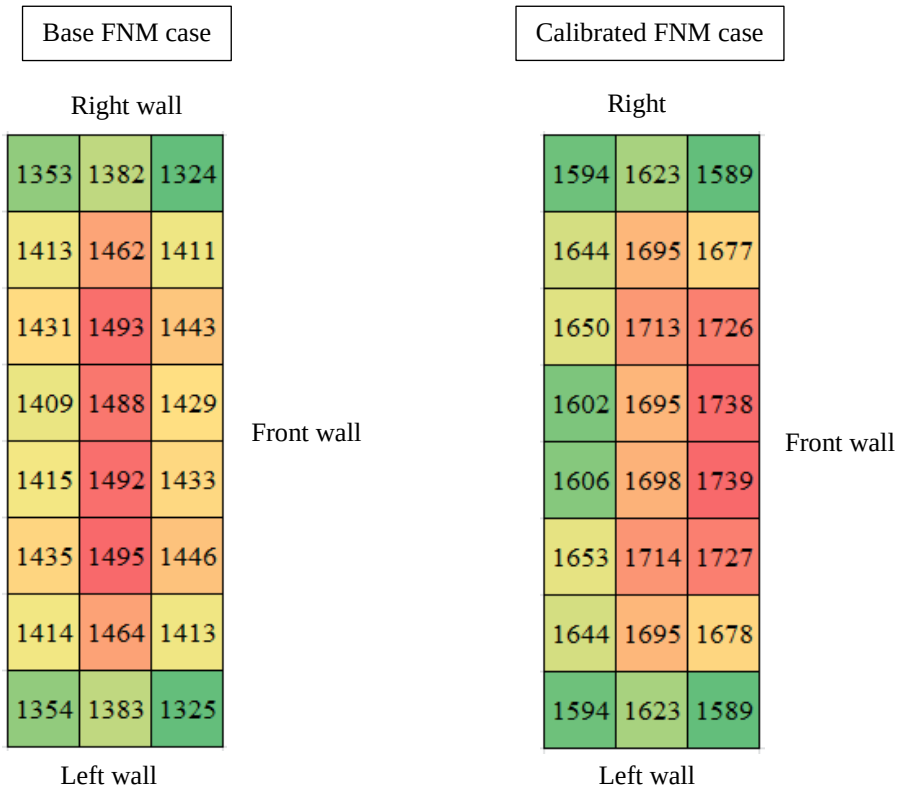

Figure 47 - The two-dimensional furnace exit gas temperature on the outlet plane for the base and calibrated FNM case (temperatures in kelvin).

A comparison of the heat fluxes to the furnace walls to the base FNM case and calibrated FNM case at 99% load is shown in Figure 48 to Figure 53. The heat fluxes to each wall of the base FNM case are compared in Figure 48, Figure 50 and Figure 52 to the CFD results. The heat fluxes to each wall of the calibrated FNM case are compared in Figure 49, Figure 51 and Figure 53 to the CFD results. It should be noted that the CFD results for the front and rear wall is only half of the wall due to the cut of the symmetry plane along the centre. The burners are indicated with thicker borders.

The scale of the CFD results indicates that the expected heat fluxes should range between 17.5 to 350 kW/m^2. The majority of heat fluxes predicted by the based FNM case and calibrated FNM case are similar order of magnitude when compared to the CFD. The highest heat fluxes for all the models in the front and rear wall are predicted around the burners. The base FNM case predicted much higher hot spots around the burners. These higher heat fluxes around the burners for the base FNM case are the most probable cause of why calibration was necessary for the absorption coefficient. An overprediction of the absorption coefficients caused higher radiation heat transfer predictions in the near burner region of the base FNM case. Further research focussing on the appropriate absorption coefficient models in this region might lessen the need for calibration.

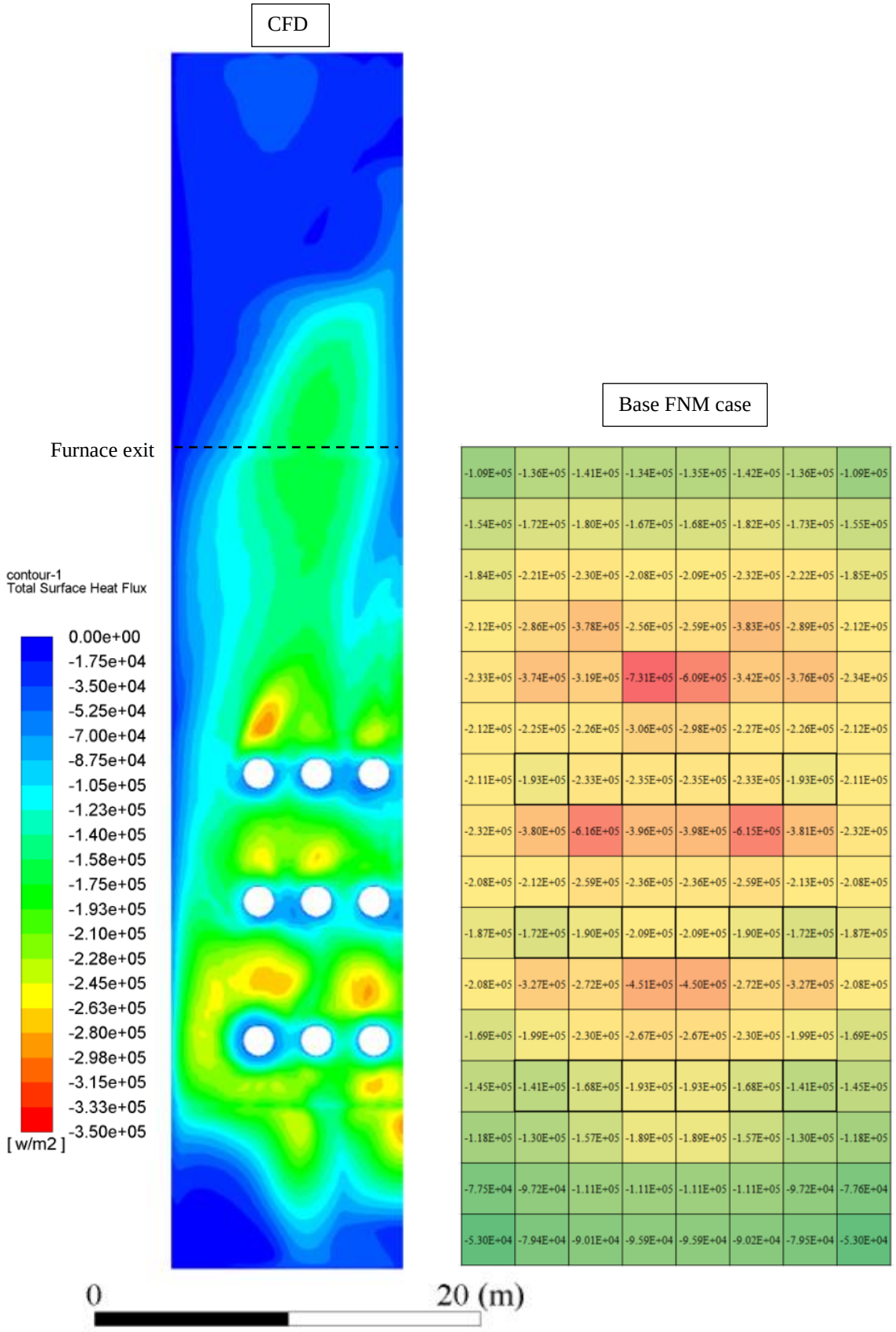

Figure 48 - The heat flux distribution (in W/m^2) to the front wall for the CFD and base FNM case at 99% (the heat flux results for the FNM case is enlarged in the appendix).

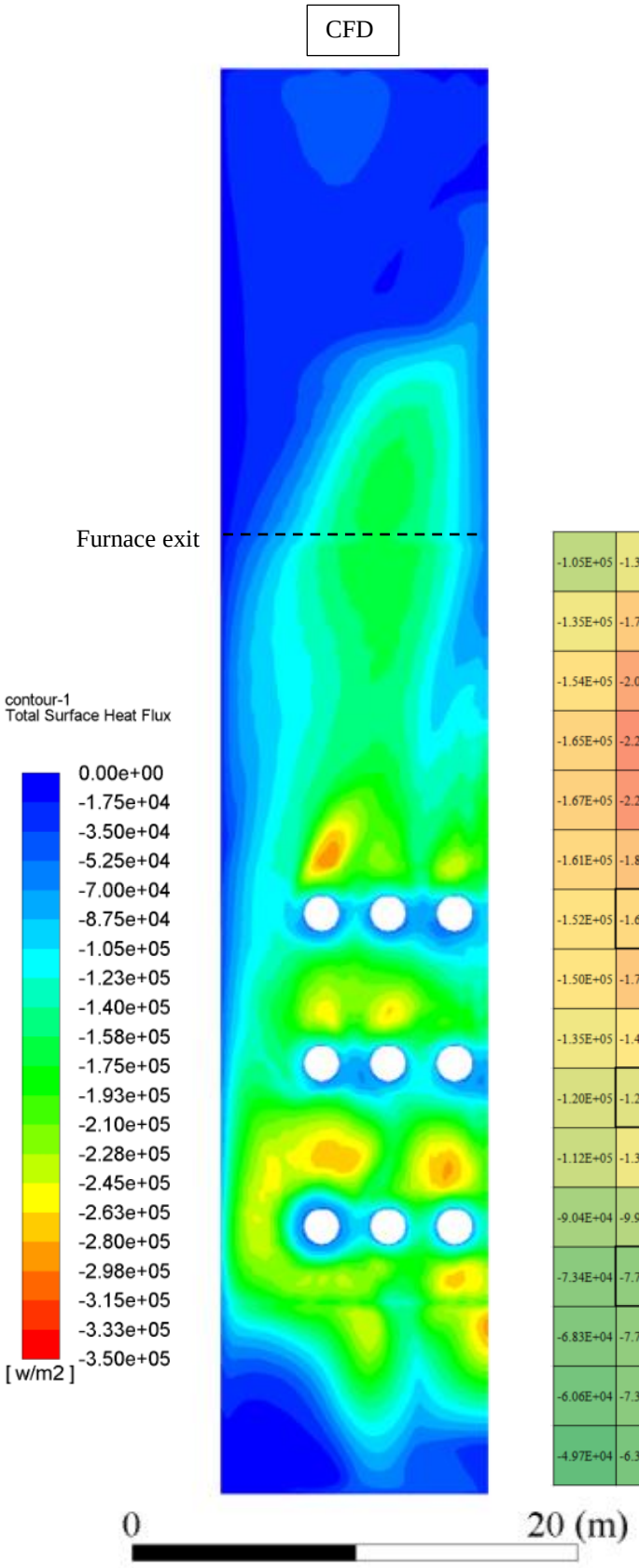

Calibrated FNM case

-1.05E+05	-1.30E+05	-1.40E+05	-1.40E+05	-1.41E+05	-1.40E+05	-1.31E+05	-1.05E+05
-1.35E+05	-1.74E+05	-1.87E+05	-1.83E+05	-1.85E+05	-1.89E+05	-1.74E+05	-1.35E+05
-1.54E+05	-2.05E+05	-2.24E+05	-2.08E+05	-2.14E+05	-2.28E+05	-2.06E+05	-1.54E+05
-1.65E+05	-2.26E+05	-2.58E+05	-2.36E+05	-2.65E+05	-2.63E+05	-2.27E+05	-1.65E+05
-1.67E+05	-2.21E+05	-2.43E+05	-2.41E+05	-2.46E+05	-2.44E+05	-2.21E+05	-1.68E+05
-1.61E+05	-1.81E+05	-1.93E+05	-1.98E+05	-1.99E+05	-1.93E+05	-1.82E+05	-1.61E+05
-1.52E+05	-1.60E+05	-1.72E+05	-1.78E+05	-1.79E+05	-1.73E+05	-1.60E+05	-1.53E+05
-1.50E+05	-1.76E+05	-1.85E+05	-1.88E+05	-1.88E+05	-1.85E+05	-1.76E+05	-1.50E+05
-1.35E+05	-1.47E+05	-1.54E+05	-1.58E+05	-1.58E+05	-1.54E+05	-1.47E+05	-1.35E+05
-1.20E+05	-1.25E+05	-1.34E+05	-1.37E+05	-1.37E+05	-1.34E+05	-1.25E+05	-1.21E+05
-1.12E+05	-1.34E+05	-1.54E+05	-1.57E+05	-1.57E+05	-1.54E+05	-1.34E+05	-1.12E+05
-9.04E+04	-9.96E+04	-1.04E+05	-1.06E+05	-1.06E+05	-1.04E+05	-9.98E+04	-9.06E+04
-7.34E+04	-7.74E+04	-8.08E+04	-8.21E+04	-8.22E+04	-8.10E+04	-7.76E+04	-7.36E+04
-6.83E+04	-7.78E+04	-8.18E+04	-8.31E+04	-8.31E+04	-8.19E+04	-7.80E+04	-6.85E+04
-6.06E+04	-7.36E+04	-8.02E+04	-8.31E+04	-8.32E+04	-8.03E+04	-7.38E+04	-6.07E+04
-4.97E+04	-6.31E+04	-7.13E+04	-7.42E+04	-7.42E+04	-7.13E+04	-6.32E+04	-4.98E+04

Figure 49 - The heat flux distribution (in W/m^2) to the front wall for the CFD and calibrated FNM case at 99% (the heat flux results for the FNM case is enlarged in the appendix).

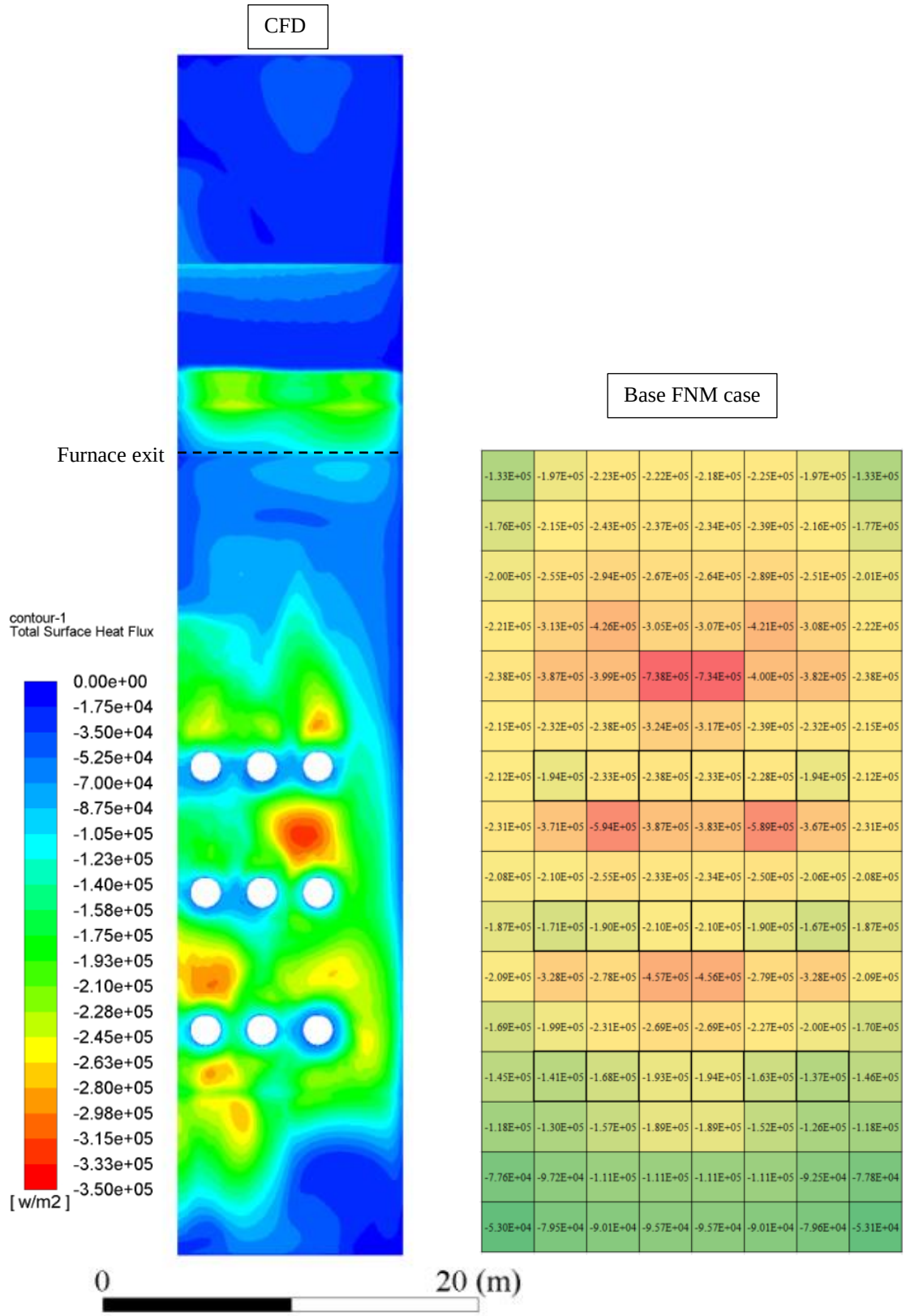

Figure 50 - The heat flux distribution (in W/m^2) to the rear wall for the CFD and base FNM case at 99% (the heat flux results for the FNM case is enlarged in the appendix).

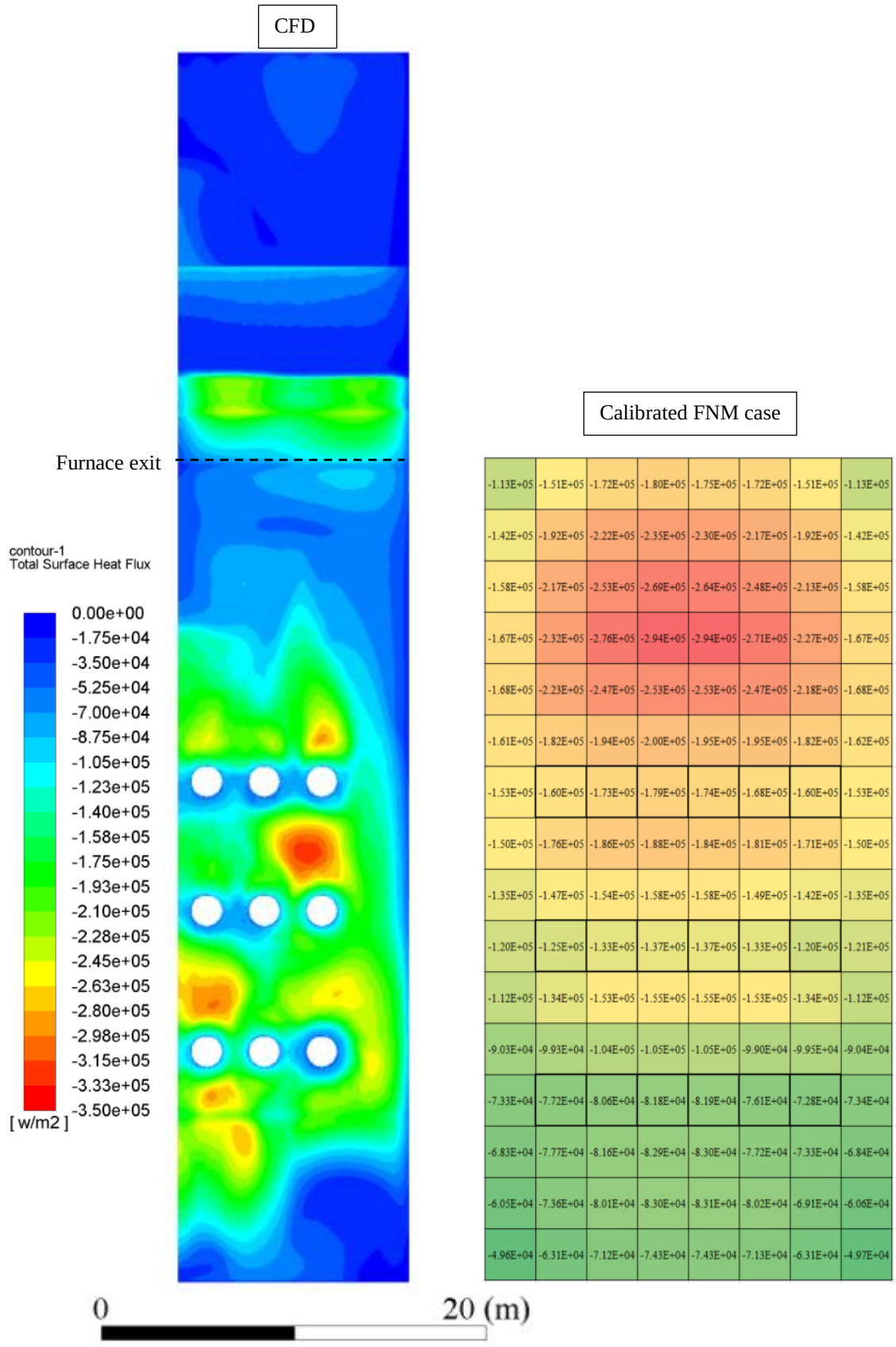

Figure 51 - The heat flux distribution (in W/m^2) to the rear wall for the CFD and calibrated FNM case at 99% (the heat flux results for the FNM case is enlarged in the appendix).

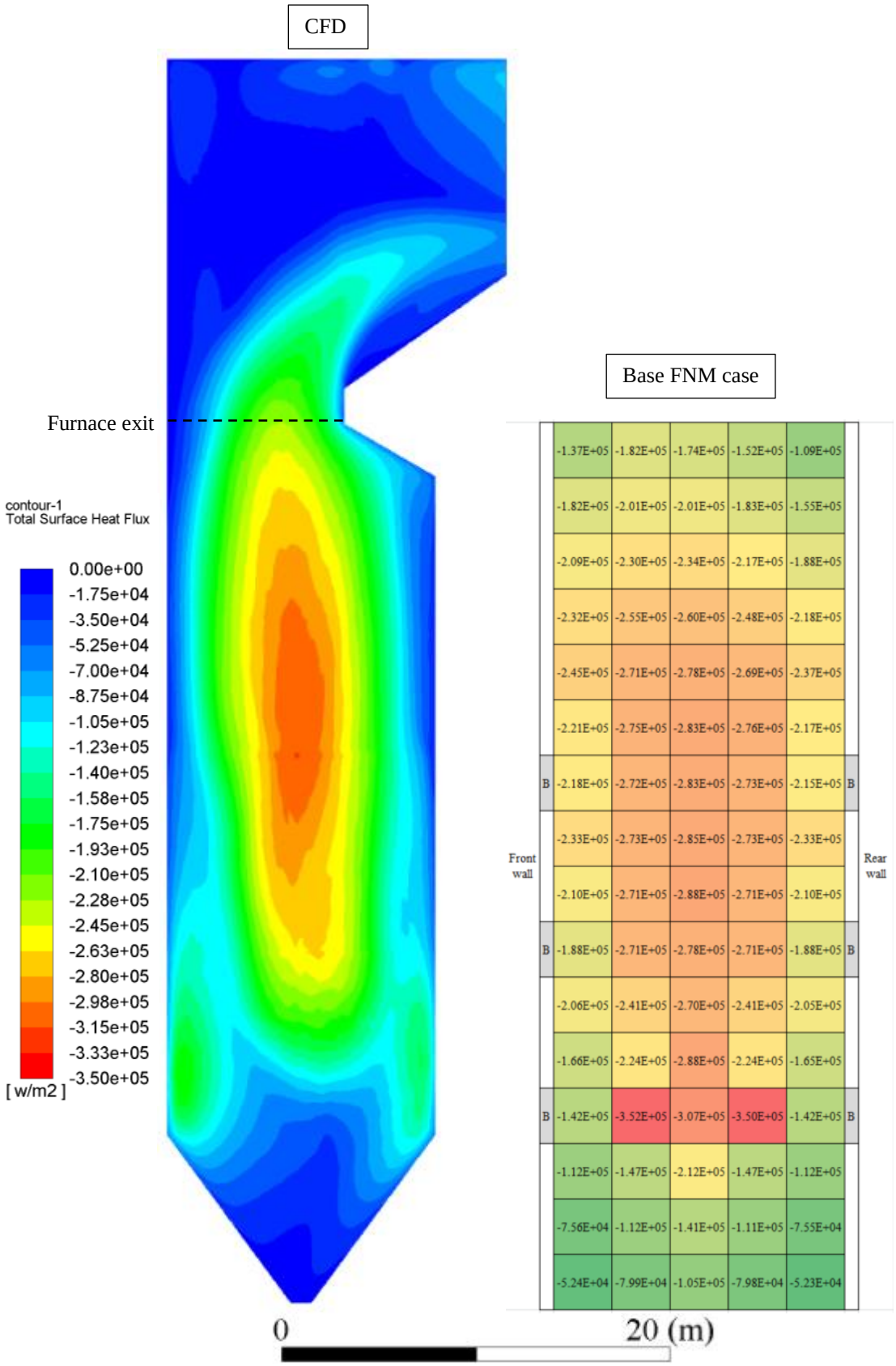

Figure 52 - The heat flux distribution (in W/m^2) to the side wall for the CFD and base FNM case at 99% (the heat flux results for the FNM case is enlarged in the appendix).

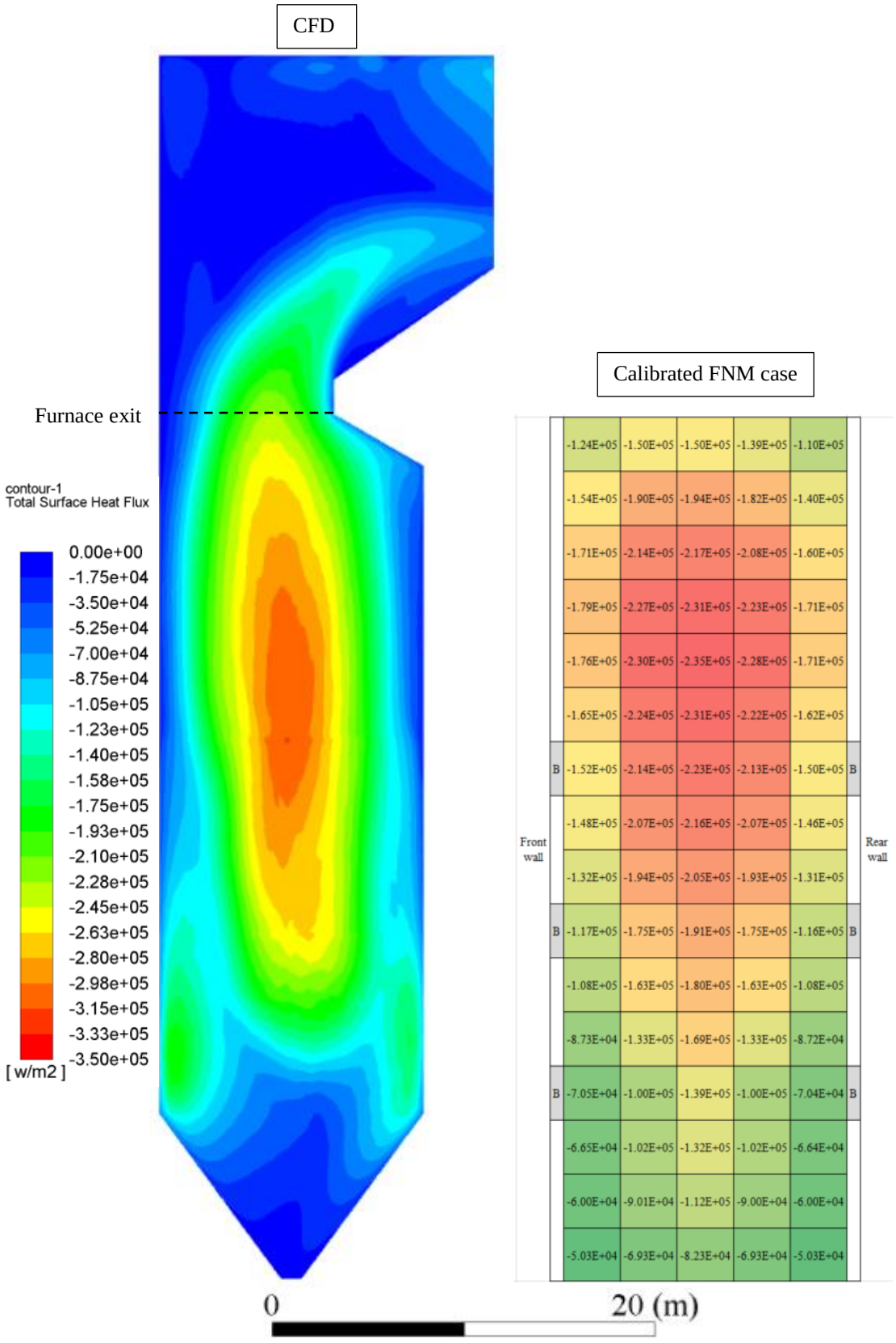

Figure 53 - The heat flux distribution (in W/m^2) to the side wall for the CFD and calibrated FNM case at 99% (the heat flux results for the FNM case is enlarged in the appendix).

The order of magnitude of the heat fluxes for the base FNM case and calibrated FNM case correlates well with the side wall results of the CFD. This supports the finding that the near burner region is the most likely cause of why calibration was needed to decrease the total heat absorption due to radiation heat transfer of the base FNM case. The heat flux distribution of the calibrated FNM case showed the best correlation with the heat flux distribution of the CFD.

All the models predict a decrease in the heat fluxes on all the walls further away from the burners. The base FNM case and calibrated FNM case do not capture the same magnitude of decrease in the gradient near the corner which is most likely due to the discretisation fineness used in these models. The lowest heat fluxes in the bottom at the hopper region for the base FNM case and calibrated FNM case agree with the CFD results having this region also as the coolest zones.

For this multiple-burner base case having 640 zones, the Scilab® code solved within 4 minutes and the Matlab® code within 22 seconds on a laptop computer (2.7 GHz CPU with 2 cores). The CFD solution required 6 hours to solve on a computer with 40 cores for the same multiple-burner furnace. The Gurvich method as implemented in Flownex® SE solved in less than one second.

4.2.9 Conclusion of validation

Only the surface reaction coefficient model required calibration for the single-burner case and the extinction coefficient models provided prediction within an acceptable range. For the multiple-burner case, the comparison between the base FNM case with the CFD and measured results did not provide satisfactory predictions using the selected models to calculate the surface reaction coefficients for the combustion model and the extinction coefficients for the radiation. This confirms the necessity for calibration to modify the coefficients of the correlations and models to provide satisfactory results.

It was clear with the calibration of the surface reaction coefficients and the extinction coefficients to match a higher fidelity model (albeit CFD or measurements) at a single operating load that it was possible to successfully calibrate the FNM to match the benchmark. This calibrated model accurately predicted the heat absorption by the furnace walls and furnace exit gas temperature (mass-averaged value over the outlet plane) at other input conditions of the coal and air mass flow rate. The other results such as the gas temperature distribution, carbon burnout as well as the oxygen and carbon dioxide concentration are available at the furnace exit plane. Therefore, all the capabilities required by the hypothesis for a full-scale utility furnace were demonstrated

(section 1.2). The calibrated FNM model can be applied for further studies as demonstrated in the next chapter.

The gas temperatures and burnout profile for the single-burner case were not accurately predicted by the FNM near the burner. Therefore, the FNM is limited to predictions outside the in-flame region, which will remain one of the exclusions. For the multiple-burner case, some refinement with regard to the mass flow maps will also be necessary to improve the accuracy of the furnace exit temperature profile predictions.

Unfortunately, the selected surface reaction rate and extinction coefficient model did not provide satisfactory predictions prior to calibration. Therefore, the FNM cannot be realistically used as a prediction tool without prior calibration with measurements or CFD results. When experience is gained within a specific configuration, then more reliable input values can be provided beforehand to enable satisfactory predictions without the need for higher fidelity models. The need for calibration, particularly for the multiple burner furnace, indicates a weakness in the selected models and is a drawback of the current methodology. It is recommended that further work be done in comparing different surface reaction rate and extinction coefficient models applied to the FNM to determine which one is more applicable to different furnace configurations and fuels.

5. Case studies

With a validated FNM model of a multiple-burner furnace available, the applicability to a coal-fired furnace will be demonstrated with the various case studies presented in this chapter. The case studies demonstrate the predicted change in the heat absorption, FEGT, carbon burnout and oxygen concentration for:

- Different particle size distributions.
- The same total coal and air flow rate but having certain burners out of operation.
- Fouling present on the furnace wall increasing the conduction resistance while emissivity remains the same.
- Different coal qualities (coal switching).
- A normalised mass flow map created at a single load and applied in the normalised form together with a load set-point to impose the flow map for other load conditions.
- Steady-state and transient co-simulation with Flownex® SE to demonstrate the integration between the flue gas in the furnace and the water/steam in the water wall.
- Integrated study imposing unequally distributed coal flow and pulverized fuel distribution per burner and the influence thereof on the FEGT and platen superheater.

The results for section 5.1 to 5.5 can be completed within a single working day. The Scilab® version of the code was used for section 5.5 to 5.6, while the Matlab® version of the code was used for section 5.7.

5.1 Particle size distribution sensitivity

The goal of this case study is to demonstrate whether the calibrated FNM provides consistent predictions when the particle size distribution changes. The calibrated FNM case from the validation in section 4.2.6 to 4.2.8 was used. The coal quality, as well as coal and combustion air flow rates, remained the same. The calibration multipliers as reported in section 4.2.7 for the surface reaction rate and absorption coefficient were unchanged.

The coal and mass flow rates were kept constant for all the cases, even though in an actual boiler the combustion air flow will be adjusted to the oxygen concentration set-point at the boiler exit. The control system will increase the combustion air flow rate when the oxygen concentration drops below the set-point and vice versa. The specification of the particle size distributions is shown in

Table 19. The particle distribution for the base case is the same as in the validation, while the finer and coarser particle distributions were arbitrarily chosen for demonstration purposes.

Table 19 - Comparison of the particle size distribution input of the base case to the finer and coarser case.

Description	Unit	Base	Finer	Coarser
Spread factor	-	1.156	1.156	1.156
Mean particle size	µm	68	58	78
Minimum particle size	µm	6.8	6.8	6.8
Maximum particle size	µm	300	200	400

A comparison of the predicted change of the heat input, evaporator heat absorption and mass-averaged FEGT when the particle size distribution changes are shown in Figure 54.

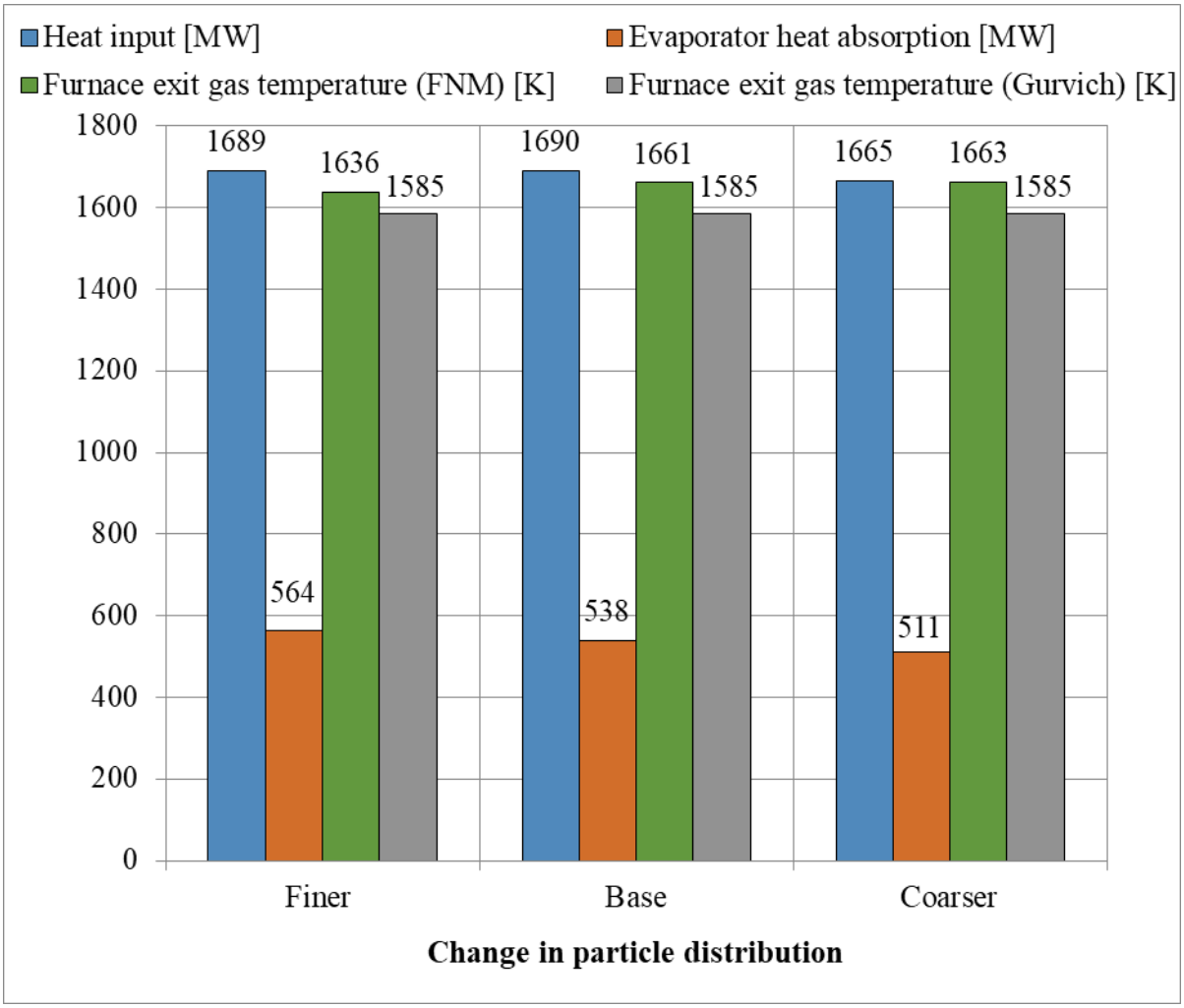

Figure 54 - Comparison of the predicted heat input, evaporator heat absorption and furnace exit gas temperature change for different particle distributions.

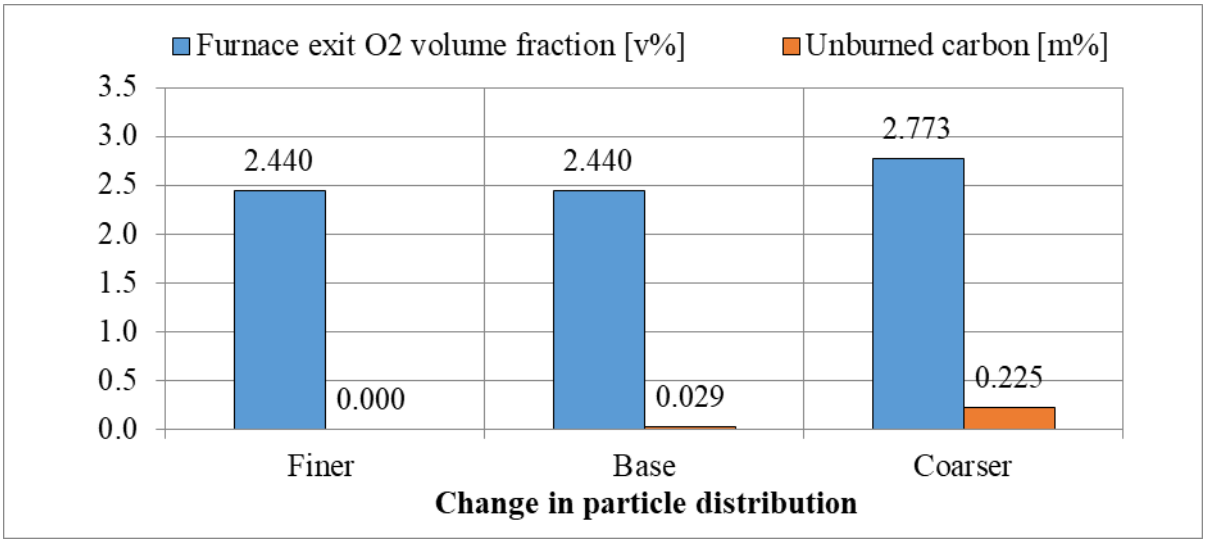

Figure 55 - Comparison of the predicted oxygen concentration and unburned carbon change for different particle distributions.

There is an increase in the evaporator heat transfer (36 MW more) while the heat input remains about the same (2 MW less) when the particle size distribution is finer. The combustion efficiency also increases as shown by the increase in carbon burnout (complete burnout) in Figure 55. This increase in combustion efficiency is due to more surface area available for the same mass when the particle distribution is finer. The mass-averaged FEGT decreases (by 25 K) because most of the combustion occurs earlier during the particle's propagation through the furnace, resulting in higher temperatures lower down in the furnace. The higher flue gas temperatures lower down in the furnace increase the local radiation heat transfer potential and therefore the heat absorption to the evaporator increases.

There is a decrease in the evaporator heat transfer (27 MW less) when the particle size distribution is coarser. The heat input decreased significantly by 25 MW together with the decrease in combustion efficiency (0.196 m% less carbon burnout while oxygen increase by 0.333 v% as shown in Figure 55). This is in contrast to finer particle size distributions, because less surface area is available for the same mass. The mass-averaged FEGT is higher than the base (by 2 K) and finer case (27 K). This is most likely due to the majority of the combustion that occurs further up in the furnace. Due to the slower combustion kinetics, the particles combust later than for finer particle distributions. This illustrates the negative impact of a too coarse pulverization from the mills on the furnace subsystem. The higher gas temperatures will propagate onto the platen superheaters above the furnace exit.

The Gurvich method was also checked whether it can be applied to this particular study to predict the change in FEGT. The model as used is shown in Figure 114 in the appendix and the calculated FEGT is also indicated in Figure 54. The model does not provide a way to account for the change in combustion kinetics when the particle distribution changes. Therefore, an assumption has to be made. Without prior knowledge of how the combustion efficiency will change, the burnout of carbon at the furnace exit was kept constant. The result is that the method will predict the same FEGT for each case and not capture the effect of the change in particle size distribution.

This case study demonstrates the usefulness of the FNM for a change in the particle size distribution. The change has an impact on the temperature distribution and carbon burnout which affects the heat input, heat transfer to the evaporator and the mass-averaged FEGT. Tools such as the FNM can be applied to provide quick predictions on how the furnace operating mode can be changed to maximise the heat transfer and combustion efficiencies.

5.2 Burners out of operation

The goal of this case study is to demonstrate whether the calibrated FNM case (from the validation in section 4.2.6 to 4.2.8) provides consistent predictions when the burner operating modes change. The calibrated FNM case will be the base case. The total coal and air flow rate, as well as the calibrated factors for the absorption coefficients and surface reaction rates, were kept the same for each case.

Two cases were imposed with the first having four burners at the top of the front wall out of operation and the second having four burners at the bottom of the front wall out of operation. The coal and air flow rate were increased and redistributed equally to the other burners to impose the same total coal and air flow as the base case. The different burner configurations for the front wall are shown in Figure 56. All the burners in the rear wall were kept in operation. An iso-thermal mass flow maps were generated for each of the two new cases.

A flame centre modification factor is available in the Gurvich method to account for changes in the burner tilts (Zhang, Li and Zhou, 2016:140-141). However, it is difficult to correlate this with how the flame centre might change with individual burners out of operation. Therefore, it was not deemed useful to include the FEGT prediction using the Gurvich method for this particular case study.

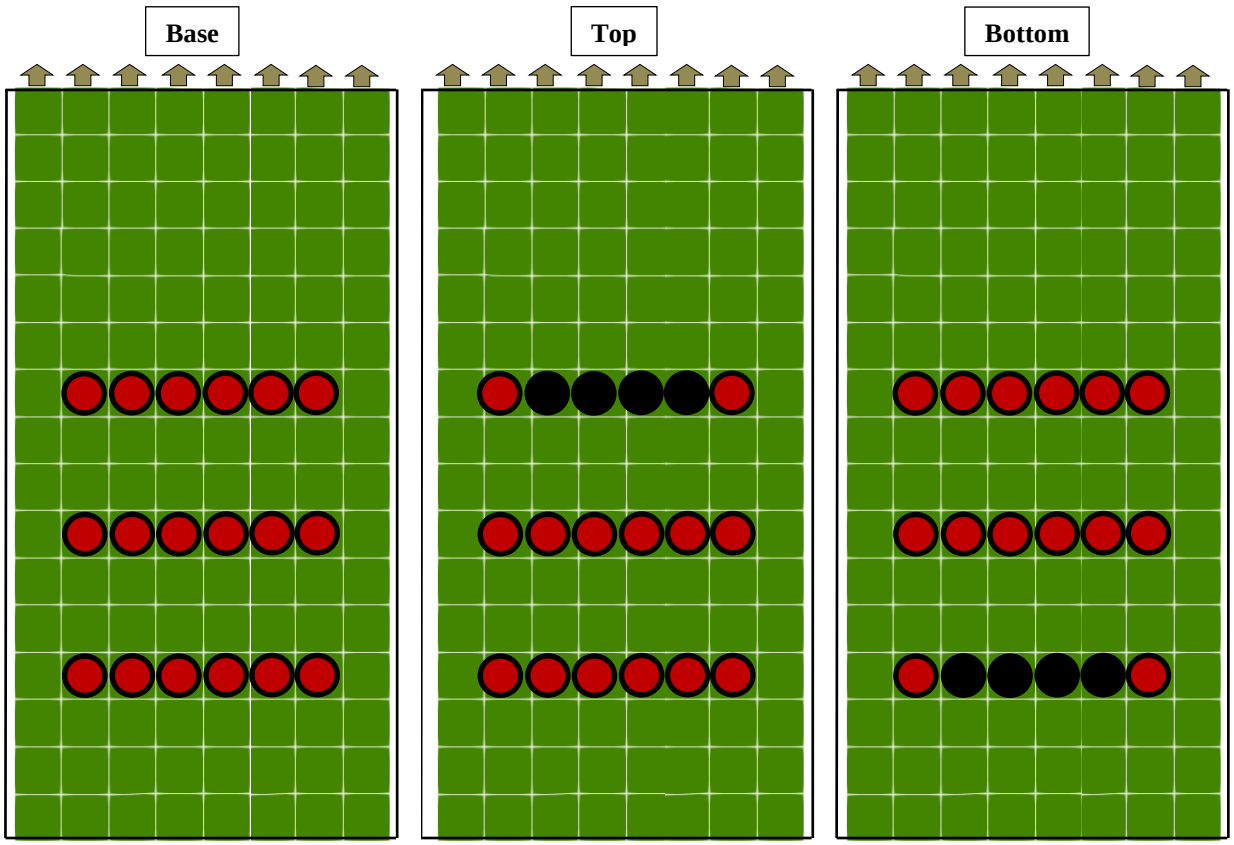

Figure 56 - View of front wall indicating the burners in (red) and out (black) of operation for the different case studies.

A comparison of the change in the heat input, evaporator heat absorption and mass-averaged FEGT when the burner operating modes change is shown in Figure 57. There is a slight change (about 5 MW) in the heat input between all three sets of results. The heat transfer to the evaporator increases by 18 MW when the burners at the top are out of operation due to more energy added further down in the furnace. The residence time available for more of the particles to combust will also be more with the burner flow biasing more to the bottom. The longer residence times also increases the combustion efficiency (increase in carbon burnout by 0.022 m% and oxygen consumption by 0.016 v%) which the results in Figure 58 confirm. The mass-averaged FEGT decreases by 15 K due to the increase in evaporator heat absorption.

When the burners at the bottom are out of operation the results are opposite to the top burners out of operation, i.e the evaporator heat transfer decreases by 14 MW and mass-averaged FEGT increases by 12 K. A slight decrease in the combustion efficiency is also noticed, but only by 0.001 m% less carbon burnout.

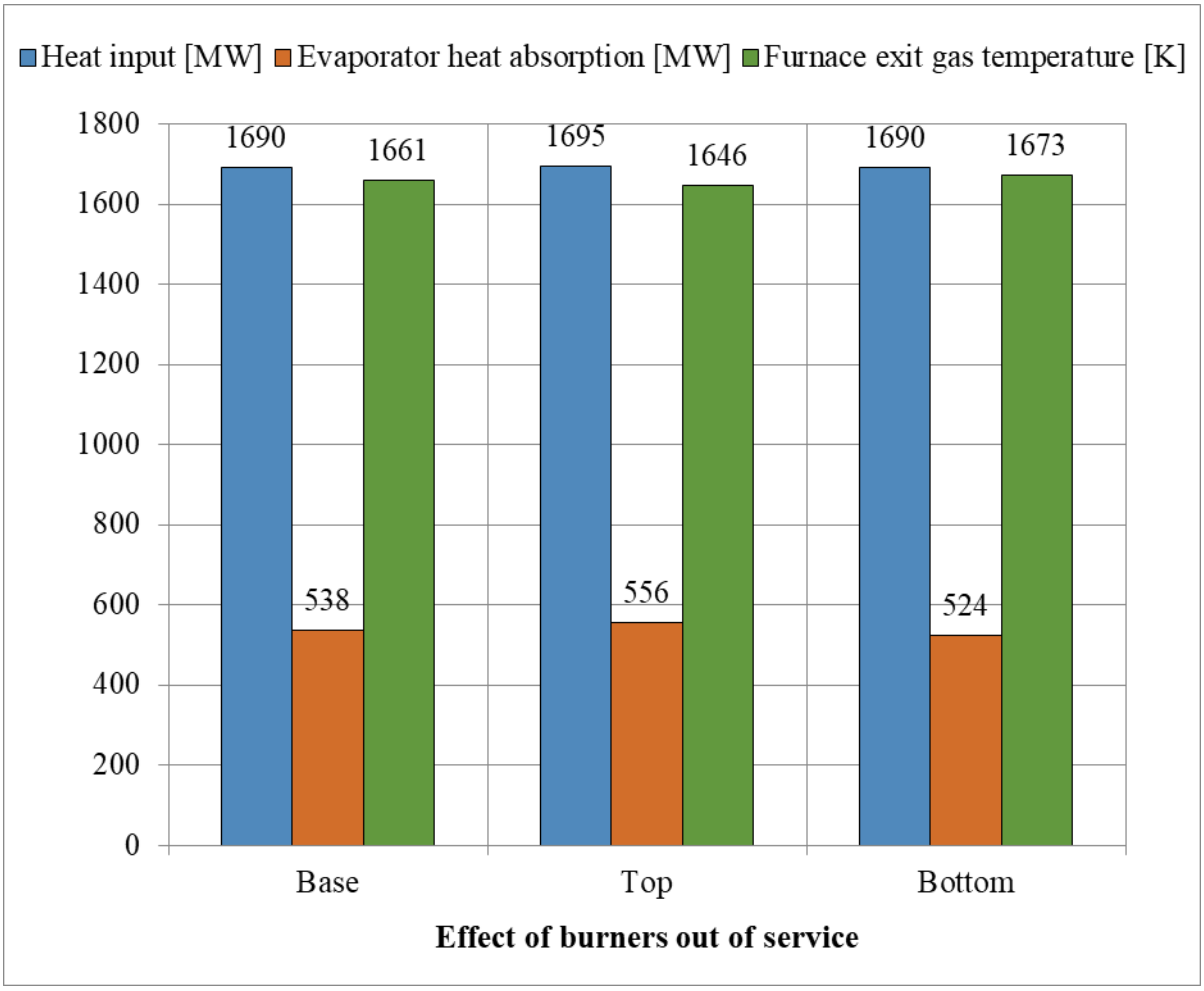

Figure 57 - Comparison of the predicted heat input, evaporator heat absorption and furnace exit gas temperature change when four burners in the top row are not in operation while keeping the total mass flow rate constant.

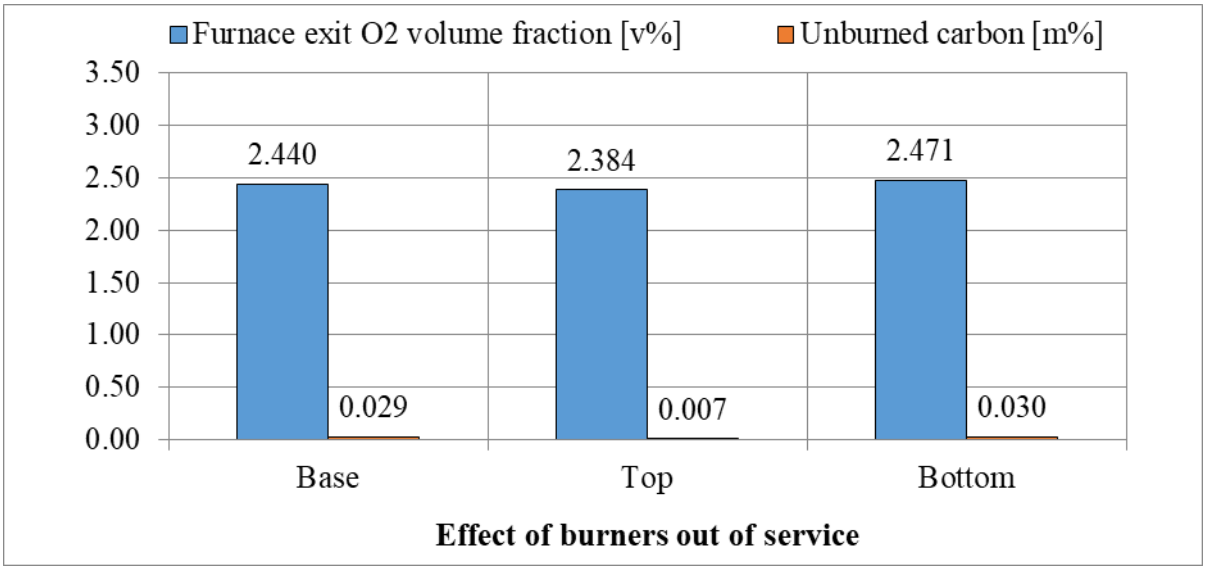

Figure 58 - Comparison of the predicted oxygen concentration and unburned carbon change when four burners in the top row are not in operation while keeping the total mass flow rate constant.

The temperature profiles at the furnace exit are shown in Figure 59. When comparing the case with burners out of operation at the top of the front wall to the case with the bottom burners out of operation, then the temperature distribution with burners out of operation at the bottom has a temperature profile with higher temperatures below the platen superheaters. The case with the burners at the top out of operation has the highest heat absorption to the evaporator and lower temperatures at the furnace exit. For this case, the performance at the platen superheater will decrease or will require less attemperation flow due to the lower gas temperatures.

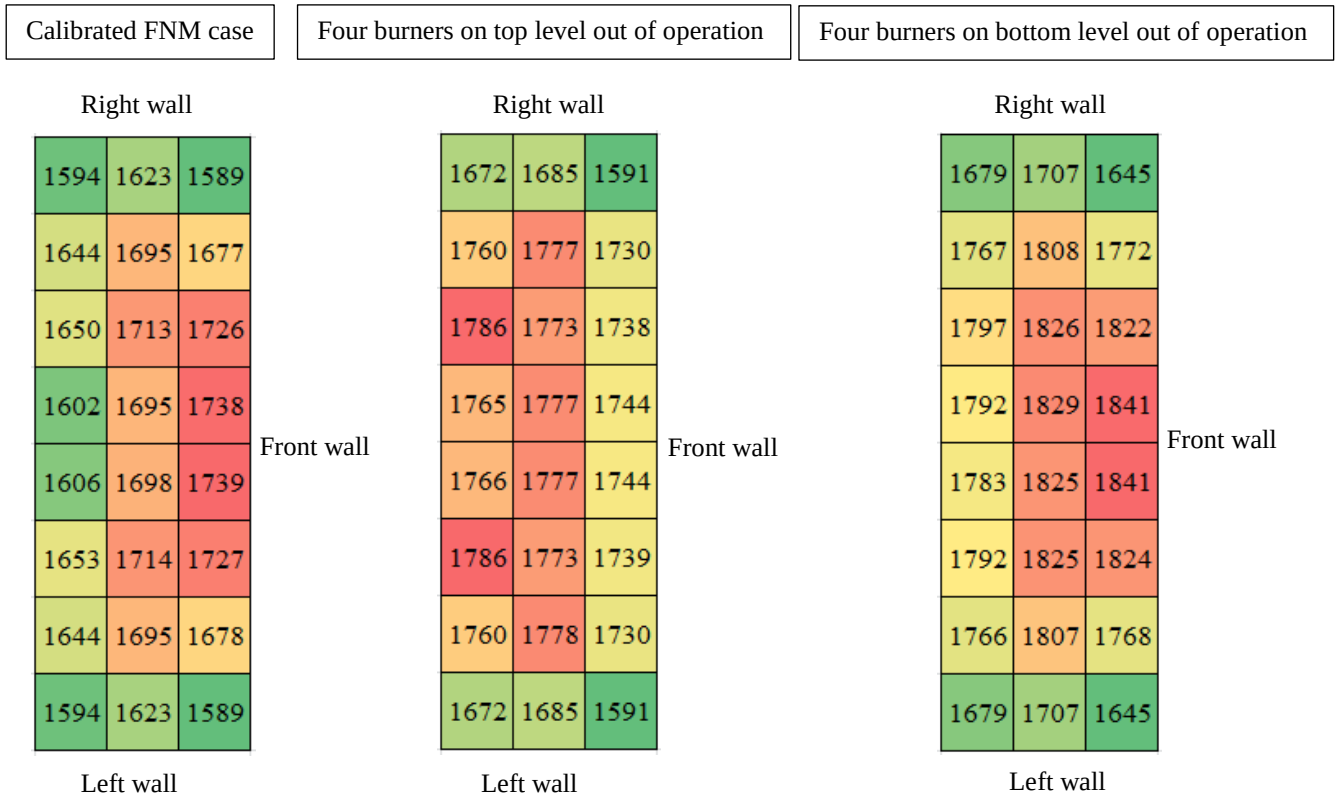

Figure 59 - Comparison of the two-dimensional furnace exit gas temperature profiles when four of the top or bottom level burners are out of operation but the total mass flow remains constant.

The opposite is true for the case with the burners at the bottom out of operation, i.e. the evaporator heat absorption decreases and temperatures at the furnace exit increases. The increase in higher temperatures at the furnace exit will either increase the platen super heater performance or require more attemperation flow. This scenario is a negative for plant operation due to the tubes exposed to significantly higher temperatures, which in turn has a negative impact on the lifetime of the superheater tubes. Therefore, the probability of an earlier boiler tube leak increases, with a subsequent negative impact on the plant reliability and decreasing the plant availability.

This case study demonstrates the suitability of the FNM for a change in the operating modes when certain burners are unavailable. Small changes are noticed in the combustion efficiency, but other changes are larger. Larger changes are noticed for the heat transfer to the evaporator and mass-averaged FEGT. The most significant changes are to the temperature distribution on the plane of the furnace exit. Tools such as the FNM can be utilised to experiment with different burner operating modes such as burner mass flow biasing to re-distribute the temperature distribution and investigate the effect on combustion efficiencies and plant reliability.

5.3 Furnace wall fouling

The goal of this case study is to demonstrate whether the calibrated FNM case (see validated model in section 4.2.6 to 4.2.8) provides consistent predictions when the fouling is increased, inhibiting the heat transfer between the gas in the furnace and the fluid in the tubes.

It should be noted that the Gurvich method also includes a method to account for the fouling on the water wall (Zhang, Li & Zhou, 2016:93-95,182,236,311). Therefore, the Gurvich method can also be used to study the change in FEGT due to fouling on the evaporator. However, the approach differs from this section which makes direct comparison not feasible.

The coal and air mass flow rates were kept constant for all the cases. The coal quality and calibration multipliers also remained the same. It was assumed that the fouling did not change the emissivity characteristics on the furnace wall. A fouling factor was incorporated as part of the network of heat transfer resistances between the water wall surface and the fluid inside the tubes by means of the formulas presented in section 3.7. The tube conductivity and convection heat transfer coefficients are in Table 16 of section 4.2.7. The values of the fouling factors are shown in Table 20.

Table 20 - The fouling factors for the different cases.

Case	Fouling factor [m^2K/W]
Case 5.3.1	0.0000
Case 5.3.2	0.0001
Case 5.3.3	0.0002

A comparison of the predicted change of the heat input, evaporator heat absorption and mass-averaged FEGT when the fouling factor increases is shown in Figure 60. A decrease in the heat transfer to the evaporator walls are noticed when the fouling increases. For case 5.3.2 it is 11 MW less when compared to case 5.3.1. Case 5.3.3 is even more at 24 MW less when compared to case

5.3.1. This translates in higher mass-averaged FEGT when the fouling increases, i.e. 13 K to 29 K more when the fouling is increased.

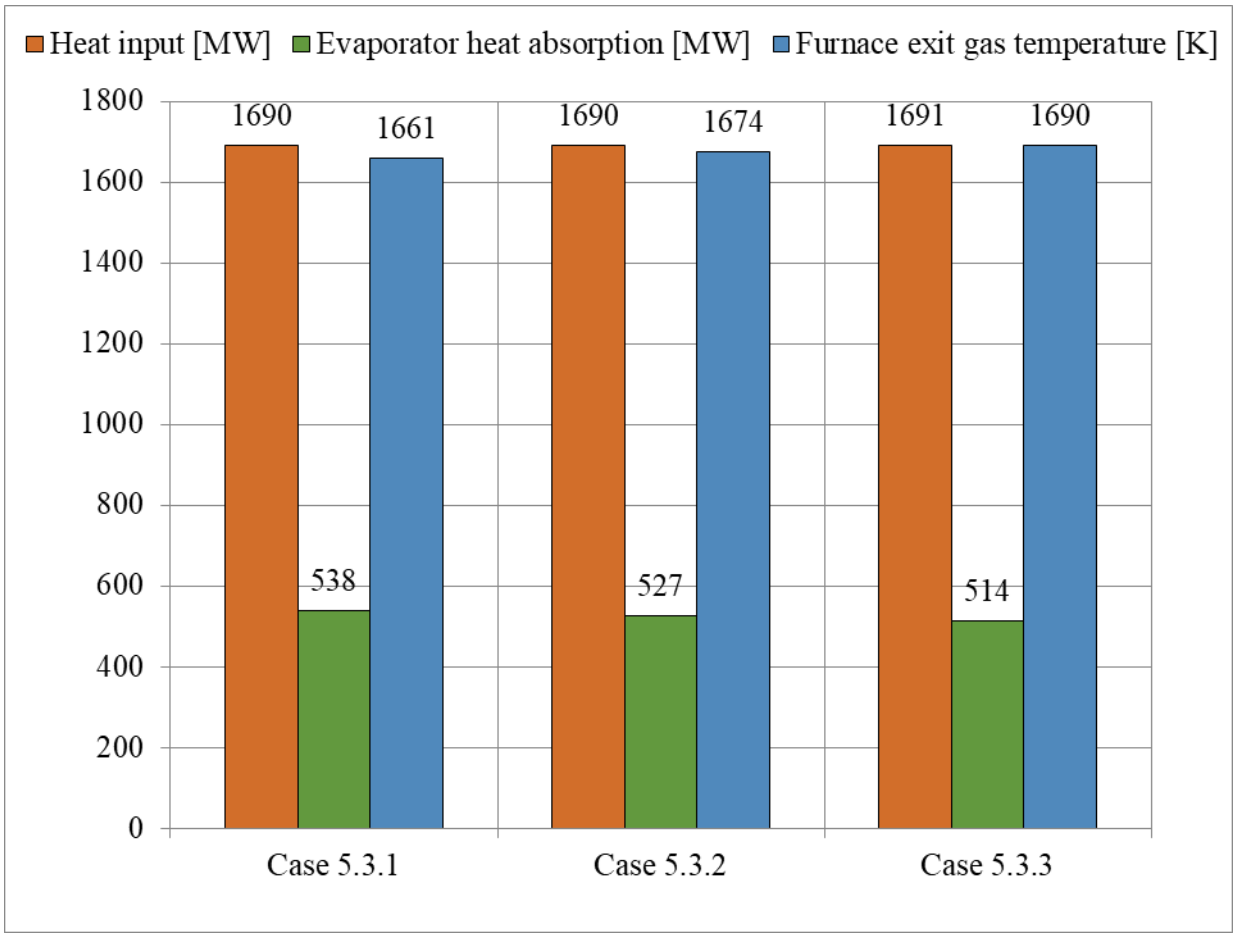

Figure 60 - Comparison of the predicted heat input, evaporator heat absorption and furnace exit gas temperature change for the three different furnace wall fouling cases.

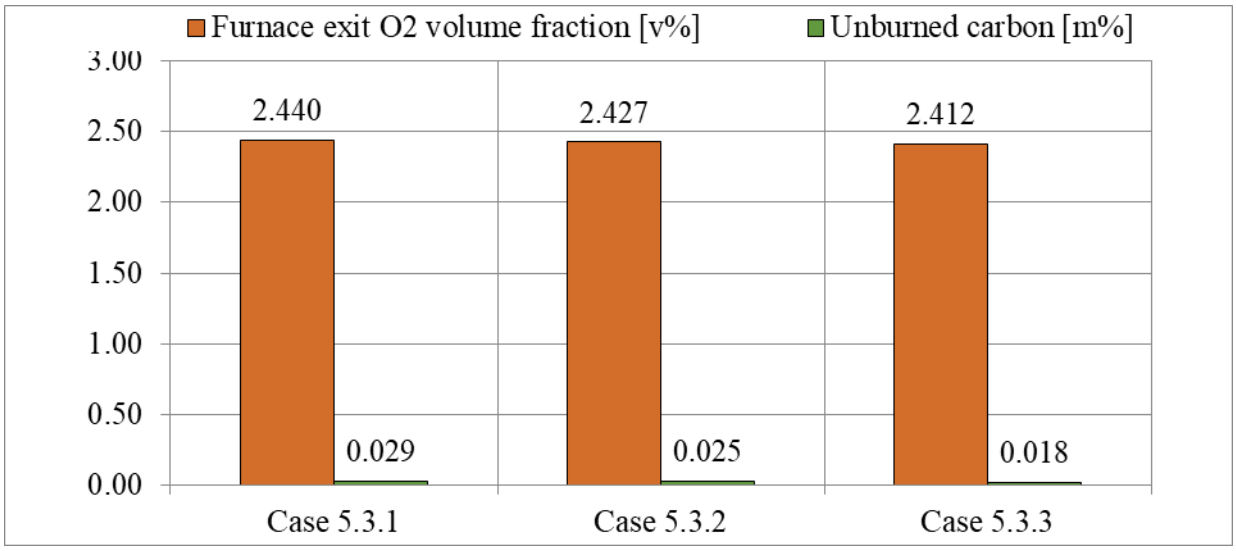

Figure 61 - Comparison of the predicted oxygen concentration and unburned carbon change for the three different furnace wall fouling cases.

The unburned carbon at the furnace outlet decrease slightly by 0.004 m% and 0.011 m% when the fouling increases as shown in Figure 60. This correlates with a slight increase in the oxygen consumption (up to 0.028 v%). The increase in carbon burnout is most probably due to the increase in furnace gas temperatures due the fouling in the wall decreasing the heat transfer to the evaporator. There is an indication of a slight increase in the heat input shown in Figure 60 due to the increase in carbon burnout, but the change is almost unnoticeable.

This case study therefore shows the usefulness of the FNM when applied to fouling case studies. The fouling increased the resistance of heat transfer to the fluid in the tubes. The major changes were seen in an increase in the mass-averaged FEGT and decrease in the heat transfer to the evaporator walls. An increase in the mass-averaged FEGT will have a negative impact on the plant reliability due to the increase in probability of boiler tube failure.

5.4 Coal quality sensitivity

The goal of this case study is to demonstrate whether the calibrated FNM case of the multiple-burner furnace provides appropriate results for variations in coal quality. This will be done by applying the operating conditions of a furnace using the currently fired coal and changing to a higher coal quality (which will be the design coal quality) as documented in Rousseau and Laubscher (2019).

The calibrated FNM as validated in section 4.2.6 to 4.2.8 was used as a baseline for this case study. Therefore, the calibrated absorption and surface reaction rate coefficients were used. The specification of the coal qualities and flow rates are shown in Table 21. The coal and air mass flow for the actual coal case used by Rousseau and Laubscher (2019) is slightly higher than the flow rates from Laubscher and Rousseau (2019a) used for the validation. A new isothermal mass flow simulation was performed with the slightly higher mass flow rates and the mass flow map imported for the actual coal case. The same was performed for the design coal case with lower mass flow rates.

A comparison of the predicted change of the heat input, evaporator heat absorption, average FEGT as well as the oxygen concentration and burnout at the outlet for the actual and design coal quality are shown in Table 22. The CFD results are from Rousseau and Laubscher (2019), with the unburned carbon and oxygen concentration at the furnace exit not published. The heat input, evaporator heat absorption and FEGT compare well between the predicted results of the calibrated FNM model and the CFD results for the actual coal with the maximum difference of -1.1%. The

FEGT prediction using the Gurvich method was also included (see Figure 112 for calculated results) assuming 0.029 m% unburned carbon at the furnace exit to correspond with the unburned carbon reported in the CFD results of Laubscher and Rousseau (2019a).

Table 21 - The specification of the coal qualities (as received) and mass flow rates for the coal sensitivity study.

	Property	FNM (calibrated at actual coal)	FNM (calibrated at design coal)
Ultimate analysis	Carbon	0.4156	0.4395
	Hydrogen	0.0222	0.0250
	Oxygen	0.0790	0.0962
	Nitrogen	0.0097	0.0110
	Sulphur	0.0094	0.0100
	Moisture	0.0550	0.1050
	Ash	0.4090	0.3133
	Other	0.0001	0.0001
Proximate analysis	Volatiles	0.1960	0.1942
	Fixed carbon	0.3400	0.3875
	Gross calorific value	15070	16410
Mass flow rates	Coal flow rate [kg/s]	117.2	107.3
	Combustion air flow rate [kg/s]	723.4	700.6

When the coal quality as well as the coal and air mass flow rates for the design coal case are imposed, the calibrated FNM predictions deviate when compared to the CFD results. The heat input and evaporator heat absorption are significantly under-predicted when using the calibrated FNM. The difference for the evaporator heat absorption is worst at 15.2% less and then followed by the heat input which is 3.6% less. The calculated unburned carbon in the calibrated FNM increases significantly from 0.018 m% to 0.502 m% when switching from actual to design coal. It is important to note that the coefficients for the surface reaction rate and calibration factor were kept the same with change of the coal quality. The correct burnout calculation of the fixed carbon with the model as implemented is strongly dependent on the correct coefficients provided to the Arrhenius equations. Due to the change in coal quality, these coefficients are expected to change and therefore cannot be kept constant. With this in mind, only the factor to modify the surface reaction rate was re-calibrated. The calibration factor for the absorption coefficients was kept constant. When the calibration factor for the surface reaction rate is increased by 74%, the unburned carbon matches the amount of unburned carbon (0.018 m%) originally predicted by the calibrated FNM using actual coal. After the re-calibration, the predicted results show good comparison

between the recalibrated FNM and the CFD results (Table 22, design coal). All the comparisons are within a 1.6% difference.

The Gurvich method was also used to calculate the FEGT when changing from actual coal to the design coal (see Figure 113 for the calculations). The combustion efficiency had to be assumed and was kept constant at 0.029 m%. The method predicts an increase in FEGT when changing from actual coal to design. This corresponds with both the CFD and FNM prediction of an increase in FEGT when the coal quality increases.

Table 22 - Predicted change in the heat input, evaporator heat absorption and FEGT at the furnace exit with a change in the coal quality.

	Actual coal						
Parameter	**Unit**	**CFD**	**FNM (calibrated at actual coal)**	**Gurvich**	**Difference**		
Heat input	MW	1766	1765		-0.1%		
Evaporator heat absorption	MW	538.7	542.7		0.7%		
Furnace exit gas temperature	K	1689	1670	1591	-1.1%		
	Design coal						
Parameter	**Unit**	**CFD**	**FNM (calibrated at higher coal quality)**	**Gurvich**	**Difference**	**FNM (re-calibrated at higher coal quality)**	**Difference**
Heat input	MW	1761	1698		-3.6%	1765	0.3%
Evaporator heat absorption	MW	560.0	474.8		-15.2%	560.2	0.0%
Furnace exit gas temperature	K	1697	1696	1636	-0.1%	1669	-1.6%

** Difference compared to CFD results.*

This case study shows that the FNM can be used for simulations with changes in coal quality. However, the surface reaction rate coefficient for the different coal qualities needs to be known. No recalibration of the absorption coefficients was necessary. Other combustion models should be investigated to test whether it is less dependent on the user to provide the correct coefficients applicable to each coal quality. This will minimise the number of inputs that needs to be modified every time the coal quality changes. To summarise, no modification of the absorption coeffcients will be necessary, but the user will be required to provide the correct surface reaction rate coefficients when using the FNM during coal switching studies.

5.5 Normalised mass flow map

During the validation of the multiple-burner furnace (see section 4.2.6 to 4.2.8), the calibrated FNM case was compared to a 60.5%, 81% and 99% load case with each load having a uniquely created mass flow map from isothermal CFD simulations. The goal of this case study is to test whether the calibration of the FNM can be done at a single load and the mass flow map at the same load normalised. The normalised mass flow map will be multiplied with the load factor to obtain the scalar quantity of the mass flow between each neighbouring zone.

For this case study, the reference point was the 99% operating condition. The fluid temperature and platen superheater temperature were fixed at 620 K and 698 K for all load conditions. The mass flow map provides the scalar quantity of mass flow rate together with the "From zone" and the "To zone" entries as illustrated in Figure 20. It was assumed that a linear relationship exists between the scalar mass flow rate values. Therefore, the mass flow rate values in the 99% load mass flow map were divided with 99. Hence, if the scalar mass flow quantities are required at another operating condition, these values are multiplied with the load setpoint. As an example, for an 81% load operating condition the multiplier to each scalar mass flow value is 81.

The ratio of change between the coal flow rate and air flow rate at the burners are not constant between the 60.5% and 99% load condition. Based on the coal and air mass flow rates shown in Table 16, the following relationships fit the different flow rates based on the load setpoint (SP_{load}):

$$\dot{m}_c = 0.0374983 SP_{load} - 0.617 \tag{29}$$

$$\dot{m}_{PA} = 0.25(0.223535 SP_{load} - \dot{m}_c) \tag{30}$$

$$\dot{m}_{SA} = 0.75(0.223535 SP_{load} - \dot{m}_c) \tag{31}$$

where $\dot{m}_c$ the coal mass flow rate, $\dot{m}_{PA}$ the primary air mass flow rate and $\dot{m}_{SA}$ the secondary mass flow rate.

The CFD and measured results are the same as for the validation in section 4.2.8. The predictions of the evaporator heat absorption and mass-averaged FEGT by the calibrated and normalised FNM case when compared to the calibrated FNM case, CFD and measurements are shown in Figure 62 and Figure 63. For the FEGT predictions of the Gurvich method, the unburned carbon was assumed to be 0.029 m% (from the CFD predictions shown in Figure 44). The Gurvich calculations are available in Figure 115 to Figure 117 in the appendix.

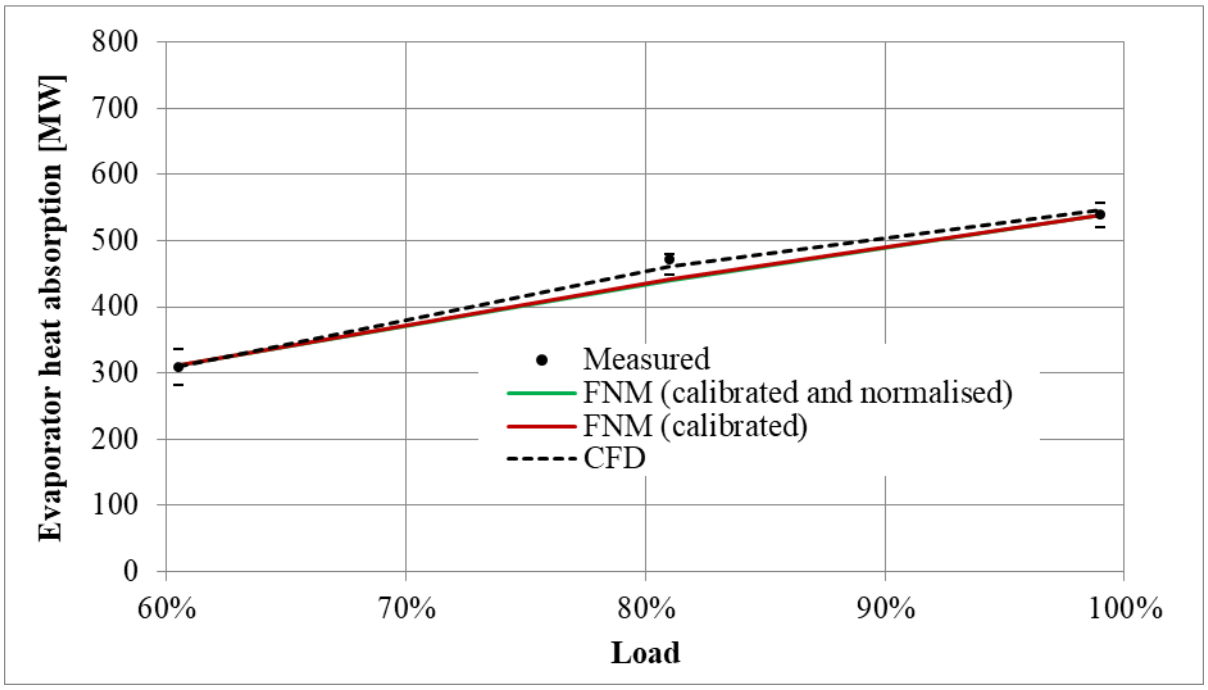

Figure 62 - Comparison of the evaporator heat absorption at various loads for the normalised mass flow map to the calibrated model as well as the measured and CFD results.

The heat absorption predicted by the calibrated and normalised FNM case closely match the benchmarks for the 60.5% and 81% load case while also remaining within the minimum and maximum range as measured. The FEGT prediction of the calibrated and normalised FNM case remained similar to the calibrated FNM.

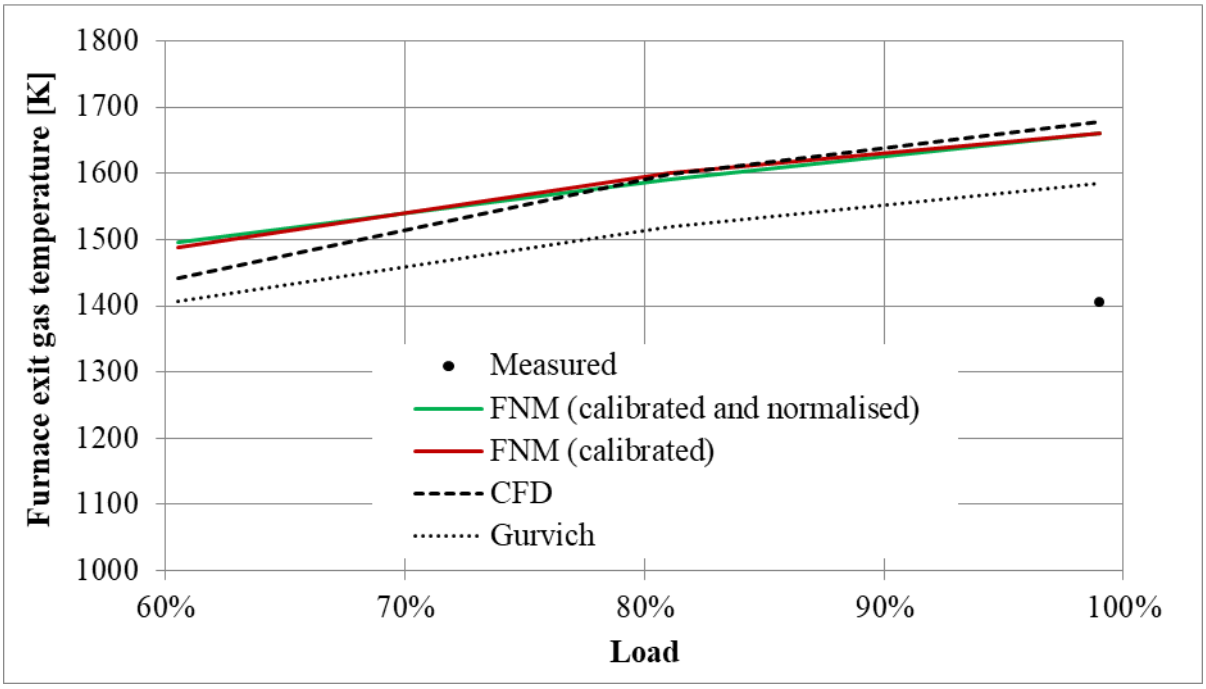

Figure 63 - Comparison of the furnace exit gas temperature at various loads for the normalised mass flow map to the calibrated model as well as the measured and CFD results.

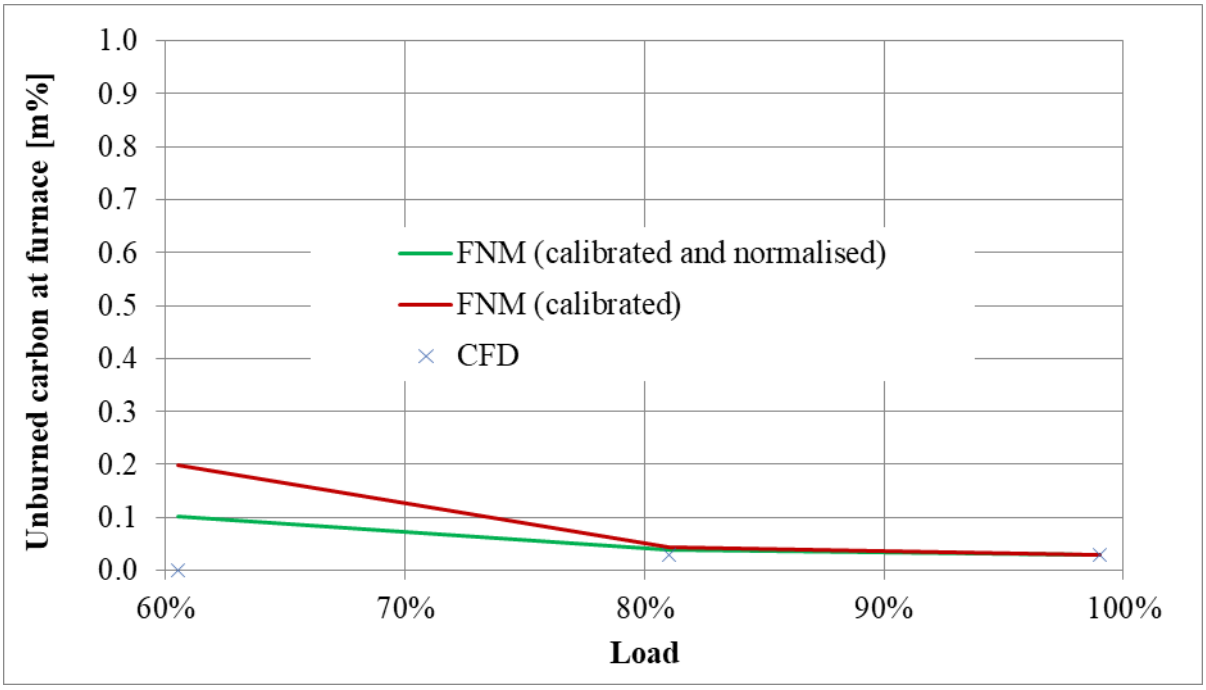

Figure 64 - Comparison of the oxygen concentration at the furnace exit at various loads for the normalised mass flow map to the calibrated model as well as the measured and CFD results.

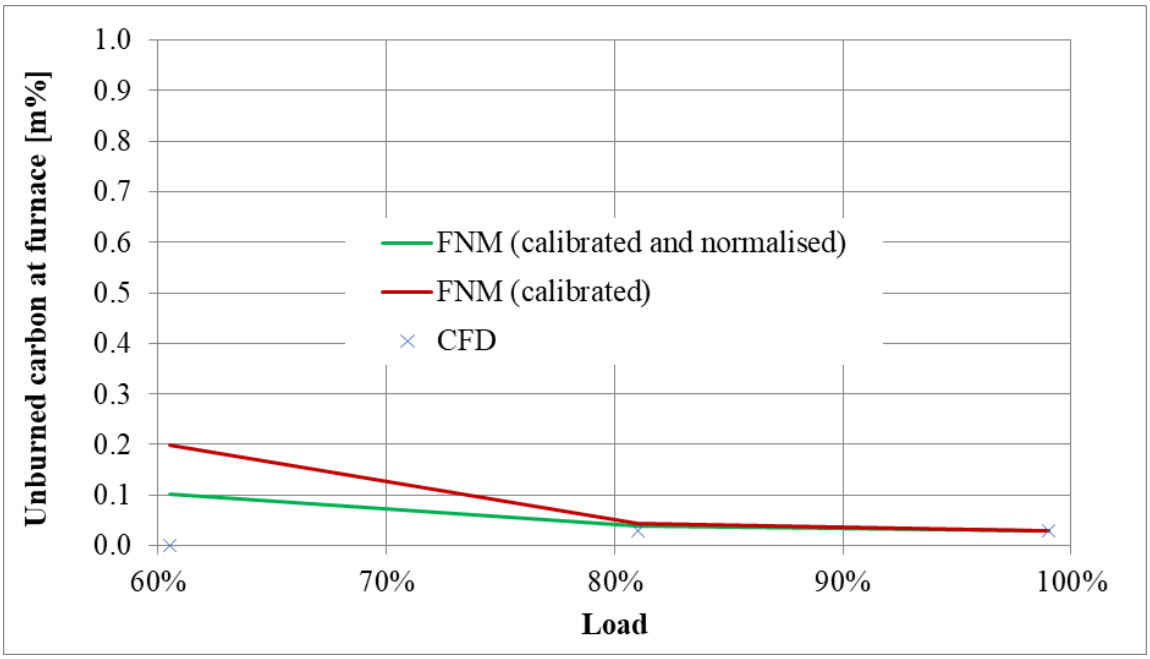

Figure 65 - Comparison of the unburned carbon at the furnace exit at various loads for the normalised mass flow map to the calibrated model and CFD results.

The prediction of the oxygen concentration and unburned carbon by the calibrated and normalised FNM case when compared to the calibrated FNM case and CFD results are shown in Figure 64 and Figure 65. The predicted values by the calibrated and normalised FNM case closely match the benchmark for the 81% load case for these parameters.

From 81% to 60.5%, the oxygen concentration and carbon burnout tend to diverge for the calibrated and normalised FNM when compared to the benchmark results. Where the calibrated FNM case is 0.17 v% more when compared to the CFD results at 60.5% load, the calibrated and normalised FNM case is 0.43 v% less. The unburned carbon prediction for the calibrated and normalised FNM is 0.2 m% more when compared to the CFD results. The difference of unburned carbon for the calibrated FNM case compared to the CFD results is 0.1 m% more.

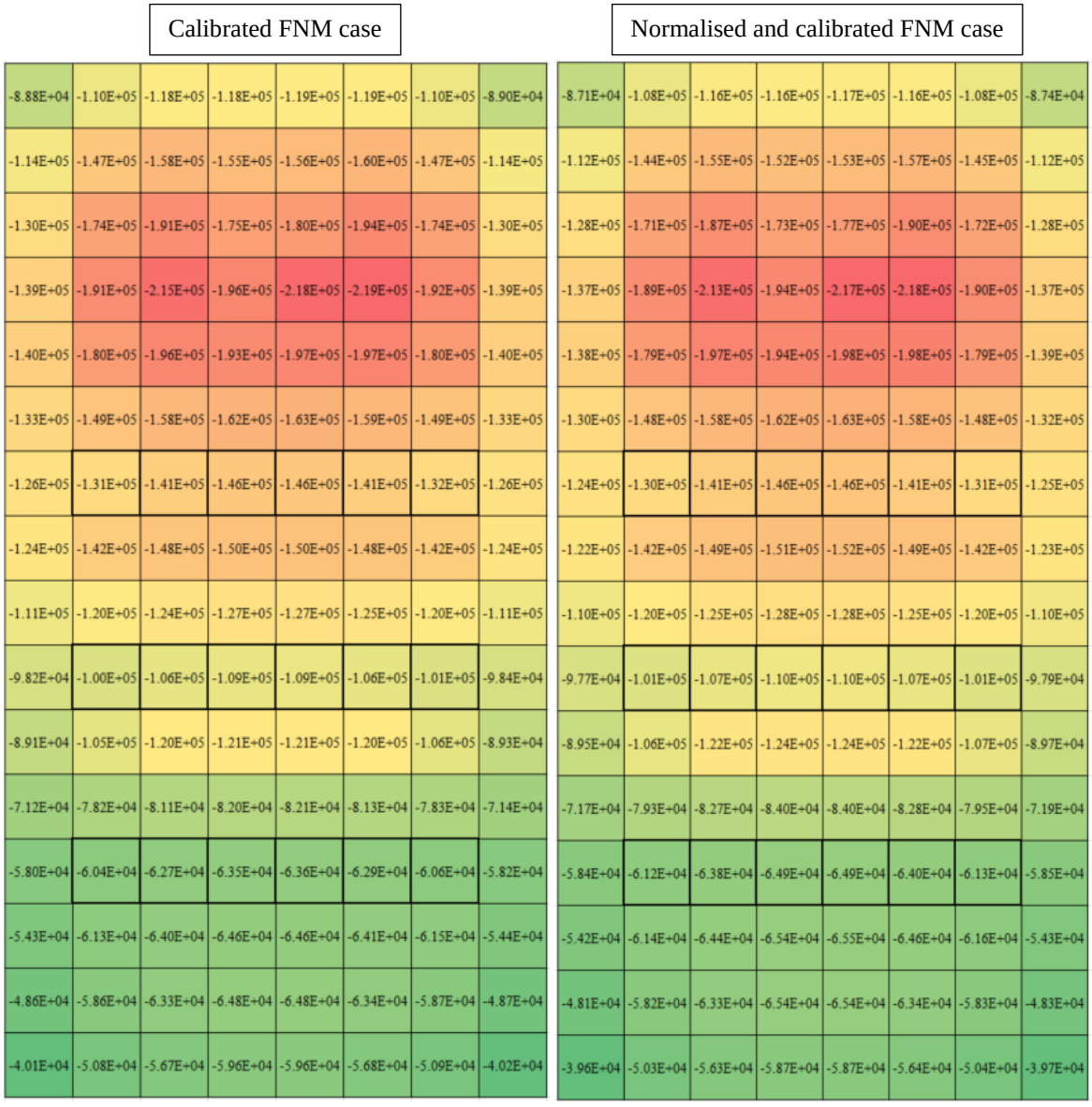

Figure 66 - The heat flux distribution (in W/m^2) to the front wall for the calibrated FNM and normalised and calibrated FNM case at 81% (the heat flux results for the FNM cases is enlarged in the appendix).

A comparison of the heat fluxes to the furnace walls between the calibrated FNM case and normalised and calibrated FNM case at 81% load is shown in Figure 66 to Figure 68. The 81% load condition is shown because the heat absorption predicted by the FNM cases had the largest

difference from the measured and CFD results at this load. Because the heat absorption between the calibrated FNM case and normalised and calibrated FNM case does not vary that much for each of the three loads, the expectation is that the heat flux will be very similar. A comparison of the heat fluxes in Figure 66 to Figure 68 confirms that the differences are insignificant with a maximum difference of 2.4%.

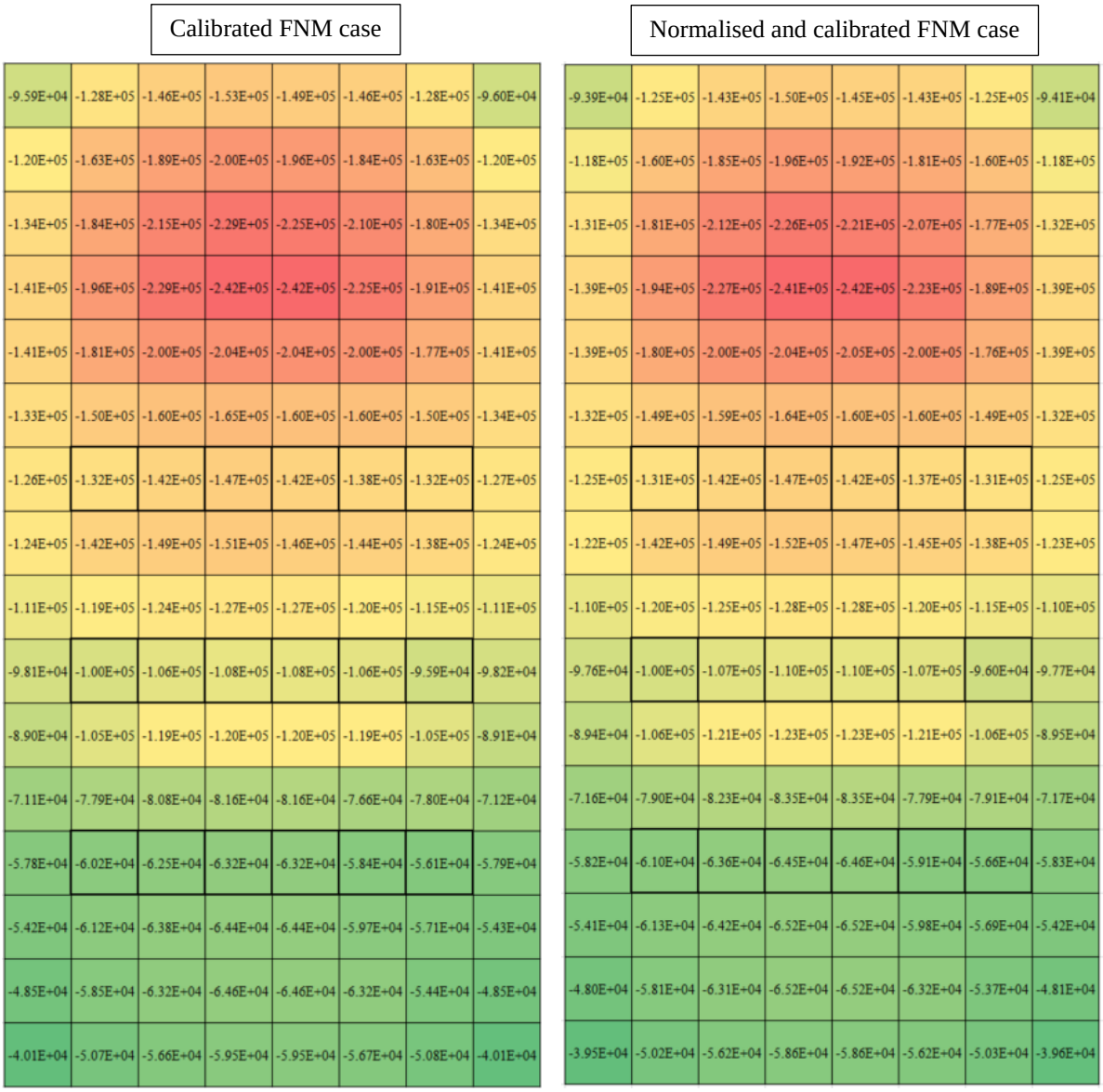

Figure 67 - The heat flux distribution (in W/m^2) to the rear wall for the calibrated FNM and normalised and calibrated FNM case at 81% (the heat flux results for the FNM cases is enlarged in the appendix).

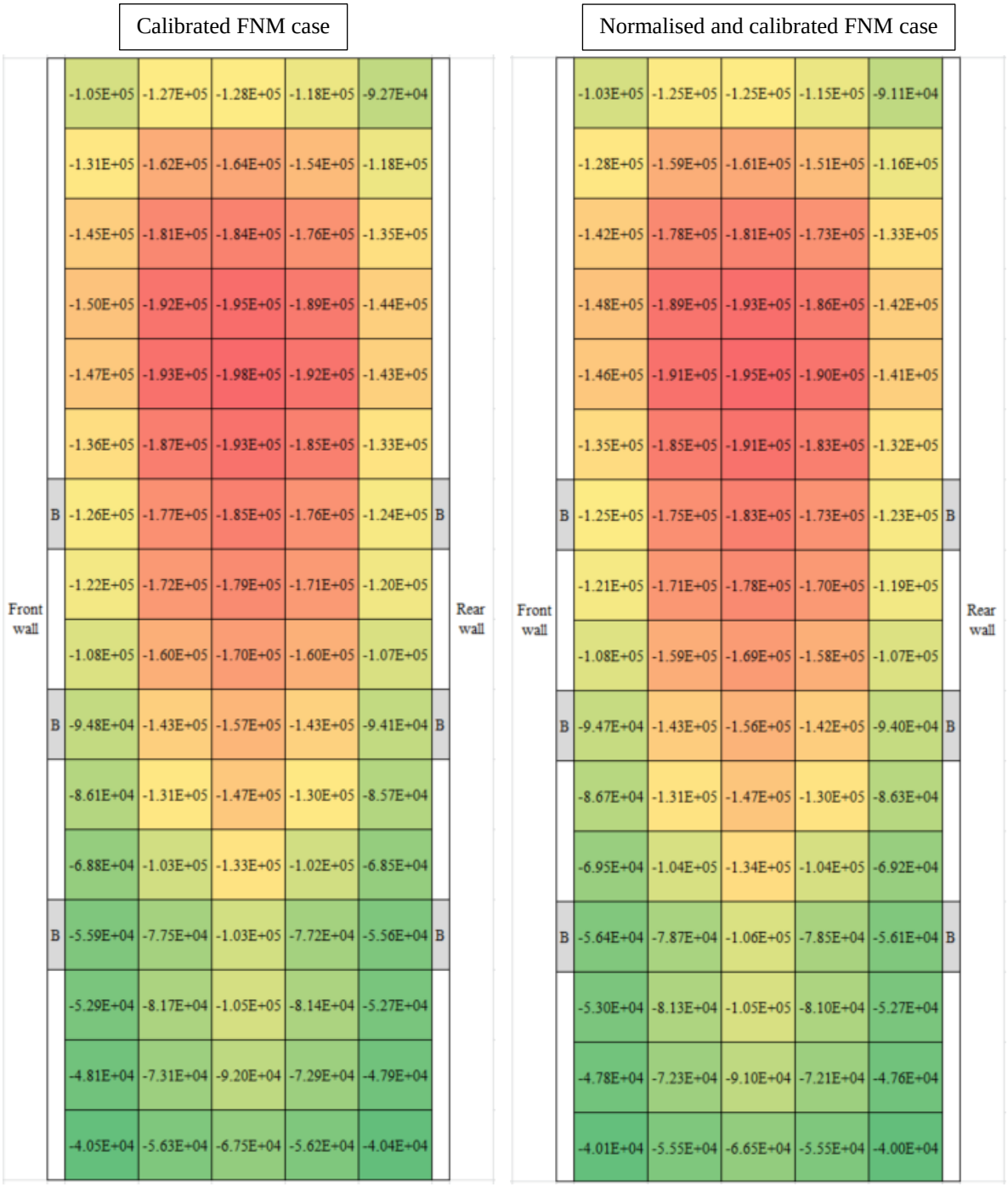

Figure 68 - The heat flux distribution (in W/m^2) to the side wall for the calibrated FNM and normalised and calibrated FNM case at 81% (the heat flux results for the FNM cases is enlarged in the appendix).

For the prediction of the evaporator heat absorption, mass-averaged FEGT, the approach of using a normalised mass flow map showed no significant loss in accuracy for the ± 40% operating range. The oxygen concentration and unburned carbon started to diverge from the benchmark results between 81% to 60.5%, but when the focus is on the heat transfer and temperatures, then the FNM remains usable.

5.6 Integrated process simulation with load change over time

At the very start of the research, the benefit of a quick-solving furnace model capable of capturing changes in the furnace while integrating with a process model to assist with multi-objective optimisations (see section 2.1) was identified. This enables the next level of interdependency studies.

A tool that provides the capability of developing a process model is Flownex® SE (version 8.10 used for this case study). The software package has a library from which a coal and air to gas as well as a water and steam cycle process model can be developed, but does not have the functionality to solve for the level of detail in a furnace of a coal-fired power station that the FNM provides. This is evident by noticing that Laubscher and Rousseau (2019c) and Rousseau and Laubscher (2019) coupled the Flownex® SE solution of the water/steam side (water wall and superheaters) with a gas side model of the boiler solved in a CFD package Ansys Fluent. In their work, the built-in application program interface (API) functionality in Flownex® SE was used to transfer data between the CFD and the process model. A similar approach can be applied to transfer the data between the FNM coded in Scilab® and Flownex® SE. A modified version of the process model in Flownex® SE provided by the above-mentioned authors is shown in Figure 69.

The Flownex® SE model includes the steam drum, downcomer and the water wall of the evaporator. The feedwater flow is a fixed mass flow at a constant temperature connected to the bottom of the steam dream. The steam flow to the superheater is connected to a pressure boundary. The valve opening position is set to remain constant for the simulations. The water wall is discretised into nine increments with coupling between the faces as shown in Figure 70. The controller changes the feedwater flow rate to maintain the drum level. The model starts from a steady-state condition of 99% load using the normalised and calibrated FNM as developed in section 5.5.

The process model calculates the natural convection circulation flow rate and heat transfer through the tube to the fluid in the water walls. The temperatures at different levels on the outside of the tubes are provided to the FNM which returns the heat transfer from the flue gas to the surface to the nodes in the Flownex® SE model. Flownex® SE is capable of modelling the two-phase flow and heat transfer inside the tube using a homogeneous two-phase fluid approach.

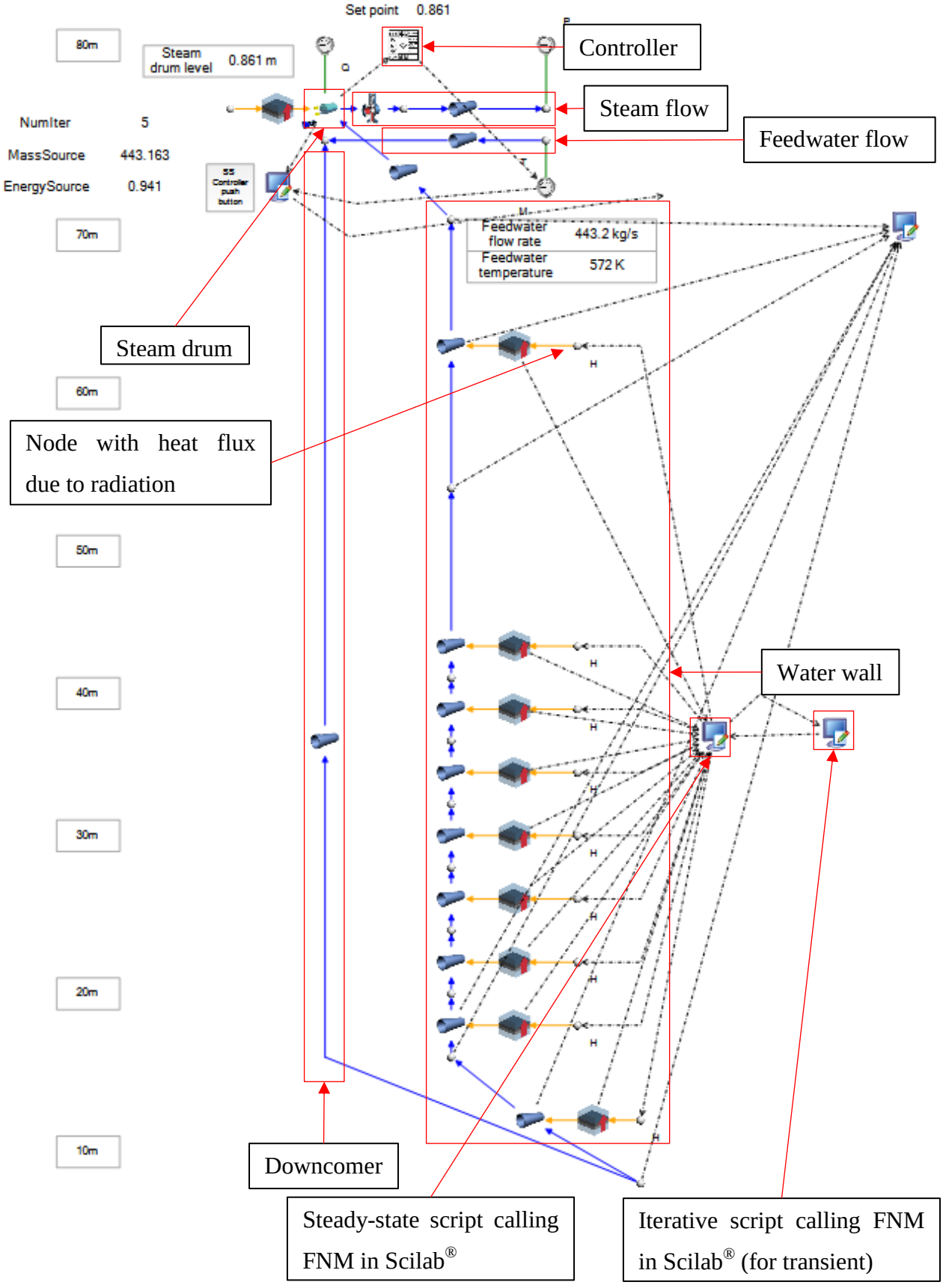

Figure 69 - The Flownex® SE model at the steady-state start condition for the co-simulation.

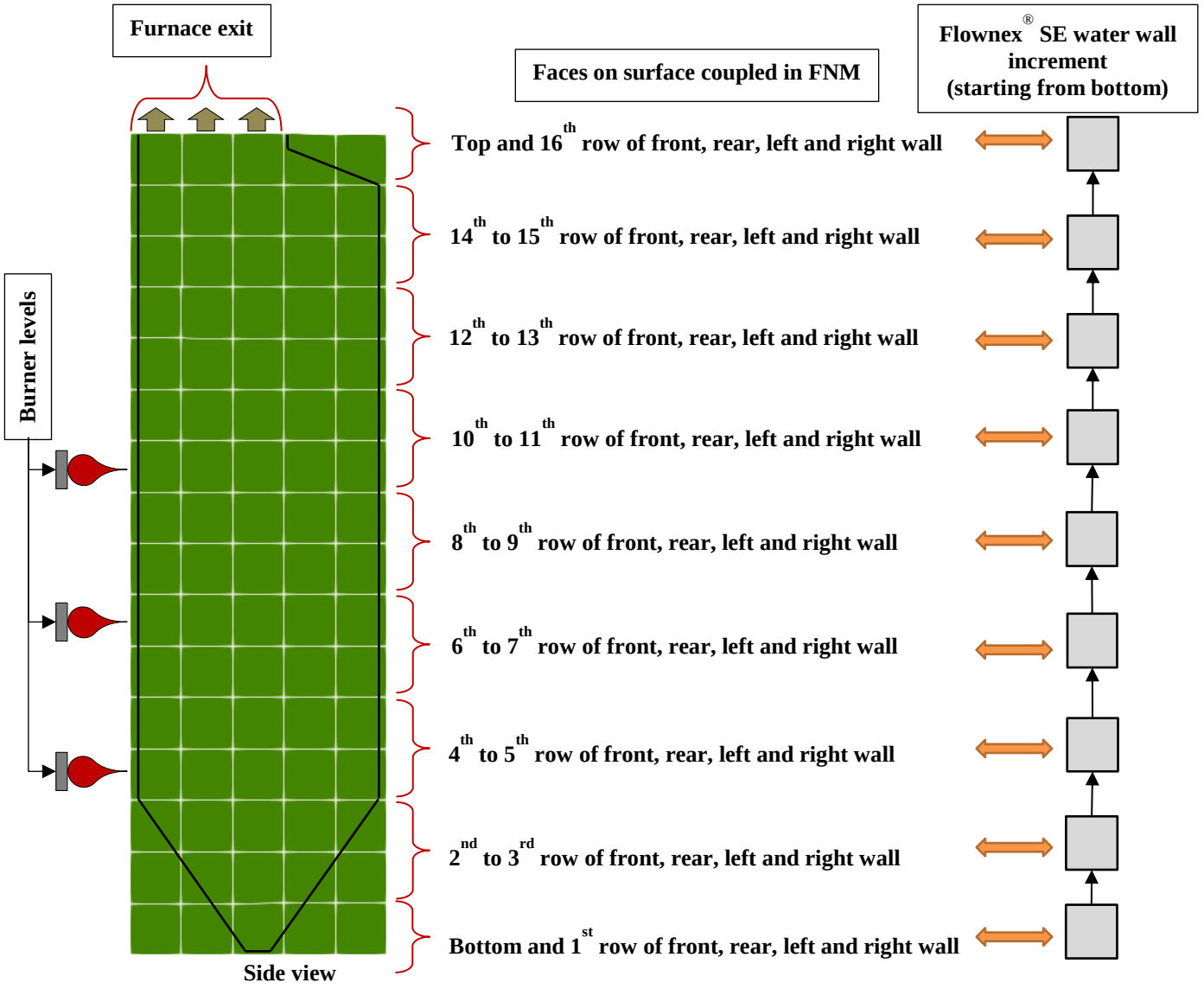

Figure 70 - The furnace face zones coupled between the FNM model and the process model in Flownex® SE.

The aim of this case study focuses on demonstrating the co-simulation behaviour and therefore the rest of the systems pertaining to the feedwater and superheater system were not included. This case study will not necessarily produce a scenario delivering results that can be evaluated whether the dynamic response is acceptable. The simulations started at 99% and decreased the load by 2% every 15 seconds. The FNM was called every instance the load changed to provide the new furnace heat fluxes to the process model. It was assumed that this is valid as long as the water wall temperatures remain fairly constant. Only a change in this temperature will have a significant effect on the radiation heat transfer calculations and requires an updated heat flux profile. Due to the fast reaction kinetics of combustion, it was assumed that the changes in the furnace heat transfer

characteristics are significantly quicker than the water/steam side. Therefore, the heat flux changes instantaneous were applied as a step change with each load drop.

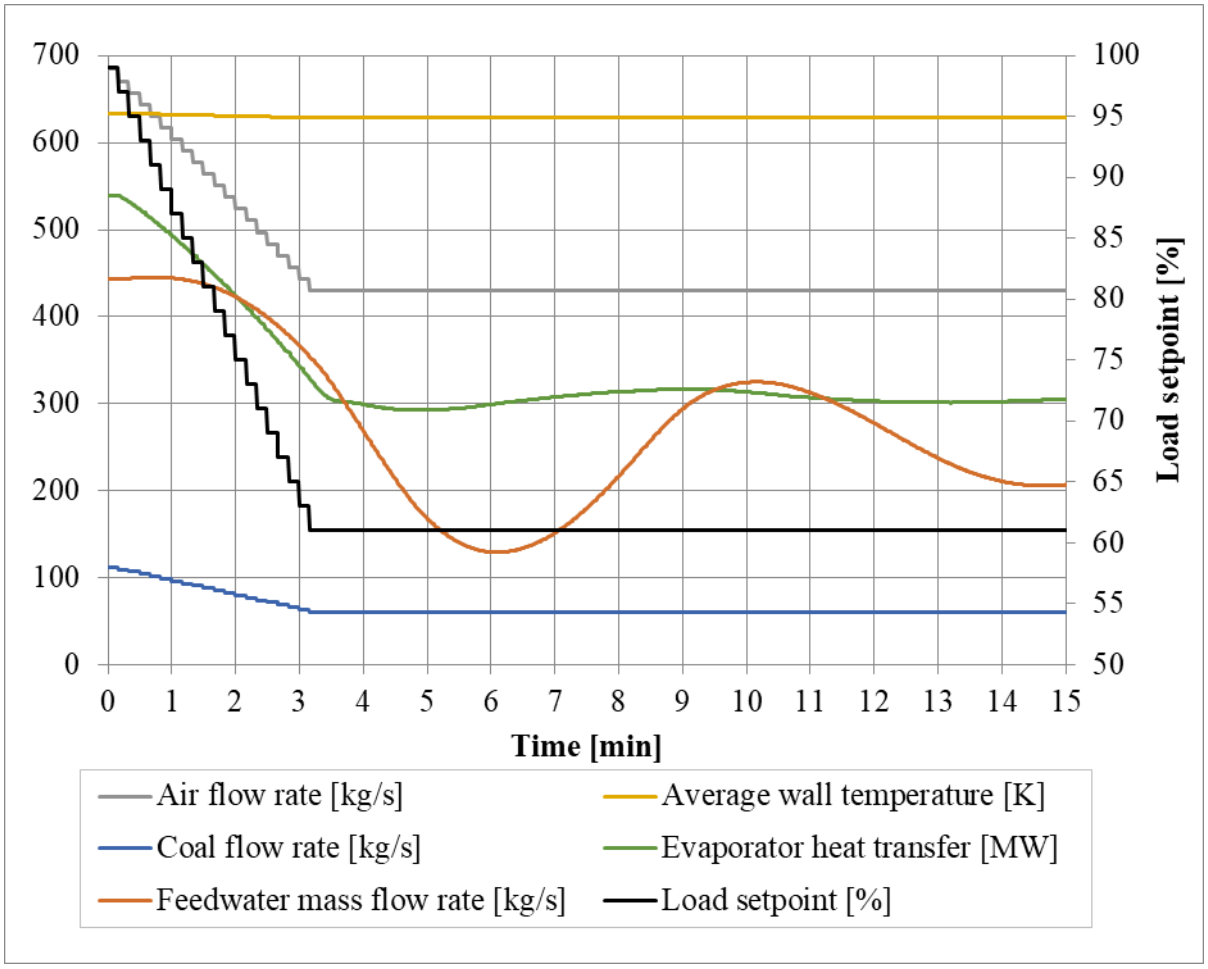

Figure 71 - Comparison of the drum level change over time while the load changes.

The predicted results for various parameters are shown in Figure 71, Figure 72 and Figure 73. In the figures, it is evident how the step changes are clearly visible for the first three minutes. With each step, the coal flow and air flow make a similar step change. The evaporator heat transfer decreases with each step and after three and a half minutes has some slight fluctuations due to the dynamic effects seen in the drum level and feedwater flow rate. For this particular simulation, the wall temperatures remain fairly constant (see Figure 71) confirming the validity of the assumption that it was not necessary to recalculate the heat flux except for the load step changes.

During the first five minutes the drum level rises due to less heat (and therefore less water evaporated to steam) added to the evaporator while the furnace load decreases (see Figure 72). The controller reduces the feedwater flow rate (see Figure 71) for the level to return to the setpoint. As soon as the load reduction stops after three minutes, the decrease in evaporator heat transfer stops

and the impact of the control is noticed. Eventually, at about 4.5 minutes the level in the tank starts to decrease. Over time the system will stabilise, returning the drum level to 0.86 m.

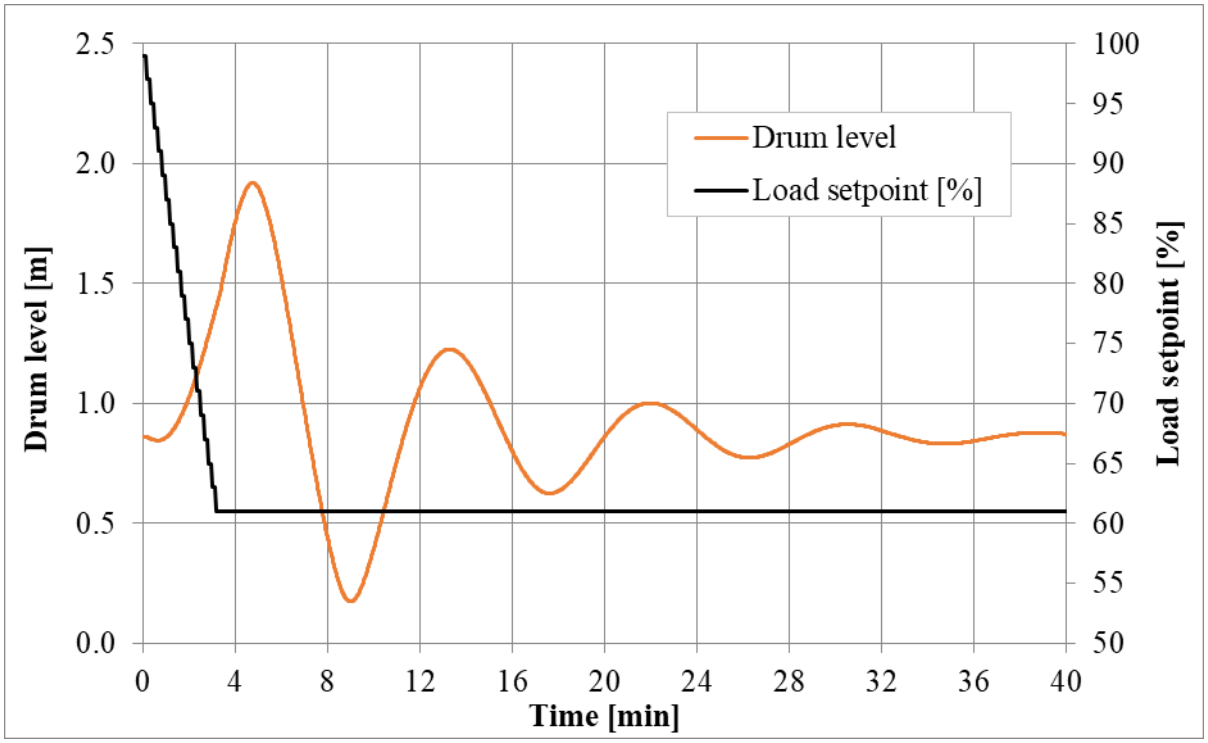

Figure 72 - Comparison of the predicted changes in drum level over time while the load changes.

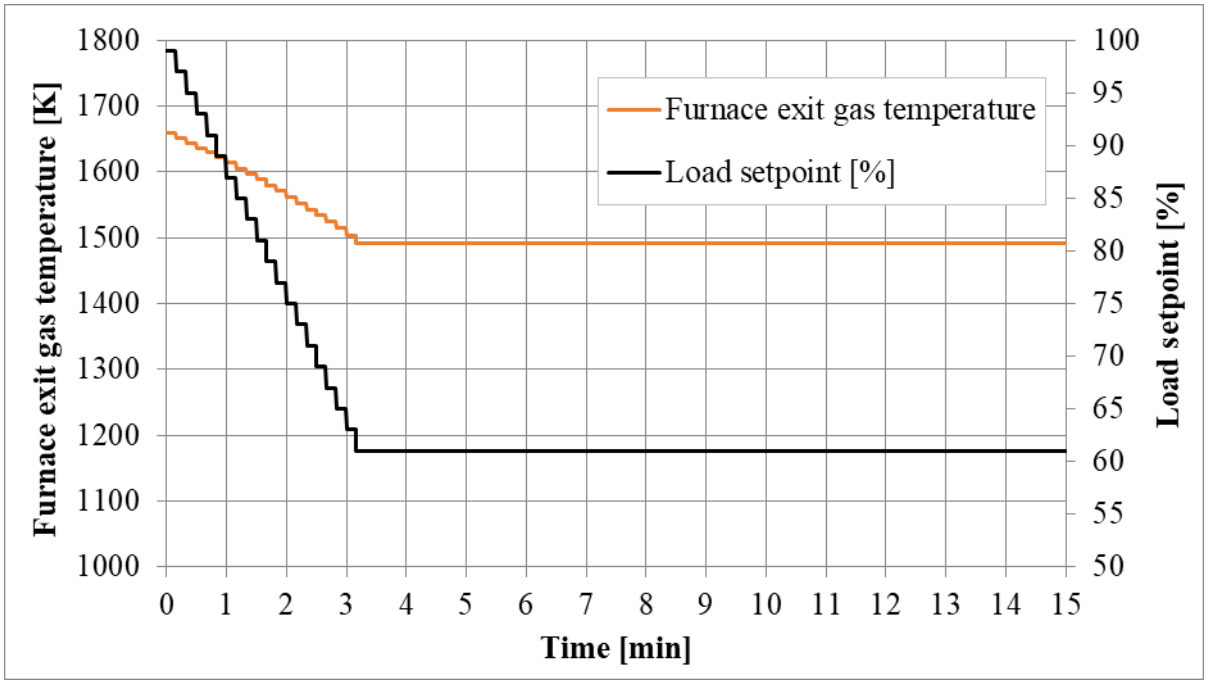

Figure 73 - Comparison of the furnace exit gas temperature change over time while the load changes.

This case study successfully showed the capability of the methodology by integrating a calibrated FNM model with a water/steam side process model in co-simulation with Flownex®. The

impact of the load change on the heat transfers, temperatures, feedwater flow rate and steam drum level was investigated on a quantitive basis. Further studies can be developed to refine the co-simulation setup and expand the process model for a multi-objective study. The following study is an example of such a co-simulation expanded to include the superheaters.

5.7 Integrating process simulation of flow and pulverized fuel distribution on superheater performance

This section continues from the previous section to demonstrate another co-simulation study of a detailed furnace model integrated with a process model to perform a multi-objective analysis. The Flownex® SE process model shown in Figure 69 was updated to include the superheaters as shown in Figure 74. The Matlab® version of the FNM code as validated in section 4.2.6 to 4.2.8 was integrated with the process model in Flownex® SE using the API functionality. Only a steady-state study was performed.

The steam flow exits from the feedwater tank to the primary superheater (superheater 1) and thereafter to the platen superheater (superheater 2) and final superheater (superheater 3). The connection between the superheater legs is shown in Figure 74 and Figure 75. The measured temperatures and flow rates from the plant are shown in Figure 75. From the measured data, the attemperation flow to the platen superheaters (SH 2A, SH 2B, SH 2C and SH 2D) is considerably higher at 38.9 kg/s than the 3.1 kg/s required at the final superheater.

The geometry and layout of the boiler remains the same as the validated multiple-burner FNM case as shown in Figure 36. The flue gases from the furnace flow to the platen superheater, the final superheater, the final reheater, the primary superheater and then the primary reheater. For each of the case studies, the combustion air flow rate was kept constant. A heat loss component (shown in Figure 74) from the water wall to the ambient conditions (4.2 W/m^2K at 25°C) was added and calibrated to match the overall mass and energy balance. A surface area of 4281 m^2 was used. The convection coefficient to the ambient conditions was calibrated until the feedwater flow equaled the measured 430.1 kg/s.

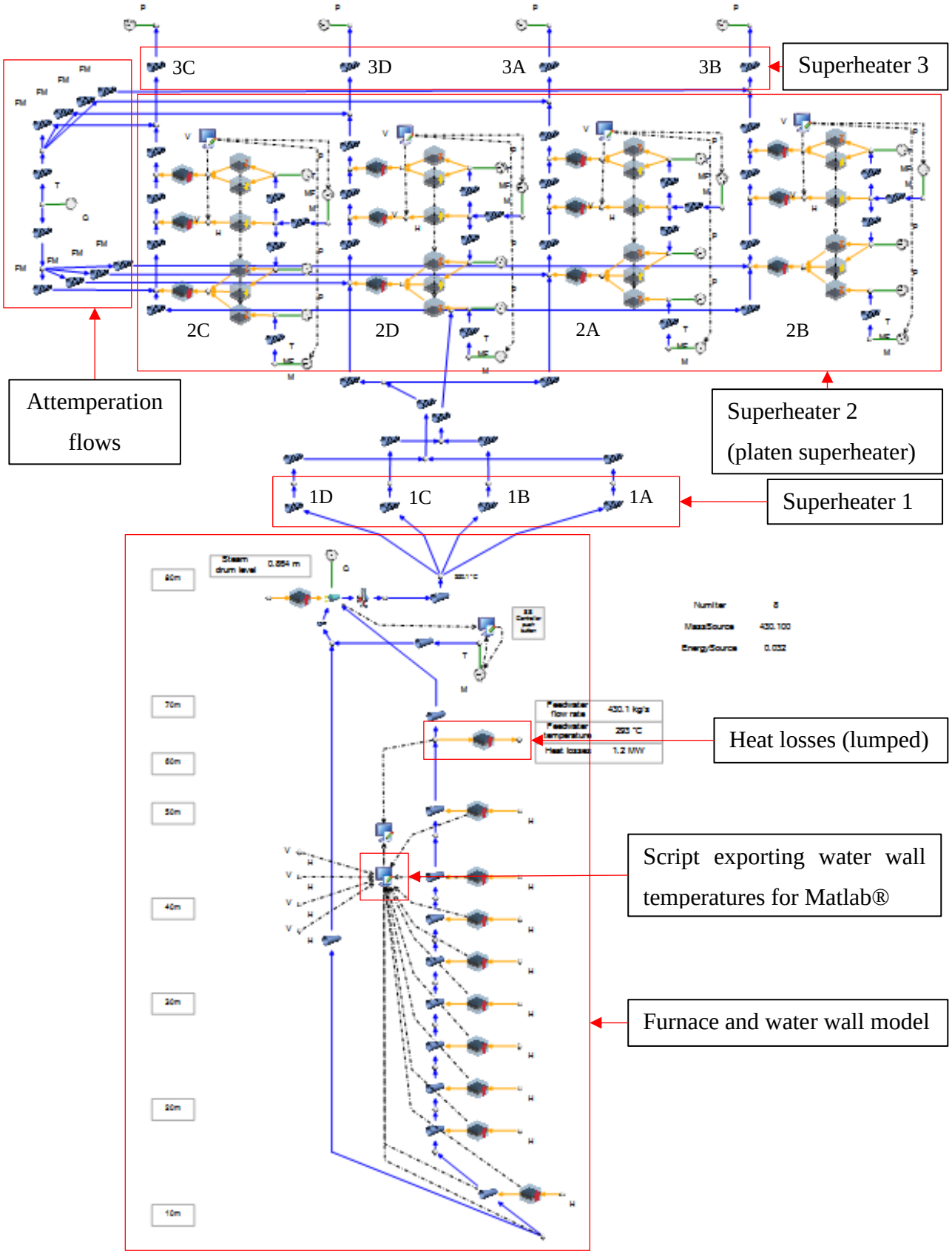

Figure 74 - The Flownex® SE process model used in a previous co-simulation updated to include the superheaters.

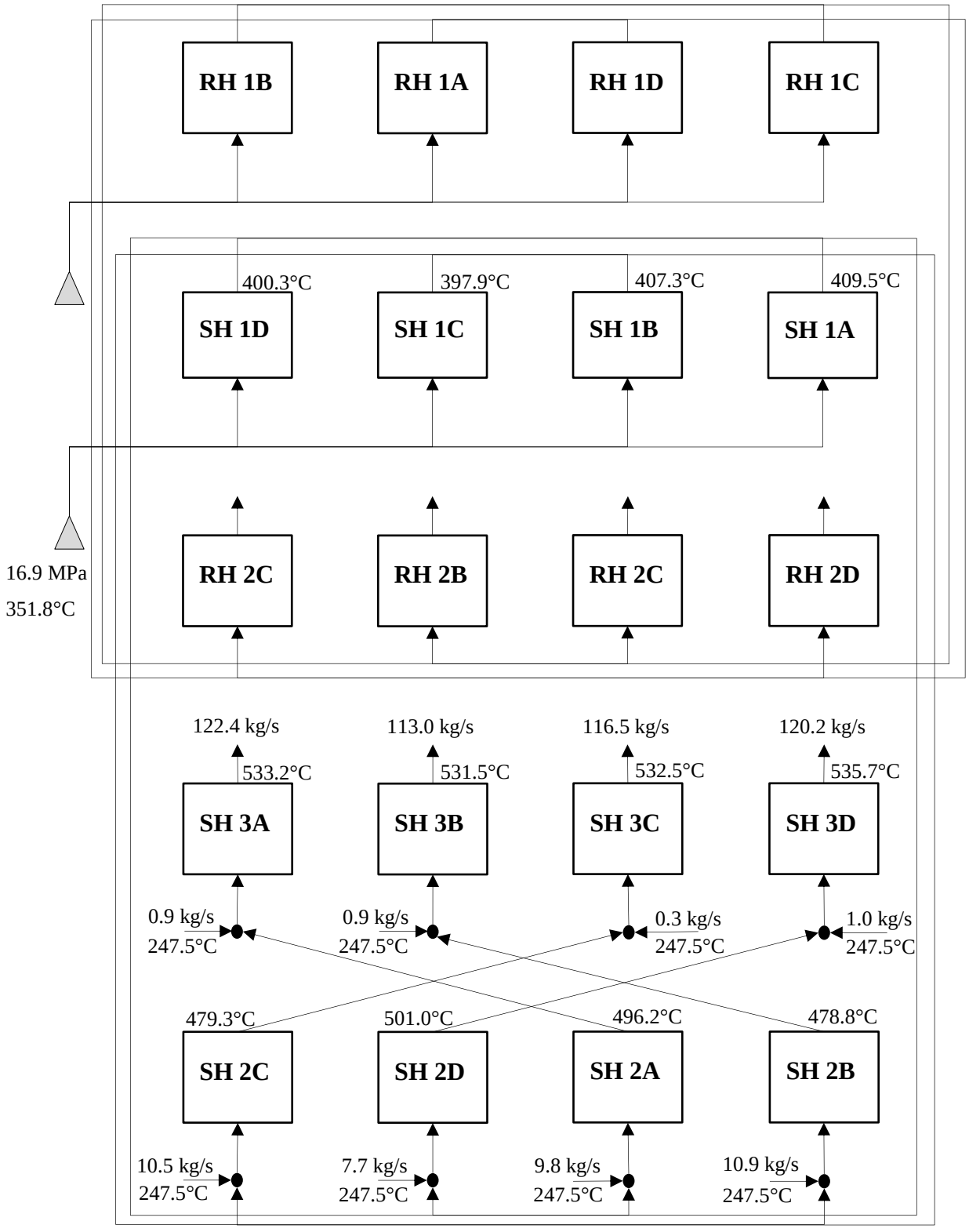

Figure 75 - The provided measured plant data consolidated with a mass and energy balance for the different superheater and reheater legs (only values for superheaters shown).

Only the platen superheater was integrated with the furnace model by means of the FEGT profile radiating to the surface at the bottom of the legs, with the coupling arrangement shown in Figure 76.

The temperature of the tube surface at the bottom of each leg of the platen superheater was coupled to the four nearest furnace exit zones of the temperature profile calculated by the calibrated FNM. The radiation heat transfer to each of these surfaces was coupled with the heat source to the platen superheater. The boundary condition of the eight zones, next to the front wall, not coupled with the platen superheater was modified to assume no radiation heat transfer through the surface, i.e. applying an emissivity of almost zero. This coupling approach to divide the radiation heat transfer between the four platen superheater legs is possible due to the methodology proposed providing a three-dimensional distribution of the temperature and radiation heat transfer of the furnace. Therefore, at the furnace exit, there is a two-dimensional heat transfer and temperature solution on the plane. This type of study will not be possible with a zero-dimensional approach such as the Gurvich method that provides a single furnace exit temperature. As a viable alternatively, CFD will be an appropriate tool if the time and resources are available.

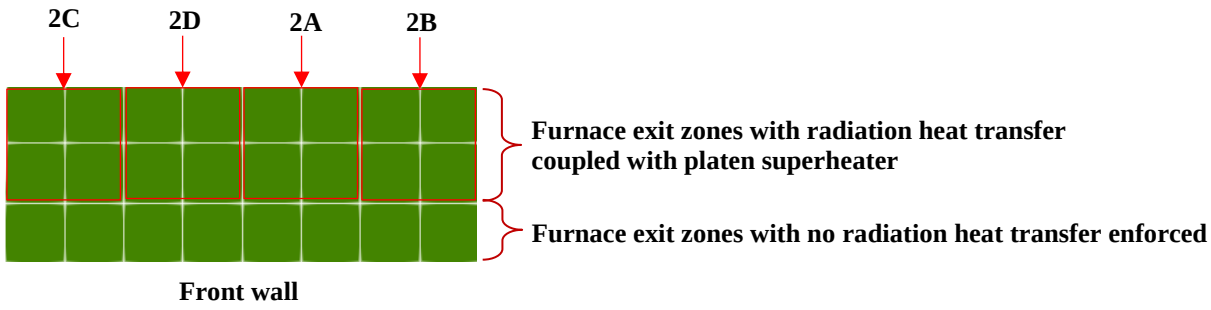

Figure 76 - The furnace exit surfaces coupled between the FNM model in Matlab® and the process model in Flownex® SE.

More detail regarding the coupling of the platen superheater is in Figure 77. The total surface area of the platen superheater is 3156 m^2. The metal thickness of the tube was 8.8 mm, thermal conductivity 47 W/mK, inside convection heat transfer coefficient 4769 W/m^2K and fouling factor 0.0066 m^2K/W (from Laubscher and Rousseau, 2019a:514). The heat transfer to each superheater leg was divided between the down-flow and up-flow leg with convection and radiation heat transfer from the passing flue gas flow as well as the bottom leg that radiates from the flue gas at the furnace exit. The flow resistance in the superheater network model shown in Figure 74 was calibrated to match the mass flow distribution provided in Figure 75.

The radiation heat transfer to the bottom leg of the platen superheater as calculated by the FNM is transferred as a heat source to the node. The Flownex® SE component applicable to conduction and convection was added to model the heat transfer from the surface to the steam flowing in the

tubes. The projected surface area for four of the surface areas (thus 31.7 m^2) on the exit was combined for the heat transfer area.

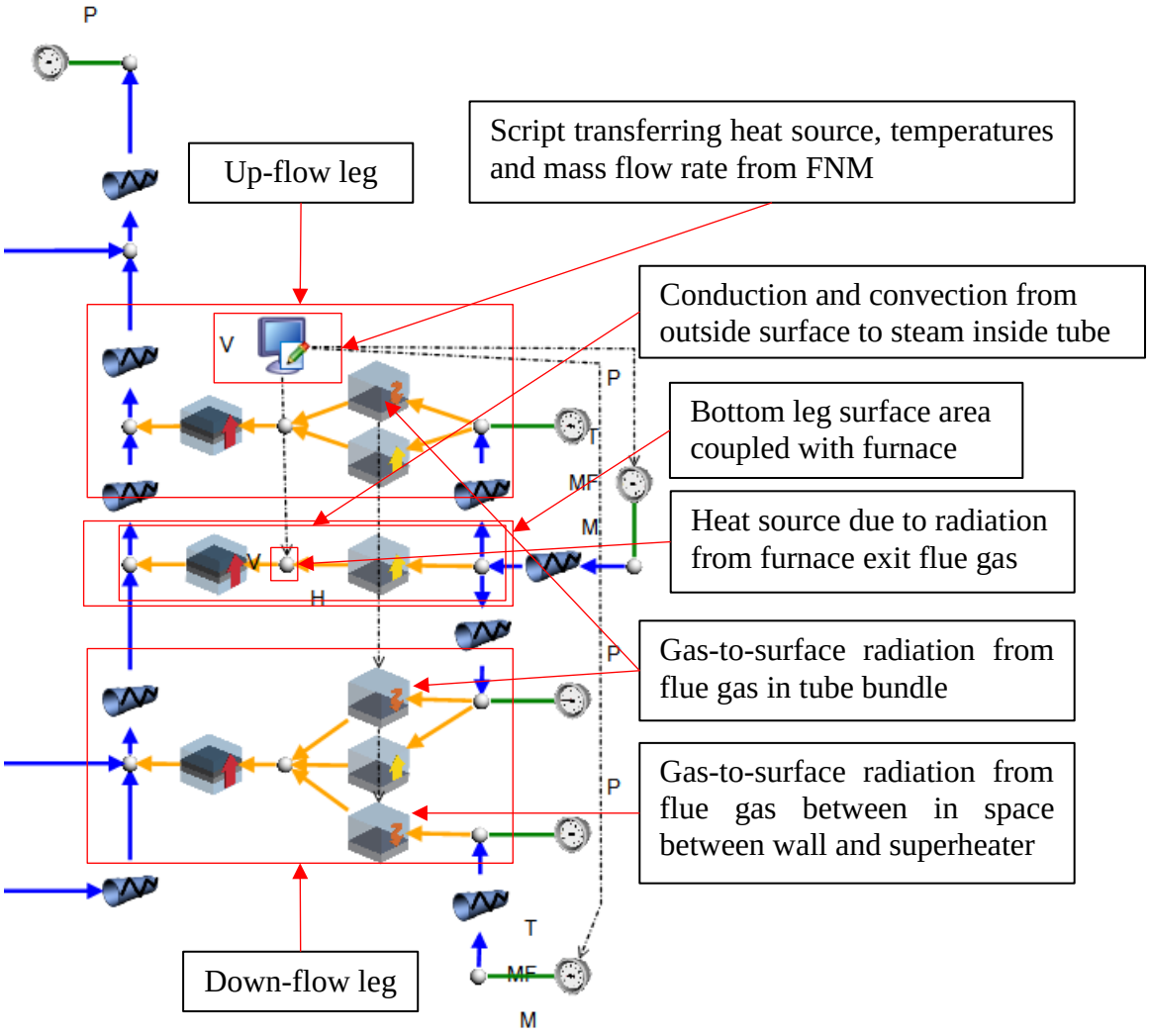

Figure 77 - Platen superheater model of each leg in the Flownex® SE process model of the water and steam cycle.

The remaining heat transfer area of the platen superheater was distributed between the down-flow and up-flow leg. A component for the conduction, convection and gas-to-surface radiation heat transfer were added to each of the up-flow and down-flow legs. A network based gas-to-fluid radiation component was included for the flue gas flow between the tube bundles as well as flue gas flowing in the space between the wall and platen superheater. The flue gas flowing in the space between the wall and platen superheater come from the furnace exit zones with no radiation heat transfer shown in Figure 76. A convection heat transfer coefficient of 1 W/m^2K was calibrated to account for 1% of the total heat transfer. The fluid emissivity input for the gas-to-surface radiation component was calibrated to match the superheater outlet temperatures provided in Figure 75. The calibrated fluid emissivities were between 0.22 and 0.29. The mass flow rate of the flue gas mass

flow rate through the superheater and passing in the space between the wall and platen superheater were transferred from the FNM in Matlab® to the process model in Flownex® SE.

The code of the FNM in Matlab® was extended to update the water wall and superheater surface temperatures solved and stored from the previous Flownex® SE steady-state results. The solution for the furnace was obtained and then the process model in Flownex® SE called via the Matlab® code to update the heat sources for the next steady-state solution of the process model.

The mass flow rates and pulverized fuel distribution were updated based on the unit's measured values shown in Figure 78 and Figure 79. The burner configuration is also indicated on the graphs. Burner 19 was not in operation. A negative mass flow indicates how far the coal flow at the burner is below the mass-averaged coal mass flow rate and vice versa. A negative grouping of pulverized fuel indicates how coarser the pulverized fuel at the burner is from the mass-averaged pulverized fuel distribution and vice versa. The pulverized fuel distribution shows how only a few burners receive coarser pulverized fuel than the mean, while the coal mass flow distribution varies considerably for a lot of the burners from the mean. After updating the pulverized fuel and mass flow distribution, the absorption coefficient and surface reaction rate required recalibration to match the heat absorption to the evaporator of 538 MW and unburned carbon mass fraction at the furnace exit of 0.029 m%. The base and pulverized fuel distribution case used the same mass flow map which differs from the mass flow rates distribution case.

The aim of this case study is to demonstrate the co-simulation behaviour and multi-dimensional integration at the platen superheaters for different sensitivity studies. The measured plant data indicate significant performance differences between the mills providing different pulverized fuel distribution and coal mass flow rates. The primary and secondary air flow rate were relatively equally distributed between the burners. This might have a notable effect on the combustion kinetics and temperature distribution in the furnace. Therefore, the case studies will investigate the possible benefit to the platen superheater surface temperatures and platen superheater outlet temperatures when the flow and pulverized fuel distribution can be balanced.

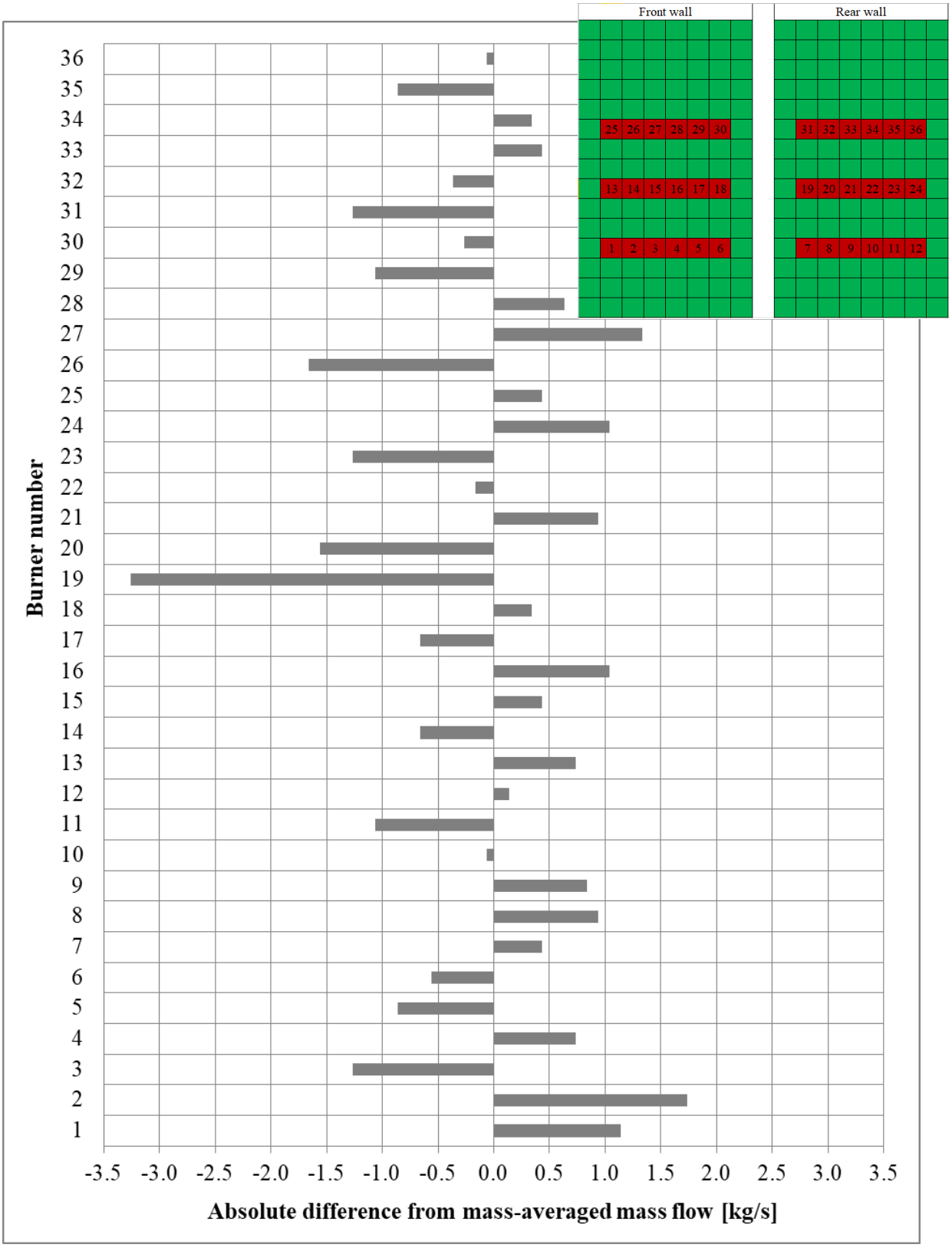

Figure 78 - Comparison of the difference from the mass-averaged coal mass flow for the different burners as measured.

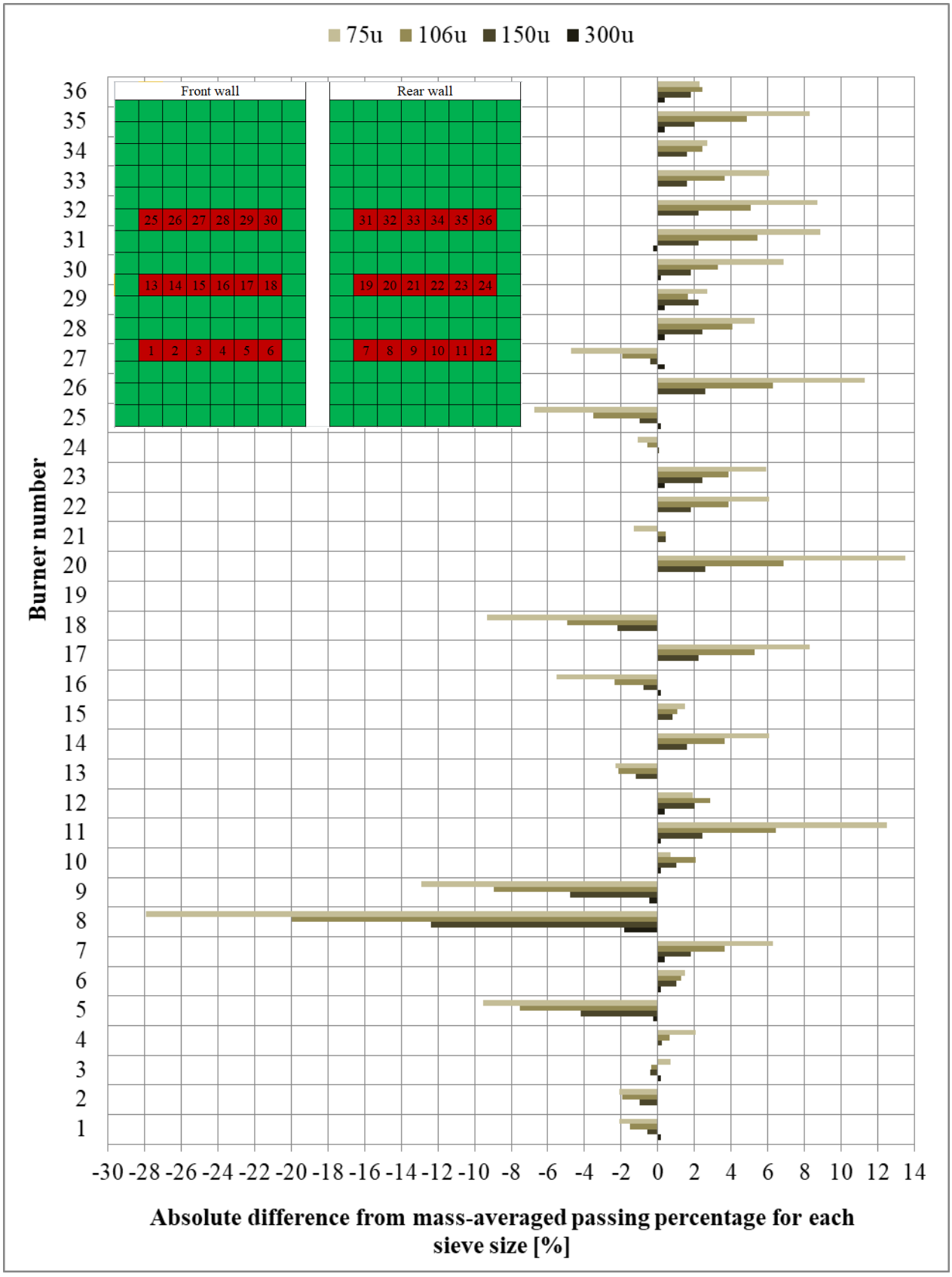

Figure 79 - Comparison of the difference from the mass-averaged pulverized distribution for the different burners as measured for each passing sieve size.

A comparison for the predicted furnace and platen superheater parameters when the flow and pulverized fuel is equally distributed is shown in Table 23. An averaged mass flow and averaged pulverized fuel distribution were applied to each burner, except burner 19 that remained out of operation.

Table 23 - Comparison of the changes between the different furnace and platen superheater parameters due to changes in the boiler operation inputs.

Case	Base	Equally distributed flow	Equally distributed pulverized fuel
Heat input [MW]	1718.5	1714.0	1721.1
Feedwater flow rate [kg/s]	430.1	427.7	433.0
Evaporator heat absorption [MW]	538.3	535.3	541.7
Furnace exit gas temperature [°C]	1433.5	1433.2	1432.6
Furnace exit O_2 volume fraction [v%]	2.481	2.522	2.449
Unburned carbon [m%]	0.029	0.035	0.011
SH 2A surface temperature [°C]	494.7	493.5	494.1
SH 2B surface temperature [°C]	498.1	499.4	497.2
SH 2C surface temperature [°C]	502.5	501.6	501.6
SH 2D surface temperature [°C]	515.7	515.9	515.5
SH 2A steam outlet temperature [°C]	496.2	493.8	494.4
SH 2B steam outlet temperature [°C]	478.8	480.6	477.4
SH 2C steam outlet temperature [°C]	479.3	479.6	478.0
SH 2D steam outlet temperature [°C]	501.0	505.0	499.1

When the flow is equally distributed, the heat input decreases by 4.5 MW due to a decrease in carbon burnout (0.006 m% less unburned carbon and 0.0.041 v% more oxygen at the furnace exit). The mass-averaged FEGT is almost the same and only small changes in the two-dimensional temperature distribution at the furnace exit are noticed. Slightly less heat absorbed of 3 MW is predicted in the evaporator and the feedwater flow rate decreases with 2.4 kg/s. Therefore, the results show no significant changes.

When the pulverized fuel is equally distributed, the heat input increases by 2.6 MW due to an increase in carbon burnout (0.018 m% less unburned carbon and 0.032 v% less oxygen at the furnace exit). The FEGT decreases slightly by 0.9°C. The two-dimensional temperature distribution at the furnace exit trends lower but the change is insignificant. When the current attemperation flow

was decreased to match comparable temperatures to the base case, 1.1 kg/s less attemperation flow was required. Thus, improving the pulverized fuel distribution at some of the burners shows no significant change in the furnace exit temperature profile. Only a slight increase in combustion efficiency is noticed.

This case study showed how a reduced order model using the methodology proposed for the FNM model can be integrated with a process model. The co-simulation was used to investigate the multi-dimensional impact of the fuel distribution from the burners on the furnace exit temperature profile and heat transfer characteristics of the platen superheaters. This particular scenario showed that none to limited success will be obtained when the coal flow and pulverized fuel distribution between the burners can be balanced. The study highlighted that other parameters should also be investigated if larger gains in boiler performance are required by using less attemperation flow at the platen superheaters.

6. Capabilities and limitations

The methodology proposed is aimed at providing sufficiently accurate solutions with more detail than the classical zero-dimensional empirical solutions and within shorten run times than the high detail CFD models. However, in an effort to find the right balance between accuracy and speed, various limitations ensued.

The following capabilities and limitations of the furnace network model (FNM) were identified based on the findings discussed in this thesis (updated from the first version presented in Van der Meer, Rousseau and Naidoo, 2019:265):

- As seen in the single-burner furnace model validation in section 4.2.5, the model results are generally smoother than that of the measurements in the immediate flame region. This is due to the fact that the discretisation scheme employed in the model is too coarse to encapsulate the particle mixing and fast transients just outside the burner mouth. Therefore, the network-based model is clearly not suited for studying the details of the near-burner flame region. CFD remains the preferred tool to better understand the details associated with particle heat-up, devolatilisation, temperature distribution and flue gas product formation in the flame region.
- The combination of models implemented enables quicker solving times when compared to alternative tools such as CFD. The furnace model solution for the case studies is able to solve within four minutes on a laptop computer (2.7 GHz CPU with 2 cores) when implementing the code in Matlab® (version 2019R). Scilab ® (version 5.5.2) was about ten times slower. The CFD solution required six hours to solve on a computer with 40 cores for the same multiple-burner furnace.
- The model delivered reasonably accurate predictions (within 100 K) of the temperature and burnout profiles outside of the immediate flame region. Therefore, the methodology shows promise when applied for predicting the temperature, burnout and gas composition in areas outside this region. Additionally, it allows the prediction of the furnace exit temperature profile and heat flux distribution to the furnace walls.
- When a single mass flow map is available for a specific load then it can be normalised and applied to other load conditions within a 40% load range (refer to section 5.5). The validity of using a normalised mass flow map reduces the amount of pre-work required

using isothermal CFD simulations to create a mass flow map for different load setpoints. This will also be valuable for possible transient simulations where the load changes dynamically.

- From the case studies, it was evident that the model is useful in studies involving changes in the coal quality, particle size distribution, operating different burner configurations and fouling on the furnace wall. For the change in coal quality, the different surface reaction rates for the combustion model needs to be known and can be obtained from calibration if a CFD benchmark is available. The predictions of the heat transfer, FEGT, oxygen concentration and carbon burnout may be utilized in optimizing efficiencies and plant reliability.
- The model can be used in co-simulations with system network codes such as Flownex® SE. The heat flux on the furnace wall is provided by the FNM and the wall temperature returned from Flownex® SE to the FNM based on the heat flux, tube conduction resistance and fluid temperature within the tube. This integration is solved iteratively and conceptually proven to work for transient solutions as well.

Based on the different findings from the investigations in this thesis, the capabilities and limitations when using CFD, the furnace network model and zero-dimensional approaches for furnace models are summarised in Table 24.

Table 24 - Summary of the capability and limitation comparison between CFD, the furnace network model, Gurvich method and other zero-dimensional approaches for a furnace model.

	Zero-dimensional models	**Gurvich method**	**FNM**	**CFD**
Solving time	< 1 second	< 1 second	± 1-4 minutes	> 5 hours
Heat transfer to evaporator walls	Yes	Yes	Yes	Yes
Mass-averaged FEGT	Yes	Yes	Yes	Yes
Two-dimensional furnace exit temperature distribution	No	No	Yes	Yes
Changes in coal quality	No	Yes	Yes	Yes
Changes in particle size distribution	No	No	Yes	Yes
Burner operating configuration	No	No	Yes	Yes

	Zero-dimensional models	**Gurvich method**	**FNM**	**CFD**
Burner tilt	No	Yes	No	Yes
In-flame studies	No	No	No	Yes
Carbon burnout efficiency (constant coal quality)	No	Yes	Yes	Yes
Carbon burnout efficiency (changing coal quality)	No	No	Yes	Yes
Oxygen concentration at furnace exit (constant coal quality)	No	No	Yes	Yes
Oxygen concentration at furnace exit (changing coal quality)	No	No	Yes	Yes
Co-simulations with system level code integrated with water wall	Yes	Yes	Yes	Yes
Particle and gas emissions	No	No	No	Yes

7. Conclusions and recommendations

7.1 Conclusion

The need was identified for a reduced order whole furnace model applicable to furnace studies or integrated with system network models to inter alia be applied in online process condition monitoring for coal-fired power plants.

The network-based methodology presented in this thesis strives to account for the three-dimensional flow field and temperature variations in order to predict the furnace exit temperature distribution, carbon burnout and heat transfer to the furnace walls with reasonable accuracy within a short solving time. The network-based methodology, as systematically explained in chapter 3, employs:

- A zone-wise discretization scheme dividing the volume occupied by the furnace into a grid of smaller homogeneous volumes, each representing a zone within the furnace.
- The zonal method to model the radiation heat transfer, while neglecting convection heat transfer.
- The Leckner (1972) and Yin (2015) models to calculate the gas and particle absorption coefficients respectively while neglecting the effect of scattering, resulting in the extinction coefficient to be equal to the absorption coefficients.
- The burnout calculated using the BCURA model.
- A mass flow map for the advection effects imported from an isothermal CFD solution generated in OpenFOAM®.

The models were combined to form the furnace network model (FNM) (section 3.9). The methodology also accounts for the possible need for calibration (section 3.10). With the current models selected and the benchmark used for validation, the need for calibration for certain cases were confirmed (section 4.2). The implementation of the models in a computer code was verified (section 4.1) by scrutinising the mass balance, heat balance, concentrations, radiation heat transfer, heat source calculations as well as the fluid and radiation property functions with secondary benchmarks.

In section 4.2.5 the furnace network model was compared against a CFD solution, the Peters and Weber (1997) mathematical model and experimental results of the IFRF furnace no. 1. The

absorption coefficients were calibrated to be equal to the mean value used by Peters and Weber (1997). The heat transfer and temperature profiles did not vary considerably and therefore showed that the selected gas and particle radiation property models were acceptable for the case modelled. The surface reaction rate was calibrated to match the unburned carbon measured at the furnace outlet. Comparison of the results showed that the model predicts the temperature, burnout, gas composition and heat flux within reasonable accuracy (within 100 K for temperature and 1% for the radiation heat flux predictions) throughout the furnace, except in the immediate burner region. This provided confidence that the combination of models applied here can be used to model the integrated behaviour of a single-burner furnace and expanded to utility scale boilers with multiple-burners.

In section 4.2.8 the furnace network model was compared against a CFD solution, FEGT prediction with the Gurvich method and measurements in a full-scale coal-fired furnace with multiple opposite wall-fired burners. The absorption and reaction rate coefficients were calibrated to match the heat transfer to the average furnace exit gas temperature and carbon burnout of the CFD solution at 99% load condition. A comparison of the calibrated furnace network model showed that the predicted heat absorption and furnace exit gas temperatures compared well with the benchmark CFD at the 60.5% and 81% load conditions. The temperature distribution at the furnace exit also showed similar profiles between the furnace network model and the CFD benchmark.

The methodology was further demonstrated with case studies predicting the change in heat absorption, FEGT, carbon burnout and oxygen concentration. The parametric studies included particle size distributions, burners out of operation, fouling on the furnace wall and employing a normalised mass flow map. The FNM successfully captured the correct effect of coal quality changes when the surface reaction rates of each coal were available for the combustion model. For the case study between the actual and design coal, this was obtained via calibration when compared to a CFD benchmark. The zero-dimensional Gurvich method was also considered for the cases and indicated where the approach required additional input information that the other methods provide as output, i.e. mainly the unburned carbon and multi-dimensional temperature distribution at the furnace exit.

Initially, the methodology was coded in Scilab® because it is an open-source application with ease of use for matrix calculations and visualisation of the results. The solution time was improved tenfold when the same code was implemented in Matlab®, typically executing within four minutes. Because the methodology provides a model that solves in a relatively short time it can be used in

co-simulation performing multi-objective analysis. The capability thereof was shown in section 5.6 and 5.7 using a co-simulation between the furnace solution of the FNM model and the steam-side model in Flownex® SE. The model can be used for steady-state case studies or transient simulations.

The FNM does have limitations due to the compromise made by integrating a de-coupled and reduced-order CFD solution into the network-based furnace model. The FNM is not suited for studying the details of the near-burner flame region. A high-order CFD simulation remains the preferred tool to better understand particle heat-up, devolatilisation, temperature distribution and flue gas product formation. The need for calibration is also a necessary shortcoming giving rise to the current methodology being dependent on existing measurements and CFD solutions.

It can thus be concluded that the methodology as set out in chapter 3 addresses the outcomes of the hypothesis as defined in section 1.2 by meeting the main objectives of this study that were set for the proposed network-based furnace model when applied to a utility scale boiler. These are:

1. Determining a two-dimensional temperature field at the furnace exit.
2. Determining the combustion efficiency (unburned carbon leaving the furnace).
3. Determining the heat flux to the evaporator (water walls) along the height of the furnace as well as at the furnace exit plane.
4. Allowing quick solution times.

7.2 Recommendations

The following recommendations are presented for consideration for the future development of the methodology and the furnace network model:

- The bulk of the current solution time is associated with the zonal method to calculate exchange areas and solving the network equations. The solution of these components can still be optimised considerably by testing specialised sparse matrix solution algorithms. Initialising the solution with a previously solved temperature and particle distribution field will further decrease the solution times, especially for the co-simulation solving for small incremental changes in the furnace.
- Even though the models in this study typically discretised the furnace into more volumes than presented in other publications, the discretisation can be tested with even smaller

volumes especially with the current solution time of fewer than four minutes using Matlab® together with other methods that decrease the overall solution time.

- One of the cumbersome activities in the current methodology was generating and exporting the mass flow map. These steps can be largely automated with a fit for purpose script including the existing OpenFOAM® mesh creation and manipulation functionalities, and solving the furnace network model code.
- For the BCURA model, it was assumed that dividing the particles into four bins will be sufficient for the initial development based on prior work from Field et al. (1967:391). It is recommended to test the sensitivity of the number of bins when used with the FNM as well.
- Investigate and test alternative devolatilisation, surface reaction rate and absorption coefficient models to reduce the dependency of calibration in the methodology to provide solutions without the need for a CFD benchmark.
- Enhance the models selected in the methodology to include the capability of non-cubically shaped zones by expanding the selected models to account for differently shaped zones. This will minimise the need for simplifying the furnace control volume geometry and assist with accounting for angled surfaces. A possibility is to explore a combination of direct numerical integration and Monte-Carlo ray tracing methods to minimise over-simplification of the furnace geometry to determine the radiation exchange areas.
- More refinement with regard to the flow map using the isothermal CFD approach will be necessary to further improve the accuracy in some of the results. One possible solution is a finer discretisation of the CFD solution and interpolated to match the zones of the zone discretisation of the network furnace based model.
- Extend the physical boundary of the FNM to include the platen superheater to avoid imaginary surface boundary conditions on the furnace exit plane.

8. List of references

Abryutin, A.A., Karasina, E.S., Livshits, B.N., Shnirman, A. & Chudnovskii, B. 1998. Development of a method and a code for the 3D zonal calculation of heat transfer in the furnaces of coal-fired boilers. *Thermal Engineering*. 45(6):461-466.

Alekhnovich, A.N., Artem'eva, N.V. & Bogomolov, V.V. 2006. Slagging properties of coals and allowance for them in the analysis of the possibility of using out-of-design fuel. *Power Technology and Engineering*. 40(3):18-23.

Alekhnovich, A.N., Artem'evab, N.V. & Chernetskii, M.Yu. 2012. Refinement of indicators characterizing fouling and slagging for coals with low slagging propensities as applied to the standard and zone-wise methods for thermal design of furnace chambers and to mathematical models. *Thermal Engineering*. 59(6):449-456.

ANSYS, (2015). *ANSYS Fluent Theory Guide*.

Authier, O., Thunin, E., Plion, P., Schonnenbeck, C. Leyssens, G., Brilhac, J. & Porcheron, L. 2014. Kinetic study of pulverized coal devolatilization for boiler CFD modelling. *Fuel*. 122:254-260.

Backreedy, R.I., Fletcher, L.M., Ma, L., Pourkashanian, M. & Williams, A. 2007. Modelling pulverised coal combustion using a detailed coal combustion model. *Combustion Science and Technology*. 178(4):763-787. DOI: 10.1080/00102200500248532.

Baum, M.M., & Street, P.J. 1971. Predicting the combustion behaviour of coal particles. *Combustion Science Technology*. 3:231–43.

Benesch, W. & Kremer, H. 1985. Mathematical modelling of fluid flow and mixing in tangentially fired furnaces. *Symposium (International) on Combustion*. 20(1):549-557.

Bhatt, M.S. 2007. Effect of air ingress on the energy performance of coal fired thermal power plants. *Energy Conversion & Management*. 48:2150-2160.

Blokh, A.G. 1987. *Heat transfer in steam boiler furnaces*. CRC Press, USA.

Bordbar, M.H. & Hyppänen, T., 2007. Modeling of radiation heat transfer in a boiler furnace. *Advanced Studies in Theoretical Physics*. 12(1):571-584.

Breussin, F., Pigari, F., and Weber, R. 1996. Predicting the Near-Burner-Zone Flow Field and Chemistry of Swirl-Stabilized Low-NOx Flames of Pulverized Coal Using the RNG-k-e, RSM and k-e Turbulence Models. *Twenty-Sixth Symposium Combustion*. 1:211–217.

Brunnemann, J., Gottelt, F., Wellner, K., Renz, A., Thüring, A., Roeder, V., Hasenbein, C., Schulze, C. et al. 2012. Status of ClaRaCCS: modelling and simulation of coal-fired power plants with CO^2 capture. *Proceedings of the 9th International Modelica Conference*. 3-5 September 2012. Munich, Germany. DOI: 10.3384/ecp12076609.

Carvalho, M.G. & Farias, T.L. 1998. Modelling of heat transfer in radiating and combusting systems. *Transactions of the Institute of Chemical Engineers*. 76(A):175-184.

Chudnovsky, B., Jinjikhashvily, G., Shweitzer, Y. Talanker, A. & Meir, R., 2005. Mitigation of carbon dioxide emissions of coal power stations. *Proceedings of ASME 2005 Power Conference*. 5-7 April 2005. Chicago, Illinois, USA.

Chudnovsky, B., Kogan, B., Talanker, A., Sella, Y. & Cohen, J. 2007. Advanced supervision and diagnostic system: the tool for improvement reliability and efficiency of utility boilers burned different coals type. *Proceedings of ASME 2007 Power Conference.* 17-19 June 2007. San Antonio, Texas.

Chudnovsky, B. & Talanker, A. 2004. Effect of bituminous coal properties on heat transfer characteristic in the boiler furnaces. *Proceedings of the ASME 2004 International Mechanical Engineering Congress and Exposition.* 13-19 November 2004. Anaheim, California, USA.

Chudnovsky, B., Talanker, A., Kogan, B., Daniliuc, M., Lev, S. & Frega, L. 2009. Combination of advanced supervision system FURNACE with continuous visual monitoring ORFEUS for proper on-line performance analysis of the furnace firing coal in large utility boilers. *Proceedings of PWR2009, ASME Power Conference*. 21-23 July 2009. American Society of Mechanical Engineers. Albuquerque, New Mexico.

Crnomarkovic, N., Sijercic, M., Belosevic, S., Tucakovic, D. & Zivanovic, T. 2013. Numerical investigation of processes in the lignite-fired furnace when simple gray gas and weighted sum of gray gases models are used. *International Journal of Heat and Mass Transfer*. 56:197-205.

Crnomarković, N., Sijerčić, M.A., Belošević, S.V., Tucaković, D.R. & Živanović, T.V. 2012. Influence of application of Hottel's zonal model and six-flux model of thermal radiation on numerical simulations results of pulverized coal fired furnace. *Thermal Science*. 16(1):271-282.

Cui, M., Chen, H. & Gao, X., 2010. Mathematical models developed by zone method considering non-gray radiation properties of gas in combustion chamber. *Journal of Iron and Steel Research.* 17(11):13-18.

Dal-Secco, S. 2000. Three dimensional modeling of pulverized coal combustion in a 600 MW corner fired boiler. *Journal of Thermal Science*. 9(4):376-380.

Drosatos, P. Nikolopoulos, N., Agraniotis, M., Itskos, G., Grammelis, P. & Kakaras, E. 2014. Decoupled CFD simulation of furnace and heat exchangers in a lignite utility boiler. *Fuel*. 117:633-648.

Eaton, A.M., Smoot, L.D., Hill, S.C. & Eatough, C.N. 1999. Components, formulations, solutions, evaluation, and application of comprehensive combustion models. *Progress in Energy and Combustion Science*. 25:387-436.

Ebrahimi, H., Zamaniyan, A., Soltan Mohammadzadeh, J.S. & Khalili, A.A. 2013. Zonal modeling of radiative heat transfer in industrial furnaces using simplified model for exchange area calculation. *Applied Mathematical Modelling*. 37(16-17):8004-8015.

Edge P.J., Heggs P.J., Pourkashanian M. & Williams A., 2011. An integrated computational fluid dynamics–process model of natural circulation steam generation in a coal-fired power plant. *Computers and Chemical Engineering*. 35(12):2618-2631.

Edge P.J., Heggs P.J., Pourkashanian M. & Williams A., 2012. A reduced order full plant model for oxyfuel combustion. *Fuel*. 101:234-243.

Edge P.J., Heggs P.J., Pourkashanian M. & Williams A., 2013. Integrated fluid dynamics-process modelling of a coal-fired plant with carbon capture. *Applied Thermal Engineering*. 60:242-250.

EPRI (Electric Power Research Institute). 1998. *Heat rate improvement reference manual*. Technical report: TR-109546. Palo Alto, CA.

EPRI (Electric Power Research Institute). 2000. *Impact of operating factors on boiler availability*. Technical report: TR-1000560. Palo Alto, CA.

EPRI (Electric Power Research Institute). 2001. *Statistical analysis methodology for predicting impact of operation factors on boiler availability*. Technical report: TR-1004064. Palo Alto, CA.

EPRI (Electric Power Research Institute). 2005. *Power plant optimization industry experience: 2005 update*. Technical report: TR-1011794. Palo Alto, CA.

Eskom. 2010. *Boiler mass and energy balance guideline & user manual.* Reference document: BoilMEB.SP-30.08.2010-Rev 4.

Fei, Y., Black, S., Szuhanszki, L., Ma, L., Ingham, D.B., Stanger, P.J. & Pourkashanian, M. 2015. Evaluation of the potential retrofitting a coal power plant to oxy-firing using CFD and process co-simulation. *Fuel Processing Technology*. 131:45-58.

Field, M.A., Gill, D.W., Morgan, B.B. & Hawksley, P.G.W. 1967. *Combustion of pulverised coal.* The British Coal Utilisation Research Association. Leatherhead.

Filkoski, R.V. 2010. Pulverised-coal combustion with staged air introduction: CFD analysis with different thermal radiation methods. *The Open Thermodynamic Journal*. 4:2-12.

Filkoski, R.V., Petrovski, I.J. & Karas, P. 2006. Optimisation of pulverised coal combustion by means of CFD/CTA modelling. *Thermal Science*. 10(3):161-179.

Gill, D.W. 1969. *Extensions to a one-dimensional mathematical model of a pulverised-coal flame.* BCURA research report no. 356.

Gupta, D.F. 2011. Modeling of Coal Fired Boiler. PhD thesis. University of Pune, India.

Hao, Z., Qian, X., Cen, K. & Fan, J. 2003. Optimizing pulverized coal combustion performance based on ANN and GA. *Fuel Processing Technology*. 85(2-3):113-124.

Harkin, T., Hoadley, A. & Hooper, B. 2011. Using multi-objective optimisation in the design of CO2 capture systems for retrofit to coal power plants. *Energy*. 41: 228-235.

Hesselmann, G. 1998. *Modelling of pulverised coal fired furnaces with advanced combustion systems by integrating performance programs.* Performance Prediction in Advanced Coal Fired Boilers, Final technical report: Contract No JOF3 - CT95 – 0005, Project Area 1 - Project 111.

Hill, S.C. & Smoot, D.G. 1993. A comprehensive three-dimensional model for simulation of combustion systems: PCGC-3. *Energy & Fuels*. 7:874-883.

Holkar, R. & Hebbal, O.D. 2013. CFD analysis of pulverised-coal combustion of burner used in furnace with different radiation models. *IOSR Journal of Mechanical and Civil Engineering*. 5(2):25-34.

Hottel, H.C. & Cohen, E.S. 1958. Radiant heat exchange in a gas-filled enclosure: allowance for nonuniformity of gas temperature. *AIChe Journal.* 4(1):3-14. DOI: 10.1002/aic.690040103.

Hottel, H.C. & Sarofim, A.F. 1967. *Radiative Transfer*. McGraw-Hill, New York.

Hovi, V., Huttunen, M., Karppinen, I., Pattikangas, T., Niemisto, H., Karvonen, L., Kallio, S., Tuuri, S. & Yla-Outinen, Y. 2017. Integrated transient simulation of a BFB boiler with CFD models for the BFB furnace and dynamic system models for the steam cycle and boiler operation. *Energy Procedia*. 120:508-515.

Hu, Y., Tan, C.K. Broughton, J. & Roach, P.A. 2016. Development of a first-principles hybrid model for large-scale reheating furnaces. *Applied Energy*. 173:555-566.

Hu, Y., Wang, J., Tan, C.K. Sun, C. & Liu, H. 2017. Further improvement of fluidized bed models by incorporating zone method with Aspen Plus interface. *Energy Procedia*. 105:1895-1901.

Hu, Y., Wang, J., Tan, C.K. Sun, C. & Liu, H. 2018a. Coupling detailed radiation model with process simulation in Aspen Plus: A case study on fluidized bed combustor. *Applied Energy*. 227:168-179.

Hu, Y., Tan, C.K., Broughton, J., Roach, P.A. & Varga, L. 2018b. Nonlinear dynamic simulation and control of large-scale reheating furnace operations using a zone method based model. *Applied Thermal Engineering*. 135:41-53.

Hu, Y., Tan, C.K. Niska, J., Chowdhury, J.I., Balta-Ozkan, N.B., Varga, L., Roach, P.A. & Wang, C. 2019. Modelling and simulation of steel reheating processes under oxy-fuel combustion conditions - Technical and environmental perspectives. *Energy*. 185:730-743.

Ivanović, V.B. 2005. Reliable simple zonal method of the furnace thermal calculation. *Thermal Science*. 9(2):44-55.

Kalogirou, S.A. 2003. Artificial intelligence for the modeling and control of combustion processes: a review. *Progress in Energy and Combustion Science*. 29(6):515-566.

Karasina, E.S., Livshits, B.N., Chudnovskii, B.R. & Talanker, A.E. 2010. Experience gained from using a computer program implementing the 3D zone-wise method for calculating heat transfer in the furnace chambers of the coal-fired boilers of the 350- and 575- MW power units. *Thermal Engineering*. 57(10):897-900.

Karasina, E.S., Shrago, Z.K., Aleksandrova, T.S. & Borevskaya, S.E. 1982. An algorithm and computer program for zonal calculation of furnace chambers. *Teploenergetika.* 8:42-50.

Karasina, L.S., Livshits, B.N., Chudnovskii, B., Talanker, A. & Abryutin, A.A. 2000. Adapting the code Furnace for calculations of heat transfer in the boiler furnace of a 575-MW power-generating unit. *Thermal Engineering*. 47(11):1031-1036.

Kim, C. & Lior, N. 1995. Easily computable good approximations for spectral radiative properties of particle-gas componets and mixture in pulverized coal combustors. *Fuel*. 74(12):1891-1902.

Knaus, H., Schneider, R., Han, X., Strohle, U. & Hein, K.R.G. 1997. Comparison of different radiative heat transfer models and their applicability to coal-fired utility boiler simulations. *Fourth International Conference on Technologies and Combustion for a Clean Environment.* Lisbon, Portugal.

Kobayashi, H., Howard, J.B. & Sarofim, A.F. 1977. Coal devolatilization at high temperatures. *16th Symposium International on Combustion*. 16(1):411-425.

Lallemant, N., Sayre, A. & Weber, R. 1996. Evaluation of emissivity correlations for H_2O-CO_2-N_2/air mixtures and coupling with solution methods of the radiative transfer equation. *Progress Energy Combustion Science*. 22(6):543-574.

Larsen, M.E. & Howell, J.R. 1986. Least-squares smoothing of direct exchange areas in zonal analysis. *Journal of Heat Transfer*. 108:239-242.

Laubscher, R. & Rousseau, P.G. 2019a. Numerical investigation into the effect of burner swirl direction on furnace and superheater absorption for a 620 MWe opposing wall-fired pulverized coal boiler. *International Journal of Heat and Mass Transfer*. 137:506-522.

Laubscher, R. & Rousseau, P.G. 2019b. CFD study of pulverized coal-fired boiler evaporator and radiant superheaters at varying loads. *Applied Thermal Engineering*. 160:1-10.

Laubscher, R. & Rousseau, P.G. 2019c. Numerical investigation of the impact of variable particle radiation properties on the heat transfer in a high ash pulverized coal boiler through co-simulation. *ICCHMT 2019*. 3-6 September 2019. Rome, Italy.

Lawson, D.A. 1995. An improved method for smoothing approximate exchange areas. *International Journal of Heat Transfer*. 38(16):3109-3110.

Lawson, D.A. & Ziesler, C.D. 1996. *An accurate program for radiation modelling in the design of high-temperature furnaces*. Journal of Management Mathematics. 7(2):109-116.

Leckner, B. 1972. Spectral and total emissivity of water vapor and carbon dioxide. *Combustion and Flame*. 19(1):33-48.

Liu, X. & Bansal, R.C. 2011. Optimizing combustion process by adaptive tuning technology based on integrated genetic algorithm and computational fluid dynamics. *Energy Conversion and Management*. 56:53-62.

Lowe, A., Wall, T.F. & Stewart, I.M. 1975. A zoned heat transfer model of a large tangentially fired pulverized coal boiler. *Symposium International on Combustion*. 15(1):1261-1270.

Ma, J., Eason J.P., Dowling, A.W., Biegler, L.T. & Miller, D.C. 2016. Development of a first-principles hybrid boiler model for oxy-combustion power generation. *International Journal of Greenhouse Gas Control*. 46(1):136-157.

Madejski, P. 2018. Coal combustion modelling in a frontal pulverized coal-fired boiler. *3rd International Conference on Energy and Environmental Protection*. E3S Web of Conferences. 45:1-8.

Madejski, P. & Modlinski, N. 2019. Numerical investigation using two different CFD codes of pulverized-coal combustion process characteristic in an industrial power plant boiler. *ICBT Poland 2018*. E3S Web of Conferences. 82:1-10.

Magnussen, B.F. & Hjertager, B. H. 1977. *On Mathematical Modelling of Turbulent Combustion with Special Emphasis on Soot Formation and Combustion.* International Symposium Combustion. 1:719-729.

Méchi, R., Farhat, H., Guedri, K., Halouani, K. & Said, R. 2009. Extension of the zonal method to inhomogeneous non-grey semi-transparent medium. *Energy*. 351:1-15.

Modest, M.F. 2003. *Radiative Heat Transfer*. 2nd edition, Elsevier Science, Burlington, Massachusetts, USA.

Monnaemang, M.O. 2015. A zonal model for radiation heat transfer in coal-fired boiler furnaces. Master's dissertation. University of Cape Town, South Africa.

Nalbandian, H. 2011. *Expert systems and coal quality in power generation.* IEA Clean Coal Centre, CCC/186.

Park H.Y., Faulkner M., Turrell M.D., Stopford P.J. & Kang D.S. 2010. Coupled fluid dynamics and whole plant simulation of coal combustion in a tangentially-fired boiler. *Fuel*. 89(8):2001-2010.

Peta, S., Du Toit, C., Naidoo, R., Schmitz, W. & Jestin, L. 2015. Investigations of operation problems at a 200 MWe PF boiler. *Chemical and Process Engineering*. 36(3):305-320.

Peters, A.F. & Weber, R. 1997. Mathematical modelling of a 2.4 MW swirling pulverized coal flame. *Combustion Science and Technology*, 122(1):131-182.

Ranade, V.V., & Gupta, D.F. 2015. *Computational modelling of pulverized coal fired boilers*. CRC Press, USA.

Richter, W. 1974. Prediction of heat and mass transfer in a pulverised fuel furnace. *Letters in Heat and Mass Transfer*. 1(1):83-4.

Rousseau, P.G., Du Toit, C.G., Jun, J.S. & Noh, J.M. 2015. Code-to-code comparison for analysing the steady-state heat transfer and natural circulation in an air-cooled RCCS using GAMMA+ and Flownex. *Nuclear Engineering and Design*. 291:71-89.

Rousseau, P.G. & Laubscher, R. 2019. Analysis of the impact of coal quality on the heat transfer distribution in a high-ash pulverized coal boiler using co-simulation. *ICCHMT*. 3-6 September 2019. Rome, Italy.

Sankar, G., Santhosh Kumar, D. & Balasubramanian, K.R. 2019. Computational modelling of pulverized coal fired boilers – A review on the current position. *Fuel.* 236:643-665.

Sanpasertparnich, T. & Aroonwilas, A. 2009. Simulation and optimization of coal-fired power plants. *Energy Procedia*. 1(1):3851-3858.

Sanpasertparnich, T., Idem, R., Bolea, I., De Montigny, D. & Tontiwachwuthikul, P. 2010. Integration of post-combustion capture and storage into a pulverized coal-fired power plant. *International Journal of Greenhouse Gas Control*. 4(3):499-510.

Sarofim, A.F. 1961. *Radiant heat transmission in enclosures*. Massachussetts Institute of Technology.

Sasse, C., Koenigsdorff, R. & Frank, S. 1995. Evaluation of an improved hybrid six-flux/zone model for radiative transfer in rectangular enclosures. *International Journal of Heat Mass Transfer*. 38(18):3423-3431.

Schnell, U., Schneider, R., Magel, H.-C, Risio, B., Lepper, J. & Hein, K.R.G. 1995. Numerical simulation of advanced coal-fired combustion systems with in-furnace NOx control technologies. *Conference on Combustion Technologies for a Clean Environment*. 3-6 July 1995. Lisbon, Spain.

Schuhbauer, C., Angerer, M., Spliethoff, H., Kluger, F. & Tschaffon, H. 2014. Coupled simulation of a tangentially hard coal fired 700°C boiler. *Fuel*. 122:149-163.

Si, F., Romero, C.E., Yao, Z., Schuster, E., Xu, Z., Morey, R.L. & Liebowitz, B.N. 2008. Optimization of coal-fired boiler SCRs based on modified support vector machine models and genetic algorithms. *Fuel*. 88(5):806-816.

Smith, I.W. 1982. *Combustion of coal rates of char – a review*. Symposium (International) on Combustion. 19(1)1045-1065.

Smoot, L. & Pratt, D. 1979. *Pulverized-coal combustion and gasification: theory and applications for continuous flow processes.* New York: Plenum Press.

Stein, O.T., Olenik, G., Kronenburg, A., Cavallo Marincola, F., Franchetti, B.M., Kempf, A.M., Ghiani, M., Vascellari, M. et al. 2013. Towards comprehensive coal combustion modelling for LES. *Flow Turbulence Combustion*. 90:859-884.

Stopford, P. 2002. Recent applications of CFD modelling in the power generation and combustion industries. *Applied Mathematical Modelling*. 26:351-374.

Ströhle, U., Knaus, H., Schnell, U. & Hein, K.R.G. 2000. A radiation model for the numerical simulation of coal-fired furnaces using body-fitted grids. *Combustion Science and Technology*. 153(1):127-139.

Sun, J.K. & Hurt, R.H. 2000. Mechanisms of extinction and near extinction in pulverized solid fuel combustion. *Proceedings of the Combustion Institute*. 28(2):2205-2213.

Tan, C.K., Jenkins, J., Ward, J., Broughton, J. & Heeley, A. 2013. Zone modelling of the thermal performances of a large-scale bloom reheating furnace. *Applied Thermal Engineering*. 50(1):1111-1118.

Tucker, R.J. 1986. Direct exchange areas for calculating radiation transfer in rectangular furnaces. *Journal of Heat Transfer*. 108:707-710.

Tzolakis G., Papanikolaou P., Kolokotronis D., Samaras N., Tourlidakis A. & Tomboulides A. 2012. Simulation of a coal-fired power plant using mathematical programming algorithms in order to optimize its efficiency. *Applied Thermal Engineering*. 48:256-267.

Van der Meer, W.A., Rousseau, P.G. & Jestin, L. 2016a. A system level model of the heat transfer of a single down-fired burner in a rectangular furnace based on a zonal approach. *Second Eskom Power Plant Engineering Institute Student Workshop*. Eskom Academy of Learning. 11 - 12 July 2016.

Van der Meer, W.A., Rousseau, P.G. & Jestin, L. 2016b. A system level modeling approach for combustion and radiative heat transfer in a single-burner furnace based on a Zonal method. *4th*

International Conference on Contemporary Problems of Thermal Engineering, CPOTE 2016. 14-16 September 2016. Katowice, Poland. Institute of Thermal Technology.

Van der Meer, W.A., Rousseau, P.G. & Jestin, L. 2016c. A methodology for the integrated system simulation of the heat transfer and combustion in a coal-fired boiler furnace. *10th South African Conference on Computational and Applied Mechanics*. 3 – 5 October 2016. Potchefstroom, South Africa.

Van der Meer, W.A., Rousseau, P.G. & Naidoo, R. 2019. A thermofluid network based methodology for integrated system simulation of heat transfer and combustion in a coal-fired furnace. *Thermal Science and Engineering Progress*. 10:253-267.

Versteeg, H.K., Malalasekera, W. 2007. *An Introduction to Computational Fluid Dynamics, 2nd edition*. Pearson Prentice Hall.

Williams, A., Pourkashanian, M. & Jones, J.M. 2000. The combustion of coal and some other solide fuels. *Proceedings of the Combustion Institute*. 28:2141-2162.

Yin, C. 2015. On gas and particle radiation in pulverized fuel combustion furnaces. *Applied Energy.* 157:554-561.

Zhang, Y., Li, Q. & Zhou, H. 2016. *Theory and calculation of heat transfer in furnaces.* Elsevier.

Appendix A. Mathematical models for particle radiation properties

The alternative models that can be considered for particle radiation properties by Zhang, Li and Zhou (2016), Kim and Lior (1995) and Smoot and Pratt (1979) are provided in this section. For Zhang, Li and Zhou (2016) the extinction coefficient of fly ash (β_{fa}) is given by:

$$\beta_{fa} = k_{fa} u_{fa} p \tag{32}$$

where is p is the gas total pressure and the fly ash concentration (u_{fa}) given by:

$$u_{fa} = \frac{a_{fa} mf_{ash}}{100 G_g} \tag{33}$$

where mf_{ash} is the fuel ash content as-received and G_g is the flue gas mass excluding the fly ash. a_{fa} is the fly ash fraction depending on the combustion type. The factor k_{fa} is calculated by:

$$k_{fa} = \frac{4300 \rho_g}{\sqrt[3]{T_g^{\,2} d_{fa}^2}} \times 10^{-5} \tag{34}$$

where ρ_g is the gas density, T_g is the flue gas temperature and d_{fa} is the fly ash particle diameter.

The extinction coefficient for a luminous flame (β_c), i.e. combustion of a solid fuel, is given by:

$$\beta_c = k_c p \tag{35}$$

k_c is given by:

$$k_c = 0.03\left(2 - \alpha_F\right)\left(1.6 \times 10^{-3} T_F'' - 0.5\right)\frac{C}{H}\frac{1}{p_0} \tag{36}$$

where $\frac{C}{H}$ is the carbon-hydrogen ratio of the fuel as-received, α_F the excess air coefficient of the furnace, T_F'' the flue gas temperature at the outlet of the furnace and p_0 the reference pressure of 98.1 kPa. k_c is zero when the excess air coefficient is larger than two.

The extinction coefficient for the coke particles (β_{co}) is given by:

$$\beta_{co} = k_{co} x_1 x_2 p \tag{37}$$

Where k_{co} is generally 10^{-5}, $x_1 = 1$ for anthracite and lean coal fuels and $x_1 = 0.5$ for bitumite and lignite fuels. $x_2 = 0.1$ for pulverized coal furnace combustion and $x_2 = 0.03$ for grate furnace combustion.

An alternative model is using the absorption efficiency factor (Q_{abs}) calculations in Kim and Lior (1995) and Smoot and Pratt (1979) to calculate the absorption coefficient of the particles (κ_p) as follows:

$$\kappa_p = N_p Q_{abs} \frac{\pi d^2}{4} \tag{38}$$

where N_p is the number of particles and d the diameter of particles. The particle scattering coefficients are calculated similarly. The values to determine the absorption efficiency factor are available in Kim and Lior (1995) and Smoot and Pratt (1979).

Appendix B. Verification benchmarks results

The results shown in Figure 80 below were used in verifying the temperature and enthalpy calculation function (see section 4.1.1).

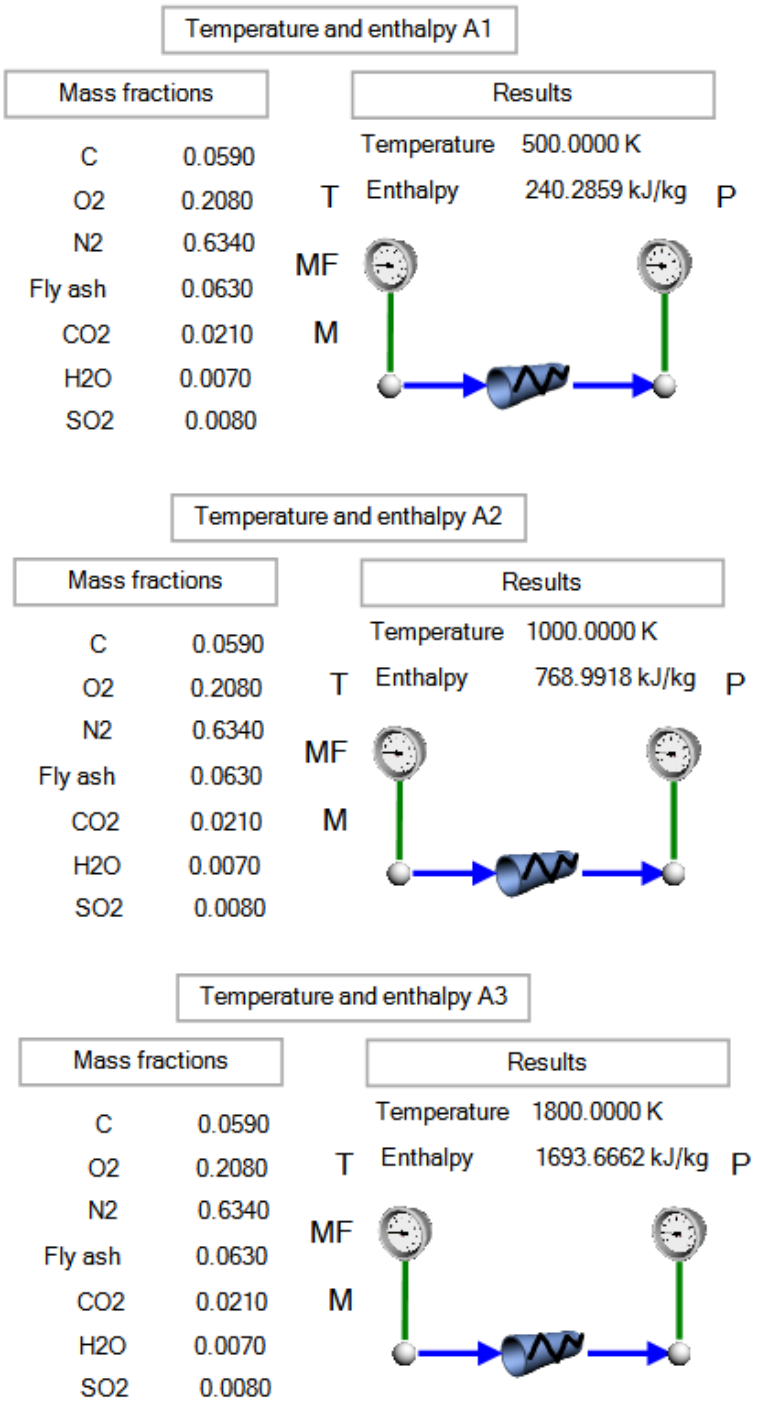

Figure 80 - Screenshot of the flue gas properties as calculated by the Flownex® SE benchmark.

The results shown in Figure 81 below were used in verifying the gas absorptivity calculation function (see section 4.1.1). The mathematical model is available in section 3.4.

Case B1

	Property	Unit	Value for H2O	Value for CO2
Inputs	Pressure	bar	0.85	0.85
	Gas partial pressure	bar	0.0765	0.1190
	Mean beam length	m	10.134	10.134
	Gas temperature	K	1100	1100
	Surface temperature	K	300	300
Emissivity results	t	-	1.1000	1.1000
	P_E	-	1.0367	0.8833
	(p_aL)_m/(p_aL)_0	-	15.9720	0.1860
	a	-	1.8030	1.0871
	b	-	0.9626	0.2300
	c	-	0.5000	1.4700
	ε_0	-	0.3243	0.1720
	ε	-	0.3260	0.1713
Absorption results	t	-	0.3000	0.3000
	P_E	-	1.2076	0.8833
	(p_aL)_m/(p_aL)_0	-	1.1880	0.6000
	a	-	2.1445	1.5730
	b	-	5.9350	0.2300
	c	-	0.5000	1.4700
	ε_0	-	0.2583	0.1074
	ε	-	0.2649	0.1057
	α	-	0.5072	0.2024

Correlation constants

i,j	H2O 0	H2O 1	H2O 2	i,j	CO2 0	CO2 1	CO2 2	CO2 3
0	-2.21180	-1.19870	0.03560	0	-3.98930	2.76690	-2.10810	0.391630
1	0.85667	0.93048	-0.14391	1	1.27100	-1.10900	1.01950	-0.218970
2	-0.10838	-0.17156	0.04592	2	-0.23678	0.19731	-0.19544	0.044644
	-2.21180	-1.31857	0.04307		-3.98930	3.04359	-2.55080	0.52126
	1.61863	1.93390	-0.32901		2.64537	-2.53901	2.56752	-0.60660
	-0.38692	-0.67371	0.19834		-1.02571	0.94021	-1.02442	0.25741

Correlation constants

	H2O 0	H2O 1	H2O 2	i,j	CO2 0	CO2 1	CO2 2	CO2 3
0	-2.21180	-1.19870	0.03560	0	-3.98930	2.76690	-2.10810	0.391630
1	0.85667	0.93048	-0.14391	1	1.27100	-1.10900	1.01950	-0.218970
2	-0.10838	-0.17156	0.04592	2	-0.23678	0.19731	-0.19544	0.044644
	-2.21180	-0.35961	0.00320		-3.98930	0.83007	-0.18973	0.01057
	1.13523	0.36991	-0.01716		1.92818	-0.50472	0.13920	-0.00897
	-0.19032	-0.09038	0.00726		-0.54494	0.13623	-0.04048	0.00277

Case B2

	Property	Unit	Value for H2O	Value for CO2
Inputs	Pressure	bar	0.85	0.85
	Gas partial pressure	bar	0.0765	0.1190
	Mean beam length	m	0.8	0.8
	Gas temperature	K	1800	1800
	Surface temperature	K	400	400
Emissivity results	t	-	1.8000	1.8000
	P_E	-	0.9960	0.8833
	(p_aL)_m/(p_aL)_0	-	42.7680	0.0694
	a	-	1.3639	1.0426
	b	-	0.4831	0.2300
	c	-	0.5000	1.4700
	ε_0	-	0.0611	0.0800
	ε	-	0.0611	0.0800
Absorption results	t	-	0.4000	0.4000
	P_E	-	1.1597	0.8833
	(p_aL)_m/(p_aL)_0	-	2.1120	0.3375
	a	-	2.1445	1.3776
	b	-	3.9674	0.2300
	c	-	0.5000	1.4700
	ε_0	-	0.0799	0.0552
	ε	-	0.0821	0.0550
	α	-	0.1741	0.1166

Correlation constants

i,j	H2O 0	H2O 1	H2O 2	i,j	CO2 0	CO2 1	CO2 2	CO2 3
0	-2.21180	-1.19870	0.03560	0	-3.98930	2.76690	-2.10810	0.391630
1	0.85667	0.93048	-0.14391	1	1.27100	-1.10900	1.01950	-0.218970
2	-0.10838	-0.17156	0.04592	2	-0.23678	0.19731	-0.19544	0.044644
	-2.21180	-2.15766	0.11533		-3.98930	4.98042	-6.83024	2.28399
	0.67399	1.31770	-0.36684		1.24385	-1.95356	3.23261	-1.24975
	-0.06708	-0.19115	0.09208		-0.22677	0.34015	-0.60646	0.24936

Correlation constants

	H2O 0	H2O 1	H2O 2	i,j	CO2 0	CO2 1	CO2 2	CO2 3
0	-2.21180	-1.19870	0.03560	0	-3.98930	2.76690	-2.10810	0.391630
1	0.85667	0.93048	-0.14391	1	1.27100	-1.10900	1.01950	-0.218970
2	-0.10838	-0.17156	0.04592	2	-0.23678	0.19731	-0.19544	0.044644
	-2.21180	-0.47948	0.00570		-3.98930	1.10676	-0.33730	0.02506
	0.11440	0.04970	-0.00307		0.41361	-0.14436	0.05308	-0.00456
	-0.00193	-0.00122	0.00013		-0.02508	0.00836	-0.00331	0.00030

Case B3

	Property	Unit	Value for H2O	Value for CO2
Inputs	Pressure	bar	0.99	0.99
	Gas partial pressure	bar	0.0300	0.0700
	Mean beam length	m	10.134	10.134
	Gas temperature	K	500	500
	Surface temperature	K	300	300
Emissivity results	t	-	0.5000	0.5000
	P_E	-	1.0986	1.0096
	(p_aL)_m/(p_aL)_0	-	3.3000	0.2160
	a	-	2.1445	1.2732
	b	-	2.9029	0.2300
	c	-	0.5000	1.4700
	ε_0	-	0.2733	0.1411
	ε	-	0.2786	0.1412
Absorption results	t	-	0.3000	0.3000
	P_E	-	1.1302	1.0096
	(p_aL)_m/(p_aL)_0	-	1.1880	0.6000
	a	-	2.1445	1.5730
	b	-	5.9350	0.2300
	c	-	0.5000	1.4700
	ε_0	-	0.2466	0.1125
	ε	-	0.2511	0.1128
	α	-	0.3241	0.1456

Correlation constants

i,j	H2O 0	H2O 1	H2O 2	i,j	CO2 0	CO2 1	CO2 2	CO2 3
0	-2.21180	-1.19870	0.03560	0	-3.98930	2.76690	-2.10810	0.391630
1	0.85667	0.93048	-0.14391	1	1.27100	-1.10900	1.01950	-0.218970
2	-0.10838	-0.17156	0.04592	2	-0.23678	0.19731	-0.19544	0.044644
	-2.21180	-0.59935	0.00890		-3.98930	1.38345	-0.52703	0.04895
	1.27036	0.68991	-0.05335		2.35247	-1.02631	0.47174	-0.05066
	-0.23833	-0.18863	0.02524		-0.81115	0.33797	-0.16738	0.01912

Correlation constants

	H2O 0	H2O 1	H2O 2	i,j	CO2 0	CO2 1	CO2 2	CO2 3
0	-2.21180	-1.19870	0.03560	0	-3.98930	2.76690	-2.10810	0.391630
1	0.85667	0.93048	-0.14391	1	1.27100	-1.10900	1.01950	-0.218970
2	-0.10838	-0.17156	0.04592	2	-0.23678	0.19731	-0.19544	0.044644
	-2.21180	-0.35961	0.00320		-3.98930	0.83007	-0.18973	0.01057
	1.08031	0.35202	-0.01633		2.07050	-0.54198	0.14947	-0.00963
	-0.17235	-0.08185	0.00657		-0.62835	0.15708	-0.04668	0.00320

Figure 81 - Screenshot of the flue gas properties absorptivity for the benchmark programmed in a worksheet.

The results shown in Figure 82 to Figure 88 below are the calculated values for the code in the FNM and benchmark code from Monnaemang (2015) for verification of the total exchange areas (see section 4.1.1).

FNM

Row \ Column	1	2	3	4	5	6	7	8	9	10	11	12	13	14	15	16	17	18	19	20	21	22	23	24
1	0.0000	0.0000	0.0000	0.0000	0.0896	0.0562	0.0562	0.0378	0.0491	0.3062	0.0240	0.0493	0.0406	0.0491	0.0262	0.0240	0.0491	0.0240	0.3062	0.0493	0.0406	0.0262	0.0491	0.0240
2	0.0000	0.0000	0.0000	0.0000	0.0562	0.0896	0.0378	0.0562	0.0406	0.0491	0.0262	0.0240	0.0491	0.3062	0.0240	0.0493	0.0240	0.0491	0.0493	0.3062	0.0262	0.0406	0.0240	0.0491
3	0.0000	0.0000	0.0000	0.0000	0.0562	0.0378	0.0896	0.0562	0.0240	0.0493	0.0491	0.3062	0.0262	0.0240	0.0406	0.0491	0.0406	0.0262	0.0491	0.0240	0.0491	0.0240	0.3062	0.0493
4	0.0000	0.0000	0.0000	0.0000	0.0378	0.0562	0.0562	0.0896	0.0262	0.0240	0.0406	0.0491	0.0240	0.0493	0.0491	0.3062	0.0262	0.0406	0.0240	0.0491	0.0240	0.0491	0.0493	0.3062
5	0.0896	0.0562	0.0562	0.0378	0.0000	0.0000	0.0000	0.0000	0.3062	0.0491	0.0493	0.0240	0.0491	0.0406	0.0240	0.0262	0.3062	0.0493	0.0491	0.0240	0.0491	0.0240	0.0406	0.0262
6	0.0562	0.0896	0.0378	0.0562	0.0000	0.0000	0.0000	0.0000	0.0491	0.0406	0.0240	0.0262	0.3062	0.0491	0.0493	0.0240	0.0493	0.3062	0.0240	0.0491	0.0240	0.0491	0.0262	0.0406
7	0.0562	0.0378	0.0896	0.0562	0.0000	0.0000	0.0000	0.0000	0.0493	0.0240	0.3062	0.0491	0.0240	0.0262	0.0491	0.0406	0.0491	0.0240	0.0406	0.0262	0.3062	0.0493	0.0491	0.0240
8	0.0378	0.0562	0.0562	0.0896	0.0000	0.0000	0.0000	0.0000	0.0240	0.0262	0.0491	0.0406	0.0493	0.0240	0.3062	0.0491	0.0240	0.0491	0.0262	0.0406	0.0493	0.3062	0.0240	0.0491
9	0.0491	0.0406	0.0240	0.0262	0.3062	0.0491	0.0493	0.0240	0.0000	0.0000	0.0000	0.0000	0.0896	0.0562	0.0562	0.0378	0.3062	0.0491	0.0493	0.0240	0.0491	0.0406	0.0240	0.0262
10	0.3062	0.0491	0.0493	0.0240	0.0491	0.0406	0.0240	0.0262	0.0000	0.0000	0.0000	0.0000	0.0562	0.0896	0.0378	0.0562	0.0493	0.0240	0.3062	0.0491	0.0240	0.0262	0.0491	0.0406
11	0.0240	0.0262	0.0491	0.0406	0.0493	0.0240	0.3062	0.0491	0.0000	0.0000	0.0000	0.0000	0.0562	0.0378	0.0896	0.0562	0.0491	0.0406	0.0240	0.0262	0.3062	0.0491	0.0493	0.0240
12	0.0493	0.0240	0.3062	0.0491	0.0240	0.0262	0.0491	0.0406	0.0000	0.0000	0.0000	0.0000	0.0378	0.0562	0.0562	0.0896	0.0240	0.0262	0.0491	0.0406	0.0493	0.0240	0.3062	0.0491
13	0.0406	0.0491	0.0262	0.0240	0.0491	0.3062	0.0240	0.0493	0.0896	0.0562	0.0562	0.0378	0.0000	0.0000	0.0000	0.0000	0.0491	0.3062	0.0240	0.0493	0.0406	0.0491	0.0262	0.0240
14	0.0491	0.3062	0.0240	0.0493	0.0406	0.0491	0.0262	0.0240	0.0562	0.0896	0.0378	0.0562	0.0000	0.0000	0.0000	0.0000	0.0240	0.0493	0.0491	0.3062	0.0262	0.0240	0.0406	0.0491
15	0.0262	0.0240	0.0406	0.0491	0.0240	0.0493	0.0491	0.3062	0.0562	0.0378	0.0896	0.0562	0.0000	0.0000	0.0000	0.0000	0.0406	0.0491	0.0262	0.0240	0.0491	0.3062	0.0240	0.0493
16	0.0240	0.0493	0.0491	0.3062	0.0262	0.0240	0.0406	0.0491	0.0378	0.0562	0.0562	0.0896	0.0000	0.0000	0.0000	0.0000	0.0262	0.0240	0.0406	0.0491	0.0240	0.0493	0.0491	0.3062
17	0.0491	0.0240	0.0406	0.0262	0.3062	0.0493	0.0491	0.0240	0.3062	0.0493	0.0491	0.0240	0.0491	0.0240	0.0406	0.0262	0.0000	0.0000	0.0000	0.0000	0.0896	0.0562	0.0562	0.0378
18	0.0240	0.0491	0.0262	0.0406	0.0493	0.3062	0.0240	0.0491	0.0491	0.0240	0.0406	0.0262	0.3062	0.0493	0.0491	0.0240	0.0000	0.0000	0.0000	0.0000	0.0562	0.0896	0.0378	0.0562
19	0.3062	0.0493	0.0491	0.0240	0.0491	0.0240	0.0406	0.0262	0.0493	0.3062	0.0240	0.0491	0.0240	0.0491	0.0262	0.0406	0.0000	0.0000	0.0000	0.0000	0.0562	0.0378	0.0896	0.0562
20	0.0493	0.3062	0.0240	0.0491	0.0240	0.0491	0.0262	0.0406	0.0240	0.0491	0.0262	0.0406	0.0493	0.3062	0.0240	0.0491	0.0000	0.0000	0.0000	0.0000	0.0378	0.0562	0.0562	0.0896
21	0.0406	0.0262	0.0491	0.0240	0.0491	0.0240	0.3062	0.0493	0.0491	0.0240	0.3062	0.0493	0.0406	0.0262	0.0491	0.0240	0.0896	0.0562	0.0562	0.0378	0.0000	0.0000	0.0000	0.0000
22	0.0262	0.0406	0.0240	0.0491	0.0240	0.0491	0.0493	0.3062	0.0406	0.0262	0.0491	0.0240	0.0491	0.0240	0.3062	0.0493	0.0562	0.0896	0.0378	0.0562	0.0000	0.0000	0.0000	0.0000
23	0.0491	0.0240	0.3062	0.0493	0.0406	0.0262	0.0491	0.0240	0.0240	0.0491	0.0493	0.3062	0.0262	0.0406	0.0240	0.0491	0.0562	0.0378	0.0896	0.0562	0.0000	0.0000	0.0000	0.0000
24	0.0240	0.0491	0.0493	0.3062	0.0262	0.0406	0.0240	0.0491	0.0262	0.0406	0.0240	0.0491	0.0240	0.0491	0.0493	0.3062	0.0378	0.0562	0.0562	0.0896	0.0000	0.0000	0.0000	0.0000

Benchmark

Row \ Column	1	2	3	4	5	6	7	8	9	10	11	12	13	14	15	16	17	18	19	20	21	22	23	24
1	0.0000	0.0000	0.0000	0.0000	0.0896	0.0562	0.0562	0.0378	0.0491	0.3062	0.0240	0.0493	0.0406	0.0491	0.0262	0.0240	0.0491	0.0240	0.3062	0.0493	0.0406	0.0262	0.0491	0.0240
2	0.0000	0.0000	0.0000	0.0000	0.0562	0.0896	0.0378	0.0562	0.0406	0.0491	0.0262	0.0240	0.0491	0.3062	0.0240	0.0493	0.0240	0.0491	0.0493	0.3062	0.0262	0.0406	0.0240	0.0491
3	0.0000	0.0000	0.0000	0.0000	0.0562	0.0378	0.0896	0.0562	0.0240	0.0493	0.0491	0.3062	0.0262	0.0240	0.0406	0.0491	0.0406	0.0262	0.0491	0.0240	0.0491	0.0240	0.3062	0.0493
4	0.0000	0.0000	0.0000	0.0000	0.0378	0.0562	0.0562	0.0896	0.0262	0.0240	0.0406	0.0491	0.0240	0.0493	0.0491	0.3062	0.0262	0.0406	0.0240	0.0491	0.0240	0.0491	0.0493	0.3062
5	0.0896	0.0562	0.0562	0.0378	0.0000	0.0000	0.0000	0.0000	0.3062	0.0491	0.0493	0.0240	0.0491	0.0406	0.0240	0.0262	0.3062	0.0493	0.0491	0.0240	0.0491	0.0240	0.0406	0.0262
6	0.0562	0.0896	0.0378	0.0562	0.0000	0.0000	0.0000	0.0000	0.0491	0.0406	0.0240	0.0262	0.3062	0.0491	0.0493	0.0240	0.0493	0.3062	0.0240	0.0491	0.0240	0.0491	0.0262	0.0406
7	0.0562	0.0378	0.0896	0.0562	0.0000	0.0000	0.0000	0.0000	0.0493	0.0240	0.3062	0.0491	0.0240	0.0262	0.0491	0.0406	0.0491	0.0240	0.0406	0.0262	0.3062	0.0493	0.0491	0.0240
8	0.0378	0.0562	0.0562	0.0896	0.0000	0.0000	0.0000	0.0000	0.0240	0.0262	0.0491	0.0406	0.0493	0.0240	0.3062	0.0491	0.0240	0.0491	0.0262	0.0406	0.0493	0.3062	0.0240	0.0491
9	0.0491	0.0406	0.0240	0.0262	0.3062	0.0491	0.0493	0.0240	0.0000	0.0000	0.0000	0.0000	0.0896	0.0562	0.0562	0.0378	0.3062	0.0491	0.0493	0.0240	0.0491	0.0406	0.0240	0.0262
10	0.3062	0.0491	0.0493	0.0240	0.0491	0.0406	0.0240	0.0262	0.0000	0.0000	0.0000	0.0000	0.0562	0.0896	0.0378	0.0562	0.0493	0.0240	0.3062	0.0491	0.0240	0.0262	0.0491	0.0406
11	0.0240	0.0262	0.0491	0.0406	0.0493	0.0240	0.3062	0.0491	0.0000	0.0000	0.0000	0.0000	0.0562	0.0378	0.0896	0.0562	0.0491	0.0406	0.0240	0.0262	0.3062	0.0491	0.0493	0.0240
12	0.0493	0.0240	0.3062	0.0491	0.0240	0.0262	0.0491	0.0406	0.0000	0.0000	0.0000	0.0000	0.0378	0.0562	0.0562	0.0896	0.0240	0.0262	0.0491	0.0406	0.0493	0.0240	0.3062	0.0491
13	0.0406	0.0491	0.0262	0.0240	0.0491	0.3062	0.0240	0.0493	0.0896	0.0562	0.0562	0.0378	0.0000	0.0000	0.0000	0.0000	0.0491	0.3062	0.0240	0.0493	0.0406	0.0491	0.0262	0.0240
14	0.0491	0.3062	0.0240	0.0493	0.0406	0.0491	0.0262	0.0240	0.0562	0.0896	0.0378	0.0562	0.0000	0.0000	0.0000	0.0000	0.0240	0.0493	0.0491	0.3062	0.0262	0.0240	0.0406	0.0491
15	0.0262	0.0240	0.0406	0.0491	0.0240	0.0493	0.0491	0.3062	0.0562	0.0378	0.0896	0.0562	0.0000	0.0000	0.0000	0.0000	0.0406	0.0491	0.0262	0.0240	0.0491	0.3062	0.0240	0.0493
16	0.0240	0.0493	0.0491	0.3062	0.0262	0.0240	0.0406	0.0491	0.0378	0.0562	0.0562	0.0896	0.0000	0.0000	0.0000	0.0000	0.0262	0.0240	0.0406	0.0491	0.0240	0.0493	0.0491	0.3062
17	0.0491	0.0240	0.0406	0.0262	0.3062	0.0493	0.0491	0.0240	0.3062	0.0493	0.0491	0.0240	0.0491	0.0240	0.0406	0.0262	0.0000	0.0000	0.0000	0.0000	0.0896	0.0562	0.0562	0.0378
18	0.0240	0.0491	0.0262	0.0406	0.0493	0.3062	0.0240	0.0491	0.0491	0.0240	0.0406	0.0262	0.3062	0.0493	0.0491	0.0240	0.0000	0.0000	0.0000	0.0000	0.0562	0.0896	0.0378	0.0562
19	0.3062	0.0493	0.0491	0.0240	0.0491	0.0240	0.0406	0.0262	0.0493	0.3062	0.0240	0.0491	0.0240	0.0491	0.0262	0.0406	0.0000	0.0000	0.0000	0.0000	0.0562	0.0378	0.0896	0.0562
20	0.0493	0.3062	0.0240	0.0491	0.0240	0.0491	0.0262	0.0406	0.0240	0.0491	0.0262	0.0406	0.0493	0.3062	0.0240	0.0491	0.0000	0.0000	0.0000	0.0000	0.0378	0.0562	0.0562	0.0896
21	0.0406	0.0262	0.0491	0.0240	0.0491	0.0240	0.3062	0.0493	0.0491	0.0240	0.3062	0.0493	0.0406	0.0262	0.0491	0.0240	0.0896	0.0562	0.0562	0.0378	0.0000	0.0000	0.0000	0.0000
22	0.0262	0.0406	0.0240	0.0491	0.0240	0.0491	0.0493	0.3062	0.0406	0.0262	0.0491	0.0240	0.0491	0.0240	0.3062	0.0493	0.0562	0.0896	0.0378	0.0562	0.0000	0.0000	0.0000	0.0000
23	0.0491	0.0240	0.3062	0.0493	0.0406	0.0262	0.0491	0.0240	0.0240	0.0491	0.0493	0.3062	0.0262	0.0406	0.0240	0.0491	0.0562	0.0378	0.0896	0.0562	0.0000	0.0000	0.0000	0.0000
24	0.0240	0.0491	0.0493	0.3062	0.0262	0.0406	0.0240	0.0491	0.0262	0.0406	0.0240	0.0491	0.0240	0.0491	0.0493	0.3062	0.0378	0.0562	0.0562	0.0896	0.0000	0.0000	0.0000	0.0000

Figure 82 - Screenshot of the captured values for each cell of the C matrix as calculated in the FNM and the benchmark code from Monnaemang (2015).

		FNM							
		Column							
		1	2	3	4	5	6	7	8
Row	1	0.0498	0.4049	0.0271	0.0438	0.0271	0.0438	0.0172	0.0169
	2	0.0271	0.0438	0.0172	0.0169	0.0498	0.4049	0.0271	0.0438
	3	0.0271	0.0438	0.0498	0.4049	0.0172	0.0169	0.0271	0.0438
	4	0.0172	0.0169	0.0271	0.0438	0.0271	0.0438	0.0498	0.4049
	5	0.4049	0.0498	0.0438	0.0271	0.0438	0.0271	0.0169	0.0172
	6	0.0438	0.0271	0.0169	0.0172	0.4049	0.0498	0.0438	0.0271
	7	0.0438	0.0271	0.4049	0.0498	0.0169	0.0172	0.0438	0.0271
	8	0.0169	0.0172	0.0438	0.0271	0.0438	0.0271	0.4049	0.0498
	9	0.4049	0.0438	0.0438	0.0169	0.0498	0.0271	0.0271	0.0172
	10	0.0438	0.4049	0.0169	0.0438	0.0271	0.0498	0.0172	0.0271
	11	0.0438	0.0169	0.4049	0.0438	0.0271	0.0172	0.0498	0.0271
	12	0.0169	0.0438	0.0438	0.4049	0.0172	0.0271	0.0271	0.0498
	13	0.0498	0.0271	0.0271	0.0172	0.4049	0.0438	0.0438	0.0169
	14	0.0271	0.0498	0.0172	0.0271	0.0438	0.4049	0.0169	0.0438
	15	0.0271	0.0172	0.0498	0.0271	0.0438	0.0169	0.4049	0.0438
	16	0.0172	0.0271	0.0271	0.0498	0.0169	0.0438	0.0438	0.4049
	17	0.4049	0.0438	0.0498	0.0271	0.0438	0.0169	0.0271	0.0172
	18	0.0438	0.0169	0.0271	0.0172	0.4049	0.0438	0.0498	0.0271
	19	0.0438	0.4049	0.0271	0.0498	0.0169	0.0438	0.0172	0.0271
	20	0.0169	0.0438	0.0172	0.0271	0.0438	0.4049	0.0271	0.0498
	21	0.0498	0.0271	0.4049	0.0438	0.0271	0.0172	0.0438	0.0169
	22	0.0271	0.0172	0.0438	0.0169	0.0498	0.0271	0.4049	0.0438
	23	0.0271	0.0498	0.0438	0.4049	0.0172	0.0271	0.0169	0.0438
	24	0.0172	0.0271	0.0169	0.0438	0.0271	0.0498	0.0438	0.4049

		Benchmark							
		Column							
		1	2	3	4	5	6	7	8
Row	1	0.0498	0.4049	0.0271	0.0438	0.0271	0.0438	0.0172	0.0169
	2	0.0271	0.0438	0.0172	0.0169	0.0498	0.4049	0.0271	0.0438
	3	0.0271	0.0438	0.0498	0.4049	0.0172	0.0169	0.0271	0.0438
	4	0.0172	0.0169	0.0271	0.0438	0.0271	0.0438	0.0498	0.4049
	5	0.4049	0.0498	0.0438	0.0271	0.0438	0.0271	0.0169	0.0172
	6	0.0438	0.0271	0.0169	0.0172	0.4049	0.0498	0.0438	0.0271
	7	0.0438	0.0271	0.4049	0.0498	0.0169	0.0172	0.0438	0.0271
	8	0.0169	0.0172	0.0438	0.0271	0.0438	0.0271	0.4049	0.0498
	9	0.4049	0.0438	0.0438	0.0169	0.0498	0.0271	0.0271	0.0172
	10	0.0438	0.4049	0.0169	0.0438	0.0271	0.0498	0.0172	0.0271
	11	0.0438	0.0169	0.4049	0.0438	0.0271	0.0172	0.0498	0.0271
	12	0.0169	0.0438	0.0438	0.4049	0.0172	0.0271	0.0271	0.0498
	13	0.0498	0.0271	0.0271	0.0172	0.4049	0.0438	0.0438	0.0169
	14	0.0271	0.0498	0.0172	0.0271	0.0438	0.4049	0.0169	0.0438
	15	0.0271	0.0172	0.0498	0.0271	0.0438	0.0169	0.4049	0.0438
	16	0.0172	0.0271	0.0271	0.0498	0.0169	0.0438	0.0438	0.4049
	17	0.4049	0.0438	0.0498	0.0271	0.0438	0.0169	0.0271	0.0172
	18	0.0438	0.0169	0.0271	0.0172	0.4049	0.0438	0.0498	0.0271
	19	0.0438	0.4049	0.0271	0.0498	0.0169	0.0438	0.0172	0.0271
	20	0.0169	0.0438	0.0172	0.0271	0.0438	0.4049	0.0271	0.0498
	21	0.0498	0.0271	0.4049	0.0438	0.0271	0.0172	0.0438	0.0169
	22	0.0271	0.0172	0.0438	0.0169	0.0498	0.0271	0.4049	0.0438
	23	0.0271	0.0498	0.0438	0.4049	0.0172	0.0271	0.0169	0.0438
	24	0.0172	0.0271	0.0169	0.0438	0.0271	0.0498	0.0438	0.4049

Figure 83 - Screenshot of the captured values for each cell of the D matrix as calculated in the FNM and the benchmark code from Monnaemang (2015).

FNM

Row \ Column	1	2	3	4	5	6	7	8	9	10	11	12	13	14	15	16	17	18	19	20	21	22	23	24
1	1.1765	0.0000	0.0000	0.0000	-0.0083	-0.0052	-0.0052	-0.0035	-0.0045	-0.0283	-0.0022	-0.0045	-0.0037	-0.0045	-0.0024	-0.0022	-0.0045	-0.0022	-0.0283	-0.0045	-0.0037	-0.0024	-0.0045	-0.0022
2	0.0000	1.1765	0.0000	0.0000	-0.0052	-0.0083	-0.0035	-0.0052	-0.0037	-0.0045	-0.0024	-0.0022	-0.0045	-0.0283	-0.0022	-0.0045	-0.0022	-0.0045	-0.0045	-0.0283	-0.0024	-0.0037	-0.0022	-0.0045
3	0.0000	0.0000	1.1765	0.0000	-0.0052	-0.0035	-0.0083	-0.0052	-0.0022	-0.0045	-0.0045	-0.0283	-0.0024	-0.0022	-0.0037	-0.0045	-0.0037	-0.0024	-0.0045	-0.0022	-0.0045	-0.0022	-0.0283	-0.0045
4	0.0000	0.0000	0.0000	1.1765	-0.0035	-0.0052	-0.0052	-0.0083	-0.0024	-0.0022	-0.0037	-0.0045	-0.0022	-0.0045	-0.0045	-0.0283	-0.0024	-0.0037	-0.0022	-0.0045	-0.0022	-0.0045	-0.0045	-0.0283
5	-0.0083	-0.0052	-0.0052	-0.0035	1.1765	0.0000	0.0000	0.0000	-0.0283	-0.0045	-0.0045	-0.0022	-0.0045	-0.0037	-0.0022	-0.0024	-0.0283	-0.0045	-0.0045	-0.0022	-0.0045	-0.0022	-0.0037	-0.0024
6	-0.0052	-0.0083	-0.0035	-0.0052	0.0000	1.1765	0.0000	0.0000	-0.0045	-0.0037	-0.0022	-0.0024	-0.0283	-0.0045	-0.0045	-0.0022	-0.0045	-0.0283	-0.0022	-0.0045	-0.0022	-0.0045	-0.0024	-0.0037
7	-0.0052	-0.0035	-0.0083	-0.0052	0.0000	0.0000	1.1765	0.0000	-0.0045	-0.0022	-0.0283	-0.0045	-0.0022	-0.0024	-0.0045	-0.0037	-0.0045	-0.0022	-0.0037	-0.0024	-0.0283	-0.0045	-0.0045	-0.0022
8	-0.0035	-0.0052	-0.0052	-0.0083	0.0000	0.0000	0.0000	1.1765	-0.0022	-0.0024	-0.0045	-0.0037	-0.0045	-0.0022	-0.0283	-0.0045	-0.0022	-0.0045	-0.0024	-0.0037	-0.0045	-0.0283	-0.0022	-0.0045
9	-0.0045	-0.0037	-0.0022	-0.0024	-0.0283	-0.0045	-0.0045	-0.0022	1.1765	0.0000	0.0000	0.0000	-0.0083	-0.0052	-0.0052	-0.0035	-0.0283	-0.0045	-0.0045	-0.0022	-0.0045	-0.0037	-0.0022	-0.0024
10	-0.0283	-0.0045	-0.0045	-0.0022	-0.0045	-0.0037	-0.0022	-0.0024	0.0000	1.1765	0.0000	0.0000	-0.0052	-0.0083	-0.0035	-0.0052	-0.0045	-0.0022	-0.0283	-0.0045	-0.0022	-0.0024	-0.0045	-0.0037
11	-0.0022	-0.0024	-0.0045	-0.0037	-0.0045	-0.0022	-0.0283	-0.0045	0.0000	0.0000	1.1765	0.0000	-0.0052	-0.0035	-0.0083	-0.0052	-0.0045	-0.0037	-0.0022	-0.0024	-0.0283	-0.0045	-0.0045	-0.0022
12	-0.0045	-0.0022	-0.0283	-0.0045	-0.0022	-0.0024	-0.0045	-0.0037	0.0000	0.0000	0.0000	1.1765	-0.0035	-0.0052	-0.0052	-0.0083	-0.0022	-0.0024	-0.0045	-0.0037	-0.0045	-0.0022	-0.0283	-0.0045
13	-0.0037	-0.0045	-0.0024	-0.0022	-0.0045	-0.0283	-0.0022	-0.0045	-0.0083	-0.0052	-0.0052	-0.0035	1.1765	0.0000	0.0000	0.0000	-0.0045	-0.0283	-0.0022	-0.0045	-0.0037	-0.0045	-0.0024	-0.0022
14	-0.0045	-0.0283	-0.0022	-0.0045	-0.0037	-0.0045	-0.0024	-0.0022	-0.0052	-0.0083	-0.0035	-0.0052	0.0000	1.1765	0.0000	0.0000	-0.0022	-0.0045	-0.0045	-0.0283	-0.0024	-0.0037	-0.0022	-0.0045
15	-0.0024	-0.0022	-0.0037	-0.0045	-0.0022	-0.0045	-0.0045	-0.0283	-0.0052	-0.0035	-0.0083	-0.0052	0.0000	0.0000	1.1765	0.0000	-0.0037	-0.0045	-0.0024	-0.0022	-0.0045	-0.0283	-0.0022	-0.0045
16	-0.0022	-0.0045	-0.0045	-0.0283	-0.0024	-0.0022	-0.0037	-0.0045	-0.0035	-0.0052	-0.0052	-0.0083	0.0000	0.0000	0.0000	1.1765	-0.0024	-0.0022	-0.0037	-0.0045	-0.0022	-0.0045	-0.0045	-0.0283
17	-0.0045	-0.0022	-0.0037	-0.0024	-0.0283	-0.0045	-0.0045	-0.0022	-0.0283	-0.0045	-0.0045	-0.0022	-0.0045	-0.0022	-0.0037	-0.0024	1.1765	0.0000	0.0000	0.0000	-0.0083	-0.0052	-0.0052	-0.0035
18	-0.0022	-0.0045	-0.0024	-0.0037	-0.0045	-0.0283	-0.0022	-0.0045	-0.0045	-0.0022	-0.0037	-0.0024	-0.0283	-0.0045	-0.0045	-0.0022	0.0000	1.1765	0.0000	0.0000	-0.0052	-0.0083	-0.0035	-0.0052
19	-0.0283	-0.0045	-0.0045	-0.0022	-0.0045	-0.0022	-0.0037	-0.0024	-0.0045	-0.0283	-0.0022	-0.0045	-0.0022	-0.0045	-0.0024	-0.0037	0.0000	0.0000	1.1765	0.0000	-0.0052	-0.0035	-0.0083	-0.0052
20	-0.0045	-0.0283	-0.0022	-0.0045	-0.0022	-0.0045	-0.0024	-0.0037	-0.0022	-0.0045	-0.0024	-0.0037	-0.0045	-0.0283	-0.0022	-0.0045	0.0000	0.0000	0.0000	1.1765	-0.0035	-0.0052	-0.0052	-0.0083
21	-0.0037	-0.0024	-0.0045	-0.0022	-0.0045	-0.0022	-0.0283	-0.0045	-0.0022	-0.0283	-0.0045	-0.0037	-0.0024	-0.0045	-0.0022	-0.0083	-0.0052	-0.0052	-0.0035	1.1765	0.0000	0.0000	0.0000	0.0000
22	-0.0024	-0.0037	-0.0022	-0.0045	-0.0022	-0.0045	-0.0045	-0.0283	-0.0037	-0.0024	-0.0045	-0.0022	-0.0045	-0.0022	-0.0283	-0.0045	-0.0052	-0.0083	-0.0035	-0.0052	0.0000	1.1765	0.0000	0.0000
23	-0.0045	-0.0022	-0.0283	-0.0045	-0.0037	-0.0024	-0.0045	-0.0022	-0.0022	-0.0045	-0.0045	-0.0283	-0.0024	-0.0037	-0.0022	-0.0045	-0.0052	-0.0035	-0.0083	-0.0052	0.0000	0.0000	1.1765	0.0000
24	-0.0022	-0.0045	-0.0045	-0.0283	-0.0024	-0.0037	-0.0022	-0.0045	-0.0024	-0.0037	-0.0022	-0.0045	-0.0022	-0.0045	-0.0045	-0.0283	-0.0035	-0.0052	-0.0052	-0.0083	0.0000	0.0000	0.0000	1.1765

Benchmark

Row \ Column	1	2	3	4	5	6	7	8	9	10	11	12	13	14	15	16	17	18	19	20	21	22	23	24
1	1.1765	0.0000	0.0000	0.0000	-0.0083	-0.0052	-0.0052	-0.0035	-0.0045	-0.0283	-0.0022	-0.0045	-0.0037	-0.0045	-0.0024	-0.0022	-0.0045	-0.0022	-0.0283	-0.0045	-0.0037	-0.0024	-0.0045	-0.0022
2	0.0000	1.1765	0.0000	0.0000	-0.0052	-0.0083	-0.0035	-0.0052	-0.0037	-0.0045	-0.0024	-0.0022	-0.0045	-0.0283	-0.0022	-0.0045	-0.0022	-0.0045	-0.0045	-0.0283	-0.0024	-0.0037	-0.0022	-0.0045
3	0.0000	0.0000	1.1765	0.0000	-0.0052	-0.0035	-0.0083	-0.0052	-0.0022	-0.0045	-0.0045	-0.0283	-0.0024	-0.0022	-0.0037	-0.0045	-0.0037	-0.0024	-0.0045	-0.0022	-0.0045	-0.0022	-0.0283	-0.0045
4	0.0000	0.0000	0.0000	1.1765	-0.0035	-0.0052	-0.0052	-0.0083	-0.0024	-0.0022	-0.0037	-0.0045	-0.0022	-0.0045	-0.0045	-0.0283	-0.0024	-0.0037	-0.0022	-0.0045	-0.0022	-0.0045	-0.0045	-0.0283
5	-0.0083	-0.0052	-0.0052	-0.0035	1.1765	0.0000	0.0000	0.0000	-0.0283	-0.0045	-0.0045	-0.0022	-0.0045	-0.0037	-0.0022	-0.0024	-0.0283	-0.0045	-0.0045	-0.0022	-0.0045	-0.0022	-0.0037	-0.0024
6	-0.0052	-0.0083	-0.0035	-0.0052	0.0000	1.1765	0.0000	0.0000	-0.0045	-0.0037	-0.0022	-0.0024	-0.0283	-0.0045	-0.0045	-0.0022	-0.0045	-0.0283	-0.0022	-0.0045	-0.0022	-0.0045	-0.0024	-0.0037
7	-0.0052	-0.0035	-0.0083	-0.0052	0.0000	0.0000	1.1765	0.0000	-0.0045	-0.0022	-0.0283	-0.0045	-0.0022	-0.0024	-0.0045	-0.0037	-0.0045	-0.0022	-0.0037	-0.0024	-0.0283	-0.0045	-0.0045	-0.0022
8	-0.0035	-0.0052	-0.0052	-0.0083	0.0000	0.0000	0.0000	1.1765	-0.0022	-0.0024	-0.0045	-0.0037	-0.0045	-0.0022	-0.0283	-0.0045	-0.0022	-0.0045	-0.0024	-0.0037	-0.0045	-0.0283	-0.0022	-0.0045
9	-0.0045	-0.0037	-0.0022	-0.0024	-0.0283	-0.0045	-0.0045	-0.0022	1.1765	0.0000	0.0000	0.0000	-0.0083	-0.0052	-0.0052	-0.0035	-0.0283	-0.0045	-0.0045	-0.0022	-0.0045	-0.0037	-0.0022	-0.0024
10	-0.0283	-0.0045	-0.0045	-0.0022	-0.0045	-0.0037	-0.0022	-0.0024	0.0000	1.1765	0.0000	0.0000	-0.0052	-0.0083	-0.0035	-0.0052	-0.0045	-0.0022	-0.0283	-0.0045	-0.0022	-0.0024	-0.0045	-0.0037
11	-0.0022	-0.0024	-0.0045	-0.0037	-0.0045	-0.0022	-0.0283	-0.0045	0.0000	0.0000	1.1765	0.0000	-0.0052	-0.0035	-0.0083	-0.0052	-0.0045	-0.0037	-0.0022	-0.0024	-0.0283	-0.0045	-0.0045	-0.0022
12	-0.0045	-0.0022	-0.0283	-0.0045	-0.0022	-0.0024	-0.0045	-0.0037	0.0000	0.0000	0.0000	1.1765	-0.0035	-0.0052	-0.0052	-0.0083	-0.0022	-0.0024	-0.0045	-0.0037	-0.0045	-0.0022	-0.0283	-0.0045
13	-0.0037	-0.0045	-0.0024	-0.0022	-0.0045	-0.0283	-0.0022	-0.0045	-0.0083	-0.0052	-0.0052	-0.0035	1.1765	0.0000	0.0000	0.0000	-0.0045	-0.0283	-0.0022	-0.0045	-0.0037	-0.0045	-0.0024	-0.0022
14	-0.0045	-0.0283	-0.0022	-0.0045	-0.0037	-0.0045	-0.0024	-0.0022	-0.0052	-0.0083	-0.0035	-0.0052	0.0000	1.1765	0.0000	0.0000	-0.0022	-0.0045	-0.0045	-0.0283	-0.0024	-0.0022	-0.0037	-0.0045
15	-0.0024	-0.0022	-0.0037	-0.0045	-0.0022	-0.0045	-0.0045	-0.0283	-0.0052	-0.0035	-0.0083	-0.0052	0.0000	0.0000	1.1765	0.0000	-0.0037	-0.0045	-0.0024	-0.0022	-0.0045	-0.0283	-0.0022	-0.0045
16	-0.0022	-0.0045	-0.0045	-0.0283	-0.0024	-0.0022	-0.0037	-0.0045	-0.0035	-0.0052	-0.0052	-0.0083	0.0000	0.0000	0.0000	1.1765	-0.0024	-0.0022	-0.0037	-0.0045	-0.0022	-0.0045	-0.0045	-0.0283
17	-0.0045	-0.0022	-0.0037	-0.0024	-0.0283	-0.0045	-0.0045	-0.0022	-0.0283	-0.0045	-0.0045	-0.0022	-0.0045	-0.0022	-0.0037	-0.0024	1.1765	0.0000	0.0000	0.0000	-0.0083	-0.0052	-0.0052	-0.0035
18	-0.0022	-0.0045	-0.0024	-0.0037	-0.0045	-0.0283	-0.0022	-0.0045	-0.0045	-0.0022	-0.0037	-0.0024	-0.0283	-0.0045	-0.0045	-0.0022	0.0000	1.1765	0.0000	0.0000	-0.0052	-0.0083	-0.0035	-0.0052
19	-0.0283	-0.0045	-0.0045	-0.0022	-0.0045	-0.0022	-0.0037	-0.0024	-0.0045	-0.0283	-0.0022	-0.0045	-0.0022	-0.0045	-0.0024	-0.0037	0.0000	0.0000	1.1765	0.0000	-0.0052	-0.0035	-0.0083	-0.0052
20	-0.0045	-0.0283	-0.0022	-0.0045	-0.0022	-0.0045	-0.0024	-0.0037	-0.0022	-0.0045	-0.0024	-0.0037	-0.0045	-0.0283	-0.0022	-0.0045	0.0000	0.0000	0.0000	1.1765	-0.0035	-0.0052	-0.0052	-0.0083
21	-0.0037	-0.0024	-0.0045	-0.0022	-0.0045	-0.0022	-0.0283	-0.0045	-0.0022	-0.0283	-0.0045	-0.0037	-0.0024	-0.0045	-0.0022	-0.0083	-0.0052	-0.0052	-0.0035	1.1765	0.0000	0.0000	0.0000	0.0000
22	-0.0024	-0.0037	-0.0022	-0.0045	-0.0022	-0.0045	-0.0045	-0.0283	-0.0037	-0.0024	-0.0045	-0.0022	-0.0045	-0.0022	-0.0283	-0.0045	-0.0052	-0.0083	-0.0035	-0.0052	0.0000	1.1765	0.0000	0.0000
23	-0.0045	-0.0022	-0.0283	-0.0045	-0.0037	-0.0024	-0.0045	-0.0022	-0.0022	-0.0045	-0.0045	-0.0283	-0.0024	-0.0037	-0.0022	-0.0045	-0.0052	-0.0035	-0.0083	-0.0052	0.0000	0.0000	1.1765	0.0000
24	-0.0022	-0.0045	-0.0045	-0.0283	-0.0024	-0.0037	-0.0022	-0.0045	-0.0024	-0.0037	-0.0022	-0.0045	-0.0022	-0.0045	-0.0045	-0.0283	-0.0035	-0.0052	-0.0052	-0.0083	0.0000	0.0000	0.0000	1.1765

Figure 84 - Screenshot of the captured values for each cell of the P matrix as calculated in the FNM and the benchmark code from Monnaemang (2015).

FNM

Row \ Column	1	2	3	4	5	6	7	8	9	10	11	12	13	14	15	16	17	18	19	20	21	22	23	24
1	0.0039	0.0021	0.0021	0.0013	0.0318	0.0034	0.0034	0.0013	0.0318	0.0034	0.0034	0.0013	0.0039	0.0021	0.0021	0.0013	0.0318	0.0034	0.0034	0.0013	0.0039	0.0021	0.0021	0.0013
2	0.0318	0.0034	0.0034	0.0013	0.0039	0.0021	0.0021	0.0013	0.0034	0.0318	0.0013	0.0034	0.0021	0.0039	0.0013	0.0021	0.0034	0.0013	0.0318	0.0034	0.0021	0.0013	0.0039	0.0021
3	0.0021	0.0013	0.0039	0.0021	0.0034	0.0013	0.0318	0.0034	0.0034	0.0013	0.0318	0.0034	0.0021	0.0013	0.0039	0.0021	0.0039	0.0021	0.0021	0.0013	0.0318	0.0034	0.0034	0.0013
4	0.0034	0.0013	0.0318	0.0034	0.0021	0.0013	0.0039	0.0021	0.0013	0.0034	0.0034	0.0318	0.0013	0.0021	0.0021	0.0039	0.0021	0.0013	0.0039	0.0021	0.0034	0.0013	0.0318	0.0034
5	0.0021	0.0039	0.0013	0.0021	0.0034	0.0318	0.0013	0.0034	0.0039	0.0021	0.0021	0.0013	0.0318	0.0034	0.0034	0.0013	0.0034	0.0318	0.0013	0.0034	0.0021	0.0039	0.0013	0.0021
6	0.0034	0.0318	0.0013	0.0034	0.0021	0.0039	0.0013	0.0021	0.0021	0.0039	0.0013	0.0021	0.0034	0.0318	0.0013	0.0034	0.0013	0.0034	0.0034	0.0318	0.0013	0.0021	0.0021	0.0039
7	0.0013	0.0021	0.0021	0.0039	0.0013	0.0034	0.0034	0.0318	0.0021	0.0013	0.0039	0.0021	0.0034	0.0013	0.0318	0.0034	0.0021	0.0039	0.0013	0.0021	0.0034	0.0318	0.0013	0.0034
8	0.0013	0.0034	0.0034	0.0318	0.0013	0.0021	0.0021	0.0039	0.0013	0.0021	0.0021	0.0039	0.0013	0.0034	0.0034	0.0318	0.0013	0.0021	0.0021	0.0039	0.0013	0.0034	0.0034	0.0318

Benchmark

Row \ Column	1	2	3	4	5	6	7	8	9	10	11	12	13	14	15	16	17	18	19	20	21	22	23	24
1	0.0039	0.0021	0.0021	0.0013	0.0318	0.0034	0.0034	0.0013	0.0318	0.0034	0.0034	0.0013	0.0039	0.0021	0.0021	0.0013	0.0318	0.0034	0.0034	0.0013	0.0039	0.0021	0.0021	0.0013
2	0.0318	0.0034	0.0034	0.0013	0.0039	0.0021	0.0021	0.0013	0.0034	0.0318	0.0013	0.0034	0.0021	0.0039	0.0013	0.0021	0.0034	0.0013	0.0318	0.0034	0.0021	0.0013	0.0039	0.0021
3	0.0021	0.0013	0.0039	0.0021	0.0034	0.0013	0.0318	0.0034	0.0034	0.0013	0.0318	0.0034	0.0021	0.0013	0.0039	0.0021	0.0039	0.0021	0.0021	0.0013	0.0318	0.0034	0.0034	0.0013
4	0.0034	0.0013	0.0318	0.0034	0.0021	0.0013	0.0039	0.0021	0.0013	0.0034	0.0034	0.0318	0.0013	0.0021	0.0021	0.0039	0.0021	0.0013	0.0039	0.0021	0.0034	0.0013	0.0318	0.0034
5	0.0021	0.0039	0.0013	0.0021	0.0034	0.0318	0.0013	0.0034	0.0039	0.0021	0.0021	0.0013	0.0318	0.0034	0.0034	0.0013	0.0034	0.0318	0.0013	0.0034	0.0021	0.0039	0.0013	0.0021
6	0.0034	0.0318	0.0013	0.0034	0.0021	0.0039	0.0013	0.0021	0.0021	0.0039	0.0013	0.0021	0.0034	0.0318	0.0013	0.0034	0.0013	0.0034	0.0034	0.0318	0.0013	0.0021	0.0021	0.0039
7	0.0013	0.0021	0.0021	0.0039	0.0013	0.0034	0.0034	0.0318	0.0021	0.0013	0.0039	0.0021	0.0034	0.0013	0.0318	0.0034	0.0021	0.0039	0.0013	0.0021	0.0034	0.0318	0.0013	0.0034
8	0.0013	0.0034	0.0034	0.0318	0.0013	0.0021	0.0021	0.0039	0.0013	0.0021	0.0021	0.0039	0.0013	0.0034	0.0034	0.0318	0.0013	0.0021	0.0021	0.0039	0.0013	0.0034	0.0034	0.0318

Figure 85 - Screenshot of the captured values for each cell of the Q matrix as calculated in the FNM and the benchmark code from Monnaemang (2015).

FNM

Row \ Column	1	2	3	4	5	6	7	8	9	10	11	12	13	14	15	16	17	18	19	20	21	22	23	24
1	0.0423	0.0230	0.0230	0.0146	0.3441	0.0372	0.0372	0.0144	0.3441	0.0372	0.0372	0.0144	0.0423	0.0230	0.0230	0.0146	0.3441	0.0372	0.0372	0.0144	0.0423	0.0230	0.0230	0.0146
2	0.3441	0.0372	0.0372	0.0144	0.0423	0.0230	0.0230	0.0146	0.0372	0.3441	0.0144	0.0372	0.0230	0.0423	0.0146	0.0230	0.0372	0.0144	0.3441	0.0372	0.0230	0.0146	0.0423	0.0230
3	0.0230	0.0146	0.0423	0.0230	0.0372	0.0144	0.3441	0.0372	0.0372	0.0144	0.3441	0.0372	0.0230	0.0146	0.0423	0.0230	0.0423	0.0230	0.0230	0.0146	0.3441	0.0372	0.0372	0.0144
4	0.0372	0.0144	0.3441	0.0372	0.0230	0.0146	0.0423	0.0230	0.0144	0.0372	0.0372	0.3441	0.0146	0.0230	0.0230	0.0423	0.0230	0.0146	0.0423	0.0230	0.0372	0.0144	0.3441	0.0372
5	0.0230	0.0423	0.0146	0.0230	0.0372	0.3441	0.0144	0.0372	0.0423	0.0230	0.0230	0.0146	0.3441	0.0372	0.0372	0.0144	0.0372	0.3441	0.0144	0.0372	0.0230	0.0423	0.0146	0.0230
6	0.0372	0.3441	0.0144	0.0372	0.0230	0.0423	0.0146	0.0230	0.0230	0.0423	0.0146	0.0230	0.0372	0.3441	0.0144	0.0372	0.0144	0.0372	0.3441	0.0146	0.0230	0.0372	0.0230	0.0423
7	0.0146	0.0230	0.0230	0.0423	0.0144	0.0372	0.0372	0.3441	0.0230	0.0146	0.0423	0.0230	0.0372	0.0144	0.3441	0.0372	0.0230	0.0423	0.0146	0.0230	0.0372	0.3441	0.0144	0.0372
8	0.0144	0.0372	0.0372	0.3441	0.0146	0.0230	0.0230	0.0423	0.0146	0.0230	0.0230	0.0423	0.0144	0.0372	0.0372	0.3441	0.0146	0.0230	0.0230	0.0423	0.0144	0.0372	0.0372	0.3441

Benchmark

Row \ Column	1	2	3	4	5	6	7	8	9	10	11	12	13	14	15	16	17	18	19	20	21	22	23	24
1	0.0423	0.0230	0.0230	0.0146	0.3441	0.0372	0.0372	0.0144	0.3441	0.0372	0.0372	0.0144	0.0423	0.0230	0.0230	0.0146	0.3441	0.0372	0.0372	0.0144	0.0423	0.0230	0.0230	0.0146
2	0.3441	0.0372	0.0372	0.0144	0.0423	0.0230	0.0230	0.0146	0.0372	0.3441	0.0144	0.0372	0.0230	0.0423	0.0146	0.0230	0.0372	0.0144	0.3441	0.0372	0.0230	0.0146	0.0423	0.0230
3	0.0230	0.0146	0.0423	0.0230	0.0372	0.0144	0.3441	0.0372	0.0372	0.0144	0.3441	0.0372	0.0230	0.0146	0.0423	0.0230	0.0423	0.0230	0.0230	0.0146	0.3441	0.0372	0.0372	0.0144
4	0.0372	0.0144	0.3441	0.0372	0.0230	0.0146	0.0423	0.0230	0.0144	0.0372	0.0372	0.3441	0.0146	0.0230	0.0230	0.0423	0.0230	0.0146	0.0423	0.0230	0.0372	0.0144	0.3441	0.0372
5	0.0230	0.0423	0.0146	0.0230	0.0372	0.3441	0.0144	0.0372	0.0423	0.0230	0.0230	0.0146	0.3441	0.0372	0.0372	0.0144	0.0372	0.3441	0.0144	0.0372	0.0230	0.0423	0.0146	0.0230
6	0.0372	0.3441	0.0144	0.0372	0.0230	0.0423	0.0146	0.0230	0.0230	0.0423	0.0146	0.0230	0.0372	0.3441	0.0144	0.0372	0.0144	0.0372	0.3441	0.0146	0.0230	0.0372	0.0230	0.0423
7	0.0146	0.0230	0.0230	0.0423	0.0144	0.0372	0.0372	0.3441	0.0230	0.0146	0.0423	0.0230	0.0372	0.0144	0.3441	0.0372	0.0230	0.0423	0.0146	0.0230	0.0372	0.3441	0.0144	0.0372
8	0.0144	0.0372	0.0372	0.3441	0.0146	0.0230	0.0230	0.0423	0.0146	0.0230	0.0230	0.0423	0.0144	0.0372	0.0372	0.3441	0.0146	0.0230	0.0230	0.0423	0.0144	0.0372	0.0372	0.3441

Figure 86 - Screenshot of the captured values for each cell of the R matrix as calculated in the FNM and the benchmark code from Monnaemang (2015).

		FNM							
		Column							
		1	2	3	4	5	6	7	8
Row	1	1.0000	0.0000	0.0000	0.0000	0.0000	0.0000	0.0000	0.0000
	2	0.0000	1.0000	0.0000	0.0000	0.0000	0.0000	0.0000	0.0000
	3	0.0000	0.0000	1.0000	0.0000	0.0000	0.0000	0.0000	0.0000
	4	0.0000	0.0000	0.0000	1.0000	0.0000	0.0000	0.0000	0.0000
	5	0.0000	0.0000	0.0000	0.0000	1.0000	0.0000	0.0000	0.0000
	6	0.0000	0.0000	0.0000	0.0000	0.0000	1.0000	0.0000	0.0000
	7	0.0000	0.0000	0.0000	0.0000	0.0000	0.0000	1.0000	0.0000
	8	0.0000	0.0000	0.0000	0.0000	0.0000	0.0000	0.0000	1.0000
		Benchmark							
		Column							
		1	2	3	4	5	6	7	8
Row	1	1.0000	0.0000	0.0000	0.0000	0.0000	0.0000	0.0000	0.0000
	2	0.0000	1.0000	0.0000	0.0000	0.0000	0.0000	0.0000	0.0000
	3	0.0000	0.0000	1.0000	0.0000	0.0000	0.0000	0.0000	0.0000
	4	0.0000	0.0000	0.0000	1.0000	0.0000	0.0000	0.0000	0.0000
	5	0.0000	0.0000	0.0000	0.0000	1.0000	0.0000	0.0000	0.0000
	6	0.0000	0.0000	0.0000	0.0000	0.0000	1.0000	0.0000	0.0000
	7	0.0000	0.0000	0.0000	0.0000	0.0000	0.0000	1.0000	0.0000
	8	0.0000	0.0000	0.0000	0.0000	0.0000	0.0000	0.0000	1.0000

Figure 87 - Screenshot of the captured values for each cell of the W matrix as calculated in the FNM and the benchmark code from Monnaemang (2015).

		FNM							
		Column							
		1	2	3	4	5	6	7	8
Row	1	0.0000	0.0287	0.0287	0.0131	0.0287	0.0131	0.0131	0.0082
	2	0.0287	0.0000	0.0131	0.0287	0.0131	0.0287	0.0082	0.0131
	3	0.0287	0.0131	0.0000	0.0287	0.0131	0.0082	0.0287	0.0131
	4	0.0131	0.0287	0.0287	0.0000	0.0082	0.0131	0.0131	0.0287
	5	0.0287	0.0131	0.0131	0.0082	0.0000	0.0287	0.0287	0.0131
	6	0.0131	0.0287	0.0082	0.0131	0.0287	0.0000	0.0131	0.0287
	7	0.0131	0.0082	0.0287	0.0131	0.0287	0.0131	0.0000	0.0287
	8	0.0082	0.0131	0.0131	0.0287	0.0131	0.0287	0.0287	0.0000
		Benchmark							
		Column							
		1	2	3	4	5	6	7	8
Row	1	0.0000	0.0287	0.0287	0.0131	0.0287	0.0131	0.0131	0.0082
	2	0.0287	0.0000	0.0131	0.0287	0.0131	0.0287	0.0082	0.0131
	3	0.0287	0.0131	0.0000	0.0287	0.0131	0.0082	0.0287	0.0131
	4	0.0131	0.0287	0.0287	0.0000	0.0082	0.0131	0.0131	0.0287
	5	0.0287	0.0131	0.0131	0.0082	0.0000	0.0287	0.0287	0.0131
	6	0.0131	0.0287	0.0082	0.0131	0.0287	0.0000	0.0131	0.0287
	7	0.0131	0.0082	0.0287	0.0131	0.0287	0.0131	0.0000	0.0287
	8	0.0082	0.0131	0.0131	0.0287	0.0131	0.0287	0.0287	0.0000

Figure 88 - Screenshot of the captured values for each cell of the C matrix as calculated in the FNM and the benchmark code from Monnaemang (2015).

Appendix C. Isothermal mass flow maps

The isothermal CFD simulations were created in OpenFOAM® to create a mass flow map from. Screenshots of the flow vectors and stream lines are shown in the figures below.

Cut in yz- plane with velocity magnitude imposed

Burner inlet

Cut in yz-plane with x-direction flow velocity imposed

Cut in yz- plane with y-direction flow velocity imposed

Cut in yz- plane with z-direction flow velocity imposed

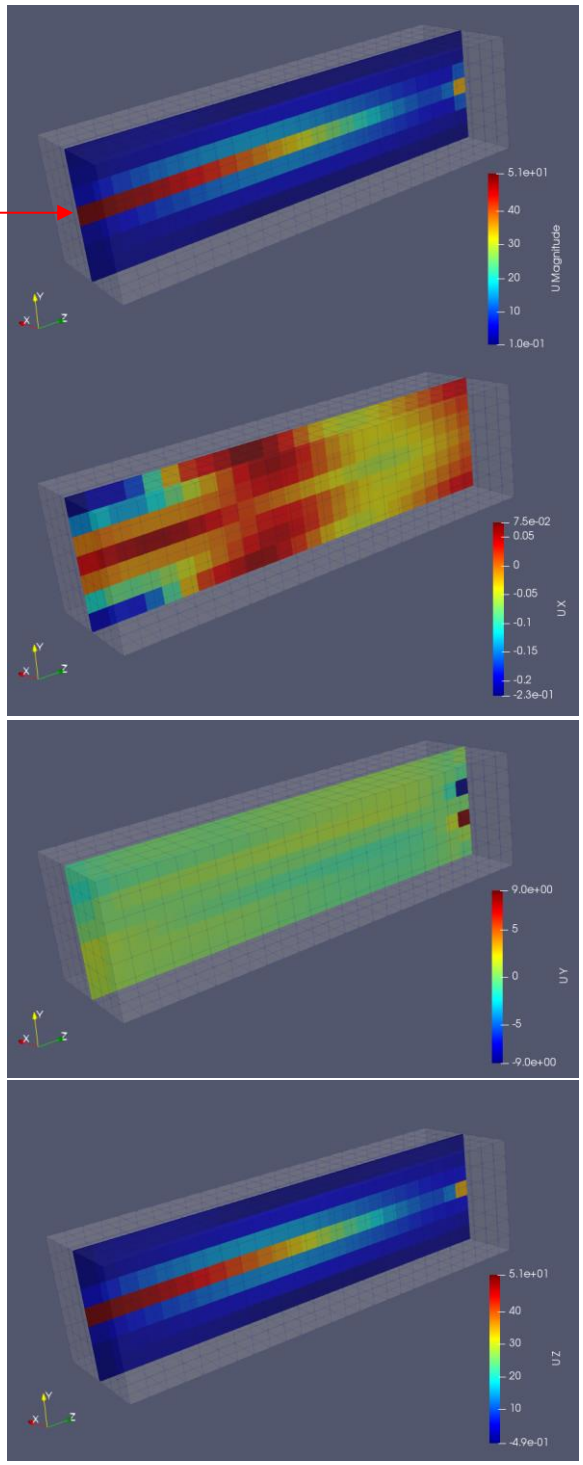

Figure 89 - Flow vectors for the isothermal CFD runs for the single-burner furnace.

Cut in xy-plane with velocity magnitude imposed

Burner inlet

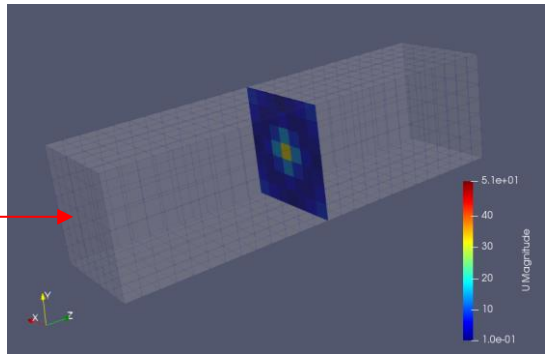

Cut in xy-plane with x-direction flow velocity imposed

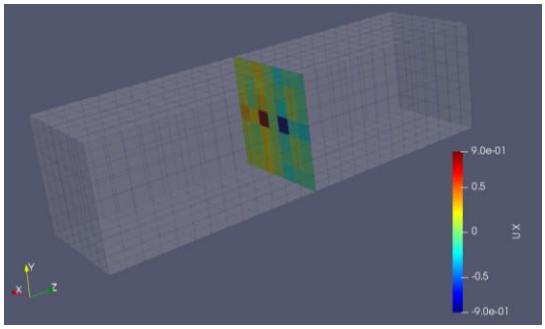

Cut in xy-plane with y-direction flow velocity imposed

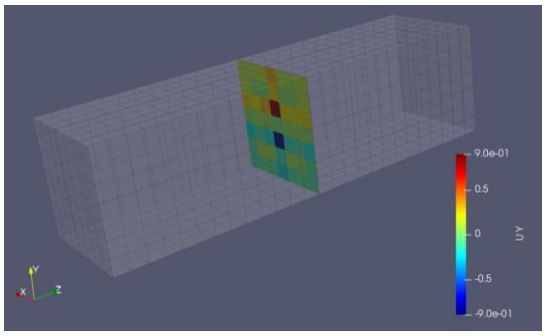

Cut in xy-plane with z-direction flow velocity imposed

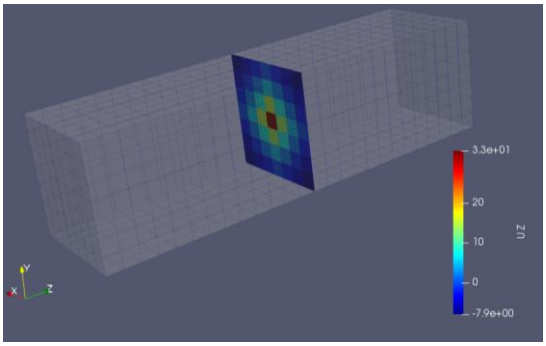

Figure 90 - Flow vectors for the isothermal CFD runs for the single-burner furnace (continued).

Stream lines with velocity magnitude imposed

Burner inlet

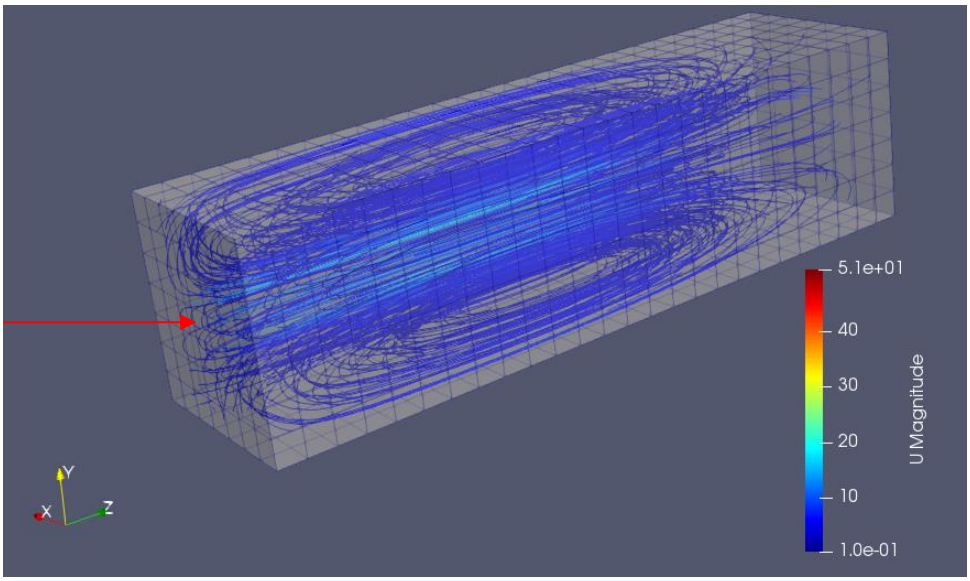

Figure 91 - Stream lines for the isothermal CFD runs for the single-burner furnace.

Cut in yz-plane with x-direction flow velocity imposed

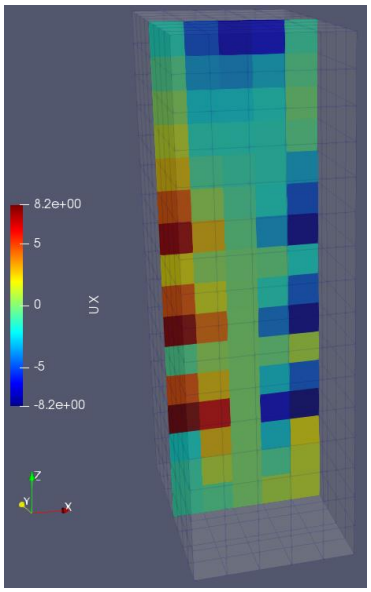

Cut in yz- plane with velocity magnitude imposed

Top

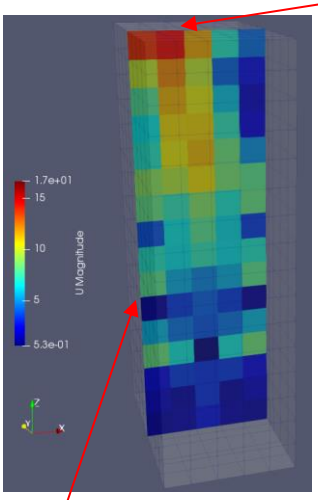

Front wall side

Cut in yz- plane with y-direction flow velocity imposed

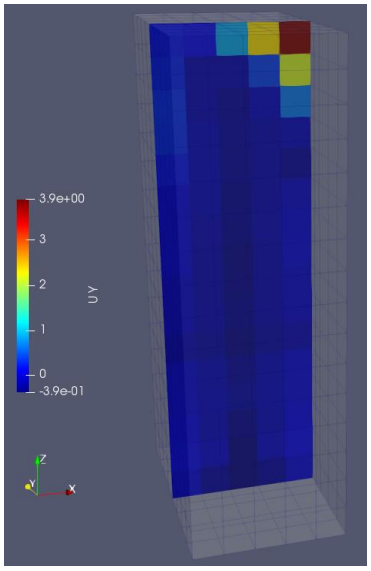

Cut in yz- plane with z-direction flow velocity imposed

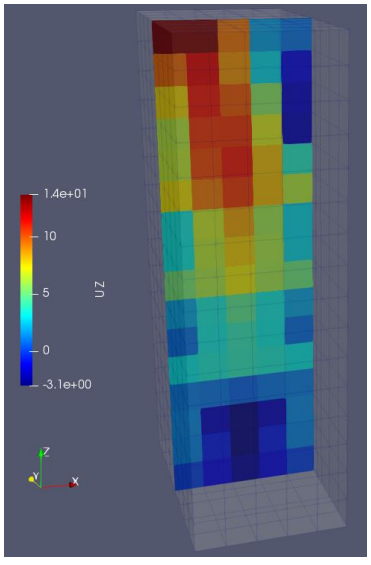

Figure 92 - Flow vectors for the isothermal CFD runs for the multiple-burner furnace (99% load).

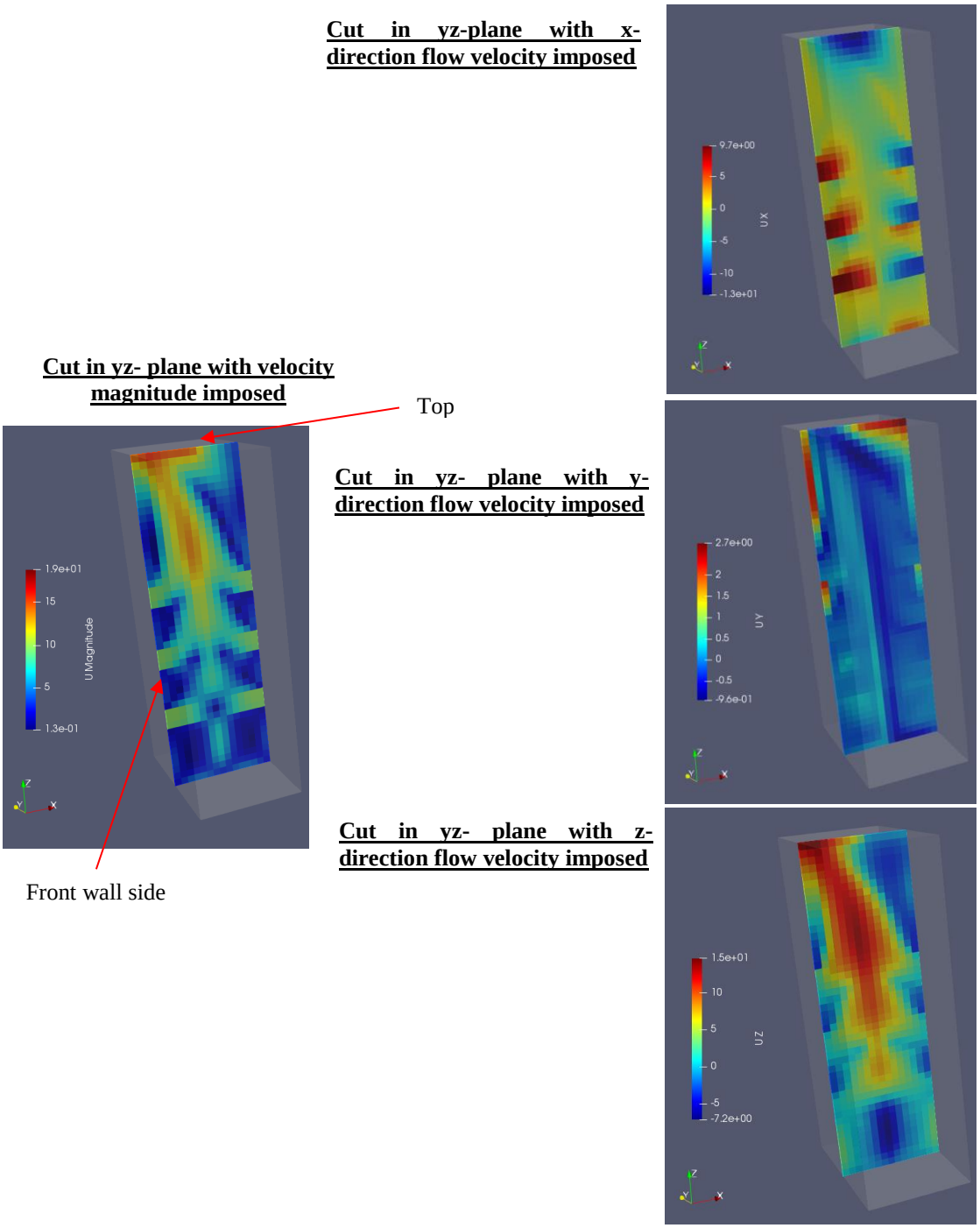

Figure 93 - Flow vectors for the isothermal CFD runs with a finer discretisation than Figure 92 for the multiple-burner furnace (99% load).

Cut in yz-plane with x-direction flow velocity imposed

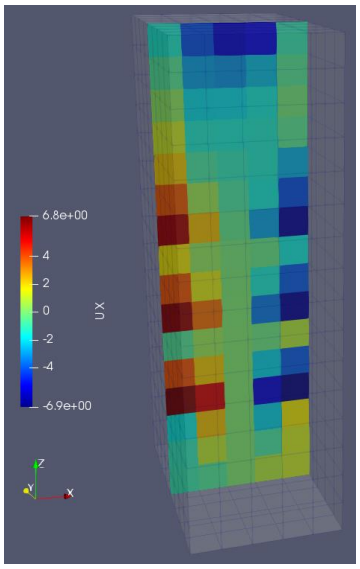

Cut in yz- plane with velocity magnitude imposed

Top

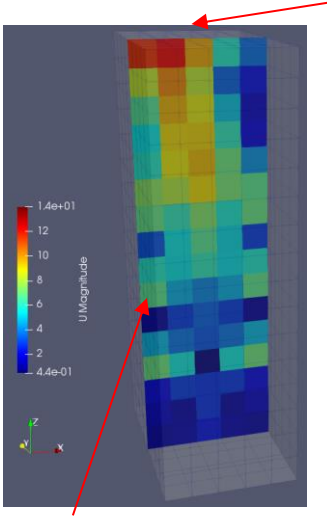

Front wall side

Cut in yz- plane with y-direction flow velocity imposed

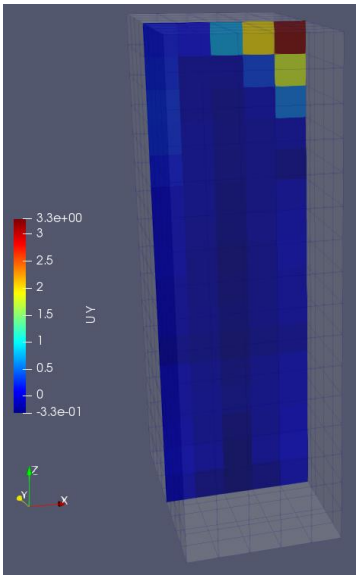

Cut in yz- plane with z-direction flow velocity imposed

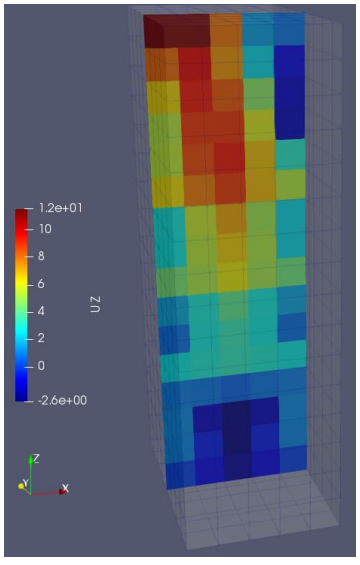

Figure 94 - Flow vectors for the isothermal CFD runs for the multiple-burner furnace (81% load).

Cut in yz-plane with x-direction flow velocity imposed

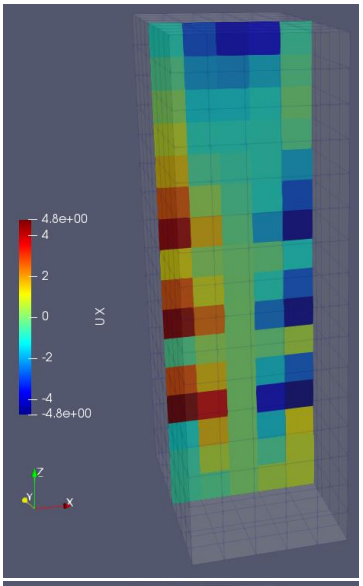

Cut in yz- plane with velocity magnitude imposed

Top

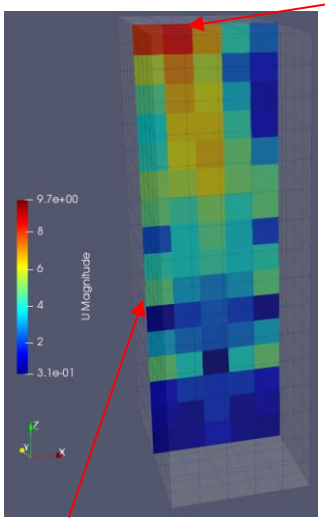

Front wall side

Cut in yz- plane with y-direction flow velocity imposed

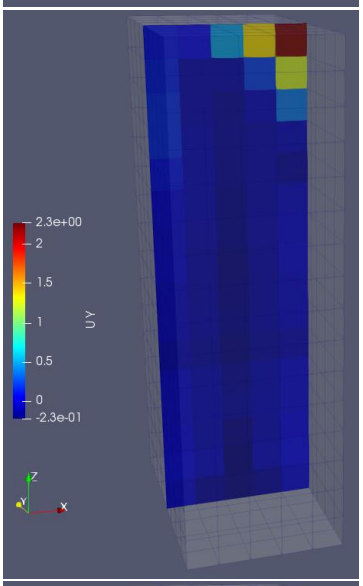

Cut in yz- plane with z-direction flow velocity imposed

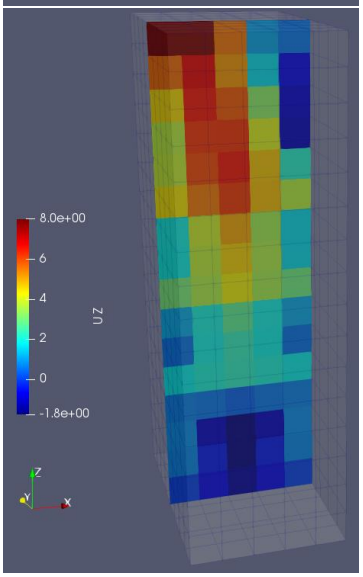

Figure 95 - Flow vectors for the isothermal CFD runs for the multiple-burner furnace (60.5% load).

Appendix D. Heat flux results

The heat flux results for the CFD and FNM cases in section 4.2.8 and 5.5 are duplicates and enlarged version to better visualise the numbers within the figures.

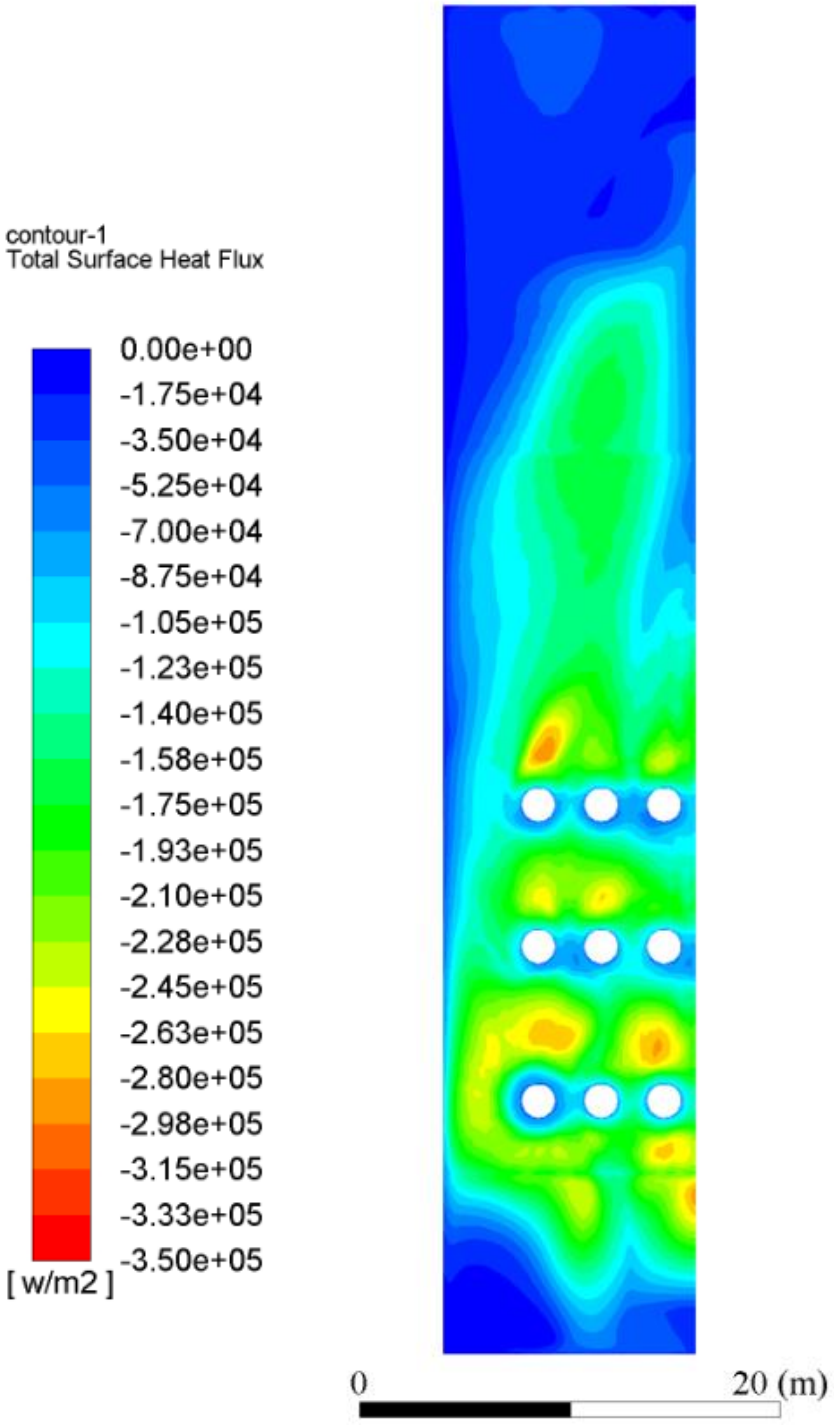

Figure 96 - The heat flux distribution (in W/m^2) to the front wall for the CFD case at 99%.

-1.09E+05	-1.36E+05	-1.41E+05	-1.34E+05	-1.35E+05	-1.42E+05	-1.36E+05	-1.09E+05
-1.54E+05	-1.72E+05	-1.80E+05	-1.67E+05	-1.68E+05	-1.82E+05	-1.73E+05	-1.55E+05
-1.84E+05	-2.21E+05	-2.30E+05	-2.08E+05	-2.09E+05	-2.32E+05	-2.22E+05	-1.85E+05
-2.12E+05	-2.86E+05	-3.78E+05	-2.56E+05	-2.59E+05	-3.83E+05	-2.89E+05	-2.12E+05
-2.33E+05	-3.74E+05	-3.19E+05	-7.31E+05	-6.09E+05	-3.42E+05	-3.76E+05	-2.34E+05
-2.12E+05	-2.25E+05	-2.26E+05	-3.06E+05	-2.98E+05	-2.27E+05	-2.26E+05	-2.12E+05
-2.11E+05	-1.93E+05	-2.33E+05	-2.35E+05	-2.35E+05	-2.33E+05	-1.93E+05	-2.11E+05
-2.32E+05	-3.80E+05	-6.16E+05	-3.96E+05	-3.98E+05	-6.15E+05	-3.81E+05	-2.32E+05
-2.08E+05	-2.12E+05	-2.59E+05	-2.36E+05	-2.36E+05	-2.59E+05	-2.13E+05	-2.08E+05
-1.87E+05	-1.72E+05	-1.90E+05	-2.09E+05	-2.09E+05	-1.90E+05	-1.72E+05	-1.87E+05
-2.08E+05	-3.27E+05	-2.72E+05	-4.51E+05	-4.50E+05	-2.72E+05	-3.27E+05	-2.08E+05
-1.69E+05	-1.99E+05	-2.30E+05	-2.67E+05	-2.67E+05	-2.30E+05	-1.99E+05	-1.69E+05
-1.45E+05	-1.41E+05	-1.68E+05	-1.93E+05	-1.93E+05	-1.68E+05	-1.41E+05	-1.45E+05
-1.18E+05	-1.30E+05	-1.57E+05	-1.89E+05	-1.89E+05	-1.57E+05	-1.30E+05	-1.18E+05
-7.75E+04	-9.72E+04	-1.11E+05	-1.11E+05	-1.11E+05	-1.11E+05	-9.72E+04	-7.76E+04
-5.30E+04	-7.94E+04	-9.01E+04	-9.59E+04	-9.59E+04	-9.02E+04	-7.95E+04	-5.30E+04

Figure 97 - The heat flux distribution (in W/m^2) to the front wall for the base FNM case at 99%.

-1.05E+05	-1.30E+05	-1.40E+05	-1.40E+05	-1.41E+05	-1.40E+05	-1.31E+05	-1.05E+05
-1.35E+05	-1.74E+05	-1.87E+05	-1.83E+05	-1.85E+05	-1.89E+05	-1.74E+05	-1.35E+05
-1.54E+05	-2.05E+05	-2.24E+05	-2.08E+05	-2.14E+05	-2.28E+05	-2.06E+05	-1.54E+05
-1.65E+05	-2.26E+05	-2.58E+05	-2.36E+05	-2.65E+05	-2.63E+05	-2.27E+05	-1.65E+05
-1.67E+05	-2.21E+05	-2.43E+05	-2.41E+05	-2.46E+05	-2.44E+05	-2.21E+05	-1.68E+05
-1.61E+05	-1.81E+05	-1.93E+05	-1.98E+05	-1.99E+05	-1.93E+05	-1.82E+05	-1.61E+05
-1.52E+05	-1.60E+05	-1.72E+05	-1.78E+05	-1.79E+05	-1.73E+05	-1.60E+05	-1.53E+05
-1.50E+05	-1.76E+05	-1.85E+05	-1.88E+05	-1.88E+05	-1.85E+05	-1.76E+05	-1.50E+05
-1.35E+05	-1.47E+05	-1.54E+05	-1.58E+05	-1.58E+05	-1.54E+05	-1.47E+05	-1.35E+05
-1.20E+05	-1.25E+05	-1.34E+05	-1.37E+05	-1.37E+05	-1.34E+05	-1.25E+05	-1.21E+05
-1.12E+05	-1.34E+05	-1.54E+05	-1.57E+05	-1.57E+05	-1.54E+05	-1.34E+05	-1.12E+05
-9.04E+04	-9.96E+04	-1.04E+05	-1.06E+05	-1.06E+05	-1.04E+05	-9.98E+04	-9.06E+04
-7.34E+04	-7.74E+04	-8.08E+04	-8.21E+04	-8.22E+04	-8.10E+04	-7.76E+04	-7.36E+04
-6.83E+04	-7.78E+04	-8.18E+04	-8.31E+04	-8.31E+04	-8.19E+04	-7.80E+04	-6.85E+04
-6.06E+04	-7.36E+04	-8.02E+04	-8.31E+04	-8.32E+04	-8.03E+04	-7.38E+04	-6.07E+04
-4.97E+04	-6.31E+04	-7.13E+04	-7.42E+04	-7.42E+04	-7.13E+04	-6.32E+04	-4.98E+04

Figure 98 - The heat flux distribution (in W/m^2) to the front wall for the calibrated FNM case at 99%.

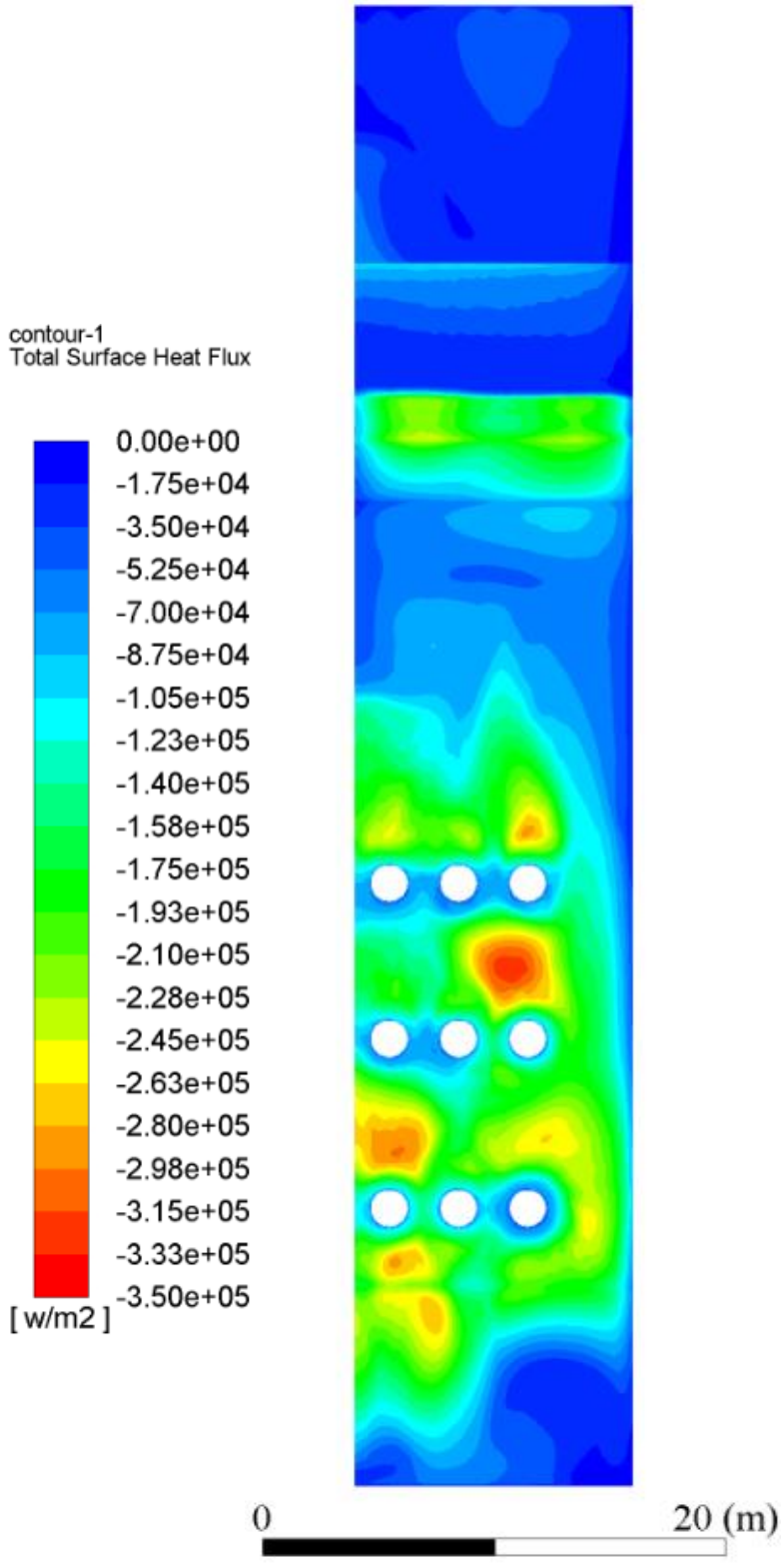

Figure 99 - The heat flux distribution (in W/m^2) to the rear wall for the CFD case at 99%.

-1.33E+05	-1.97E+05	-2.23E+05	-2.22E+05	-2.18E+05	-2.25E+05	-1.97E+05	-1.33E+05
-1.76E+05	-2.15E+05	-2.43E+05	-2.37E+05	-2.34E+05	-2.39E+05	-2.16E+05	-1.77E+05
-2.00E+05	-2.55E+05	-2.94E+05	-2.67E+05	-2.64E+05	-2.89E+05	-2.51E+05	-2.01E+05
-2.21E+05	-3.13E+05	-4.26E+05	-3.05E+05	-3.07E+05	-4.21E+05	-3.08E+05	-2.22E+05
-2.38E+05	-3.87E+05	-3.99E+05	-7.38E+05	-7.34E+05	-4.00E+05	-3.82E+05	-2.38E+05
-2.15E+05	-2.32E+05	-2.38E+05	-3.24E+05	-3.17E+05	-2.39E+05	-2.32E+05	-2.15E+05
-2.12E+05	-1.94E+05	-2.33E+05	-2.38E+05	-2.33E+05	-2.28E+05	-1.94E+05	-2.12E+05
-2.31E+05	-3.71E+05	-5.94E+05	-3.87E+05	-3.83E+05	-5.89E+05	-3.67E+05	-2.31E+05
-2.08E+05	-2.10E+05	-2.55E+05	-2.33E+05	-2.34E+05	-2.50E+05	-2.06E+05	-2.08E+05
-1.87E+05	-1.71E+05	-1.90E+05	-2.10E+05	-2.10E+05	-1.90E+05	-1.67E+05	-1.87E+05
-2.09E+05	-3.28E+05	-2.78E+05	-4.57E+05	-4.56E+05	-2.79E+05	-3.28E+05	-2.09E+05
-1.69E+05	-1.99E+05	-2.31E+05	-2.69E+05	-2.69E+05	-2.27E+05	-2.00E+05	-1.70E+05
-1.45E+05	-1.41E+05	-1.68E+05	-1.93E+05	-1.94E+05	-1.63E+05	-1.37E+05	-1.46E+05
-1.18E+05	-1.30E+05	-1.57E+05	-1.89E+05	-1.89E+05	-1.52E+05	-1.26E+05	-1.18E+05
-7.76E+04	-9.72E+04	-1.11E+05	-1.11E+05	-1.11E+05	-1.11E+05	-9.25E+04	-7.78E+04
-5.30E+04	-7.95E+04	-9.01E+04	-9.57E+04	-9.57E+04	-9.01E+04	-7.96E+04	-5.31E+04

Figure 100 - The heat flux distribution (in W/m^2) to the rear wall for the base FNM case at 99%.

-1.13E+05	-1.51E+05	-1.72E+05	-1.80E+05	-1.75E+05	-1.72E+05	-1.51E+05	-1.13E+05
-1.42E+05	-1.92E+05	-2.22E+05	-2.35E+05	-2.30E+05	-2.17E+05	-1.92E+05	-1.42E+05
-1.58E+05	-2.17E+05	-2.53E+05	-2.69E+05	-2.64E+05	-2.48E+05	-2.13E+05	-1.58E+05
-1.67E+05	-2.32E+05	-2.76E+05	-2.94E+05	-2.94E+05	-2.71E+05	-2.27E+05	-1.67E+05
-1.68E+05	-2.23E+05	-2.47E+05	-2.53E+05	-2.53E+05	-2.47E+05	-2.18E+05	-1.68E+05
-1.61E+05	-1.82E+05	-1.94E+05	-2.00E+05	-1.95E+05	-1.95E+05	-1.82E+05	-1.62E+05
-1.53E+05	-1.60E+05	-1.73E+05	-1.79E+05	-1.74E+05	-1.68E+05	-1.60E+05	-1.53E+05
-1.50E+05	-1.76E+05	-1.86E+05	-1.88E+05	-1.84E+05	-1.81E+05	-1.71E+05	-1.50E+05
-1.35E+05	-1.47E+05	-1.54E+05	-1.58E+05	-1.58E+05	-1.49E+05	-1.42E+05	-1.35E+05
-1.20E+05	-1.25E+05	-1.33E+05	-1.37E+05	-1.37E+05	-1.33E+05	-1.20E+05	-1.21E+05
-1.12E+05	-1.34E+05	-1.53E+05	-1.55E+05	-1.55E+05	-1.53E+05	-1.34E+05	-1.12E+05
-9.03E+04	-9.93E+04	-1.04E+05	-1.05E+05	-1.05E+05	-9.90E+04	-9.95E+04	-9.04E+04
-7.33E+04	-7.72E+04	-8.06E+04	-8.18E+04	-8.19E+04	-7.61E+04	-7.28E+04	-7.34E+04
-6.83E+04	-7.77E+04	-8.16E+04	-8.29E+04	-8.30E+04	-7.72E+04	-7.33E+04	-6.84E+04
-6.05E+04	-7.36E+04	-8.01E+04	-8.30E+04	-8.31E+04	-8.02E+04	-6.91E+04	-6.06E+04
-4.96E+04	-6.31E+04	-7.12E+04	-7.43E+04	-7.43E+04	-7.13E+04	-6.31E+04	-4.97E+04

Figure 101 - The heat flux distribution (in W/m^2) to the rear wall for the calibrated FNM case at 99%.

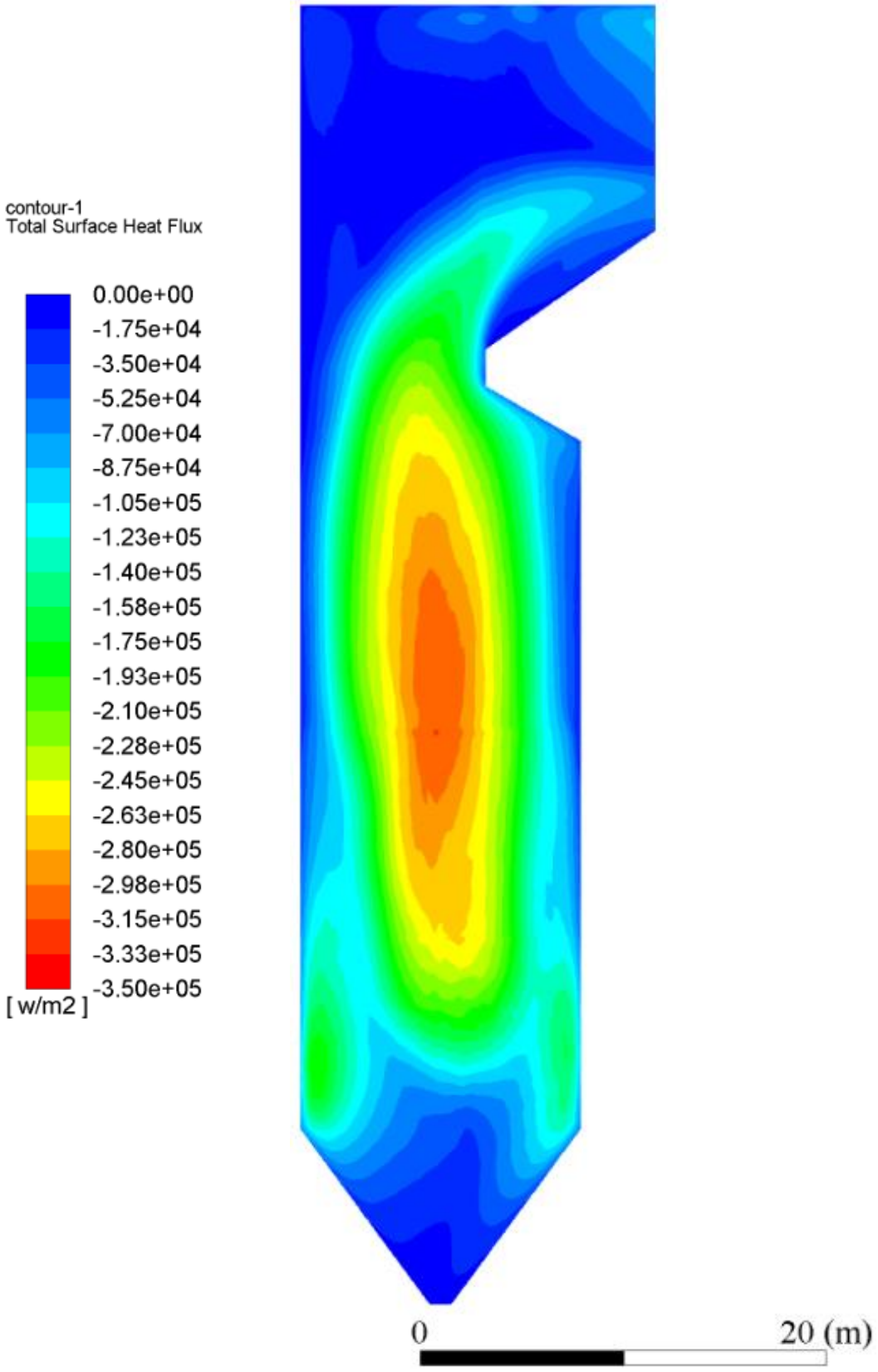

Figure 102 - The heat flux distribution (in W/m^2) to the side wall for the CFD case at 99%.

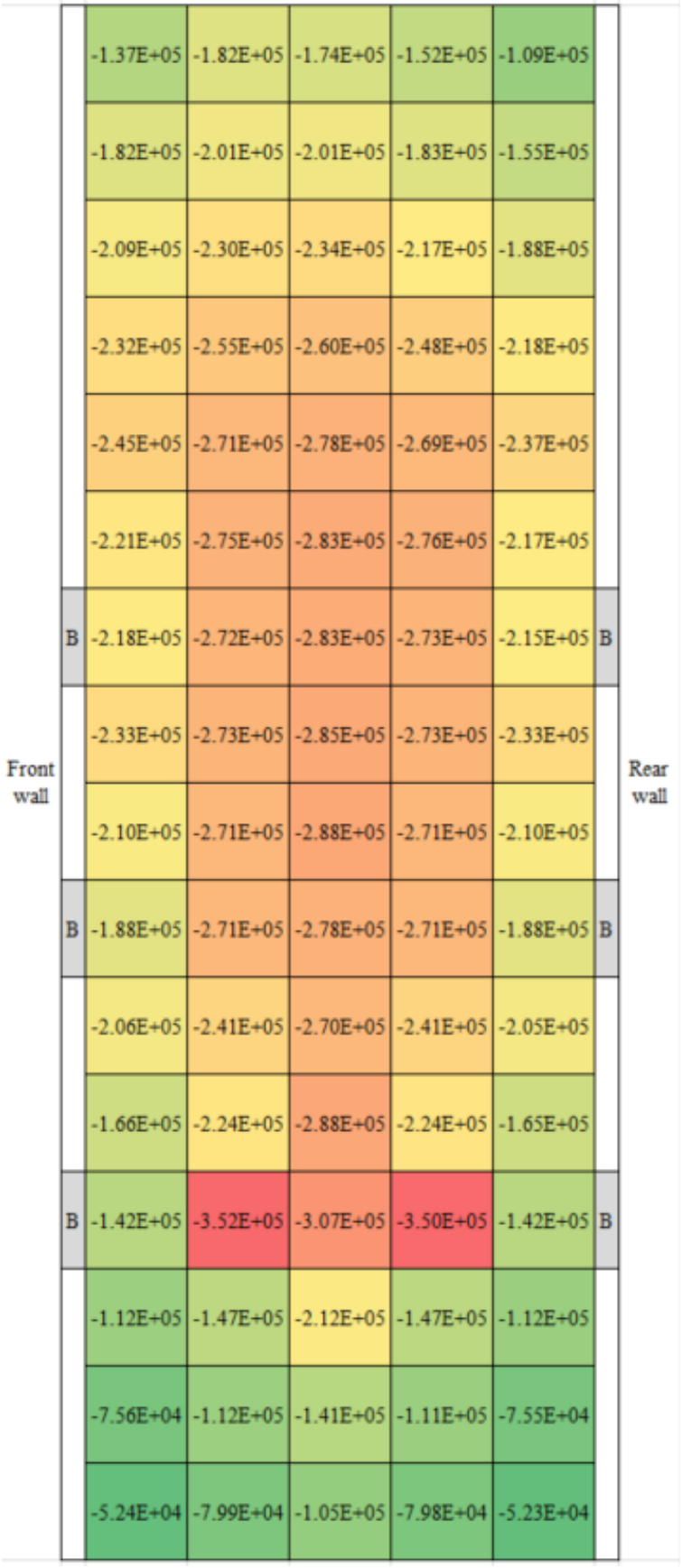

Figure 103 - The heat flux distribution (in W/m^2) to the side wall for the base FNM case at 99%.

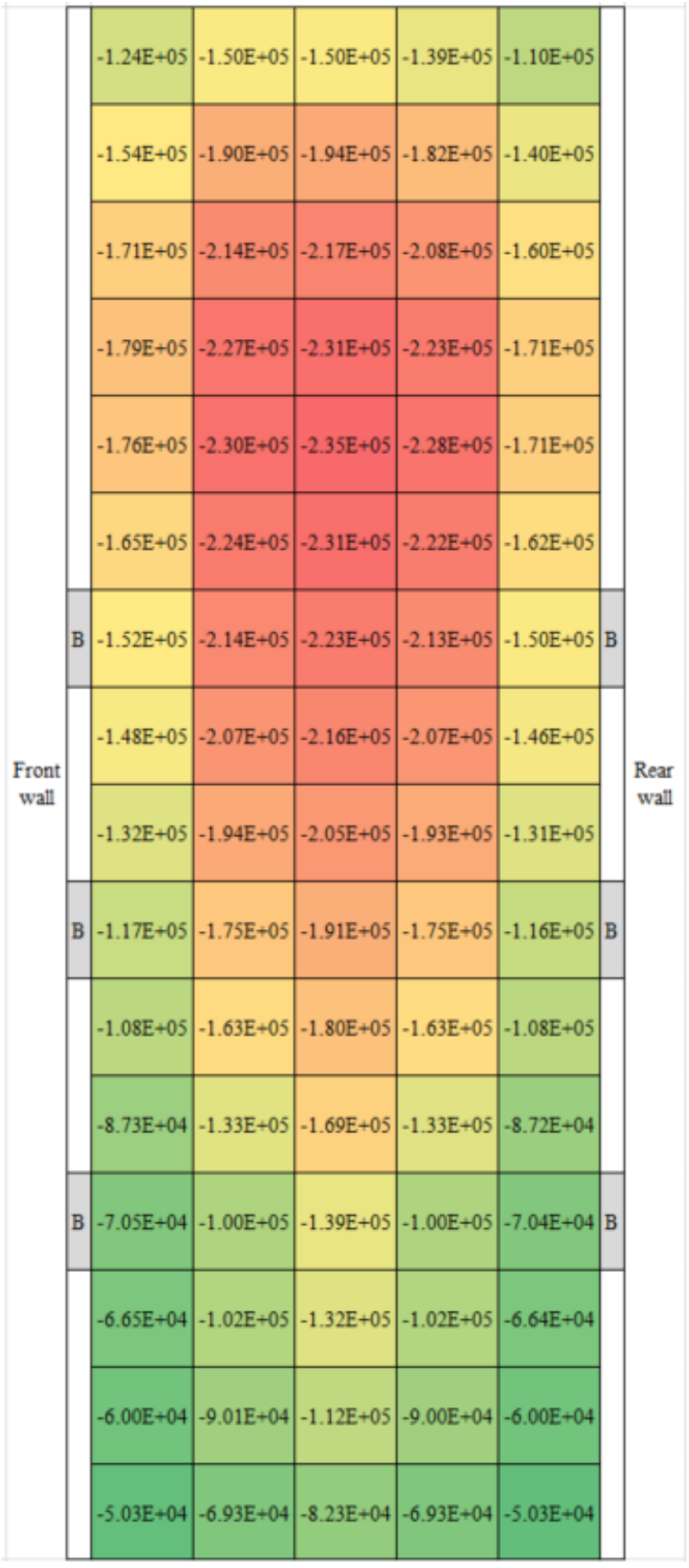

Figure 104 - The heat flux distribution (in W/m^2) to the side wall for the calibrated FNM case at 99%.

-8.88E+04	-1.10E+05	-1.18E+05	-1.18E+05	-1.19E+05	-1.19E+05	-1.10E+05	-8.90E+04
-1.14E+05	-1.47E+05	-1.58E+05	-1.55E+05	-1.56E+05	-1.60E+05	-1.47E+05	-1.14E+05
-1.30E+05	-1.74E+05	-1.91E+05	-1.75E+05	-1.80E+05	-1.94E+05	-1.74E+05	-1.30E+05
-1.39E+05	-1.91E+05	-2.15E+05	-1.96E+05	-2.18E+05	-2.19E+05	-1.92E+05	-1.39E+05
-1.40E+05	-1.80E+05	-1.96E+05	-1.93E+05	-1.97E+05	-1.97E+05	-1.80E+05	-1.40E+05
-1.33E+05	-1.49E+05	-1.58E+05	-1.62E+05	-1.63E+05	-1.59E+05	-1.49E+05	-1.33E+05
-1.26E+05	-1.31E+05	-1.41E+05	-1.46E+05	-1.46E+05	-1.41E+05	-1.32E+05	-1.26E+05
-1.24E+05	-1.42E+05	-1.48E+05	-1.50E+05	-1.50E+05	-1.48E+05	-1.42E+05	-1.24E+05
-1.11E+05	-1.20E+05	-1.24E+05	-1.27E+05	-1.27E+05	-1.25E+05	-1.20E+05	-1.11E+05
-9.82E+04	-1.00E+05	-1.06E+05	-1.09E+05	-1.09E+05	-1.06E+05	-1.01E+05	-9.84E+04
-8.91E+04	-1.05E+05	-1.20E+05	-1.21E+05	-1.21E+05	-1.20E+05	-1.06E+05	-8.93E+04
-7.12E+04	-7.82E+04	-8.11E+04	-8.20E+04	-8.21E+04	-8.13E+04	-7.83E+04	-7.14E+04
-5.80E+04	-6.04E+04	-6.27E+04	-6.35E+04	-6.36E+04	-6.29E+04	-6.06E+04	-5.82E+04
-5.43E+04	-6.13E+04	-6.40E+04	-6.46E+04	-6.46E+04	-6.41E+04	-6.15E+04	-5.44E+04
-4.86E+04	-5.86E+04	-6.33E+04	-6.48E+04	-6.48E+04	-6.34E+04	-5.87E+04	-4.87E+04
-4.01E+04	-5.08E+04	-5.67E+04	-5.96E+04	-5.96E+04	-5.68E+04	-5.09E+04	-4.02E+04

Figure 105 - The heat flux distribution (in W/m^2) to the front wall for the calibrated FNM case at 81%.

-8.71E+04	-1.08E+05	-1.16E+05	-1.16E+05	-1.17E+05	-1.16E+05	-1.08E+05	-8.74E+04
-1.12E+05	-1.44E+05	-1.55E+05	-1.52E+05	-1.53E+05	-1.57E+05	-1.45E+05	-1.12E+05
-1.28E+05	-1.71E+05	-1.87E+05	-1.73E+05	-1.77E+05	-1.90E+05	-1.72E+05	-1.28E+05
-1.37E+05	-1.89E+05	-2.13E+05	-1.94E+05	-2.17E+05	-2.18E+05	-1.90E+05	-1.37E+05
-1.38E+05	-1.79E+05	-1.97E+05	-1.94E+05	-1.98E+05	-1.98E+05	-1.79E+05	-1.39E+05
-1.30E+05	-1.48E+05	-1.58E+05	-1.62E+05	-1.63E+05	-1.58E+05	-1.48E+05	-1.32E+05
-1.24E+05	-1.30E+05	-1.41E+05	-1.46E+05	-1.46E+05	-1.41E+05	-1.31E+05	-1.25E+05
-1.22E+05	-1.42E+05	-1.49E+05	-1.51E+05	-1.52E+05	-1.49E+05	-1.42E+05	-1.23E+05
-1.10E+05	-1.20E+05	-1.25E+05	-1.28E+05	-1.28E+05	-1.25E+05	-1.20E+05	-1.10E+05
-9.77E+04	-1.01E+05	-1.07E+05	-1.10E+05	-1.10E+05	-1.07E+05	-1.01E+05	-9.79E+04
-8.95E+04	-1.06E+05	-1.22E+05	-1.24E+05	-1.24E+05	-1.22E+05	-1.07E+05	-8.97E+04
-7.17E+04	-7.93E+04	-8.27E+04	-8.40E+04	-8.40E+04	-8.28E+04	-7.95E+04	-7.19E+04
-5.84E+04	-6.12E+04	-6.38E+04	-6.49E+04	-6.49E+04	-6.40E+04	-6.13E+04	-5.85E+04
-5.42E+04	-6.14E+04	-6.44E+04	-6.54E+04	-6.55E+04	-6.46E+04	-6.16E+04	-5.43E+04
-4.81E+04	-5.82E+04	-6.33E+04	-6.54E+04	-6.54E+04	-6.34E+04	-5.83E+04	-4.83E+04
-3.96E+04	-5.03E+04	-5.63E+04	-5.87E+04	-5.87E+04	-5.64E+04	-5.04E+04	-3.97E+04

Figure 106 - The heat flux distribution (in W/m^2) to the front wall for the calibrated and normalised FNM case at 81%.

-9.59E+04	-1.28E+05	-1.46E+05	-1.53E+05	-1.49E+05	-1.46E+05	-1.28E+05	-9.60E+04
-1.20E+05	-1.63E+05	-1.89E+05	-2.00E+05	-1.96E+05	-1.84E+05	-1.63E+05	-1.20E+05
-1.34E+05	-1.84E+05	-2.15E+05	-2.29E+05	-2.25E+05	-2.10E+05	-1.80E+05	-1.34E+05
-1.41E+05	-1.96E+05	-2.29E+05	-2.42E+05	-2.42E+05	-2.25E+05	-1.91E+05	-1.41E+05
-1.41E+05	-1.81E+05	-2.00E+05	-2.04E+05	-2.04E+05	-2.00E+05	-1.77E+05	-1.41E+05
-1.33E+05	-1.50E+05	-1.60E+05	-1.65E+05	-1.60E+05	-1.60E+05	-1.50E+05	-1.34E+05
-1.26E+05	-1.32E+05	-1.42E+05	-1.47E+05	-1.42E+05	-1.38E+05	-1.32E+05	-1.27E+05
-1.24E+05	-1.42E+05	-1.49E+05	-1.51E+05	-1.46E+05	-1.44E+05	-1.38E+05	-1.24E+05
-1.11E+05	-1.19E+05	-1.24E+05	-1.27E+05	-1.27E+05	-1.20E+05	-1.15E+05	-1.11E+05
-9.81E+04	-1.00E+05	-1.06E+05	-1.08E+05	-1.08E+05	-1.06E+05	-9.59E+04	-9.82E+04
-8.90E+04	-1.05E+05	-1.19E+05	-1.20E+05	-1.20E+05	-1.19E+05	-1.05E+05	-8.91E+04
-7.11E+04	-7.79E+04	-8.08E+04	-8.16E+04	-8.16E+04	-7.66E+04	-7.80E+04	-7.12E+04
-5.78E+04	-6.02E+04	-6.25E+04	-6.32E+04	-6.32E+04	-5.84E+04	-5.61E+04	-5.79E+04
-5.42E+04	-6.12E+04	-6.38E+04	-6.44E+04	-6.44E+04	-5.97E+04	-5.71E+04	-5.43E+04
-4.85E+04	-5.85E+04	-6.32E+04	-6.46E+04	-6.46E+04	-6.32E+04	-5.44E+04	-4.85E+04
-4.01E+04	-5.07E+04	-5.66E+04	-5.95E+04	-5.95E+04	-5.67E+04	-5.08E+04	-4.01E+04

Figure 107 - The heat flux distribution (in W/m^2) to the rear wall for the calibrated FNM case at 81%.

-9.39E+04	-1.25E+05	-1.43E+05	-1.50E+05	-1.45E+05	-1.43E+05	-1.25E+05	-9.41E+04
-1.18E+05	-1.60E+05	-1.85E+05	-1.96E+05	-1.92E+05	-1.81E+05	-1.60E+05	-1.18E+05
-1.31E+05	-1.81E+05	-2.12E+05	-2.26E+05	-2.21E+05	-2.07E+05	-1.77E+05	-1.32E+05
-1.39E+05	-1.94E+05	-2.27E+05	-2.41E+05	-2.42E+05	-2.23E+05	-1.89E+05	-1.39E+05
-1.39E+05	-1.80E+05	-2.00E+05	-2.04E+05	-2.05E+05	-2.00E+05	-1.76E+05	-1.39E+05
-1.32E+05	-1.49E+05	-1.59E+05	-1.64E+05	-1.60E+05	-1.60E+05	-1.49E+05	-1.32E+05
-1.25E+05	-1.31E+05	-1.42E+05	-1.47E+05	-1.42E+05	-1.37E+05	-1.31E+05	-1.25E+05
-1.22E+05	-1.42E+05	-1.49E+05	-1.52E+05	-1.47E+05	-1.45E+05	-1.38E+05	-1.23E+05
-1.10E+05	-1.20E+05	-1.25E+05	-1.28E+05	-1.28E+05	-1.20E+05	-1.15E+05	-1.10E+05
-9.76E+04	-1.00E+05	-1.07E+05	-1.10E+05	-1.10E+05	-1.07E+05	-9.60E+04	-9.77E+04
-8.94E+04	-1.06E+05	-1.21E+05	-1.23E+05	-1.23E+05	-1.21E+05	-1.06E+05	-8.95E+04
-7.16E+04	-7.90E+04	-8.23E+04	-8.35E+04	-8.35E+04	-7.79E+04	-7.91E+04	-7.17E+04
-5.82E+04	-6.10E+04	-6.36E+04	-6.45E+04	-6.46E+04	-5.91E+04	-5.66E+04	-5.83E+04
-5.41E+04	-6.13E+04	-6.42E+04	-6.52E+04	-6.52E+04	-5.98E+04	-5.69E+04	-5.42E+04
-4.80E+04	-5.81E+04	-6.31E+04	-6.52E+04	-6.52E+04	-6.32E+04	-5.37E+04	-4.81E+04
-3.95E+04	-5.02E+04	-5.62E+04	-5.86E+04	-5.86E+04	-5.62E+04	-5.03E+04	-3.96E+04

Figure 108 - The heat flux distribution (in W/m^2) to the rear wall for the calibrated and normalised FNM case at 81%.

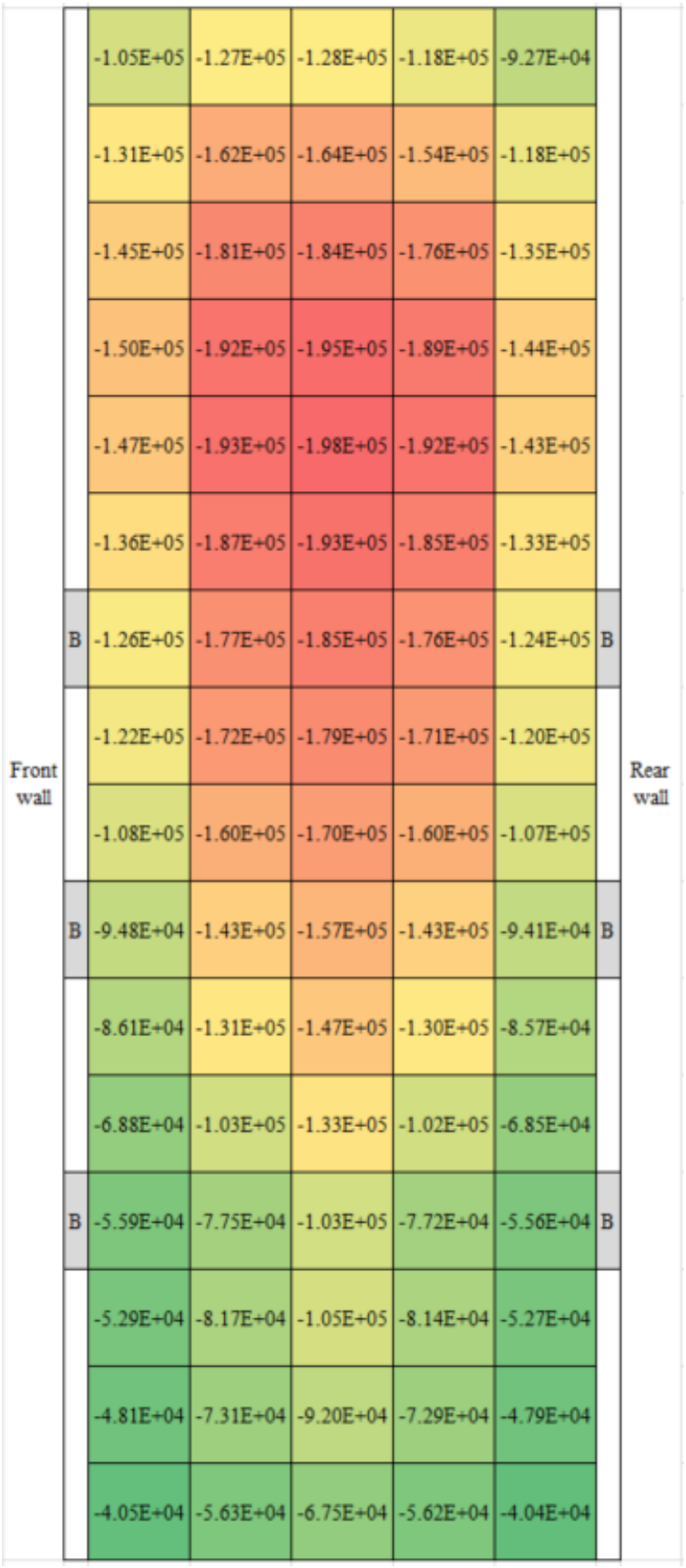

Figure 109 - The heat flux distribution (in W/m^2) to the side wall for the calibrated FNM case at 81%.

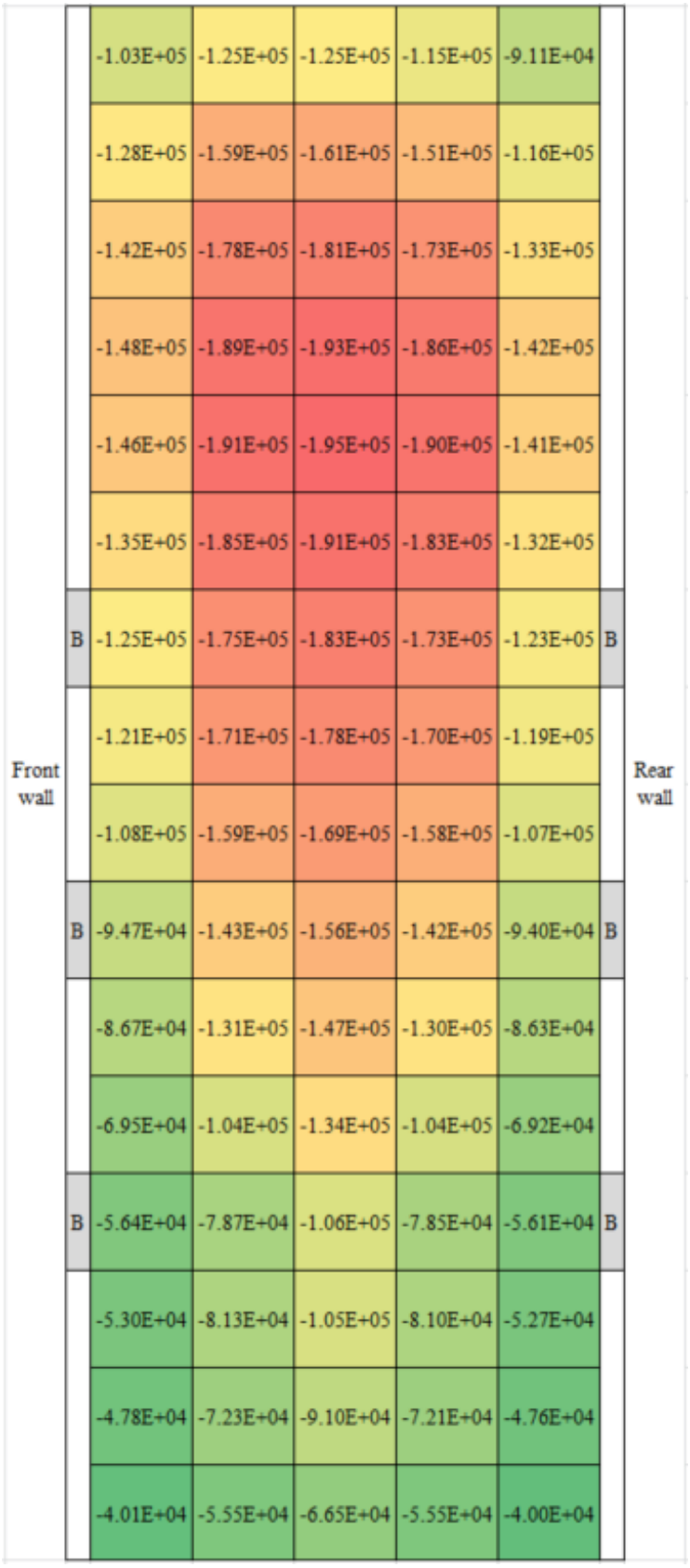

Figure 110 - The heat flux distribution (in W/m^2) to the side wall for the calibrated and normalised FNM case at 81%.

Appendix E. Gurvich calculations

The scripting and fluid function properties in combination with the mass and energy conservation solvers in Flownex® SE were used to implement the Gurvich method to predict the furnace exit temperature. A screenshot of the model and results displayed is shown in Figure 111.

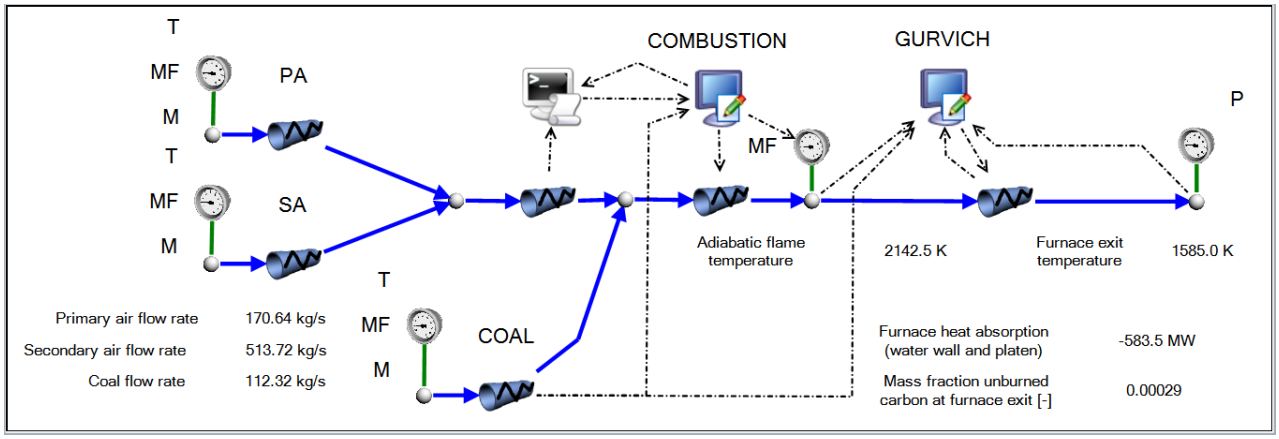

Figure 111 - Screenshot of the furnace exit temperature calculations using the Gurvich method for the multiple-burner validation case study in section 4.2.6 as implemented in Flownex® SE.

The inputs and assumptions for the model are as follows:

- Flame emissivity as per Yin's (2015) model assuming 33.99% unburned carbon remaining in flame after devolitalisation.
- Assumed no heat transfer losses for the heat retention coefficient.
- Furnace wall fouling factor calculated for an angular coefficient of 0.95 and a water wall fouling factor of 0.45 (Zhang, Li and Zhou, 2016:311).
- Flame modification factor as per Zhang, Li and Zhou (2016:140-141,312).
- Furnace surface heat transfer area of 4281 m^2.

The following screenshots are the captured results for the case studies in chapter 5.

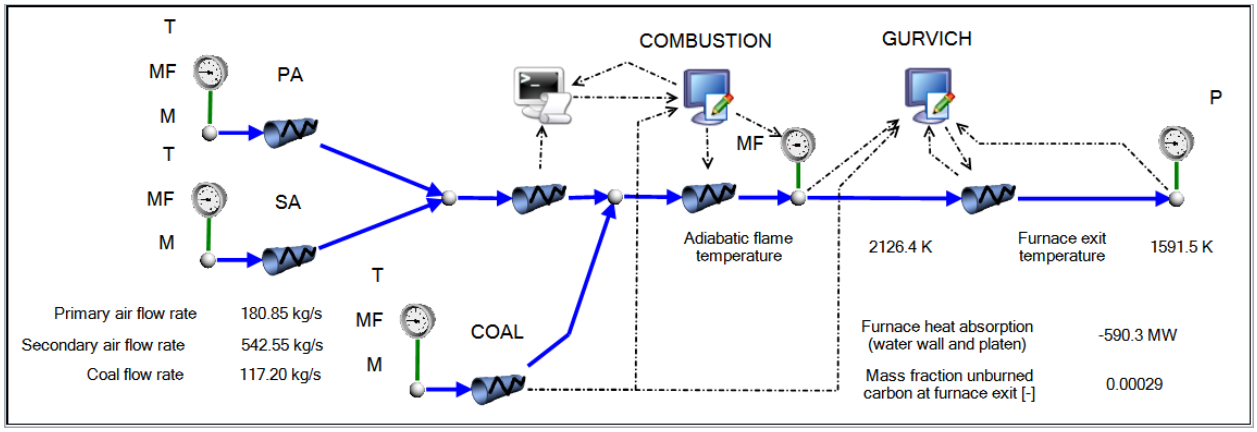

Figure 112 - Screenshot of the furnace exit temperature calculations using the Gurvich method for the multiple-burner case study using the actual coal for section 5.4 as implemented in Flownex® SE.

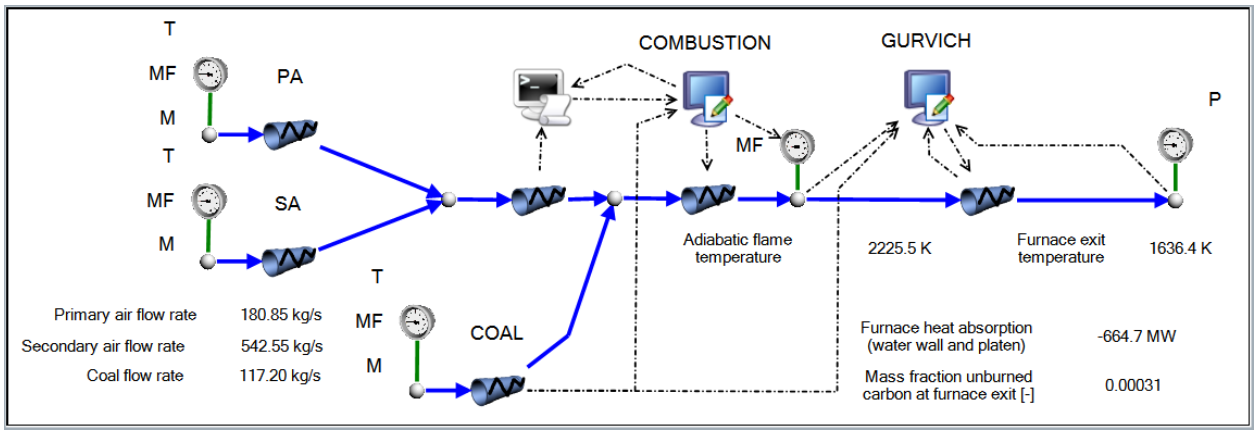

Figure 113 - Screenshot of the furnace exit temperature calculations using the Gurvich method for the multiple-burner case study using the design coal for section 5.4 as implemented in Flownex® SE.

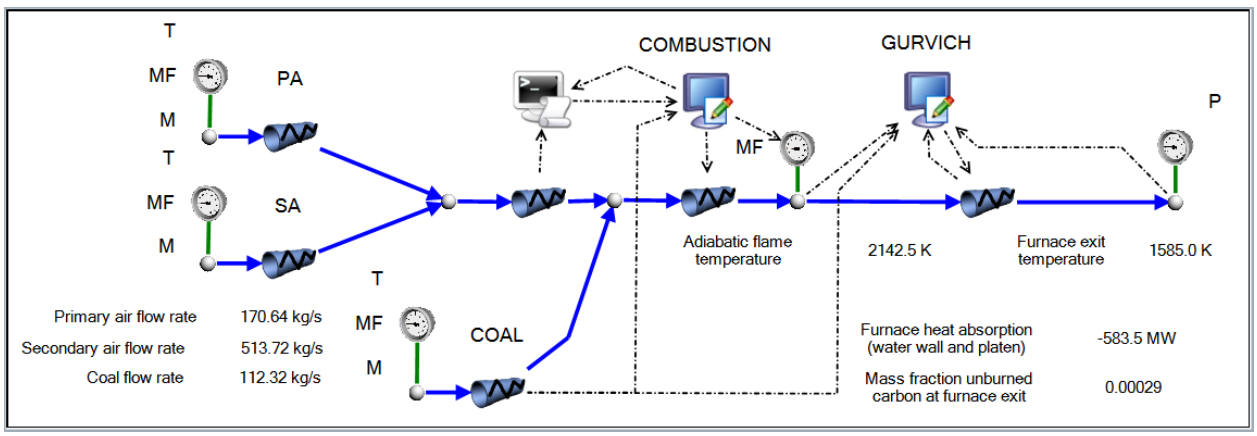

Figure 114 - Screenshot of the furnace exit temperature calculations using the Gurvich method for the multiple-burner case study when the particle size distribution changes (section 5.1) as implemented in Flownex® SE.

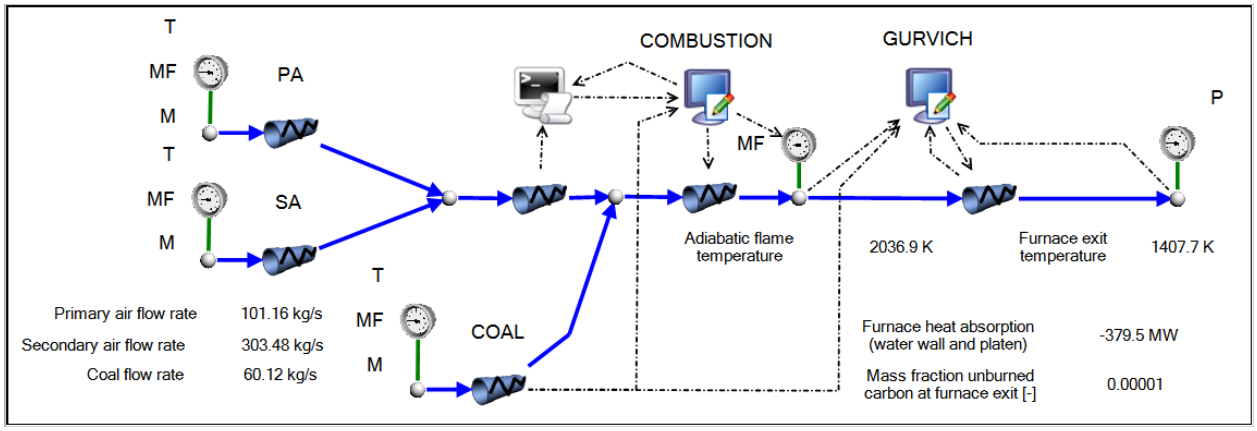

Figure 115 - Screenshot of the furnace exit temperature calculations using the Gurvich method for the multiple-burner case study at 60.5% load for the case study in section 5.5 as implemented in Flownex® SE.

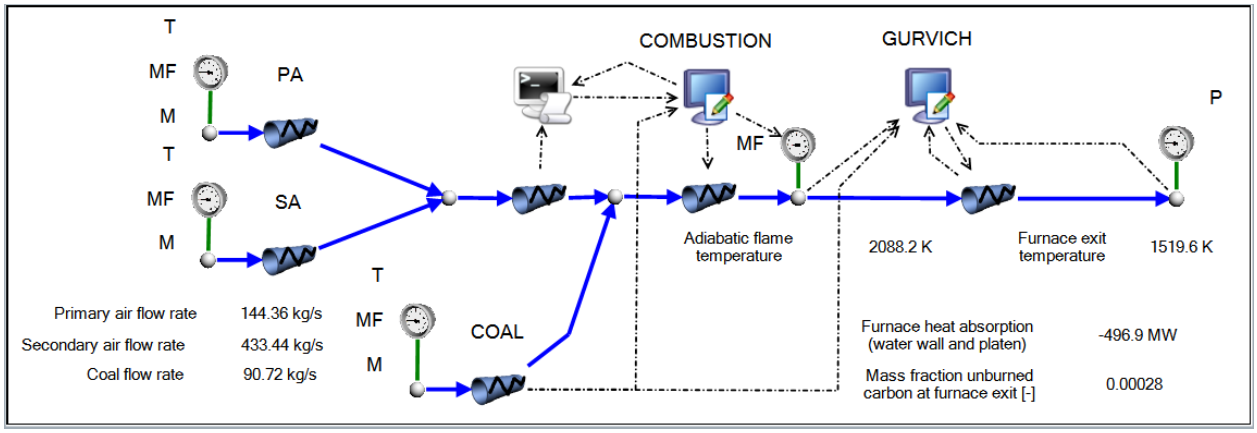

Figure 116 - Screenshot of the furnace exit temperature calculations using the Gurvich method for the multiple-burner case study at 81% load for the case study in section 5.5 as implemented in Flownex® SE.

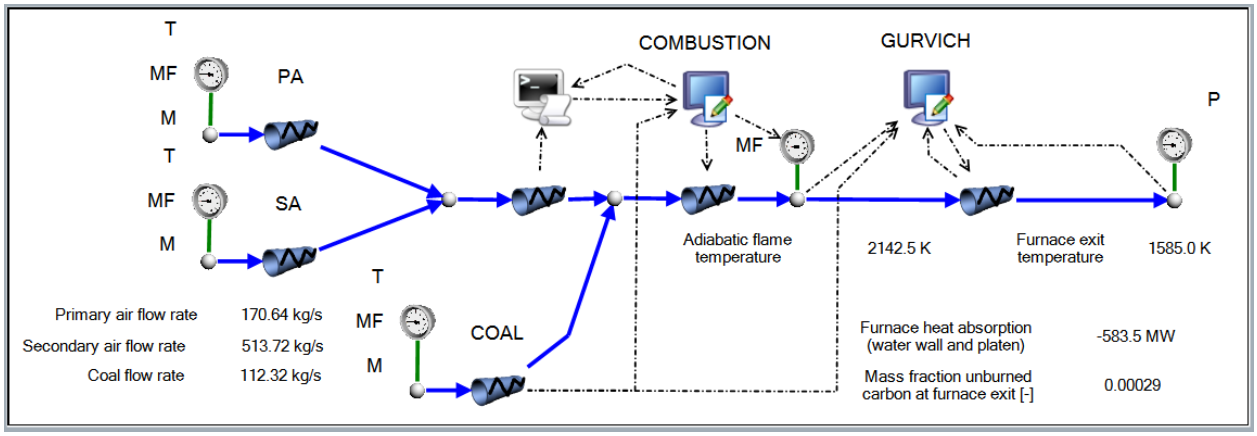

Figure 117 - Screenshot of the furnace exit temperature calculations using the Gurvich method for the multiple-burner case study at 99% load for the case study in section 5.5 as implemented in Flownex® SE.

Appendix F. Program code

Below is the Scilab® (version 5.2.2) code for the single-burner furnace validation in Section 4.2.1:

```
//oneburner validation - single-burner
//Radiation properties calculation from Monnaemang (2015)
clear
stacksize('max')
//currentStackSize = stacksize();
tic()
time = 0;

//---------------------------------------------------------------------------
//Function to calculate enthalpy of volume from temperature and composition
function [h]=ENTHALPY(T, mf_C, mf_CO2, mf_H2, mf_H2O, mf_O2, mf_N2, mf_NO2, mf_S, mf_SO2, mf_ASH)
//Limit temperature within boundaries
//Neglect contribution of H2,NO2,S
T_min = 300;
T_max = 3000;
T = max(T,T_min);
T = min(T,T_max);

//Enthalpy calculation for Carbon (C)
a_0 = -193.9365;a_1 = 0.71;a_2 = 0;a_3 = 0;a_4 = 0;a_5 = 0;a_6 = 0;a_7 = 0;a_8 = 0;a_9 = 0;
h_C = a_0 + a_1.*T + a_2.*T^2 + a_3.*T^3 + a_4.*T^4 + a_5.*T^5 + a_6.*T^6 + a_7.*T^7 + a_8.*T^8 + a_9.*T^9;

//Enthalpy calculation for Carbon dioxide (CO2)
a_0 = -213.537;a_1 = 0.654235;a_2 = 0.000457616;a_3 = -1.33464E-07;a_4 = 1.51982E-11;a_5 = 0;a_6 = 0;a_7 = 0;a_8 = 0;a_9 =
0;
h_CO2 = a_0 + a_1.*T + a_2.*T^2 + a_3.*T^3 + a_4.*T^4 + a_5.*T^5 + a_6.*T^6 + a_7.*T^7 + a_8.*T^8 + a_9.*T^9;

//Enthalpy calculation for Hydrogen(H2)
mf_H2 = 0 .*mf_H2;
h_H2 = 0;

//Enthalpy calculation for Water(gas phase)(H2O)
a_0 = 1970.45;a_1 = 1.88948;a_2 = 0.000153417;a_3 = 1.60768E-07;a_4 = -5.06893E-11;a_5 = 0;a_6 = 0;a_7 = 0;a_8 = 0;a_9 = 0;
h_H2Og = a_0 + a_1.*T + a_2.*T^2 + a_3.*T^3 + a_4.*T^4 + a_5.*T^5 + a_6.*T^6 + a_7.*T^7 + a_8.*T^8 + a_9.*T^9;

//Enthalpy calculation for Oxygen (O2)
a_0 = -235.19;a_1 = 0.80307;a_2 = 0.0002181;a_3 = -6.0835E-08;a_4 = 7.3371E-12;a_5 = 0;a_6 = 0;a_7 = 0;a_8 = 0;a_9 = 0;
h_O2 = a_0 + a_1.*T + a_2.*T^2 + a_3.*T^3 + a_4.*T^4 + a_5.*T^5 + a_6.*T^6 + a_7.*T^7 + a_8.*T^8 + a_9.*T^9;

//Enthalpy calculation for Nitrogen (N2)
a_0 = -254.732;a_1 = 0.897187;a_2 = 0.000184791;a_3 = -3.66561E-08;a_4 = 2.77984E-12;a_5 = 0;a_6 = 0;a_7 = 0;a_8 = 0;a_9 =
0;
h_N2 = a_0 + a_1.*T + a_2.*T^2 + a_3.*T^3 + a_4.*T^4 + a_5.*T^5 + a_6.*T^6 + a_7.*T^7 + a_8.*T^8 + a_9.*T^9;

//Enthalpy calculation for Nitrogen dioxide (NO2)
mf_NO2 = 0 .*mf_NO2;
h_NO2 = 0;

//Enthalpy calculation for Sulphur (S)
mf_S = 0 .*mf_S;
h_S = 0;

//Enthalpy calculation for Sulphur dioxide (SO2)
a_0 = -161.723;a_1 = 0.541535;a_2 = 0.000185;a_3 = 1.01157E-19;a_4 = 1.05879E-22;a_5 = 0;a_6 = 0;a_7 = 0;a_8 = 0;a_9 = 0;
h_SO2 = a_0 + a_1.*T + a_2.*T^2 + a_3.*T^3 + a_4.*T^4 + a_5.*T^5 + a_6.*T^6 + a_7.*T^7 + a_8.*T^8 + a_9.*T^9;

//Enthalpy calculation for Fly ash (ASH)
a_0 = -199.3995;a_1 = 0.73;a_2 = 0;a_3 = 0;a_4 = 0;a_5 = 0;a_6 = 0;a_7 = 0;a_8 = 0;a_9 = 0;
```

```
h_ASH = a_0 + a_1.*T + a_2.*T^2 + a_3.*T^3 + a_4.*T^4 + a_5.*T^5 + a_6.*T^6 + a_7.*T^7 + a_8.*T^8 + a_9.*T^9;

mf_C = mf_C./(mf_C+mf_CO2+mf_H2+mf_H2O+mf_O2+mf_N2+mf_NO2+mf_S+mf_SO2+mf_ASH);
mf_CO2 = mf_CO2./(mf_C+mf_CO2+mf_H2+mf_H2O+mf_O2+mf_N2+mf_NO2+mf_S+mf_SO2+mf_ASH);
mf_H2 = mf_H2./(mf_C+mf_CO2+mf_H2+mf_H2O+mf_O2+mf_N2+mf_NO2+mf_S+mf_SO2+mf_ASH);
mf_H2O = mf_H2O./(mf_C+mf_CO2+mf_H2+mf_H2O+mf_O2+mf_N2+mf_NO2+mf_S+mf_SO2+mf_ASH);
mf_O2 = mf_O2./(mf_C+mf_CO2+mf_H2+mf_H2O+mf_O2+mf_N2+mf_NO2+mf_S+mf_SO2+mf_ASH);
mf_N2 = mf_N2./(mf_C+mf_CO2+mf_H2+mf_H2O+mf_O2+mf_N2+mf_NO2+mf_S+mf_SO2+mf_ASH);
mf_NO2 = mf_NO2./(mf_C+mf_CO2+mf_H2+mf_H2O+mf_O2+mf_N2+mf_NO2+mf_S+mf_SO2+mf_ASH);
mf_S = mf_S./(mf_C+mf_CO2+mf_H2+mf_H2O+mf_O2+mf_N2+mf_NO2+mf_S+mf_SO2+mf_ASH);
mf_SO2 = mf_SO2./(mf_C+mf_CO2+mf_H2+mf_H2O+mf_O2+mf_N2+mf_NO2+mf_S+mf_SO2+mf_ASH);
mf_ASH = mf_ASH./(mf_C+mf_CO2+mf_H2+mf_H2O+mf_O2+mf_N2+mf_NO2+mf_S+mf_SO2+mf_ASH);

h = (mf_C.*h_C + mf_CO2.*h_CO2 + mf_H2.*h_H2 + mf_H2O.*h_H2Og + mf_O2.*h_O2 + mf_N2.*h_N2 + mf_NO2.*h_NO2
+ mf_S.*h_S + mf_SO2.*h_SO2 + mf_ASH.*h_ASH);

endfunction
//---------------------------------------------------------------------------
[verification_h] = ENTHALPY(500,0.059,0.021,0.000,0.007,0.208,0.634,0.000,0.000,0.008,0.063);//Verification check for enthalpy

//---------------------------------------------------------------------------
//Function to calculate temperature of volume from enthalpy and composition
function [T, errout]=TEMPERATURE(h, mf_C, mf_CO2, mf_H2, mf_H2O, mf_O2, mf_N2, mf_NO2, mf_S, mf_SO2,
mf_ASH, T_guess, Tmin, Tmax)
for a = 1:length(h)
   //Newton Rhapson iterative solver
   b = 1;
   T_new(b) = T_guess(a);//Initial guess temperature [K]
   [h_new(b)] =
ENTHALPY(T_new(b),mf_C(a),mf_CO2(a),mf_H2(a),mf_H2O(a),mf_O2(a),mf_N2(a),mf_NO2(a),mf_S(a),mf_SO2(a),mf_AS
H(a));
   err(a) = h_new(b) - h(a);
   EndLoop(a) = 0;
   while (EndLoop(a) == 0)
      b = b + 1;
      T_L(b) = T_new(b-1) - 0.001;
      T_R(b) = T_new(b-1) + 0.001;
      [h_L(b)] =
ENTHALPY(T_L(b),mf_C(a),mf_CO2(a),mf_H2(a),mf_H2O(a),mf_O2(a),mf_N2(a),mf_NO2(a),mf_S(a),mf_SO2(a),mf_ASH(a
));
      [h_R(b)] =
ENTHALPY(T_R(b),mf_C(a),mf_CO2(a),mf_H2(a),mf_H2O(a),mf_O2(a),mf_N2(a),mf_NO2(a),mf_S(a),mf_SO2(a),mf_ASH(a
));
      m(b) = (h_L(b) - h_R(b))/(T_L(b) - T_R(b) + 1e-8);
      T_new(b) = max(Tmin,min(Tmax,T_new(b-1) - err(a)/(m(b) + 1e-8)));
      [h_new(b)] =
ENTHALPY(T_new(b),mf_C(a),mf_CO2(a),mf_H2(a),mf_H2O(a),mf_O2(a),mf_N2(a),mf_NO2(a),mf_S(a),mf_SO2(a),mf_AS
H(a));
      err(a) = h_new(b) - h(a);

      if ((abs(err(a)) > 0.00001) & (b < 20)) then
         EndLoop(a) = 0;
      else
         EndLoop(a) = 1;
      end
      errout(a) = b;
   end
   T(a) = T_new(b);
end

endfunction
//---------------------------------------------------------------------------
[verification_T,calc_error] =
TEMPERATURE(240.285870353750,0.059,0.021,0.000,0.007,0.208,0.634,0.000,0.000,0.008,0.063,1000,300,2000);//Verification
check for temperature
```

```
//------------------------------------------------------------------------
//GEOMETRY INPUTS
B = 0.25;//Length of zone [m]
n_x = 7; //Number of zones in x-direction
n_y = 7; //Number of zones in y-direction
n_z = 26; //Number of zones in z-direction
L_x = B*n_x;//Furnace length in x-direction (W)
L_y = B*n_y;//Furnace length in y-direction (L)
L_z = B*n_z; //Furnace length in z-direction (H)
A_s = B^2;//surface area [m^2]
V_g = B^3;//cell volume [m^3]

//Specify the surface and volume numbers for the burners and outlets
Burners = [25];//Inlet volume of burners
Outlet1 = [1250];//Outlet volumes
Outlet_n = [438];//Outlet surface nodes

//Nodalization
n_t=n_y*n_x*n_z+2*(n_y*n_z)+2*(n_x*n_z)+2*(n_y*n_x)  //Total nr of nodes++
n_s=2*(n_y*n_z)+2*(n_x*n_z)+2*(n_y*n_x)  // Total nr of surface nodes
n_v=n_x*n_y*n_z  // Total nr of volume nodes

////Surface nodes
F_n=1:n_x*n_z;//Front surface
B_n=n_x*n_z+1:2*(n_x*n_z);//Back surface
Bo_n=2*(n_x*n_z)+1:2*(n_x*n_z)+n_y*n_x;//Bottom surface
T_n=2*(n_x*n_z)+(n_y*n_x)+1:2*(n_x*n_z)+2*(n_y*n_x);//Top surface
L_n=2*(n_x*n_z)+2*(n_y*n_x)+1:2*(n_x*n_z)+2*(n_y*n_x)+n_y*n_z;//Left surface
R_n=2*(n_x*n_z)+2*(n_y*n_x)+n_y*n_z+1:2*(n_x*n_z)+2*(n_y*n_x)+2*(n_y*n_z);//Right surface
//------------------------------------------------------------------------

//------------------------------------------------------------------------
//COMBUSTION MODEL INPUTS
CRC = 1;//Surface reaction coefficient rate selector
f_NOx = 0;//NOx conversion factor
p_atm = 1.0;//furnace pressure [bar]
x_f = 0.5//distance to complete volatile evolution [m]
C_f = 0.543; //Fraction of dry ash-free fuel remaining to be burnt as fixed carbon immediately after devolitisation [-]
alpha = 1; //Devolitisation swelling parameter [-]
rho_f = 1000000; //Density of dry ash-free raw fuel [g/m^3]
d_ash = 13;//Fly ash particle size [um]

//Cell distance from nearest burner (for devol model)
x_b = ones(n_v,1)*B*26;
for i = 1:length(Burners)
    x_b(Burners(1,i),1) = x_f/2;
end
//------------------------------------------------------------------------

//------------------------------------------------------------------------
//RADIATION MODEL INPUTS
constRadProperties = 0;//0 = Use radiation property model; 1 = Use constant properties
constant_kappa_p = 0.07/0.07*0.5;//initial or constant absorptivity value for particles
constant_kappa_g = 0.27/0.27*1;//initial or constant absorptivity value for gas
constant_sigma = 0;//initial or constant scattering value
epsilon_w = 0.40;//Wall emmissivity [-]
eps = ones(1,n_s)*epsilon_w;//Wall emissivities [-]
eps(1,T_n) = 0.50;//Emissivities [-]
eps(1,Bo_n) = 0.50;//Emissivities [-]
//eps(1,F_n(1,1):F_n(1,m*o)) = 0.85;//Emissivities [-]
//eps(1,B_n(1,1):B_n(1,m*o)) = 0.85;//Emissivities [-]
//eps(1,L_n(1,1):L_n(1,m*o)) = 0.85;//Emissivities [-]
//eps(1,R_n(1,1):R_n(1,m*o)) = 0.85;//Emissivities [-]
//eps(1,Burners(:)) = 0.85;//Emissivities [-]
```

```
//eps(1,Outlet_n(:)) = 0.85;//Emissivities [-]
kappa_p = ones(1,n_v).*constant_kappa_p;//constant absorptivity value
kappa_g = ones(1,n_v).*constant_kappa_g;//constant absorptivity value
kappa_v = kappa_p + kappa_g;//constant absorptivity value
sigma_v = ones(1,n_v).*constant_sigma;
//------------------------------------------------------------------------

//------------------------------------------------------------------------
//FURNACE WALL HEAT TRANSFER
//Tube wall heat transfer inputs
L_w = 0.0056;//Tube wall thickness [m]
k_w = 47;//Thermal conductivity of tube wall [W/mK]
h_i = 20000;//Internal convection coefficient [W/m2K]
R_w = L_w/(k_w*A_s);//Resistance due to thermal conductivity through tube wall
R_fo = 0;//Resistance due to fouling on the tube wall outside
R_fi = 0;//Resistance due to fouling on the tube wall inside
R_i = 1/(h_i*A_s);//Resistance to heat transfer in tube inside
R_t = R_i + R_fi + R_w + R_fo;//Total resistance due to heat transfer through tube wall
R_t = 0;//Total resistance due to heat transfer through tube wall
T_f = ones(1,n_s)*1000;//Fluid temperature on the inside of the tube wall [K]
T_f(1,T_n) = 1300;//Emissivities [-]
T_f(1,Bo_n) = 1400;//Emissivities [-]
//------------------------------------------------------------------------

//------------------------------------------------------------------------
//SOLVER INPUTS
//Overall limits
T_min = 343.15;//Minimum temperature [K]
T_max = 3000;//Maximum temperature [K]
max_iter = 200;//Maximum amount of iterations
min_iter = 10;//Minimum amount of iterations
rad_iter = 40;//Every number of iteration when radiation properties should be updated
for i = 1:max_iter//If a relaxation factor of 0 is used then model is switched off
    relax_Qrad(i) = min(0.2*i,1);//Relaxation for radiation heat transfer
    relax_Char(i) = min(0.2*i,1);//Relaxation for char combustion
    relax_Devol(i) = min(0.2*i,1);//Relaxation for devolitalization
    relax_h(i) = min(0.1*i,0.99);//Relaxation for enthalpy
end
//------------------------------------------------------------------------

//------------------------------------------------------------------------
//Rosin-Rammler pf distribution calculation
a_RR = 4.5e-5;//mean particle size [m]
b_RR = 1.36;//spread factor
dp_min = 1.0e-6;//minimum particle size [m]
dp_max = 3.0e-4;//maximum particle size [m]
bins = 4;//number of bins

cdf_RR(1) = 0;
x_RR(1) = dp_min;
for i=2:(bins)
    cdf_RR(i) = cdf_RR(i-1) + 0.25;
    x_RR(i) = a_RR*(-log(1-cdf_RR(i)))^(1/b_RR);
    dp(i-1) = 0.5*(x_RR(i-1) + x_RR(i));
    mf_RR(i-1) = cdf_RR(i) - cdf_RR(i-1);
end

cdf_RR(bins+1) = 1;
x_RR(bins+1) = dp_max;
dp(bins) = 0.5*(x_RR(bins+1) + x_RR(bins));
mf_RR(bins) = cdf_RR(bins+1) - cdf_RR(bins);
//------------------------------------------------------------------------
clear cdf_RR
//------------------------------------------------------------------------
//BURNER INPUTS
```

```
//------------------------------Burner 1------------------------------
b = 1;
//VC_coal(b) = 0.1939;//Volatile fraction [-]
//C_coal(b) = 0.5430;//Carbon fraction [-]
VC_coal(b) = 0.3699;//Volatile fraction [-]
C_coal(b) = 0.3670;//Carbon fraction [-]
C_coal1(b) = C_coal(b)*mf_RR(1);//Carbon in 1th fraction [-]
C_coal2(b) = C_coal(b)*mf_RR(2);//Carbon in 2th fraction [-]
C_coal3(b) = C_coal(b)*mf_RR(3);//Carbon in 3th fraction [-]
C_coal4(b) = C_coal(b)*mf_RR(4);//Carbon in 3th fraction [-]
H_coal(b) = 0.04658;//Hydrogen fraction [-]
O_coal(b) = 0.1116;//Oxygen mass fraction [-]
N_coal(b) = 0.0133;//Nitrogen fraction [-]
S_coal(b) = 0.00862;//Sulphur fraction [-]
ASH_coal(b) = 0.083;//Ash fraction [-]
H2O_coal(b) = 0.0;//H2O fraction [-]
m_total(b) = 0.93556;//Total mass flow rate [kg/s]
m_PA(b) = 0.11694;//Primary air flow rate [kg/s]
m_SA(b) = 0.74556;//Secondary air flow rate [kg/s]
m_c(b) = 0.07306;//Coal flow rate [kg/s]
T_SA(b) = 573.15;//Secondary air Temperature [K]
T_PA(b) = 343.15;//Secondary air Temperature [K]
T_c(b) = 343.15;//Coal Temperature [K]
omega(b) = 0.0;//specific humidity of air [kg water/kg air]
HAR(b) = m_total(b)/m_c(b) - 1;//Humid air to fuel ratio [kg Air/kg Coal]
DAR(b) = HAR(b)/(1+omega(b));//Dry air to fuel ratio [kg Air/kg Coal]
TAR(b) = (32/12*(C_coal(b)+VC_coal(b)) + 32/32*S_coal(b) + 8*(H_coal(b)) + f_NOx*32/14*N_coal(b) -
O_coal(b))/0.23;//Theoretical air to fuel ratio [kg Air/kg Coal]
EA(b) = DAR(b)/TAR(b) - 1;//Excess air ratio [-]
m_air(b) = m_SA(b) + m_PA(b);//Total air mass flow rate [kg/s]
T_air(b) = (m_SA(b)*T_SA(b) + m_PA(b)*T_PA(b) + m_c(b)*T_c(b))/(m_SA(b) + m_PA(b) + m_c(b));//Temperature of air
assuming perfectly mixed SA and PA [kg/s]
d_p1(b) = dp(1)*100;//Particle size of 1th fraction [cm]
d_p2(b) = dp(2)*100;//Particle size of 2th fraction [cm]
d_p3(b) = dp(3)*100;//Particle size of 3th fraction [cm]
d_p4(b) = dp(4)*100;//Particle size of 4th fraction [cm]

//-----------------------------------------------------------------------------
//FLOWMAP IMPORT
m_in = zeros(n_v,1);
m_out = zeros(n_v,1);
M_a = zeros(n_v,n_v);
phi = csvRead('c://FNM/oneburner/validation/Flowmap/phi.csv',",");//mass flow rate [kg/s]
owner = csvRead('c://FNM/oneburner/validation/Flowmap/owner.csv',",");//cell owner number [-]
neighbour = csvRead('c://FNM/oneburner/validation/Flowmap/neigbour.csv',",");//cell neigbours [-]

for count = 1:length(neighbour)
   M_a(owner(count,1)+1,neighbour(count,1)+1) = phi(count);
   M_a(neighbour(count,1)+1,owner(count,1)+1) = -1*phi(count);
end

for i = 1:size(M_a,1)
   for j = 1:size(M_a,2)
      M_a(i,j) = max(M_a(i,j),0);
   end
end

for i = 1:n_v
   m_in(i,1) = sum(M_a(:,i));
   m_out(i,1) = sum(M_a(i,:));
end

for i = 1:length(Burners)
   m_in(Burners(1,i),1) = m_in(Burners(1,i),1) + m_total(i);
```

```
end

for i = 1:length(Outlet1)
   m_furn_e(i) = m_in(Outlet1(1,i),1) - m_out(Outlet1(1,i),1);
   m_out(Outlet1(1,i),1) = m_in(Outlet1(1,i),1);
end

count = 0;
for k=1:n_v
   for j=1:n_v
      if abs(M_a(k,j)) > 1e-16 then
         count = count + 1;
         M_a_sparse(count, 1) = k;
         M_a_sparse(count, 2) = j;
         M_a_sparse(count, 3) = M_a(k,j);
      end
   end
end

m_diff_per_zones = abs(m_in-m_out);
verification_masflow_ave = mean(m_diff_per_zones);
verification_masflow_max = max(m_diff_per_zones);

//---------------------------------------------------------------------------
clear owner neighbour phi
//---------------------------------------------------------------------------
//Averages from burner inlets for initial field and general
VC_coal_ave = mean(VC_coal);//Volatile fraction [-]
C_coal_ave = mean(C_coal);//Carbon fraction [-]
C_coal1_ave = C_coal_ave*mf_RR(1);//Carbon in 1th fraction [-]
C_coal2_ave = C_coal_ave*mf_RR(2);//Carbon in 2th fraction [-]
C_coal3_ave = C_coal_ave*mf_RR(3);//Carbon in 3th fraction [-]
C_coal4_ave = C_coal_ave*mf_RR(4);//Carbon in 3th fraction [-]
H_coal_ave = mean(H_coal);//Hydrogen fraction [-]
O_coal_ave = mean(O_coal);//Oxygen mass fraction [-]
N_coal_ave = mean(N_coal);//Nitrogen fraction [-]
S_coal_ave = mean(S_coal);//Sulphur fraction [-]
ASH_coal_ave = mean(ASH_coal);//Ash fraction [-]
H2O_coal_ave = mean(H2O_coal);//H2O fraction [-]
m_total_ave = mean(m_total);//Total mass flow rate [kg/s]
m_PA_ave = mean(m_PA);//Primary air flow rate [kg/s]
m_SA_ave = mean(m_SA);//Secondary air flow rate [kg/s]
EA_ave = mean(EA);//Excess air ratio [-]
omega_ave = mean(omega);//specific humidity of air [kg water/kg air]
DAR_ave = mean(DAR);//Dry air to fuel ratio [kg Air/kg Coal]
HAR_ave = mean(HAR);//Humid air to fuel ratio [kg Air/kg Coal]
m_c_ave = mean(m_c);//Total coal flow rate [kg/s]
T_air_ave = mean(T_air);//Temperature of air assuming perfectly mixed SA and PA [kg/s]
d_p1_ave = mean(d_p1);//Particle size of 1th fraction [cm]
d_p2_ave = mean(d_p2);//Particle size of 2th fraction [cm]
d_p3_ave = mean(d_p3);//Particle size of 3th fraction [cm]
d_p4_ave = mean(d_p4);//Particle size of 4th fraction [cm]
//---------------------------------------------------------------------------

//---------------------------------------------------------------------------
//INITIAL FIELD
      //-------------------------------------------------------------------
      //Combustion model initial values into cell
      mf_C1i = ones(n_v,1)*mean(C_coal1_ave);//Carbon 1 mass fraction [-]
      mf_C2i = ones(n_v,1)*mean(C_coal2_ave);
      mf_C3i = ones(n_v,1)*mean(C_coal3_ave);
      mf_C4i = ones(n_v,1)*mean(C_coal4_ave);
      mf_Ci = mf_C1i + mf_C2i + mf_C3i + mf_C4i;
      mf_VCi = ones(n_v,1)*mean(VC_coal_ave);//Volatile mass fraction [-]
      mf_H2i = ones(n_v,1)*mean(H_coal_ave);//Hydrogen fraction [-]
```

```
mf_O2i = zeros(n_v,1);//Oxygen mass fraction [-]
mf_N2i = zeros(n_v,1);//Nitrogen fraction [-]
mf_Si = ones(n_v,1)*mean(S_coal_ave);//Sulphur fraction [-]
mf_Ashi = ones(n_v,1)*mean(ASH_coal_ave);//Ash mass fraction [-]
mf_CO2i = zeros(n_v,1);//Carbon dioxide fraction [-]
mf_H2Oi = zeros(n_v,1);//H2O fraction [-]
mf_NO2i = zeros(n_v,1);//Nitrogen dioxide fraction [-]
mf_SO2i = zeros(n_v,1);//Sulphur dioxide fraction [-]
y_10 = d_p1_ave*0.01*ones(n_v,1); //Initial particle diameter of 1th fraction [cm]*0.01 = [m]
y_20 = d_p2_ave*0.01*ones(n_v,1); //Initial particle diameter of 2th fraction [cm]*0.01 = [m]
y_30 = d_p3_ave*0.01*ones(n_v,1); //Initial particle diameter of 3th fraction [cm]*0.01 = [m]
y_40 = d_p4_ave*0.01*ones(n_v,1); //Initial particle diameter of 4th fraction [cm]*0.01 = [m]
x_1i = alpha*y_10; //Particle diameter of 1th fraction after devolitation [cm]*0.01 = [m]
x_2i = alpha*y_20; //Particle diameter of 2th fraction after devolitation [cm]*0.01 = [m]
x_3i = alpha*y_30; //Particle diameter of 3th fraction after devolitation [cm]*0.01 = [m]
x_4i = alpha*y_40; //Particle diameter of 4th fraction after devolitation [cm]*0.01 = [m]
S_1i0 = 6*alpha^2*(C_coal1_ave/C_coal_ave)/(C_f*rho_f*d_p1_ave*0.01);//specific surface area [cm^2/g]*0.0001 = [m^2/g]
S_2i0 = 6*alpha^2*(C_coal2_ave/C_coal_ave)/(C_f*rho_f*d_p2_ave*0.01);//specific surface area [cm^2/g]*0.0001 = [m^2/g]
S_3i0 = 6*alpha^2*(C_coal3_ave/C_coal_ave)/(C_f*rho_f*d_p3_ave*0.01);//specific surface area [cm^2/g]*0.0001 = [m^2/g]
S_4i0 = 6*alpha^2*(C_coal4_ave/C_coal_ave)/(C_f*rho_f*d_p4_ave*0.01);//specific surface area [cm^2/g]*0.0001 = [m^2/g]
S_1i = ones(n_v,1).*S_1i0;//specific surface area [cm^2/g]*0.0001 = [m^2/g]
S_2i = ones(n_v,1).*S_2i0;//specific surface area [cm^2/g]*0.0001 = [m^2/g]
S_3i = ones(n_v,1).*S_3i0;//specific surface area [cm^2/g]*0.0001 = [m^2/g]
S_4i = ones(n_v,1).*S_4i0;//specific surface area [cm^2/g]*0.0001 = [m^2/g]

mk_fi = max(1e-8,mf_C1i + mf_C2i + mf_C3i + mf_C4i + mf_VCi + mf_H2i + mf_Si + mf_Ashi);//All nitrogen and water
consider part of gas as soon as leaving the first cell
mk_fgi = (1 - mf_Ashi - mf_C1i - mf_C2i - mf_C3i - mf_C4i - mf_VCi - mf_Si - mf_H2i + HAR_ave);//flue gas into of cell [kg
O2/kg Coal]
mk_N2i = (N_coal_ave + 0.77*DAR_ave);
mk_CO2i = mf_CO2i.*mk_fgi;
mk_H2Oi = (H2O_coal_ave + omega_ave*DAR_ave);
mk_NO2i = mf_NO2i.*mk_fgi;
mk_SO2i = mf_SO2i.*mk_fgi;
mk_O2i = mk_fgi - mk_CO2i - mk_N2i - mk_H2Oi - mk_NO2i - mk_SO2i;
mf_O2i = mk_O2i./mk_fgi;
mf_N2i =  mk_N2i./mk_fgi;
mf_H2Oi = mk_H2Oi./mk_fgi;
//---------------------------------------------------------------------

//---------------------------------------------------------------------
//Combustion model initial values out cell
mf_C1o = mf_C1i;
mf_C2o = mf_C2i;
mf_C3o = mf_C3i;
mf_C4o = mf_C4i;
mf_Co = mf_C1o + mf_C2o + mf_C3o + mf_C4o;
mf_VCo = mf_VCi;
mf_H2o = mf_H2i;
mf_O2o = mf_O2i;
mf_N2o = mf_N2i;
mf_So = mf_Si;
mf_Asho = mf_Ashi;
mf_CO2o = mf_CO2i;
mf_H2Oo = mf_H2Oi;
mf_NO2o = mf_NO2i;
mf_SO2o = mf_SO2i;
x_1o = x_1i;
x_2o = x_2i;
x_3o = x_3i;
x_4o = x_4i;

mk_fo = mk_fi;//All nitrogen and water consider part of gas as soon as leaving the first cell
mk_fgo = mk_fgi;//flue gas into of cell [kg O2/kg Coal]
mk_N2o = mk_N2i;
```

```
        mk_CO2o = mk_CO2i;
        mk_H2Oo = mk_H2Oi;
        mk_NO2o = mk_NO2i;
        mk_SO2o = mk_SO2i;
        mk_O2o = mk_O2i;
        mf_O2o = mf_O2i;
        mf_N2o = mf_N2i;

        S_1o = S_1i;
        S_2o = S_2i;
        S_3o = S_3i;
        S_4o = S_4i;
        //---------------------------------------------------------------

        //---------------------------------------------------------------
        //Energy balance model initial values out cell
        T_ai = ones(n_v,1)*T_air_ave;//Temperature of air entering volume [K]
        [h_ai] =
ENTHALPY(T_ai,(mf_Ci+mf_VCi).*mk_fgi./(mk_fgi+mk_fi),mf_CO2i.*mk_fgi./(mk_fgi+mk_fi),mf_H2i.*mk_fgi./(mk_fgi+mk_
fi),mf_H2Oi.*mk_fgi./(mk_fgi+mk_fi),mf_O2i.*mk_fgi./(mk_fgi+mk_fi),mf_N2i.*mk_fgi./(mk_fgi+mk_fi),mf_NO2i.*mk_fgi./(m
k_fgi+mk_fi),mf_Si.*mk_fgi./(mk_fgi+mk_fi),mf_SO2i.*mk_fgi./(mk_fgi+mk_fi),mf_Ashi.*mk_fgi./(mk_fgi+mk_fi));
        H_ai = ones(n_v,1).*m_in.*h_ai;//Heat of air leaving volume
        H_ao = H_ai;//Heat of air entering volume
        h_ao = H_ao./m_out;
        [T_ao,errT] =
TEMPERATURE(h_ao,(mf_Co+mf_VCo).*mk_fgo./(mk_fgo+mk_fo),mf_CO2o.*mk_fgo./(mk_fgo+mk_fo),mf_H2o.*mk_fgo./(m
k_fgo+mk_fo),mf_H2Oo.*mk_fgo./(mk_fgo+mk_fo),mf_O2o.*mk_fgo./(mk_fgo+mk_fo),mf_N2o.*mk_fgo./(mk_fgo+mk_fo),mf_
NO2o.*mk_fgo./(mk_fgo+mk_fo),mf_So.*mk_fgo./(mk_fgo+mk_fo),mf_SO2o.*mk_fgo./(mk_fgo+mk_fo),mf_Asho.*mk_fgo./(mk
_fgo+mk_fo),T_ai,T_min,T_max);
        T_gi = zeros(n_v,1);//average volume temperature [K]
        Q_s = zeros(n_s,1);//Radiation heat transfer to walls [W]

        //---------------------------------------------------------------

//BURNER INLET
//It is assumed that the oxygen, nitrogen and water is already not part of the fuel as soon as it enters the furnace
for i = 1:length(Burners)
    //---------------------------------------------------------------
    //Combustion model burner conditions
    mf_C1i(Burners(i),1) = C_coal1(i);
    mf_C2i(Burners(i),1) = C_coal2(i);
    mf_C3i(Burners(i),1) = C_coal3(i);
    mf_C4i(Burners(i),1) = C_coal4(i);
    mf_VCi(Burners(i),1) = VC_coal(i);
    mf_H2i(Burners(i),1) = H_coal(i);
    mf_Si(Burners(i),1) = S_coal(i);
    mf_Ashi(Burners(i),1) = ASH_coal(i);
    x_1i(Burners(i),1) = alpha*d_p1(i)*0.01;
    x_2i(Burners(i),1) = alpha*d_p2(i)*0.01;
    x_3i(Burners(i),1) = alpha*d_p3(i)*0.01;
    x_4i(Burners(i),1) = alpha*d_p4(i)*0.01;

    mf_Ci(Burners(i),1) = mf_C1i(Burners(i),1) + mf_C2i(Burners(i),1) + mf_C3i(Burners(i),1) + mf_C4i(Burners(i),1);
    mk_fgi(Burners(i),1) = (1 - mf_Ashi(Burners(i),1) - mf_C1i(Burners(i),1) - mf_C2i(Burners(i),1) - mf_C3i(Burners(i),1) -
mf_C4i(Burners(i),1) - mf_VCi(Burners(i),1) - mf_Si(Burners(i),1) - mf_H2i(Burners(i),1) + HAR(i));//flue gas into of cell [kg
O2/kg Coal]
    mk_N2i(Burners(i),1) = (N_coal(i) + 0.77*DAR(i));
    mk_CO2i(Burners(i),1) = mf_CO2i(Burners(i),1)*mk_fgi(Burners(i),1);

    mk_H2Oi(Burners(i),1) = (H2O_coal(i) + omega(i)*DAR(i));
    mk_NO2i(Burners(i),1) = mf_NO2i(Burners(i),1)*mk_fgi(Burners(i),1);
    mk_SO2i(Burners(i),1) = mf_SO2i(Burners(i),1)*mk_fgi(Burners(i),1);
    mk_O2i(Burners(i),1) = mk_fgi(Burners(i),1) - mk_CO2i(Burners(i),1) - mk_N2i(Burners(i),1) - mk_H2Oi(Burners(i),1) -
mk_NO2i(Burners(i),1) - mk_SO2i(Burners(i),1);//O2 out of cell [kg O2/kg Coal]
    mf_O2i(Burners(i),1) = mk_O2i(Burners(i),1)/mk_fgi(Burners(i),1);
```

```
    mf_N2i(Burners(i),1) =  mk_N2i(Burners(i),1)/mk_fgi(Burners(i),1);
    mf_CO2i(Burners(i),1) = mk_CO2i(Burners(i),1)/mk_fgi(Burners(i),1);
    mf_H2Oi(Burners(i),1) = mk_H2Oi(Burners(i),1)/mk_fgi(Burners(i),1);
    mf_NO2i(Burners(i),1) = mk_NO2i(Burners(i),1)/mk_fgi(Burners(i),1);
    mf_SO2i(Burners(i),1) = mk_SO2i(Burners(i),1)/mk_fgi(Burners(i),1);

    mf_C1o(Burners(i),1) = mf_C1i(Burners(i),1);
    mf_C2o(Burners(i),1) = mf_C2i(Burners(i),1);
    mf_C3o(Burners(i),1) = mf_C3i(Burners(i),1);
    mf_C4o(Burners(i),1) = mf_C4i(Burners(i),1);
    mf_Co(Burners(i),1) = mf_Ci(Burners(i),1);
    mf_VCo(Burners(i),1) = mf_VCi(Burners(i),1);
    mf_H2o(Burners(i),1) = mf_H2i(Burners(i),1);
    mf_So(Burners(i),1) = mf_Si(Burners(i),1);
    mf_Asho(Burners(i),1) = mf_Ashi(Burners(i),1);
    x_1o(Burners(i),1) = x_1i(Burners(i),1);
    x_2o(Burners(i),1) = x_2i(Burners(i),1);
    x_3o(Burners(i),1) = x_3i(Burners(i),1);
    x_4o(Burners(i),1) = x_4i(Burners(i),1);

    mk_fgo(Burners(i),1) = mk_fgi(Burners(i),1);
    mk_N2o(Burners(i),1) = mk_N2i(Burners(i),1);
    mk_CO2o(Burners(i),1) = mk_CO2i(Burners(i),1);
    mk_H2Oo(Burners(i),1) = mk_H2Oi(Burners(i),1);
    mk_NO2o(Burners(i),1) = mk_NO2i(Burners(i),1);
    mk_SO2o(Burners(i),1) = mk_SO2i(Burners(i),1);
    mk_O2o(Burners(i),1) = mk_O2i(Burners(i),1);
    mf_O2o(Burners(i),1) = mf_O2i(Burners(i),1);
    mf_N2o(Burners(i),1) =  mf_N2i(Burners(i),1);
    mf_CO2o(Burners(i),1) = mf_CO2i(Burners(i),1);
    mf_H2Oo(Burners(i),1) = mf_H2Oi(Burners(i),1);
    mf_NO2o(Burners(i),1) = mf_NO2i(Burners(i),1);
    mf_SO2o(Burners(i),1) = mf_SO2i(Burners(i),1);
    //---------------------------------------------------------------------

    //---------------------------------------------------------------------
    //Energy balance model burner conditions
    T_ai(Burners(i),1) = T_air(i); //air inlet temperature[K]
    [h_ai(Burners(i),1)] =
ENTHALPY(T_ai(Burners(i),1),(mf_Ci(Burners(i),1)+mf_VCi(Burners(i),1))*mk_fgi(Burners(i),1)/(mk_fgi(Burners(i),1)+mk_fi(Burners(i),1)),mf_CO2i(Burners(i),1)*mk_fgi(Burners(i),1)/(mk_fgi(Burners(i),1)+mk_fi(Burners(i),1)),mf_H2i(Burners(i),1)*mk_fgi(Burners(i),1)/(mk_fgi(Burners(i),1)+mk_fi(Burners(i),1)),mf_H2Oi(Burners(i),1)*mk_fgi(Burners(i),1)/(mk_fgi(Burners(i),1)+mk_fi(Burners(i),1)),mf_O2i(Burners(i),1)*mk_fgi(Burners(i),1)/(mk_fgi(Burners(i),1)+mk_fi(Burners(i),1)),mf_N2i(Burners(i),1)*mk_fgi(Burners(i),1)/(mk_fgi(Burners(i),1)+mk_fi(Burners(i),1)),mf_NO2i(Burners(i),1)*mk_fgi(Burners(i),1)/(mk_fgi(Burners(i),1)+mk_fi(Burners(i),1)),mf_Si(Burners(i),1)*mk_fgi(Burners(i),1)/(mk_fgi(Burners(i),1)+mk_fi(Burners(i),1)),mf_SO2i(Burners(i),1)*mk_fgi(Burners(i),1)/(mk_fgi(Burners(i),1)+mk_fi(Burners(i),1)),mf_Ashi(Burners(i),1)*mk_fgi(Burners(i),1)/(mk_fgi(Burners(i),1)+mk_fi(Burners(i),1)));
    H_ai = ones(n_v,1).*m_in.*h_ai;//Heat of air leaving volume
    H_ao(Burners(i),1) = H_ai(Burners(i),1);
    h_ao(Burners(i),1) = H_ao(Burners(i),1)./m_out(Burners(i),1);
    [T_ao(Burners(i),1),errT(Burners(i),1)] =
TEMPERATURE(h_ao(Burners(i),1),(mf_Co(Burners(i),1)+mf_VCo(Burners(i),1))*mk_fgo(Burners(i),1)/(mk_fgo(Burners(i),1)+mk_fo(Burners(i),1)),mf_CO2o(Burners(i),1)*mk_fgo(Burners(i),1)/(mk_fgo(Burners(i),1)+mk_fo(Burners(i),1)),mf_H2o(Burners(i),1)*mk_fgo(Burners(i),1)/(mk_fgo(Burners(i),1)+mk_fo(Burners(i),1)),mf_H2Oo(Burners(i),1)*mk_fgo(Burners(i),1)/(mk_fgo(Burners(i),1)+mk_fo(Burners(i),1)),mf_O2o(Burners(i),1)*mk_fgo(Burners(i),1)/(mk_fgo(Burners(i),1)+mk_fo(Burners(i),1)),mf_N2o(Burners(i),1)*mk_fgo(Burners(i),1)/(mk_fgo(Burners(i),1)+mk_fo(Burners(i),1)),mf_NO2o(Burners(i),1)*mk_fgo(Burners(i),1)/(mk_fgo(Burners(i),1)+mk_fo(Burners(i),1)),mf_So(Burners(i),1)*mk_fgo(Burners(i),1)/(mk_fgo(Burners(i),1)+mk_fo(Burners(i),1)),mf_SO2o(Burners(i),1)*mk_fgo(Burners(i),1)/(mk_fgo(Burners(i),1)+mk_fo(Burners(i),1)),mf_Asho(Burners(i),1)*mk_fgo(Burners(i),1)/(mk_fgo(Burners(i),1)+mk_fo(Burners(i),1)),T_ai(Burners(i),1),T_min,T_max);
    //---------------------------------------------------------------------
end
//-----------------------------------------------------------------------

t(1,1) = toc()
time = time + t(1,1)
```

```
tic()
//---------------------------------------------------------------------------
// PARTICIPATING MEDIA PROPERTIES
//Absorptivity & Scattering
function [epsilon_H2O, alpha_H2O]=RadiationPropertiesH2O(p, p_a_H2O, L_H2O, T_H2O, T_s)
    c_H2O = [-2.2118 -1.1987 0.035596;0.85667 0.93048 -0.14391;-0.10838 -0.17156 0.045915];
    T_0 = 1000;//[K]
    p_0 = 1;//bar
    p_a_0 = 1;//bar
    L_0 = 0.01;//m
    ta = T_H2O/T_0;
    tb = T_s/1000;
    P_Ea = (p + 2.56*p_a_H2O/sqrt(ta))/p_0;
    P_Eb = (p + 2.56*p_a_H2O/sqrt(tb))/p_0;
    aa = 1.888-2.053*log10(max(0.75,ta));
    ab = 1.888-2.053*log10(max(0.75,tb));
    ba = 1.1/ta^1.4;
    bb = 1.1/tb^1.4;
    c = 0.5;
    G36b = 0;
    G53b = 0;
    for i = 1:3
        G36a = 0;
        G53a = 0;
        for j = 1:3
            G36a = G36a + c_H2O(i,j)*ta^(j - 1);
            G53a = G53a + c_H2O(i,j)*tb^(j - 1);
        end

        G36b = G36b + G36a*(log10(p_a_H2O*L_H2O*100))^(i - 1);
        G53b = G53b + G53a*(log10(p_a_H2O*L_H2O*100*T_s/T_H2O))^(i - 1);
    end
    G36b = exp(G36b);
    G53b = exp(G53b);

    epsilon_H2O = (1 + ((aa*P_Ea + ba)/(aa + ba - 1 + P_Ea) - 1)*exp(-1*c*(log10(13.2*ta^2))^2))*G36b;

    epsilon_H2Ob = G53b*(1 + exp(-0.5*(log10(T_s/T_H2O*13.2*tb^2))^2)*((ab*P_Eb + bb)/(P_Eb + ab + bb - 1) - 1));
    alpha_H2O = epsilon_H2Ob*sqrt(T_H2O/T_s);
endfunction
[verification_epsilon_H2O,verification_alpha_H2O] = RadiationPropertiesH2O(0.85,0.0765,10.134,1100,300)

function [epsilon_CO2, alpha_CO2]=RadiationPropertiesCO2(p, p_a_CO2, L_CO2, T_CO2, T_s)
    c_CO2 = [-3.9893 2.7669 -2.1081 0.39163;1.2710 -1.1090 1.0195 -0.21897;-0.23678 0.19731 -0.19544 0.044644];
    T_0 = 1000;//[K]
    p_0 = 1;//bar
    p_a_0 = 1;//bar
    L_0 = 0.01;//m
    ta = T_CO2/T_0;
    tb = T_s/1000;
    P_Ea = (p + 0.28*p_a_CO2)/p_0;
    P_Eb = (p + 0.28*p_a_CO2)/p_0;

    aa = 1 + 0.1/ta^1.45;
    ab = 1 + 0.1/tb^1.45;
    ba = 0.23;
    bb = 0.23;
    H41b = 0;
    H58b = 0;
    for i = 1:3
        H41a = 0;
        H58a = 0;
        for j = 1:4
            H41a = H41a + c_CO2(i,j)*ta^(j - 1);
            H58a = H58a + c_CO2(i,j)*tb^(j - 1);
```

```
        end
        H41b = H41b + H41a*(log10(p_a_CO2*L_CO2*100))^(i - 1);
        H58b = H58b + H58a*(log10(p_a_CO2*L_CO2*100*T_s/T_CO2))^(i - 1);
    end
    H41b = exp(H41b);
    H58b = exp(H58b);

    if ta < 0.7 then
        epsilon_CO2 = H41b*(1 + exp(-1.47*(log10(0.054/ta^2))^2)*((aa*P_Ea + ba)/(P_Ea + aa + ba - 1) - 1));
    else
        epsilon_CO2 = H41b*(1 + exp(-1.47*(log10(0.255*ta^2))^2)*((aa*P_Ea + ba)/(P_Ea + aa + ba - 1) - 1));
    end

    if tb < 0.7 then
        epsilon_H2Ob = H58b*(1 + exp(-1.47*(log10(T_s/T_CO2*0.054/tb^2))^2)*((ab*P_Eb + bb)/(P_Eb + ab + bb - 1) - 1));
    else
        epsilon_H2Ob = H58b*(1 + exp(-1.47*(log10(T_s/T_CO2*0.255*tb^2))^2)*((ab*P_Eb + bb)/(P_Eb + ab + bb - 1) - 1));
    end

    alpha_CO2 = epsilon_H2Ob*sqrt(T_CO2/T_s);
endfunction
[verification_epsilon_CO2,verification_alpha_CO2] = RadiationPropertiesCO2(0.85,0.1190,10.134,1100,300)

function [eps_p, kappa_p]=RadiationPropertiesPar(n_v, mf_VC, mf_C)
for i=1:n_v
        eps_p(1,i) = 0.6 + 0.4*mf_C(i,1);
end
endfunction
[verification_kappa_flame] = RadiationPropertiesPar(1,0.07,0.31)

tic()
////////////////////////////////////////////////////////////////////////
//Radiation heat transfer properties
// SURFACE NODES: The enclosure is divided into 6 planes, they are; Front, Back, Bottom, Top, Left & Right].Each node holds information of its position in terms of the x,y & z co-ordinates of the node, the surface normal vector, the area of the small node as well as the large area of the plane without discretisation

// Volume to Surface DEAs:
function [VS]=DEA_3(SS, s_nodes)
node = 0
    for p1=1:s_nodes  // Number of nodes on the surface
        for vp1=1:n*m*o // Number of nodes in the enclosed volume
    node = node + 1
            R= sqrt((vp(vp1,1)-SS(p1,1)).^2 + (vp(vp1,2)-SS(p1,2)).^2 + (vp(vp1,3)-SS(p1,3)).^2)
            cos1=(SS(p1,4)*sqrt((SS(p1,1)-vp(vp1,1)).^2)+SS(p1,5)*sqrt((SS(p1,2)-vp(vp1,2)).^2)+SS(p1,6)*sqrt((SS(p1,3)-
vp(vp1,3)).^2))./R
            VS(vp1,p1)=((exp(-(beta_v(vp1,1)).*R)).*((cos1.*beta_v(vp1,1).*(SS(p1,7)).*(vp(vp1,4)))))./((R.^2).*(%pi))
    end
end
endfunction

// The DEA calculation from Surface to Surface:
function [SS_DEA_12]=DEA_1(AA, BB, ii, jj)
node = 0
    for p2=1:jj
        for p1=1:ii
    node = node + 1
            R= sqrt((AA(p1,1)-BB(p2,1)).^2 + (AA(p1,2)-BB(p2,2)).^2 + (AA(p1,3)-BB(p2,3)).^2)
            cos1=(AA(p1,4)*sqrt((AA(p1,1)-BB(p2,1)).^2)+AA(p1,5)*sqrt((AA(p1,2)-BB(p2,2)).^2)+AA(p1,6)*sqrt((AA(p1,3)-
BB(p2,3)).^2))./R
            cos2=(BB(p2,4)*sqrt((AA(p1,1)-BB(p2,1)).^2)+BB(p2,5)*sqrt((AA(p1,2)-BB(p2,2)).^2)+BB(p2,6)*sqrt((AA(p1,3)-
BB(p2,3)).^2))./R
            SS_DEA_12(p1,p2)=((exp(-(mean(beta_v)).*R)).*((cos1.*cos2.*(AA(p1,7)).*(BB(p2,7)))))./((R.^2).*(%pi))
    end
end
```

```
endfunction

function [Front]=S1(jj, kk)
   node = 0;
for j = 1:jj
   for k = 1:kk
         node = node + 1;
         Front(node,1) = L_x  // Front Surface
         Front(node,2) = L_y/m*(j-0.5)
         Front(node,3) = L_z/o*(k-0.5)
         Front(node,4) = 1
         Front(node,5) = 0
         Front(node,6) = 0
         Front(node,7) = (L_y/m)*(L_z/o)
         Front(node,8) = (L_y)*(L_z)
   end
end
endfunction

function [Back]=S2(jj, kk)
   node = 0;
for j = 1:jj
   for k = 1:kk
         node = node + 1;
         Back(node,1) = L_x/n*0  // Back Surface
         Back(node,2) = L_y/m*(j-0.5)
         Back(node,3) = L_z/o*(k-0.5)
         Back(node,4) = 1
         Back(node,5) = 0
         Back(node,6) = 0
         Back(node,7) = (L_y/m)*(L_z/o)
         Back(node,8) = (L_y)*(L_z)
   end
end
endfunction

function [Bottom]=S3(ii, jj)
   node = 0;
for j = 1:jj
   for i = 1:ii
         node = node + 1;
         Bottom(node,1) = L_x/n*(i-0.5)  // Bottom surface
         Bottom(node,2) = L_y/m*(j-0.5)
         Bottom(node,3) = L_z/o*0
         Bottom(node,4) = 0
         Bottom(node,5) = 0
         Bottom(node,6) = 1
         Bottom(node,7) =(L_x/n)*(L_y/m)
         Bottom(node,8) = (L_x)*(L_y)
   end
end
endfunction

function [Top]=S4(ii, jj)
   node = 0;
for j = 1:jj
   for i = 1:ii
         node = node + 1;
         Top(node,1) = L_x/n*(i-0.5)  // Top surface
         Top(node,2) = L_y/m*(j-0.5)
         Top(node,3) = L_z
         Top(node,4) = 0
         Top(node,5) = 0
         Top(node,6) = 1
         Top(node,7) = (L_x/n)*(L_y/m)
```

```
        Top(node,8) = (L_x)*(L_y)
    end
end
endfunction

function [Left]=S5(ii, kk)
    node = 0;
for i = 1:ii
    for k = 1:kk
        node = node + 1;
        Left(node,1) = L_x/n*(i-0.5)  // Left surface
        Left(node,2) = L_y/m*0
        Left(node,3) = L_z/o*(k-0.5)
        Left(node,4) = 0
        Left(node,5) = 1
        Left(node,6) = 0
        Left(node,7) = (L_x/n)*(L_z/o)
        Left(node,8) = (L_y)*(L_z)
    end
end
endfunction

function [Right]=S6(ii, kk)
    node = 0;
for i = 1:ii
    for k = 1:kk
        node = node + 1;
        Right(node,1) = L_x/n*(i-0.5)  // Right surface
        Right(node,2) = L_y
        Right(node,3) = L_z/o*(k-0.5)
        Right(node,4) = 0
        Right(node,5) = 1
        Right(node,6) = 0
        Right(node,7) = (L_x/n)*(L_z/o)
        Right(node,8) = (L_x)*(L_z)
    end
end
endfunction

function [C_bar, D_bar, P_bar, Q_bar, R_bar, W_bar, X_bar]=ExchangeAreas(eps, kappa_v, sigma_v, n_s, n_v, n_t, n, m, o)

//Emissivities of the surfaces
e=ones(n_s,1)*eps
ee=ones(n_v,1)*eps

// PARTICIPATING MEDIA PROPERTIES
//sigma_v = ones(n_v,1)*scat;//Scattering coefficient per volume
//kappa_v = ones(n_v,1)*abso;//Absorption coefficient per volume
beta_v = sigma_v + kappa_v;// Extinction coefficient (m^-1)

//Scattering albedos
www=ones(n_s,1)*(sigma_v./(sigma_v+kappa_v))'//scattering/Beta - Scattering albedo
wii=ones(n_v,1)*(sigma_v./(sigma_v+kappa_v))'//scattering/Beta - Scattering albedo

//Surfaces
Front=S1(m,o)
Back=S2(m,o)
Bottom=S3(n,m)
Top=S4(n,m)
Left=S5(n,o)
Right=S6(n,o)

//Display all the SURFACE nodes in a matrix:
p=[S1(m,o);S2(m,o);S3(n,m);S4(n,m);S5(n,o);S6(n,o)] //Surface nodes information
//VOLUME NODES: Each node holds information of its position in terms of the x,y & z co-ordinates of the node, the volume of the
```

```
small node as well as the large volume without discretisation.
node = 0;
for k = 1:o
   for j = 1:m
      for i = 1:n
         node = node + 1;
         Vol(node,1) = L_x/n*(i-0.5)
         Vol(node,2) = L_y/m*(j-0.5)
         Vol(node,3) = L_z/o*(k-0.5)
         Vol(node,4) = (L_x/n)*(L_y/m)*(L_z/o)
         Vol(node,5) = (L_x)*(L_y)*(L_z)
      end
   end
end
//Display all the VOLUME nodes in a matrix:
vp=[Vol] //Volume nodes information
// The DEA calculation from Surface to Surface:
FF=zeros(m*o,m*o)
FB=DEA_1(Front,Back,m*o,m*o)
FBo=DEA_1(Front,Bottom,m*o,n*m)
FT=DEA_1(Front,Top,m*o,n*m)
FL=DEA_1(Front,Left,m*o,n*o)
FR=DEA_1(Front,Right,m*o,n*o)
BF=DEA_1(Back,Front,m*o,m*o)
BB=zeros(m*o,m*o)
BBo=DEA_1(Back,Bottom,m*o,n*m)
BT=DEA_1(Back,Top,m*o,n*m)
BL=DEA_1(Back,Left,m*o,n*o)
BR=DEA_1(Back,Right,m*o,n*o)
BoF=DEA_1(Bottom,Front,n*m,m*o)
BoB=DEA_1(Bottom,Back,n*m,m*o)
BoBo=zeros(n*m,n*m)
BoT=DEA_1(Bottom,Top,n*m,n*m)
BoL=DEA_1(Bottom,Left,n*m,n*o)
BoR=DEA_1(Bottom,Right,n*m,n*o)
TF=DEA_1(Top,Front,n*m,m*o)
TB=DEA_1(Top,Back,n*m,m*o)
TBo=DEA_1(Top,Bottom,n*m,n*m)
TT=zeros(n*m,n*m)
TL=DEA_1(Top,Left,n*m,n*o)
TR=DEA_1(Top,Right,n*m,n*o)
LF=DEA_1(Left,Front,n*o,m*o)
LB=DEA_1(Left,Back,n*o,m*o)
LBo=DEA_1(Left,Bottom,n*o,n*m)
LT=DEA_1(Left,Top,n*o,n*m)
LL=zeros(n*o,n*o)
LR=DEA_1(Left,Right,n*o,n*o)
RF=DEA_1(Right,Front,n*o,m*o)
RB=DEA_1(Right,Back,n*o,m*o)
RBo=DEA_1(Right,Bottom,n*o,n*m)
RT=DEA_1(Right,Top,n*o,n*m)
RL=DEA_1(Right,Left,n*o,n*o)
RR=zeros(n*o,n*o)
SS=[FF FB FBo FT FL FR;
    FB BB BBo BT BL BR;
    BoF BoB BoBo BoT BoL BoR;
    TF TB TBo TT TL TR;
    LF LB LBo LT LL LR;
    RF RB RBo RT RL RR]
//Volume-Volume DEAs:
node = 0
   for vp2=1:(n*m*o)
      for vp1=1:(n*m*o)
   node = node + 1
         if ((vp2<>vp1)) then
```

```
        R= sqrt((vp(vp1,1)-vp(vp2,1)).^2 + (vp(vp1,2)-vp(vp2,2)).^2 + (vp(vp1,3)-vp(vp2,3)).^2)
        VV(vp2,vp1)=(exp(-
(0.5*(beta_v(vp2,1)+beta_v(vp1,1))).*R).*((0.5*(beta_v(vp2,1)+beta_v(vp1,1))).^2).*((vp(vp1,4)*vp(vp2,4)))./((R.^2).*(%pi))
      else
        VV(vp2,vp1)=0
      end
    end
end
// DEAs from RIGHT to all the other surfaces;
VF=DEA_3(Front,m*o)
VB=DEA_3(Back,m*o)
VBo=DEA_3(Bottom,n*m)
VT=DEA_3(Top,n*m)
VL=DEA_3(Left,n*o)
VR=DEA_3(Right,n*o)
VS=[VF VB VBo VT VL VR]
// (3) LEAST SQUARES SMOOTHING USING LAGRANGE
XX=[SS VS';VS VV] //All the DEAs assembled into one matrix
//The weights that allow for DEAs to be adjusted proportionally
W=XX.^2
//Totals along rows and columns
for i=1:n_t
  for j=1:n_t
    //Sum of the rows of every column of the DEAs matrix
      AA(1,j)=sum(XX(:,j))
    //Sum of the rows of every column of the weights matrix
      WW(1,j)=sum(W(:,j))
  end
end
//The conservation constraints that must be satisfied
b=[p(:,7)' (4*beta_v.*vp(:,4))']
C=b-AA
//Weights used to calculate the Lagrange multipliers
R=W+(ones(n_t,1)*WW).*eye(n_t,n_t)
//Lagrange multipliers
L=lsq(R,C')
//Lagrangian transpose for every DEA (rows)
L1=ones(n_t,1)*L'
//Lagrangian for every DEA (columns)
L2=L*(ones(1,n_t))
//Lagrange multipliers for every DEA
lam=L1+L2
//Least squares smoothing using Lagrange multipliers (Smoothed DEAs)
XXX=XX+W.*lam
//DEAs extracted from the entire DEAs system
DEA_ss=XXX(1:n_s,1:n_s)  //Surface to surface
DEA_sg=XXX(1:n_s,n_s+1:n_t)
DEA_gs=XXX(n_s+1:n_t,1:n_s)  //Volume to surface
DEA_gg=XXX(n_s+1:n_t,n_s+1:n_t)  //Volume to volume
//Developing the T matrix
for i=1:n_s
  for j=1:n_s
    if j==i then
      T(i,j)=(1/e(i,j))-(DEA_ss(i,j).*((1-e(i,j))./e(i,j)))./p(i,7)
    else
      T(i,j)=(-1)*DEA_ss(i,j).*((1-e(i,j))./e(i,j))./p(i,7)
    end
  end
end
// S matrix
S=DEA_ss.*e
// sg matrix
sg=DEA_sg
//R matrix
R_bar=DEA_gs.*ee
```

```
//Q matrix
Q_bar=(DEA_gs./(ones(n_v,1)*p(:,7)')).*((1-ee)./ee)
//U matrix
U=(DEA_sg./(4*ones(n_s,1)*(kappa_v.*vp(:,4))')).*www
//W matrix
for i=1:n_v
   for j=1:n_v
      if j==i then
         W_bar(i,j)=(1/(1-wii(i,j)))-DEA_gg(i,j).*wii(i,j)./(4*kappa_v(i,1)*vp(i,4))
      else
         W_bar(i,j)=(-1)*DEA_gg(i,j).*wii(i,j)./(4*kappa_v(i,1)*vp(i,4))
      end
   end
end
//V matrix
V=DEA_sg.*(1-www)
//X matrix
X_bar=DEA_gg.*(1-wii)
//C matrix
C_bar=S+U*lsq(W_bar,R_bar)
//D matrix
D_bar=V+U*lsq(W_bar,X_bar)
//P matrix
P_bar=T-U*lsq(W_bar,Q_bar)
endfunction
[C_bar, D_bar, P_bar, Q_bar, R_bar, W_bar, X_bar] = ExchangeAreas(eps, kappa_v', sigma_v', n_s, n_v, n_t, n_x, n_y, n_z)
[verification_C_bar, verification_D_bar, verification_P_bar, verification_Q_bar, verification_R_bar, verification_W_bar,
verification_X_bar] = ExchangeAreas(0.85*ones(1,n_s), 0.15*ones(n_v,1), 0.0*ones(n_v,1), n_s, n_v, n_t, n_x, n_y, n_z)

//---------------------------------------------------------------------------
t(2,1) = toc()
time = time + t(2,1)
tic()

counter = 2;

iter = 1;
success_converged = 0;
rad_counter = 0;
while (success_converged ~= 1)
iter = iter + 1;
   for i = 1:length(Burners)
      //---------------------------------------------------------------------
      //Combustion model burner conditions
      mf_C1i(Burners(i),iter) = mf_C1i(Burners(i),1)*m_total(i)/m_in(Burners(i),1);
      mf_C2i(Burners(i),iter) = mf_C2i(Burners(i),1)*m_total(i)/m_in(Burners(i),1);
      mf_C3i(Burners(i),iter) = mf_C3i(Burners(i),1)*m_total(i)/m_in(Burners(i),1);
      mf_C4i(Burners(i),iter) = mf_C4i(Burners(i),1)*m_total(i)/m_in(Burners(i),1);
      mf_VCi(Burners(i),iter) = mf_VCi(Burners(i),1)*m_total(i)/m_in(Burners(i),1);
      mf_H2i(Burners(i),iter) = mf_H2i(Burners(i),1)*m_total(i)/m_in(Burners(i),1);
      mf_O2i(Burners(i),iter) = mf_O2i(Burners(i),1)*m_total(i)/m_in(Burners(i),1);
      mf_N2i(Burners(i),iter) = mf_N2i(Burners(i),1)*m_total(i)/m_in(Burners(i),1);
      mf_Si(Burners(i),iter) = mf_Si(Burners(i),1)*m_total(i)/m_in(Burners(i),1);
      mf_Ashi(Burners(i),iter) = mf_Ashi(Burners(i),1)*m_total(i)/m_in(Burners(i),1);
      mf_CO2i(Burners(i),iter) = mf_CO2i(Burners(i),1)*m_total(i)/m_in(Burners(i),1);
      mf_H2Oi(Burners(i),iter) = mf_H2Oi(Burners(i),1)*m_total(i)/m_in(Burners(i),1);
      mf_NO2i(Burners(i),iter) = mf_NO2i(Burners(i),1)*m_total(i)/m_in(Burners(i),1);
      mf_SO2i(Burners(i),iter) = mf_SO2i(Burners(i),1)*m_total(i)/m_in(Burners(i),1);
      x_1i(Burners(i),iter) = x_1i(Burners(i),1)*m_total(i)/m_in(Burners(i),1);
      x_2i(Burners(i),iter) = x_1i(Burners(i),1)*m_total(i)/m_in(Burners(i),1);
      x_3i(Burners(i),iter) = x_1i(Burners(i),1)*m_total(i)/m_in(Burners(i),1);
      x_4i(Burners(i),iter) = x_1i(Burners(i),1)*m_total(i)/m_in(Burners(i),1);
      mk_fi(Burners(i),iter) = mk_fi(Burners(i),1)*m_total(i)/m_in(Burners(i),1);
      mk_fgi(Burners(i),iter) = mk_fgi(Burners(i),1)*m_total(i)/m_in(Burners(i),1);
      //---------------------------------------------------------------------
```

```
    //-----------------------------------------------------------------
    //Energy balance model burner conditions
    H_ai(Burners(i),iter) = H_ai(Burners(i),1)*m_total(i)/m_in(Burners(i),1);//enthalpy of air into cell [kJ/kg]
    //-----------------------------------------------------------------
  end

  for k=1:size(M_a_sparse,1)
    //-----------------------------------------------------------------
    //Combustion model volume inflow
    mf_C1i(M_a_sparse(k,2),iter) = mf_C1i(M_a_sparse(k,2),iter) + mf_C1o(M_a_sparse(k,1),iter-
1)*M_a_sparse(k,3)/m_in(M_a_sparse(k,2),1);
    mf_C2i(M_a_sparse(k,2),iter) = mf_C2i(M_a_sparse(k,2),iter) + mf_C2o(M_a_sparse(k,1),iter-
1)*M_a_sparse(k,3)/m_in(M_a_sparse(k,2),1);
    mf_C3i(M_a_sparse(k,2),iter) = mf_C3i(M_a_sparse(k,2),iter) + mf_C3o(M_a_sparse(k,1),iter-
1)*M_a_sparse(k,3)/m_in(M_a_sparse(k,2),1);
    mf_C4i(M_a_sparse(k,2),iter) = mf_C4i(M_a_sparse(k,2),iter) + mf_C4o(M_a_sparse(k,1),iter-
1)*M_a_sparse(k,3)/m_in(M_a_sparse(k,2),1);
    mf_VCi(M_a_sparse(k,2),iter) = mf_VCi(M_a_sparse(k,2),iter) + mf_VCo(M_a_sparse(k,1),iter-
1)*M_a_sparse(k,3)/m_in(M_a_sparse(k,2),1);
    mf_H2i(M_a_sparse(k,2),iter) = mf_H2i(M_a_sparse(k,2),iter) + mf_H2o(M_a_sparse(k,1),iter-
1)*M_a_sparse(k,3)/m_in(M_a_sparse(k,2),1);
    mf_O2i(M_a_sparse(k,2),iter) = mf_O2i(M_a_sparse(k,2),iter) + mf_O2o(M_a_sparse(k,1),iter-
1)*M_a_sparse(k,3)/m_in(M_a_sparse(k,2),1);
    mf_N2i(M_a_sparse(k,2),iter) = mf_N2i(M_a_sparse(k,2),iter) + mf_N2o(M_a_sparse(k,1),iter-
1)*M_a_sparse(k,3)/m_in(M_a_sparse(k,2),1);
    mf_Si(M_a_sparse(k,2),iter) = mf_Si(M_a_sparse(k,2),iter) + mf_So(M_a_sparse(k,1),iter-
1)*M_a_sparse(k,3)/m_in(M_a_sparse(k,2),1);
    mf_Ashi(M_a_sparse(k,2),iter) = mf_Ashi(M_a_sparse(k,2),iter) + mf_Asho(M_a_sparse(k,1),iter-
1)*M_a_sparse(k,3)/m_in(M_a_sparse(k,2),1);
    mf_CO2i(M_a_sparse(k,2),iter) = mf_CO2i(M_a_sparse(k,2),iter) + mf_CO2o(M_a_sparse(k,1),iter-
1)*M_a_sparse(k,3)/m_in(M_a_sparse(k,2),1);
    mf_H2Oi(M_a_sparse(k,2),iter) = mf_H2Oi(M_a_sparse(k,2),iter) + mf_H2Oo(M_a_sparse(k,1),iter-
1)*M_a_sparse(k,3)/m_in(M_a_sparse(k,2),1);
    mf_NO2i(M_a_sparse(k,2),iter) = mf_NO2i(M_a_sparse(k,2),iter) + mf_NO2o(M_a_sparse(k,1),iter-
1)*M_a_sparse(k,3)/m_in(M_a_sparse(k,2),1);
    mf_SO2i(M_a_sparse(k,2),iter) = mf_SO2i(M_a_sparse(k,2),iter) + mf_SO2o(M_a_sparse(k,1),iter-
1)*M_a_sparse(k,3)/m_in(M_a_sparse(k,2),1);
    x_1i(M_a_sparse(k,2),iter) = x_1i(M_a_sparse(k,2),iter) + x_1o(M_a_sparse(k,1),iter-
1)*M_a_sparse(k,3)/m_in(M_a_sparse(k,2),1);
    x_2i(M_a_sparse(k,2),iter) = x_2i(M_a_sparse(k,2),iter) + x_2o(M_a_sparse(k,1),iter-
1)*M_a_sparse(k,3)/m_in(M_a_sparse(k,2),1);
    x_3i(M_a_sparse(k,2),iter) = x_3i(M_a_sparse(k,2),iter) + x_3o(M_a_sparse(k,1),iter-
1)*M_a_sparse(k,3)/m_in(M_a_sparse(k,2),1);
    x_4i(M_a_sparse(k,2),iter) = x_4i(M_a_sparse(k,2),iter) + x_4o(M_a_sparse(k,1),iter-
1)*M_a_sparse(k,3)/m_in(M_a_sparse(k,2),1);
    mk_fi(M_a_sparse(k,2),iter) = mk_fi(M_a_sparse(k,2),iter) + mk_fo(M_a_sparse(k,1),iter-
1)*M_a_sparse(k,3)/m_in(M_a_sparse(k,2),1);
    mk_fgi(M_a_sparse(k,2),iter) = mk_fgi(M_a_sparse(k,2),iter) + mk_fgo(M_a_sparse(k,1),iter-
1)*M_a_sparse(k,3)/m_in(M_a_sparse(k,2),1);
    //-----------------------------------------------------------------

    //-----------------------------------------------------------------
    //Enengy balance model volume inflow
    //Summation of the enthalpy of the incoming air/gas
    H_ai(M_a_sparse(k,2),iter) = H_ai(M_a_sparse(k,2),iter) + M_a_sparse(k,3)*h_ao(M_a_sparse(k,1),iter-1);
    //-----------------------------------------------------------------
  end

  //-----------------------------------------------------------------
  //Combustion model calculation for inflow
  mf_C1i = max(mf_C1i,1e-8);
  mf_C2i = max(mf_C2i,1e-8);
  mf_C3i = max(mf_C3i,1e-8);
  mf_C4i = max(mf_C4i,1e-8);
```

```
    mf_Ci = max(mf_C1i + mf_C2i + mf_C3i + mf_C4i,1e-8);
    mf_VCi = max(mf_VCi,1e-8);
    mf_H2i = max(mf_H2i,1e-8);
    mf_O2i = max(mf_O2i,1e-8);
    mf_N2i = max(mf_N2i,1e-8);
    mf_Si = max(mf_Si,1e-8);
    mf_Ashi = max(mf_Ashi,1e-8);
    mf_CO2i = max(mf_CO2i,1e-8);
    mf_H2Oi = max(mf_H2Oi,1e-8);
    mf_NO2i = max(mf_NO2i,1e-8);
    mf_SO2i = max(mf_SO2i,1e-8);
    x_1i = max(x_1i,1e-8);
    x_2i = max(x_2i,1e-8);
    x_3i = max(x_3i,1e-8);
    x_4i = max(x_4i,1e-8);

    mk_fi = max(1e-8,mf_C1i + mf_C2i + mf_C3i + mf_C4i + mf_VCi + mf_H2i + mf_Si + mf_Ashi);
    mk_O2i = mf_O2i.*mk_fgi;
    mk_N2i = mf_N2i.*mk_fgi;
    mk_CO2i = mf_CO2i.*mk_fgi;
    mk_H2Oi = mf_H2Oi.*mk_fgi;
    mk_NO2i = mf_NO2i.*mk_fgi;
    mk_SO2i = mf_SO2i.*mk_fgi;

    vk_O2i = 22.4*mk_O2i./32;
    vk_N2i = 22.4*mk_N2i./28;
    vk_CO2i = 22.4*mk_CO2i./44;
    vk_H2Oi = 22.4*mk_H2Oi./14;
    vk_NO2i = 22.4*mk_NO2i./46;
    vk_SO2i = 22.4*mk_SO2i./64;
    vk_fgi = max(vk_O2i + vk_N2i + vk_CO2i + vk_H2Oi + vk_NO2i + vk_SO2i,1e-8);

    vf_O2i = max(1e-8,vk_O2i./vk_fgi);
    vf_N2i = max(1e-8,vk_N2i./vk_fgi);
    vf_CO2i = max(1e-8,vk_CO2i./vk_fgi);
    vf_H2Oi = max(1e-8,vk_H2Oi./vk_fgi);
    vf_NO2i = max(1e-8,vk_NO2i./vk_fgi);
    vf_SO2i = max(1e-8,vk_SO2i./vk_fgi);
    vf_O2i_dry = max(1e-8,vk_O2i./(vk_fgi - vk_H2Oi));
    vf_CO2i_dry = max(1e-8,vk_CO2i./(vk_fgi - vk_H2Oi));
    //-------------------------------------------------------------------------

    t(3,iter) = toc()
    time = time + t(3,iter)
    tic()

    counter = counter + 1;

    //-------------------------------------------------------------------------
    //Energy balance model calculation for inflow
    //Calculating the temperature of the incoming gas and particles from the enthalpy
    h_ai(:,iter) = H_ai(:,iter)./m_in(:,1);
    [T_ai(:,iter),errT(:,iter)] =
TEMPERATURE(h_ai(:,iter),(mf_Ci(:,iter)+mf_VCi(:,iter)).*mk_fgi(:,iter)./(mk_fgi(:,iter)+mk_fi(:,iter)),mf_CO2i(:,iter).*mk_fgi(:,
iter)./(mk_fgi(:,iter)+mk_fi(:,iter)),mf_H2i(:,iter).*mk_fgi(:,iter)./(mk_fgi(:,iter)+mk_fi(:,iter)),mf_H2Oi(:,iter).*mk_fgi(:,iter)./(mk_
fgi(:,iter)+mk_fi(:,iter)),mf_O2i(:,iter).*mk_fgi(:,iter)./(mk_fgi(:,iter)+mk_fi(:,iter)),mf_N2i(:,iter).*mk_fgi(:,iter)./(mk_fgi(:,iter)+m
k_fi(:,iter)),mf_NO2i(:,iter).*mk_fgi(:,iter)./(mk_fgi(:,iter)+mk_fi(:,iter)),mf_Si(:,iter).*mk_fgi(:,iter)./(mk_fgi(:,iter)+mk_fi(:,iter)),
mf_SO2i(:,iter).*mk_fgi(:,iter)./(mk_fgi(:,iter)+mk_fi(:,iter)),mf_Ashi(:,iter).*mk_fgi(:,iter)./(mk_fgi(:,iter)+mk_fi(:,iter)),T_ai(:,iter
-1),T_min,T_max);

    //Calculating the wall temperature based on the heat flux and fluid inside temperature
    T_w(:,iter) = T_f' + (-1)*Q_s(:,1).*R_t;//Wall temperature [K] (minus is because sign convection for radiation heat transfer is in
the other direction)
    //-------------------------------------------------------------------------
```

```
    //-----------------------------------------------------------------------
    //Combustion model reactions

    //Devolatilisation calculation
    dVC_ds(:,iter) = min(mf_VCi(:,iter),mf_VCi(:,iter).*x_b(:)./x_f)*relax_Devol(iter);//Devol of carbon
    dH2_ds(:,iter) = min(mf_H2i(:,iter),mf_H2i(:,iter).*x_b(:)./x_f)*relax_Devol(iter);//Devol of hydrogen
    dS_ds(:,iter) = min(mf_Si(:,iter),mf_Si(:,iter).*x_b(:)./x_f)*relax_Devol(iter);//Devol of sulphur

    //Calculating the combustion reaction coefficients
    if (CRC == 1) then//Field et al (1967) for low surface reaction rate
        K_s(:,iter) = 0.565*max(1e-8,10000*1.65.*exp(-1*17000 ./(1.986.*T_ai(:,iter))));//Surface reaction coefficient
[g/cm^2*s*atm]*10000 = [g/m^2*s*atm] //Calibrated
        //K_s(:,iter) = 1.0*max(1e-8,10000*1.65.*exp(-1*17000 ./(1.986.*T_ai(:,iter))));//Surface reaction coefficient
[g/cm^2*s*atm]*10000 = [g/m^2*s*atm] //Base
    end
    if (CRC == 2) then//Field et al (1967) for high surface reaction rate
        K_s(:,iter) = max(1e-8,10000*8710.*exp(-1*35700 ./(1.986.*T_ai(:,iter))));//Surface reaction coefficient
[g/cm^2*s*atm]*10000 = [g/m^2*s*atm]
    end
    if (CRC == 3) then//Gill (1969)
        K_s(:,iter) = max(1e-8,10000*(-0.224 + 5.85e-5*T_ai(:,iter) + 9.58e-8*T_ai(:,iter).^2));//Surface reaction coefficient
[g/cm^2*s*atm]*10000 = [g/m^2*s*atm]
    end

    w1(:,iter) = mf_C1i(:,iter)./(mf_Ci(:,iter)+mf_VCi(:,iter)+mf_Si(:,iter)+mf_H2i(:,iter)+mf_Ashi(:,iter));//Weight of raw coal in 1th
size fraction per unit weight of raw coal [-]
    w2(:,iter) = mf_C2i(:,iter)./(mf_Ci(:,iter)+mf_VCi(:,iter)+mf_Si(:,iter)+mf_H2i(:,iter)+mf_Ashi(:,iter));//Weight of raw coal in 2th
size fraction per unit weight of raw coal [-]
    w3(:,iter) = mf_C3i(:,iter)./(mf_Ci(:,iter)+mf_VCi(:,iter)+mf_Si(:,iter)+mf_H2i(:,iter)+mf_Ashi(:,iter));//Weight of raw coal in 3th
size fraction per unit weight of raw coal [-]
    w4(:,iter) = mf_C4i(:,iter)./(mf_Ci(:,iter)+mf_VCi(:,iter)+mf_Si(:,iter)+mf_H2i(:,iter)+mf_Ashi(:,iter));//Weight of raw coal in 4th
size fraction per unit weight of raw coal [-]
    S_1i(:,iter) = S_1i0.*(x_1i(:,iter)./(alpha*d_p1_ave*0.01)).^2; //Surface area of 1th size fraction after devolitisation per unit
weight of residual char (cm^2/g)
    S_2i(:,iter) = S_2i0.*(x_2i(:,iter)./(alpha*d_p2_ave*0.01)).^2; //Surface area of 2th size fraction after devolitisation per unit
weight of residual char (cm^2/g)
    S_3i(:,iter) = S_3i0.*(x_3i(:,iter)./(alpha*d_p3_ave*0.01)).^2; //Surface area of 3th size fraction after devolitisation per unit
weight of residual char (cm^2/g)
    S_4i(:,iter) = S_4i0.*(x_4i(:,iter)./(alpha*d_p4_ave*0.01)).^2; //Surface area of 4th size fraction after devolitisation per unit
weight of residual char (cm^2/g)

    p_o = vf_O2i*(p_atm/1);//Oxygen partial pressure in air [atm]
    K_diff(:,iter) = 10000*(-8.685e-11*T_ai(:,iter).^3 + 1.2116e-6*T_ai(:,iter).^2 + 0.00046639*T_ai(:,iter)); //Diffusion rate constant
[g/cm^2*s*atm]*10000 = [g/m^2*s*atm]

    dC_ds1(:,iter) =
max(0,(((mf_C1i(:,iter)./w1(:,iter)).^(2/3)).*S_1i(:,iter).*p_o(:,iter))./(((mf_C1i(:,iter)./w1(:,iter)).^(1/3))./K_diff(:,iter) +
(K_s(:,iter)).^(-1))*relax_Char(iter));
    dC_ds2(:,iter) =
max(0,(((mf_C2i(:,iter)./w2(:,iter)).^(2/3)).*S_2i(:,iter).*p_o(:,iter))./(((mf_C2i(:,iter)./w2(:,iter)).^(1/3))./K_diff(:,iter) +
(K_s(:,iter)).^(-1))*relax_Char(iter));
    dC_ds3(:,iter) =
max(0,(((mf_C3i(:,iter)./w3(:,iter)).^(2/3)).*S_3i(:,iter).*p_o(:,iter))./(((mf_C3i(:,iter)./w3(:,iter)).^(1/3))./K_diff(:,iter) +
(K_s(:,iter)).^(-1))*relax_Char(iter));
    dC_ds4(:,iter) =
max(0,(((mf_C4i(:,iter)./w4(:,iter)).^(2/3)).*S_4i(:,iter).*p_o(:,iter))./(((mf_C4i(:,iter)./w4(:,iter)).^(1/3))./K_diff(:,iter) +
(K_s(:,iter)).^(-1))*relax_Char(iter));
    //-----------------------------------------------------------------------

    //-----------------------------------------------------------------------
    //Combustion model outflow
    mf_C1o = max(mf_C1i - dC_ds1,0);
    mf_C2o = max(mf_C2i - dC_ds2,0);
    mf_C3o = max(mf_C3i - dC_ds3,0);
    mf_C4o = max(mf_C4i - dC_ds4,0);
```

```
    mf_Co = max(mf_C1o + mf_C2o + mf_C3o + mf_C4o,1e-8);
    mf_VCo = max(mf_VCi - dVC_ds,0);
    mf_H2o = max(mf_H2i - dH2_ds,0);
    mf_So = max(mf_Si - dS_ds,0);
    mf_Asho = mf_Ashi;

    mk_fo = max(1e-8,mf_C1o + mf_C2o + mf_C3o + mf_C4o + mf_VCo + mf_H2o + mf_So + mf_Asho);//All nitrogen and water
consider part of gas as soon as leaving the first cell
    mk_fgo =  mk_fgi + (mf_C1i - mf_C1o) + (mf_C2i - mf_C2o) + (mf_C3i - mf_C3o) + (mf_C4i - mf_C4o) + (mf_VCi -
mf_VCo);//flue gas out of cell [kg O2/kg Coal]
    mk_CO2o = mk_CO2i + 44/12*(mf_C1i - mf_C1o) + 44/12*(mf_C2i - mf_C2o) + 44/12*(mf_C3i - mf_C3o) + 44/12*(mf_C4i -
mf_C4o) + 44/12*(mf_VCi - mf_VCo);
    mk_H2Oo = mk_H2Oi + 18/2*(mf_H2i - mf_H2o);
    mk_NO2o = mk_NO2i;
    mk_SO2o = mk_SO2i + 64/32*(mf_Si - mf_So);
    mk_N2o = mk_N2i;
    mk_O2o = mk_fgo - mk_CO2o - mk_N2o - mk_H2Oo - mk_NO2o - mk_SO2o;//O2 out of cell [kg O2/kg Coal]

    mf_N2o = mk_N2o./mk_fgo;
    mf_O2o = mk_O2o./mk_fgo;
    mf_CO2o = mk_CO2o./mk_fgo;
    mf_H2Oo = mk_H2Oo./mk_fgo;
    mf_NO2o = mk_NO2o./mk_fgo;
    mf_SO2o = mk_SO2o./mk_fgo;

    vk_O2o = 22.4*mk_O2o./32;
    vk_N2o = 22.4*mk_N2o./28;
    vk_CO2o = 22.4*mk_CO2o./44;
    vk_H2Oo = 22.4*mk_H2Oo./14;
    vk_NO2o = 22.4*mk_NO2o./46;
    vk_SO2o = 22.4*mk_SO2o./64;
    vk_fgo = max(vk_O2o + vk_N2o + vk_CO2o + vk_H2Oo + vk_NO2o + vk_SO2o,1e-8);

    vf_O2o = max(1e-8,vk_O2o./vk_fgo);
    vf_N2o = max(1e-8,vk_N2o./vk_fgo);
    vf_CO2o = max(1e-8,vk_CO2o./vk_fgo);
    vf_H2Oo = max(1e-8,vk_H2Oo./vk_fgo);
    vf_NO2o = max(1e-8,vk_NO2o./vk_fgo);
    vf_SO2o = max(1e-8,vk_SO2o./vk_fgo);
    vf_O2o_dry = max(1e-8,vk_O2o./(vk_fgo - vk_H2Oo));
    vf_CO2o_dry = max(1e-8,vk_CO2o./(vk_fgo - vk_H2Oo));

    //Calculating the outgoing particle sizes
    x_1o(:,iter) = 0.01*alpha*d_p1_ave.*(mf_C1o(:,iter)./w1(:,iter)).^(1/3);
    x_2o(:,iter) = 0.01*alpha*d_p2_ave.*(mf_C2o(:,iter)./w2(:,iter)).^(1/3);
    x_3o(:,iter) = 0.01*alpha*d_p3_ave.*(mf_C3o(:,iter)./w3(:,iter)).^(1/3);
    x_4o(:,iter) = 0.01*alpha*d_p4_ave.*(mf_C4o(:,iter)./w4(:,iter)).^(1/3);
    //---------------------------------------------------------------------

    //---------------------------------------------------------------------
    //Gas and particle radiation properties calculation model
    rad_counter = rad_counter + 1;

    t(4,iter) = toc()
    time = time + t(4,iter)
    tic()

    if rad_counter == rad_iter then
        if constRadProperties == 1 then
            kappa_p = ones(1,n_v).*constant_kappa_p;//constant absorptivity value
            kappa_g = ones(1,n_v).*constant_kappa_g;//constant absorptivity value
            kappa_v = kappa_p + kappa_g;//constant absorptivity value
            sigma_v = ones(1,n_v).*constant_sigma;
        else
            L_m=3.6*(V_g/A_s);// Mean beam length [m]
```

```
        p_a_H2O = max(vf_H2Oi(:,iter)*(p_atm/1),1e-8);//H2O partial pressure[bar]
        p_a_CO2 = max(vf_CO2i(:,iter)*(p_atm/1),1e-8);//CO2 partial pressure[bar]
        for k = 1:n_v

          [epsH2O(k),alpH2O(k)] = RadiationPropertiesH2O(p_atm,p_a_H2O(k),L_m,T_gi(k,1),mean(T_w(:,iter)));//furnace
pressure [bar],H2O partial pressure[bar],Mean beam length [m],Gas temperature[K],Wall tempterature[K]
          [epsCO2(k),alpCO2(k)] = RadiationPropertiesCO2(p_atm,p_a_CO2(k),L_m,T_gi(k,1),mean(T_w(:,iter)));
          zeta(k) = p_a_H2O(k)/(p_a_H2O(k) + p_a_CO2(k));
          delta_eps(k) = (zeta(k)/(10.7 + 101*zeta(k)) - 0.0089*zeta(k)^10.4)*(max(log10((p_a_H2O(k) +
p_a_CO2(k))*L_m*100/(1)),0))^2.76;
        end
        alpha_g = alpH2O + alpCO2 - delta_eps;
        kappa_g(:) = -1*log(1 - alpha_g(:))./L_m;//constant absorptivity value

        [epsilon_p1,kappa_p1] = RadiationPropertiesPar(n_v,mf_VCi(:,iter),mf_C1i(:,iter));
        [epsilon_p2,kappa_p2] = RadiationPropertiesPar(n_v,mf_VCi(:,iter),mf_C2i(:,iter));
        [epsilon_p3,kappa_p3] = RadiationPropertiesPar(n_v,mf_VCi(:,iter),mf_C3i(:,iter));
        [epsilon_p4,kappa_p4] = RadiationPropertiesPar(n_v,mf_VCi(:,iter),mf_C4i(:,iter));

        kappa_p = -1*log(1 - mf_RR(1)*epsilon_p1 - mf_RR(2)*epsilon_p2 - mf_RR(3)*epsilon_p3 -
mf_RR(4)*epsilon_p4)./L_m;//constant absorptivity value

        //Absorptivity and scattering per volume
        kappa_v = (1.5/mean(kappa_p + kappa_g)).*(kappa_p + kappa_g);//Calibrated
        //kappa_v = (kappa_p + kappa_g);//Base
        sigma_v = ones(1,n_v).*constant_sigma;
      end
      [C_bar, D_bar, P_bar, Q_bar, R_bar, W_bar, X_bar] = ExchangeAreas(eps, kappa_v', sigma_v', n_s, n_v, n_t, n_x, n_y, n_z)
      rad_counter = 0;
    end
    t(5,iter) = toc()
    time = time + t(5,iter)
    tic()

    //---------------------------------------------------------------------
    //Radiation heat transfer model
    //Zonal model to calculate radiation heat transfer leaving cell
    T_gi(:,1) = T_ai(:,iter);//Upwind scheme
    //T_gi(:,1) = T_ao(:,iter-1);//Downwind scheme
    e_bs=5.67e-8*T_w(:,iter).^4;  //Surface Emissive powers  [W/m2]
    e_bg=5.67e-8*T_gi.^4;  //Gas Emissive powers  [W/m2]
    h_s=(lsq(P_bar,C_bar)*e_bs+lsq(P_bar,D_bar)*e_bg);
    h_g=lsq(W_bar,(Q_bar*lsq(P_bar,C_bar)+R_bar))*e_bs+lsq(W_bar,(Q_bar*lsq(P_bar,D_bar)+X_bar))*e_bg;
    Q_s=(A_s.*eps'.*e_bs-h_s);
    Q_g=(4*V_g.*kappa_v'.*e_bg-h_g);
    Q_overall=sum(Q_s)+sum(Q_g);
    Qg_rad(:,iter) =  0.001*Q_g(:,1)*relax_Qrad(iter);//Radiation heat transfer [kW]
    //---------------------------------------------------------------------

    //---------------------------------------------------------------------
    //Energy balance model
    Q_gen(:,iter) = ((m_c_ave/m_total_ave)*m_in(:,1).*(32765*(mf_VCi(:,iter)-mf_VCo(:,iter))+(119959-21820)*(mf_H2i(:,iter)-
mf_H2o(:,iter))+9256*(mf_Si(:,iter)-mf_So(:,iter))) + (m_c_ave/m_total_ave)*m_in(:,1).*(32765*(mf_Ci(:,iter)-mf_Co(:,iter))));
    H_ao(:,iter) = H_ai(:,iter) - Qg_rad(:,iter) + Q_gen(:,iter);
    h_ao(:,iter) = H_ao(:,iter)./m_out(:,1);
    h_ao(:,iter) = relax_h(iter)*h_ao(:,iter) + (1 - relax_h(iter))*h_ao(:,iter-1);//Relaxation of outlet enthalpy change
    [T_ao(:,iter),errT(:,iter)] =
TEMPERATURE(h_ao(:,iter),(mf_Co(:,iter)+mf_VCo(:,iter)).*mk_fgo(:,iter)./(mk_fgo(:,iter)+mk_fo(:,iter)),mf_CO2o(:,iter).*mk_f
go(:,iter)./(mk_fgo(:,iter)+mk_fo(:,iter)),mf_H2o(:,iter).*mk_fgo(:,iter)./(mk_fgo(:,iter)+mk_fo(:,iter)),mf_H2Oo(:,iter).*mk_fgo(:,it
er)./(mk_fgo(:,iter)+mk_fo(:,iter)),mf_O2o(:,iter).*mk_fgo(:,iter)./(mk_fgo(:,iter)+mk_fo(:,iter)),mf_N2o(:,iter).*mk_fgo(:,iter)./(mk
_fgo(:,iter)+mk_fo(:,iter)),mf_NO2o(:,iter).*mk_fgo(:,iter)./(mk_fgo(:,iter)+mk_fo(:,iter)),mf_So(:,iter).*mk_fgo(:,iter)./(mk_fgo(:,it
er)+mk_fo(:,iter)),mf_SO2o(:,iter).*mk_fgo(:,iter)./(mk_fgo(:,iter)+mk_fo(:,iter)),mf_Asho(:,iter).*mk_fgo(:,iter)./(mk_fgo(:,iter)+m
k_fo(:,iter)),T_ao(:,iter-1),T_min,T_max);
    //---------------------------------------------------------------------
```

```
    //-------------------------------------------------------------------------
    //Numerical iteration check
    //Convergence calculation
    err1(:,iter) = abs(T_ai(:,iter) - T_ai(:,iter-1));
    meanerror(iter,1) = mean(err1(:,iter));
    err2(:,iter) = abs(Qg_rad(:,iter) - Qg_rad(:,iter-1));
    meanerror(iter,2) = mean(err2(:,iter));
    err3(:,iter) = abs(T_ao(Outlet1(:),iter) - T_ao(Outlet1(:),iter-1));
    meanerror(iter,3) = mean(err3(:,iter));
    err4(:,iter) = abs(mf_Co(Outlet1(:),iter) - mf_Co(Outlet1(:),iter-1));
    meanerror(iter,4) = mean(err4(:,iter));
    err5(:,iter) = abs(mf_Ci(:,iter) - mf_Ci(:,iter-1));
    meanerror(iter,5) = mean(err5(:,iter));
    err6(:,iter) = abs(mf_C1i(:,iter) - mf_C1i(:,iter-1));
    meanerror(iter,6) = mean(err6(:,iter));
    err7(:,iter) = abs(mf_C2i(:,iter) - mf_C2i(:,iter-1));
    meanerror(iter,7) = mean(err7(:,iter));
    err8(:,iter) = abs(mf_C3i(:,iter) - mf_C3i(:,iter-1));
    meanerror(iter,8) = mean(err8(:,iter));
    err9(:,iter) = abs(mf_C4i(:,iter) - mf_C4i(:,iter-1));
    meanerror(iter,9) = mean(err9(:,iter));
    if (iter == max_iter) then//maximum iteration check
       success_converged = 1;
    end
    if meanerror(iter,1) < 0.1 then
       if meanerror(iter,2) < 1 then
          if meanerror(iter,6) < 0.0001 then
             if meanerror(iter,7) < 0.0001 then
                if meanerror(iter,8) < 0.0001 then
                   if meanerror(iter,9) < 0.0001 then
                      success_converged = 1;
                   end
                end
             end
          end
       end
    end
    if (iter < min_iter) then//minimum iteration check
       success_converged = 0;
    end
    counter = counter + 1;
    //-------------------------------------------------------------------------

    t(6,iter) = toc()
    time = time + t(6,iter)
    tic()
end

x_axis(1) = 1;
y_axis(1) = T_ai(25,iter);
for k=0:n_z-1
    x_axis(k+1) = k+1;
    y_axis(k+1) = T_ai(25 + k*n_x*n_y,iter);
end
scf(1);
clf(1);
plot(x_axis,y_axis);

x_axis2(1) = 1;
y_axis2(1) = mf_Ci(25,iter);
for k=0:n_z-1
    x_axis2(k+1) = k+1;
    y_axis2(k+1) = mf_Ci(25 + k*n_x*n_y,iter);
end
scf(2);
```

```
clf(2);
plot(x_axis2,y_axis2);

x_axis3(1) = 1;
y_axis3(1) = vf_O2i_dry(25,iter);
for k=0:n_z-1
    x_axis3(k+1) = k+1;
    y_axis3(k+1) = vf_O2i_dry(25 + k*n_x*n_y,iter);
end
scf(3);
clf(3);
plot(x_axis3,y_axis3);

x_axis4(1) = 1;
y_axis4(1) = vf_CO2i_dry(25,iter);
for k=0:n_z-1
    x_axis4(k+1) = k+1;
    y_axis4(k+1) = vf_CO2i_dry(25 + k*n_x*n_y,iter);
end
scf(4);
clf(4);
plot(x_axis4,y_axis4);

x_axis5(1) = 1;
y_axis5(1) = mf_VCi(25,iter);
for k=0:n_z-1
    x_axis5(k+1) = k+1;
    y_axis5(k+1) = mf_VCi(25 + k*n_x*n_y,iter);
end
scf(5);
clf(5);
plot(x_axis5,y_axis5);

TempInlet=T_ai(4*n_x*n_y+1:5*n_x*n_y,iter)
scf(2)  //Bottom Gas Temperature
clf(2);
zm=min(matrix(TempInlet,n_x,n_y)); zM=max(matrix(TempInlet,n_x,n_y))
xset("colormap",jetcolormap(32))
colorbar(zm,zM)
surf(matrix(TempInlet,n_x,n_y),'facecol','interp')

TempExit=T_ao((n_z-3)*(n_x*n_y)+1:n_x*n_y*(n_z-2),iter)
scf(3)  //Exit Gas Temperature
clf(3);
zm=min(matrix(TempExit,n_x,n_y)); zM=max(matrix(TempExit,n_x,n_y))
xset("colormap",jetcolormap(32))
colorbar(zm,zM)
surf(matrix(TempExit,n_x,n_y),'facecol','interp')

////////////////////////////////////////////////////////////////////////////////Verification check energy balance
Q_g_tot = sum(0.001*Q_g(:,1));//[kW]
Q_s_tot = sum(0.001*Q_s(:,1));//[kW]
Q_gen_tot = sum(Q_gen(:,iter));//[kW]
Q_rad_tot = sum(Qg_rad(:,iter));//[kW]

for i=1:length(Burners)
   [h_in(i)] =
ENTHALPY(T_air(i,1),(mf_VCi(Burners(1,i),1)+mf_Ci(Burners(1,i),1)),mf_CO2i(Burners(1,i),1),mf_H2i(Burners(1,i),1),mf_H2Oi
(Burners(1,i),1),mf_O2i(Burners(1,i),1),mf_N2i(Burners(1,i),1),mf_NO2i(Burners(1,i),1),mf_Si(Burners(1,i),1),mf_SO2i(Burners(1,
i),1),mf_Ashi(Burners(1,i),1));
    H_in(i) = m_total(i,1)*h_in(i);
end

//Averaged outlet temperature, oxygen, unburned carbon. "Surface heat flux across outlet"
m_outlet(1) = 0;
```

```
T_outlet(1) = 0;
for k=1:length(Outlet1)
   m_outlet(k) = m_out(Outlet1(k),1);
   T_out(k) = T_ao(Outlet1(k),iter);
   T_outlet(k) = m_outlet(k)*T_ao(Outlet1(k),iter);
   O2_out_wet(k) = vf_O2i(Outlet1(k),iter);
   C_unburned(k) = mf_Co(Outlet1(k),iter);
   mfC1_out(k) = mf_C1o(Outlet1(k),iter);
   mfC2_out(k) = mf_C2o(Outlet1(k),iter);
   mfC3_out(k) = mf_C3o(Outlet1(k),iter);
   mfC4_out(k) = mf_C4o(Outlet1(k),iter);
   [h_out(k)] =
ENTHALPY(T_ao(Outlet1(1,k),iter),(mf_VCo(Outlet1(1,k),iter)+mf_Co(Outlet1(1,k),iter)),mf_CO2o(Outlet1(1,k),iter),mf_H2o(Outlet1(1,k),iter),mf_H2Oo(Outlet1(1,k),iter),mf_O2o(Outlet1(1,k),iter),mf_N2o(Outlet1(1,k),iter),mf_NO2o(Outlet1(1,k),iter),mf_So(Outlet1(1,k),iter),mf_SO2o(Outlet1(1,k),iter),mf_Asho(Outlet1(1,k),iter));
end
FEGT = mean(T_out);
FEO2_wet = mean(O2_out_wet);
FEUBC = mean(C_unburned);
//FEQs = 1e-6*(sum(Q_s(F_n(:),1)) + sum(Q_s(B_n(:),1)) + sum(Q_s(Bo_n(:),1)) + sum(Q_s(L_n(:),1)) + sum(Q_s(R_n(:),1)) + sum(Q_s(T_n(:),1)) - sum(Q_s(Outlet_n(:),1)));//[MW]
FEQs = 1e-6*(sum(Q_s(F_n(:),1)) + sum(Q_s(B_n(:),1)) + sum(Q_s(Bo_n(:),1)) + sum(Q_s(L_n(:),1)) + sum(Q_s(R_n(:),1)) + sum(Q_s(T_n(:),1)));//[MW]
FEQ_cc = 1e-3*(sum(Q_s(B_n(:),1)) + sum(Q_s(L_n(:),1)) + sum(Q_s(R_n(:),1)) + sum(Q_s(T_n(:),1)));//[kW]
H_in_sum = sum(H_in);
H_out = m_furn_e(:,1).*h_out(:);
H_out_sum = sum(H_out);

//Verification for concentration solver
mfC1_out_mass_ave = sum(m_outlet.*mfC1_out)/sum(m_outlet);
mfC2_out_mass_ave = sum(m_outlet.*mfC2_out)/sum(m_outlet);
mfC3_out_mass_ave = sum(m_outlet.*mfC3_out)/sum(m_outlet);
mfC4_out_mass_ave = sum(m_outlet.*mfC4_out)/sum(m_outlet);

t(7,iter) = toc()
time = time + t(7,iter)
disp(time, 'time in seconds')

y=loadwave("SCI/modules/sound/demos/chimes.wav");
playsnd(y)
```